

# Polyaniline/Silicon Dioxide Composite-Based Coating for Corrosion Protection in Geothermal Systems

Inaugural-Dissertation

to obtain the academic degree

Doctor rerum naturalium (Dr. rer. nat.)

submitted to the Department of Biology, Chemistry, and Pharmacy

of Freie Universität Berlin

By

Gabriela Amanda Gita Aristia

2019



This work has been carried out between April 2016 and September 2019 in the Division 7.6 of Corrosion and Corrosion Protection at Bundesanstalt für Materialforschung und -prüfung (BAM), Berlin, Germany, under the supervision of Dr. rer. nat. Ralph Bäßler.

1<sup>st</sup> Reviewer: Dr. rer. nat. Ralph Bäßler

2<sup>nd</sup> Reviewer: Prof. Dr. Biprajit Sarkar

Date of defense: 24.01.2020



# Declaration

I hereby declare that the thesis submitted is my own unaided work. All direct or indirect sources used are acknowledged as references.

Berlin, September 2019

Gabriela Aristia



# Summary

Geothermal energy is one of the cleanest renewable alternatives to reduce the dependency on fossil fuel [1, 2]. Despite its promising future, its implementation faces various challenges, one of them being corrosion processes. To implement this energy, hot fluids are pumped from a geothermal well. These hot fluids originate from deep within the earth, so consist of different ionic species and gases in a wide range of temperatures, which lead to their corrosive nature. In terms of geothermal energy resources, Indonesia is at the forefront, with the highest preserved geothermal energy in the world of about 29 GWe and 312 potential geothermal locations [3]. Geothermal wells in Sibayak (North Sumatera), Indonesia, belong to young stratovolcanoes and have operating temperatures varying from 36 °C at the near ground surface to 310 °C at the bottom of the well, which is liquid-dominated with acidic and saline properties [4, 5]. Therefore, this geothermal fluid creates an aggressive environment that is conducive to corrosion of the powerplant infrastructure.

Parts of the geothermal powerplant infrastructure, such as pipelines and heat exchangers, are commonly made of metals, e.g. carbon steel and stainless steel. Consequently, they may undergo corrosion and scaling when exposed to the geothermal fluid, especially for carbon steel. To ensure the safety and longevity of a geothermal powerplant, the infrastructure is constructed of expensive corrosion resistant alloys [6–10], e.g., titanium and Ni-Cr based alloys, or carbon steel which needs to be protected by coatings or inhibitors.

To address the corrosion of carbon steel in the geothermal environment, artificial geothermal water was used to simulate a geothermal well in Sibayak, Indonesia, with pH 4 and a saline composition of 1,500 mg/l Cl<sup>-</sup>, 20 mg/l SO<sub>4</sub><sup>2-</sup>, 15 mg/l HCO<sub>3</sub><sup>-</sup>, 200 mg/l Ca<sup>2+</sup>, 250 mg/l K<sup>+</sup>, and 600 mg/l Na<sup>+</sup>. Carbon steel underwent the most severe corrosion at 150°C in an oxygen-containing solution with a corrosion rate of 0.34 mm/year, which is approximately ten times higher than that in the absence of dissolved oxygen. In all conditions, pitting corrosion was observed, which necessitate a protection strategy on carbon steel. In order to promote a cost effective and locally available option, this work focused on an easily applicable coating which utilized local resources.

Toward developing such protective coating based on the locally available resources in Indonesia which can yield good corrosion resistance and thermal stability in geothermal environment, two additional components, i.e. polyaniline (PANI) and silicon dioxide, were used to modify an alkyd-based commercial coating. The selection of the alkyd-based coating as a matrix focused on the industrial convenience basis, where the coating application procedure should be simple and easy to apply within reasonable costs. The alkyd-based coating underwent severe blistering when exposed to the artificial geothermal water at 70 and 150°C due to the reaction between CaCO<sub>3</sub> (as one of its components) and the artificial geothermal water, as well as a possible alkyd hydrolysis in the initial stage of exposure. In the oxygen-free solution, the degradation was controlled by chemical and thermal reactions, whereas in the aerated condition, oxidization at the coating surface further accelerated polymer degradation.

PANI was chosen as one of the anticorrosion pigments which was widely developed over the past decades. To investigate the interaction between PANI and the artificial geothermal water, PANI film was electrochemically deposited on the carbon steel surface and exposed to the artificial geothermal water. Electrochemically synthesized oxalate-doped PANI was

protective against corrosion of carbon steel in artificial geothermal water at room temperature. The mechanism involved an exchange of electroactive species within the coating layer, as confirmed by electrochemical impedance spectra. Interaction of ionic species, such as  $\text{Cl}^-$ ,  $\text{Na}^+$ ,  $\text{Ca}^{2+}$  from the artificial geothermal water, with the outer layer of PANI is suggested both at  $25^\circ\text{C}$  and  $150^\circ\text{C}$ , based on the EDX spectra of the coating surface after exposure to the artificial geothermal water. Thus, the protection mechanism of PANI is not solely based on the physical barrier layer properties, but rather associated with the redox mediated properties of PANI, which selectively allow ionic species intrusion from the electrolyte into the PANI layer. Although PANI is a promising candidate as an anticorrosion coating, its morphological characterization reveals that electrochemically deposited PANI is not stable for an application at  $150^\circ\text{C}$ . Therefore, another approach was used to promote better protective behavior of PANI by dispersing chemically synthesized PANI in the alkyd-based coating.

To enhance the thermal stability of the coating, silicon dioxide ( $\text{SiO}_2$ ) was added, which was able to prolong the sustainability of coated metals until 28 days compared to the unmodified alkyd-based coating, which underwent a change in color to brown/orange only within 7 days of exposure. This improvement might be associated with the role of  $\text{SiO}_2$  to proportionate the thermal expansion coefficient of the coating system to be compatible with that of carbon steel. Although the coating is thermally enhanced, the electrolyte might still intrude through the coating resulting in the change of coating color after 28 days of exposure in the artificial geothermal water. When PANI was added, the coating system provided an active corrosion protection on the carbon steel surface. The chemical and morphological characterization of the PANI-alkyd and  $\text{SiO}_2$ -alkyd coating system showed that coatings were improved, and no blisters were observed, albeit the degradation continued. Based on the results of exposure tests, the combined coating system was further investigated.

The combinational coating of PANI/ $\text{SiO}_2$ -alkyd was used with 2 wt% of PANI and 15 wt% of  $\text{SiO}_2$ . Electrochemical tests indicated cathodic protection at  $150^\circ\text{C}$ , as the  $E_{\text{corr}}$  of PANI/ $\text{SiO}_2$  remained approximately 400 mV lower than the carbon steel potential. The impedance spectra of the combinational coating of PANI/ $\text{SiO}_2$  showed a continuous decrease in the absolute impedance value over time. A significant decrease was observed within one day of exposure, followed by a slow gradual decrease, which might be associated with water absorption in the coating. FTIR spectra revealed that several peaks associated with the organic portion of the coatings were reduced after the specimens were exposed for 6 months. However, the absorption peaks related to the inorganic portion of the coatings remained stable until 6 months. Morphological characterization of the combinational coating of PANI/ $\text{SiO}_2$  showed that there were no blisters or significant discoloration of coatings after long-term exposure for 6 months in artificial geothermal water at  $150^\circ\text{C}$ , indicating that the chemical degradation does not significantly affect the functionality of the coating. This clearly shows the durability of PANI/ $\text{SiO}_2$  coating in the geothermal condition, suggesting that this coating can be used for such geothermal application. However, further testing of this coating should be conducted in a real geothermal environment on-site to ensure safety and viability.



# Zusammenfassung

Geothermische Energie ist eine saubere und erneuerbare Alternative, um die Nutzung von fossilen Brennstoffen zu reduzieren [1, 2]. Obwohl es eine vielversprechende Zukunft hat, müssen verschiedene Herausforderungen bei der Realisierung von Geothermieranlagen, wie z.B. Korrosionsprozesse, bewältigt werden. Um diese Energie zu verwenden, werden Geothermalwässer aus bestimmten Tiefen der Erde gefördert. Das Geothermalwasser beinhaltet verschiedene Ionen und Gase, und umfasst einen weiten Temperaturbereich, worauf dessen korrosive Wirkung zurückzuführen ist. In Bezug auf die geothermischen Energieressourcen zeichnet sich Indonesien durch das höchste Potential an geothermischer Energie der Welt von etwa 29 GWe, an 312 potenziellen Geothermiestandorten, aus [3]. Geothermalquellen in Sibayak (Nordsumatra), Indonesien, gehören zu den jungen Stratovulkanen mit Betriebstemperaturen von 36 °C an der bodennahen Oberfläche und bis 310 °C in der Tiefe. Sie sind flüssigkeitsdominiert und weisen saure und salzige Eigenschaften auf [4, 5]. Diese Geothermiefluide schaffen somit eine aggressive Umgebung, die der Korrosion der Kraftwerksinfrastruktur förderlich ist.

Die Infrastruktur von Geothermieranlagen besteht aus verschiedenen Materialien, einschließlich Metallen, z. B. C-Stahl und Edelstahl. Wenn die Infrastruktur der Geothermiefluide ausgesetzt ist, kann dieses zu Korrosion und Ablagerungen führen, insbesondere beim C-Stahl. Um einen sicheren und zuverlässigen Betrieb von Geothermieranlagen zu garantieren, werden entweder teure, korrosionsbeständige Legierungen [6-10] (z.B. Titan, Ni-Cr-Basislegierungen) verwendet oder sekundärer Korrosionsschutz für C-Stahl (z. B. Beschichtungen, Inhibitoren) eingesetzt.

Um die Wechselwirkung von C-Stahl mit dem Geothermalwasser zu untersuchen, wurde ein künstliches Geothermalwasser verwendet. Es basiert auf einer geothermischen Quelle in Sibayak, Indonesien mit einem pH-Wert von 4 und einer Zusammensetzung von 1.500 mg/l Cl<sup>-</sup>, 20 mg/l SO<sub>4</sub><sup>2-</sup>, 15 mg/l HCO<sub>3</sub><sup>-</sup>, 200 mg/l Ca<sup>2+</sup>, 250 mg/l K<sup>+</sup>, and 600 mg/l Na<sup>+</sup>. C-Stahl korrodiert in sauerstoffhaltige Lösung bei 150 °C mit einer Korrosionsrate von 0,34 mm/Jahr korrodiert, was etwa dem Zehnfachen der Korrosionsrate bei Abwesenheit von gelöstem Sauerstoff entspricht. In allen Fällen wurde Lochkorrosion beobachtet. Daher ist die Beschichtung von C-Stahl als Schutzstrategie gegen Korrosion erforderlich.

Um eine kostengünstige und unter den vor Ort-Bedingungen einfach handhabbare Möglichkeit bereitzustellen, konzentriert sich diese Arbeit auf eine anwendbare Beschichtung unter Verwendung der örtlich verfügbaren Ressourcen. Um eine solche Schutzbeschichtung zu entwickeln, die in geothermischer Umgebung eine gute Korrosions- und Temperaturbeständigkeit bietet, wurden zwei zusätzliche Komponenten verwendet, um eine alkyd-basierende Beschichtung zu modifizieren, Polyanilin und Siliciumdioxid. Dabei wurde ebenfalls die industrielle Applizierbarkeit berücksichtigt. Ebenso sollte das Beschichtungsverfahren einfach und kostengünstig sein. Die ursprüngliche Beschichtung auf Alkydbasis zeigte in künstlichen Geothermalwasser bei 70 °C und 150 °C im Anfangsstadium starke Blasenbildung aufgrund der Reaktion zwischen CaCO<sub>3</sub> (als einer seiner Komponente) und dem Wasser und einer möglichen Alkydhydrolyse. In der sauerstofffreien Lösung wurde die Degradation durch chemische und thermische Reaktionen kontrolliert, während in der

sauerstoffhaltigen Lösung eine Oxidation an der Beschichtungsoberfläche die Polymerdegradation weiter beschleunigt.

In den letzten Jahrzehnten wurden Polyaniline als eine Art der Korrosionsschutzzusätze verwendet. Elektrochemisch hergestelltes oxalat-dotiertes Polyanilin schützt C-Stahl in künstlichen Geothermalwasser bei Raumtemperatur vor Korrosion. Der Polyanilinschutzmechanismus beinhaltet den Austausch elektroaktiver Spezies innerhalb der Schicht, was mittels elektrochemischer Impedanzspektroskopie bestätigt wird. EDX-Spektren der Beschichtungsoberfläche nach Auslagerungsversuchen in künstlichem Geothermalwasser bei 25 °C und 150 °C weisen auf die Wechselwirkung von ionischen Spezies wie  $\text{Cl}^-$ ,  $\text{Na}^+$ ,  $\text{Ca}^{2+}$  aus dem künstlichen Geothermalwasser mit der äußeren Schicht aus Polyanilin hin. Obwohl Polyanilin ein vielversprechender Kandidat als Korrosionsschutzbeschichtung ist, zeigt die morphologische Charakterisierung von Polyanilin, dass elektrochemisch abgeschiedenes Polyanilin für eine Anwendung bei 150 °C nicht stabil ist. Daher wurde ein anderer Ansatz verwendet, um das Schutzverhalten von Polyanilin zu verbessern, indem chemisch synthetisiertes Polyanilin in einer Beschichtung auf Alkydbasis dispergiert wurde.

Zur Verbesserung der thermischen Stabilität von Beschichtungen wurde dem Beschichtungssystem  $\text{SiO}_2$  zugesetzt. Das  $\text{SiO}_2$ -Alkyd-Beschichtungssystem konnte die Beständigkeit der beschichteten Metalle bis zu 28 Tagen verlängern. Im Vergleich zeigte die unmodifizierte alkydbasierte Beschichtung, innerhalb von 7 Tagen nach den Auslagerungsversuchen eine Farbänderung auf braun/orange. Diese Verbesserung könnte mit der Rolle von Siliziumdioxid in Verbindung gebracht werden, das den Wärmeausdehnungskoeffizienten des komplexen Beschichtungssystems so kontrolliert, dass dieser dem von C-Stahl kompatibel ist. Obwohl die Beschichtung thermisch verstärkt ist, kann der Elektrolyt immer noch durch die Beschichtung hindurchdringen, was nach 28-tägigem Auslagerungsversuch im künstlichen Geothermalwasser zu einer Änderung der Beschichtungsfarbe auf braun/orange im Zusammenhang mit Eisenoxid führt. Nach Zugabe von Polyanilin wurde das Beschichtungssystem beständig und kann einen aktiven Korrosionsschutz auf der C-Stahloberfläche bewirken. Die chemische und morphologische Charakterisierung des PANI-Alkyd- und  $\text{SiO}_2$ -Alkyd-Beschichtungssystems zeigten, dass die Beschichtungen verbessert wurden. Es wurden keine Blasen beobachtet, obwohl sich die Degradation fortsetzte wurde.

Die kombinatorische Beschichtung von PANI/ $\text{SiO}_2$ -Alkyd wurde mit 2 Gew.-% PANI und 15 Gew.-%  $\text{SiO}_2$  verwendet. Elektrochemische Versuche deuteten auf kathodischen Schutz bei 150 °C hin, da  $E_{\text{corr}}$  von PANI/ $\text{SiO}_2$  um etwa 400 mV niedriger blieb, als das Potential des C-Stahl. Die Impedanzspektren der kombinatorischen Beschichtung von PANI/ $\text{SiO}_2$  zeigen, dass es im Laufe der Zeit zu einer kontinuierlichen Abnahme des absoluten Impedanzwertes kam. Der stärkste Rückgang wurde innerhalb eines Tages nach dem Auslagerungsversuch beobachtet, gefolgt von einer langsamen allmählichen Abnahme, die mit der Wasseraufnahme in der Beschichtung verbunden sein könnte. FTIR-Spektren zeigten, dass mehrere Peaks, die mit dem organischen Teil von Beschichtungen verbunden sind, innerhalb von 6 Monaten reduziert werden. Die Absorptionspeaks in Bezug auf den anorganischen Teil der Beschichtungen blieben jedoch bis zu 6 Monaten stabil. Die morphologische Charakterisierung der kombinierten Beschichtung aus PANI/ $\text{SiO}_2$  zeigt, dass sich nach einem 6-monatigen Auslagerungsversuch im künstlichen Geothermalwasser bei 150 °C keine Blasen oder

signifikanten Verfärbungen der Beschichtungen gebildet haben. Das zeigt, dass die chemische Degradation nicht signifikant ist, um die Funktionalität der Beschichtung zu beeinflussen. Diese Ergebnisse weisen auf eine Beständigkeit der PANI/SiO<sub>2</sub>-Beschichtung unter geothermalen Bedingungen hin. Somit kann dieser für den Korrosionsschutz von C-Stahl vielversprechende Kandidat zum Einsatz kommen. Tests unter realen Betriebsbedingungen werden für zukünftige Untersuchungen empfohlen, um eine sichere Betriebsweise zu gewährleisten.



# Table of Contents

Declaration .....	v
Summary .....	vii
Zusammenfassung .....	ix
Table of Contents .....	xiii
List of Tables .....	xvii
List of Figures .....	xix
List of Units, Chemicals, and Abbreviation .....	xxvi
Chapter 1. Introduction and Motivation .....	1
1.1. Introduction .....	1
1.2. Motivation of Study .....	3
1.3. Research Objectives .....	3
1.4. Thesis Structure .....	4
Chapter 2. Literature Review and State of the Art .....	5
2.1. Geothermal Energy .....	5
2.1.1. Utilization of Geothermal Energy .....	5
2.1.2. Geothermal Energy in Indonesia .....	6
2.1.3. Basic Technology and Challenges of Geothermal Energy .....	6
2.2. Corrosion in the Geothermal Environment .....	7
2.2.1. Chemistry of the Geothermal Environment .....	8
2.2.2. Types of Corrosion and Coating Degradation .....	9
2.2.3. Influencing Factors .....	12
2.3. Material Properties and Coating Components .....	15
2.3.1. Carbon Steel .....	15
2.3.2. Protective Coatings .....	19
2.3.3. Polyaniline .....	21
2.3.4. Silicon Dioxide .....	29
Chapter 3. Methodology and Experimental Techniques: Theory and Practice .....	31
3.1. Investigated Material .....	31
3.1.1. Carbon Steel .....	32
3.1.2. Coating System .....	32
3.2. Coating Application and Characterization .....	33
3.2.1. Electrochemical Deposition .....	33

## Table of Contents

---

3.2.2. Polyaniline/Silica Composite Coating .....	33
3.3. Experimental Conditions .....	34
3.4. Evaluation Techniques .....	34
3.4.1. Exposure Test.....	34
3.4.2. Microscopic Study .....	35
3.4.3. Spectroscopy Methods .....	35
3.4.4. X-Ray Diffractometry .....	36
3.4.5. Thermogravimetry Analysis (TGA).....	36
3.4.6. Electrochemical Measurement.....	36
3.4.7. Adhesion Test .....	43
3.5. Test Set-up.....	43
3.5.1. Specimens .....	43
3.5.2. Testing Cell.....	44
Chapter 4. Carbon Steel Corrosion in Artificial Geothermal Water .....	47
4.1. Effect of Temperature.....	47
4.1.1. Influence of Dissolved Gases on the Corrosion Rate of Carbon Steel .....	47
4.1.2. Morphological Characterization .....	48
4.1.3. Influence of Temperature on the Electrochemical Behavior of Carbon Steel .....	49
4.2. Effect of Dissolved Oxygen .....	53
4.2.1. Influence of Exposure Time on the Corrosion Rate of Carbon Steel .....	53
4.2.2. Identification of Pitting Corrosion .....	54
4.2.3. Corrosion Mechanism at Room Temperature.....	56
4.2.4. Corrosion Mechanism of Carbon Steel at 150 °C.....	60
4.3. Influence of pH on Carbon Steel Corrosion .....	64
4.3.1. Morphological Characterization .....	65
4.3.2. Influence of pH on Carbon Steel $E_{\text{corr}}$ .....	66
4.4. Summary and Conclusion.....	66
Chapter 5. Electrochemical Deposition of Polyaniline and its Suitability in Geothermal Solution .....	69
5.1. Electrochemical Polymerization of Polyaniline on Graphite Electrode .....	69
5.2. Interaction of Polyaniline Coated Graphite with the Geothermal Solution.....	72
5.3. Electrochemical Polymerization of Polyaniline on Carbon Steel .....	74
5.3.1. Choosing the Medium for Polymerization.....	74
5.3.2. Optimization of Potential Range.....	75

---

5.3.3. Effect of Aniline to Oxalic Acid Ratio .....	77
5.3.4. Optimization of Cycle Number .....	78
5.4. Electrochemical Behavior of PANI-coated Carbon Steel in the Geothermal Solution.	83
5.4.1. Electrochemical Test at Room Temperature.....	83
5.4.2. Electrochemical Test at 150 °C.....	85
5.4.3. Surface Morphological Characterization .....	87
5.5. Conclusion .....	88
Chapter 6. Synthesis and Characterization of Polyaniline and Silicon Dioxide Composite Coatings.....	89
6.1. Alkyd-Based Matrix .....	89
6.1.1. Chemical and Morphological Characterization .....	89
6.1.2. Exposure Test in the Artificial Geothermal Water at Different Temperatures.....	91
6.1.3. Alkyd Coating Stability in the Oxygen-Containing Solution at 150 °C.....	93
6.2. Polyaniline .....	96
6.2.1. Polyaniline Synthesis and Characterization .....	97
6.2.2. The Effect of Polyaniline Addition .....	99
6.3. Silicon Dioxide Filled Alkyd Coating .....	101
6.3.1. Silicon Dioxide Characterization .....	101
6.3.2. The Effect of Silicon Dioxide Addition .....	103
6.4. Conclusion .....	105
Chapter 7. Corrosion Study of Polyaniline/Silicon Dioxide Modified Alkyd Coating .....	107
7.1. Combinational Properties of Pigments .....	107
7.1.1. Morphological and Chemical Analysis.....	107
7.1.2. Mechanical Testing Using Pressure Sensitive Adhesive .....	111
7.2. Effect of Temperature on the Corrosion Behavior of Coatings.....	112
7.3. Suitability of Coatings in the Oxygen Containing Solution .....	117
7.4. Compatibility of the Electrochemical Test and Exposure Test at 150 °C.....	118
7.5. Durability of Coatings .....	119
7.6. Conclusion .....	122
Chapter 8. Conclusion and Outlook .....	125
8.1. Conclusion .....	125
8.2. Novel Aspects and Relevance to Future Work and Industry.....	127
8.3. Outlook .....	128
Bibliography.....	131

## Table of Contents

---

Appendix .....	141
1. Error Bar.....	141
2. Crystallography Data for Quartz, and results from Match!3 .....	142
Publication List .....	143
Acknowledgements .....	145



# List of Tables

<b>Table 2.1.</b> Corrosivity Classification Systems of Geothermal Fluid [26, 50] .....	9
<b>Table 2.2.</b> Geothermal Brines Enthalpy Resources Classification [51-54].....	9
<b>Table 2.3.</b> Type of Corrosion in Geothermal Environment: descriptions and examples .....	10
<b>Table 2.4.</b> Possible forms of iron oxides [72].....	17
<b>Table 2.5.</b> Composition of resulting corrosion products in different conditions [72].....	18
<b>Table 2.6.</b> Crystal structures and properties of the possible corrosion products discussed in this thesis [72–74]. .....	19
<b>Table 2.7.</b> Corrosion prevention methods .....	20
<b>Table 2.8.</b> Relevant references supporting the protection mechanism of conducting polymer via barrier protection.....	25
<b>Table 2.9.</b> Relevant references supporting the protection mechanism of conducting polymer via anodic protection.....	26
<b>Table 2.10.</b> Relevant references supporting the protection mechanism of conducting polymer via controlled inhibitor release.....	27
<b>Table 2.11.</b> Relevant references supporting the protection mechanism of conducting polymer via cathodic protection.....	27
<b>Table 2.12.</b> Relevant references supporting the protection mechanism of conducting polymer via corrosion inhibition .....	28
<b>Table 3.1.</b> Elemental composition of carbon steel based on arc/spark emission spectroscopy .....	32
<b>Table 3.2.</b> Coatings type description and its formulation with the different types of PANI presented in brackets .....	34
<b>Table 3.3.</b> Chemical Composition of Artificial Geothermal Water .....	34
<b>Table 4.1.</b> Fitting output of EIS in aerated condition at 25 °C .....	59
<b>Table 4.2.</b> Fitting output of EIS in deaerated condition at 25 °C .....	59
<b>Table 4.3.</b> Fitting output at 150 °C: aerated condition .....	63
<b>Table 4.4.</b> Fitting output at 150 °C: deaerated condition.....	63
<b>Table 5.1.</b> ATR-FTIR spectra assignment of PANI/H <sub>3</sub> PO <sub>4</sub> synthesized using chemical and electrochemical polymerization compared and assigned to the reference [112].....	72
<b>Table 5.2.</b> Fitting output of EIS data obtained during the polyaniline deposition on carbon steel.....	80
<b>Table 5.3.</b> Fitting output of impedance spectra of the PANI/CS exposed to the artificial geothermal water at room temperature.....	85

<b>Table 5.4.</b> Fitting output of impedance spectra of PANI/CS exposed to the artificial geothermal water at 150 °C.....	86
<b>Table 6.1.</b> FTIR peak assignment to the functional group of esters [112, 143]. .....	91
<b>Table 6.2.</b> Peak assignment for FTIR spectra of chemically synthesized polyaniline [112] .....	99
<b>Table 7.1.</b> Peak position of FTIR spectra and its assignment to the functional group of binder, SiO <sub>2</sub> particles, PANI particles, and combinational coating PANI-1/SiO <sub>2</sub> [112, 143, 164].....	110
<b>Table 7.2.</b> Mass loss of PANI-1/SiO <sub>2</sub> coatings with respect to time.....	120
<b>Table 7.3.</b> FTIR spectra assignment of PANI-1/SiO <sub>2</sub> coatings after exposed in the artificial geothermal water for different exposure time .....	121

# List of Figures

<b>Figure 2.1.</b> Global geothermal capacity in 2015 equating to 12.1 GWe [41] .....	5
<b>Figure 2.2.</b> World map showing the lithospheric plate boundaries (red dots = active volcanoes) [38].....	6
<b>Figure 2.3.</b> Structure of the earth and geothermal gradient (left) and basic technology and utilization of a geothermal power plant (right) [45].....	7
<b>Figure 2.4.</b> Iron-iron carbide phase diagram [49, 61].....	13
<b>Figure 2.5.</b> Microstructure of low alloy carbon steel St37 [62] .....	13
<b>Figure 2.6.</b> Transformation pathways of iron oxide from $Fe^{2+}$ and $Fe^{3+}$ [72] .....	18
<b>Figure 2.7.</b> An example of a simplified chemical formulation of alkyd [82].....	21
<b>Figure 2.8.</b> General polymeric structure of polyaniline [22].....	21
<b>Figure 2.9.</b> Polymeric structure of emeraldine salt [22].....	22
<b>Figure 2.10.</b> Polymerization steps of polyaniline via electrochemical polymerization [22] .....	23
<b>Figure 2.11.</b> Polymerization steps of polyaniline via chemical polymerization [22].....	24
<b>Figure 2.12.</b> Pourbaix diagram of polyaniline in different oxidation states [95] .....	26
<b>Figure 2.13.</b> Various schemes of polyaniline-based protective coatings (adapted from [85]).....	28
<b>Figure 2.14.</b> Phase diagram of silicon dioxide in high temperature and high pressure, according to the calculations of Swamy et al. [109]. Tridymite is not shown, the dashed curves represent the metastable extensions of the melting curves of quartz and coesite. ....	30
<b>Figure 3.1.</b> Overview of the experimental procedure.....	31
<b>Figure 3.2.</b> Schematic representation of the effect of increasing oxidizing power of the environment on the corrosion of an active-passive type alloy, such as stainless steel, where the x-axis represents the applied potential, and y-axis is the current density in logarithmic scale [55].....	37
<b>Figure 3.3.</b> Electrical circuit of (a) a blocking system consisting of $R_s$ in series with C and (b) a Randles cell consisting of $R_s$ , C, and R [114] .....	39
<b>Figure 3.4.</b> Impedance-plane or Nyquist plot of impedance data for $R_s = 20 \Omega$ , $R = 200 \Omega$ , and $C = 1 \text{ mF}$ simulated by Gamry Echem Analyst. The blocking system (Figure 3.3a) is represented by the red lines, and the reactive system (Figure 3.3b) is represented by the blue lines (adapted from [114]) .....	40
<b>Figure 3.5.</b> Bode representation of impedance data for $R_s = 20 \Omega$ , $R = 200 \Omega$ , and $C = 1 \text{ mF}$ simulated by Gamry Echem Analyst. The blocking system (Figure 3.3a) is represented by the red lines, and the reactive system (Figure 3.3b) is represented by the	

---

blue lines. Characteristic frequencies are noted as $f_{RC} = 1/(2\pi RC)$ and $f_c = 1/(2\pi R_s C)$ , (a) magnitude and (b) phase angle (adapted from [114]) .....	41
<b>Figure 3.6.</b> Theoretical impedance spectra of degraded polymer coated metal shown in (a) Bode plot [118], and (b) the related equivalent electrical circuit [118].....	42
<b>Figure 3.7.</b> Specimen dimensions for (a) exposure test and (b) electrochemistry test.....	44
<b>Figure 3.8.</b> Exposure test set-up for lower temperatures, illustration of specimen arrangement inside the glass vessel.....	44
<b>Figure 3.9.</b> Electrochemical test set-up in a glass vessel for lower temperature experiments: (a) illustration and description of test set-up, and (b) image of test set-up and the electrodes arrangement .....	44
<b>Figure 3.10.</b> Exposure test set-up for higher temperatures: (a) illustration of specimen arrangement inside the autoclave, and (b) image of autoclaves.....	45
<b>Figure 3.11.</b> Electrochemical test set-up in an autoclave for higher temperature experiments up to 150 °C: (a) illustration and description of test set-up, and (b) image of the test set-up.....	45
<b>Figure 4.1.</b> Corrosion rate of carbon steel as a function of temperature in artificial geothermal water at 25, 70 and 150 °C in different dissolved gas composition. Corrosion rates of specimens exposed to deaerated solution has error values of 0.001 mm/year. ....	47
<b>Figure 4.2.</b> SEM images of carbon steel exposed in deaerated geothermal solution at (a) 25 °C (b) 70 °C (c) 150 °C .....	48
<b>Figure 4.3.</b> SEM images of carbon steel exposed to deaerated geothermal solution at 150 °C for 28 days (a) surface morphology (b) cross section.....	49
<b>Figure 4.4.</b> $E_{corr}$ of carbon steel exposed to different temperatures in the artificial geothermal water for seven days. ....	50
<b>Figure 4.5.</b> Corrosion potential of iron with hydrogen evolution at pH 0. Potentials are in SHE [56, 58].....	50
<b>Figure 4.6.</b> Open circuit potential of carbon steel exposed to the artificial geothermal water within the first few hours (a) at 25 °C, (b) at 70 °C and (c) at 150°C.....	51
<b>Figure 4.7.</b> EIS of carbon steel in deaerated geothermal solution at different temperatures: (a) Bode magnitude plot and (b) phase angle plot of the first day; (c) Bode magnitude plot and (d) phase angle plot of the seventh day .....	52
<b>Figure 4.8.</b> Corrosion rate of carbon steel exposed at 150 °C for 7 and 28 days in aerated and deaerated artificial geothermal water. Error bars are between $10^{-3}$ and $10^{-6}$ mm/year.....	54
<b>Figure 4.9.</b> Optical microscope images of the surface appearance of carbon steel after exposure to artificial geothermal water (a) in aerated condition after 7 days, and (b) in deaerated condition after 28 days. SEM images of the cross section (c) in aerated condition after 7 days, and (d) in deaerated condition after 28 days .....	55

<b>Figure 4.10.</b> OCP of carbon steel in aerated and deaerated artificial geothermal water at 25 °C.....	57
<b>Figure 4.11.</b> Nyquist plot of carbon steel exposed to artificial geothermal water at room temperature in (a) aerated and (b) deaerated solution .....	57
<b>Figure 4.12.</b> EIS results of carbon steel exposed to artificial geothermal water at 25 °C (a) Bode magnitude plot, and (b) phase angle plot in aerated solution; (c) Bode magnitude plot, and (d) phase angle plot in deaerated solution.....	58
<b>Figure 4.13.</b> EIS fitting parameter as a function of time (a) $R_{ct}$ (b) $C_{dl}$ (c) $R_{po}$ and (d) $C_f$ .....	60
<b>Figure 4.14.</b> OCP of carbon steel in aerated and deaerated artificial geothermal water at 150 °C.....	61
<b>Figure 4.15.</b> Nyquist plot of carbon steel exposed to artificial geothermal water at 150 °C (a) in aerated and (b) deaerated solution .....	62
<b>Figure 4.16.</b> EIS results of carbon steel exposed to artificial geothermal water at 150 °C (a) Bode magnitude plot, and (b) phase angle plot in aerated solution; (c) Bode magnitude plot, and (d) phase angle plot in deaerated solution.....	63
<b>Figure 4.17.</b> EIS fitting parameter as a function of time of carbon steel exposed at 150 °C in aerated and deaerated solution, with the parameter of (a) $R_{ct}$ (b) $C_{dl}$ (c) $R_{po}$ (d) $C_f$ .....	64
<b>Figure 4.18.</b> Solution pH at 25 °C in the renewed solution with an interval of 24 and 48 hours .....	65
<b>Figure 4.19.</b> SEM image of carbon steel after exposed at 150 °C for seven days in the solution with (a) pH 4 and (b) pH 7 .....	65
<b>Figure 4.20.</b> OCP of carbon steel in deaerated artificial geothermal water at 150 °C with pH 4 and 7 .....	66
<b>Figure 4.21.</b> $R_{ct}$ representing corrosion resistance as a function of time. ....	67
<b>Figure 5.1.</b> Electrochemical deposition of PANI/H <sub>3</sub> PO <sub>4</sub> on a graphite electrode (a) Cyclic voltammogram, 20 mV/s, (potential is vs. Ag/AgCl) (b) Nyquist plot (c) Bode magnitude plot (d) phase angle plot. ....	70
<b>Figure 5.2.</b> Nyquist plot of a porous film with different types of diffusions and the illustration of diffusion in the coated electrode under a semi-infinite boundary and a reflective boundary condition [114]......	71
<b>Figure 5.3.</b> ATR- FTIR spectra of PANI/H <sub>3</sub> PO <sub>4</sub> synthesized using chemical and electrochemical polymerization .....	72
<b>Figure 5.4.</b> Impedance spectra of uncoated (written as C) and polyaniline coated graphite electrode (written as PANI/C) at 25, 55, and 75 °C (a) Nyquist plot (b) magnification of Nyquist plot (c) Bode magnitude plot (d) phase angle plot .....	73
<b>Figure 5.5.</b> Equivalent electrical circuit of Randles cell with diffusion, with different types of diffusion element representing (a) semi-infinite diffusion, and (b) reflective finite diffusion .....	74

<b>Figure 5.6.</b> Impedance spectra of polyaniline coated graphite electrode at 25 °C fitted to the equivalent circuit with semi-infinite and reflective boundary of diffusion element, presented in (a) Nyquist plot, and (b) Bode magnitude and phase angle plot.....	74
<b>Figure 5.7.</b> Cyclic voltammogram of polyaniline/oxalate deposition on carbon steel with a scan rate of 10 mV/s (a) in 0.05 M aniline + 0.1 M oxalic acid, from -0.6 to 1.0 V (b) in 0.05 M aniline + 0.1 M oxalic acid, from -0.6 to 1.5 V vs. Ag/AgCl (c) in 0.1 M oxalic acid, from -0.6 to 1.5 V vs. Ag/AgCl, and (d) the corresponding SEM image after CV with experimental parameters (c).....	76
<b>Figure 5.8.</b> Electrochemical deposition using cyclic voltammetry with 10 cycles (a) PANI/oxalate-1 with pores still visible (b) PANI/oxalate-2 (c) SEM image of (a), and; (d) SEM image of (b).....	78
<b>Figure 5.9.</b> EIS during the polymerization for 10 cycles with an interval of 1 cycle (a) Nyquist plot (b) magnified Nyquist plot between 0-500 $\Omega$ (c) Bode magnitude plot, (d) phase angle plot, and (e) equivalent electrical circuit .....	79
<b>Figure 5.10.</b> EIS during the polymerization between 10 <sup>th</sup> – 50 <sup>th</sup> cycles with an interval of 10 cycles (a) Nyquist plot, (b) magnified Nyquist plot, (c) Bode magnitude plot, and (d) phase angle plot.....	81
<b>Figure 5.11.</b> Characterization of polyaniline/oxalate coated carbon steel after 10 cycles (a,c,e,g) and after 50 cycles (b, d, f, h). Higher SEM magnification presenting the morphology of polyaniline/oxalate (c and d). The EDX spectra (e and f) show the elemental composition of (c and d), respectively. Cross sectional images are also presented (g and h).....	82
<b>Figure 5.12.</b> $E_{corr}$ of carbon steel (CS) and PANI/CS in artificial geothermal water at room temperature (a) 0 – 7 days, and (b) 0 – 2 hours.....	83
<b>Figure 5.13.</b> Equivalent electrical circuit for EIS data fitting of carbon steel and coated carbon steel (PANI/CS) in the artificial geothermal water at 25 °C .....	84
<b>Figure 5.14.</b> Impedance spectra after the specimen was exposed to artificial geothermal water at room temperature. Nyquist plot of (a) carbon steel, (b) PANI/CS; Bode magnitude plot of (c) carbon steel, (d) PANI/CS; phase angle plot of (e) carbon steel, (f) PANI/CS.....	84
<b>Figure 5.15.</b> $E_{corr}$ of carbon steel (CS) and PANI/CS in artificial geothermal water at 150 °C (a) 0 – 7 days (b) 0 – 30 hours.....	85
<b>Figure 5.16.</b> Impedance spectra after specimen was exposed to the artificial geothermal water at 150 °C: Nyquist plot of (a) carbon steel, and (b) PANI/CS; Bode magnitude plot of (c) carbon steel, and (d) PANI/CS; phase angle plot of (e) carbon steel, and (f) PANI/CS.....	86
<b>Figure 5.17.</b> $R_{ct}$ of PANI/CS as a function of time at room temperature and at 150 °C. Error bars indicate the error value of $R_{ct}$ from the fitting of impedance spectra.....	87

---

<b>Figure 5.18.</b> SEM images of polyaniline/CS (a) at initial condition (b) after exposed to room temperature (c) after exposed to 150 °C. EDX of polyaniline/CS after exposed to the geothermal water (d) at room temperature (e) at 150 °C. ....	88
<b>Figure 6.1.</b> Characterization of alkyd binder as the primer and its application on carbon steel (a) macrophoto (b) optical microscope (c) SEM with BSE mode, and (d) SEM-EDX of the cross section. ....	90
<b>Figure 6.2.</b> FTIR spectrum of alkyd coating compared to the reference spectra of CaCO <sub>3</sub> and polyester. ....	91
<b>Figure 6.3.</b> FTIR spectra of binder before and after exposed to the aerated geothermal solution at 70 °C and 150 °C, and the corresponding images of specimens. ....	92
<b>Figure 6.4.</b> Characterization of alkyd-based coatings using macro-photo and optical microscope: (a) after exposed to the aerated geothermal solution at 150 °C for 7 days (b) after exposed to the deaerated geothermal solution at 150 °C for 7 days. Back-scattered electron images and EDX elemental mapping of the cross sections were used to identify the element distribution within the selected areas (1), (2), and (3). ....	93
<b>Figure 6.5.</b> FTIR spectra of binder before (bottom) and after (upper) exposed to the deaerated and aerated geothermal solution at 150 °C. ....	94
<b>Figure 6.6.</b> Mechanism of acid catalyzed hydrolysis of ester [147]. ....	95
<b>Figure 6.7.</b> Illustration of degradation processes of alkyd as a polymeric matrix coating on carbon steel in the geothermal solution. ....	96
<b>Figure 6.8.</b> Characterization of phosphate-doped PANI and DBSA-doped PANI using UV-Vis spectroscopy [160]. ....	98
<b>Figure 6.9.</b> Characterization of phosphate-doped PANI and DBSA-doped PANI using FTIR spectroscopy ....	98
<b>Figure 6.10.</b> SEM images of chemically synthesized polyaniline with (a) H <sub>3</sub> PO <sub>4</sub> dopant and with (b) DBSA dopant [160] ....	99
<b>Figure 6.11.</b> Optical microscope images of chemically synthesized polyaniline blended in alkyd-based matrix at the initial condition: (a) without pigment (b) PANI-1 (c) PANI-2. After exposed to the geothermal solution at 150 °C for 7 days: (d) without pigment (e) PANI-1 (f) PANI-2. ....	100
<b>Figure 6.12.</b> FTIR spectra of PANI-1 before and after exposed to the deaerated geothermal solution at 150 °C compared to that of the binder. ....	101
<b>Figure 6.13.</b> Characterization of SiO <sub>2</sub> particles (a) XRD and (b) SEM ....	102
<b>Figure 6.14.</b> Thermogravimetry analysis of alkyd-SiO <sub>2</sub> coating system with various SiO <sub>2</sub> composition from 0 – 20 wt% of SiO <sub>2</sub> under N <sub>2</sub> atmosphere. Temperature ranges from 25 – 500 °C with a temperature gradient of 10 °C/min. ....	103
<b>Figure 6.15.</b> EDX elemental mapping of the silicon dioxide composite coating cross section at the initial condition. ....	103

---

<b>Figure 6.16.</b> Optical microscope images of coatings (a) without silicon dioxide (b) with silicon dioxide (c) without silicon dioxide after exposure, and (d) with silicon dioxide after exposure in the geothermal solution at 150 °C for 7 days. ....	104
<b>Figure 6.17.</b> FTIR spectra of SiO <sub>2</sub> containing coating after exposed to the artificial geothermal water at 150 °C for seven days. ....	105
<b>Figure 7.1.</b> Optical microscope images of different types of coatings before exposure (left), after exposed to the artificial geothermal water for 7 days at 150 °C (middle), and after 28 days at 150 °C (right). ....	108
<b>Figure 7.2.</b> FTIR spectra of binder, SiO <sub>2</sub> particles, PANI particles, and combinational coating PANI-1/SiO <sub>2</sub> at the initial condition. ....	110
<b>Figure 7.3.</b> FTIR spectra of binder (left), PANI-alkyd (middle), and PANI/SiO <sub>2</sub> -alkyd (right) before and after exposed to the geothermal solution for 7 days at 150 °C. (* indicating the overlapping peak of PANI and SiO <sub>2</sub> ). ....	111
<b>Figure 7.4.</b> Images of detached coatings on a transparent tape, where the experiments performed on the specimens after exposed to the geothermal solution for 7 days at 150 °C (upper). The red areas are the selected area representing the delaminated coating, which then calculated to as a semi-quantitative estimation of the degree of delamination (bottom). ....	112
<b>Figure 7.5.</b> E <sub>corr</sub> of PANI-1/SiO <sub>2</sub> coating in comparison to carbon steel exposed to the artificial geothermal water at 25 and 150 °C. ....	113
<b>Figure 7.6.</b> Impedance spectra of PANI-1/SiO <sub>2</sub> coating in the artificial geothermal water at 25 °C and 150 °C after 1 day (a, c, e) and 5 days (b, d, f); the data were presented as (a) and (b) Nyquist plot, (c) and (d) Bode magnitude plot, and (e) and (f) phase angle plot ....	114
<b>Figure 7.7.</b> Impedance spectra of PANI-1/SiO <sub>2</sub> coating in the artificial geothermal water during the early stage of exposure between 0-12 hours: (a, b) at 25 °C and (c, d) at 150 °C, where (a) and (c) are Bode magnitude plots and (b) and (d) are phase angle plots ....	115
<b>Figure 7.8.</b> Impedance spectra of PANI-1/SiO <sub>2</sub> coating in the artificial geothermal water between 1 – 7 days: (a, b) at 25 °C and (c, d) at 150 °C, where (a) and (c) are Bode magnitude plots and (b) and (d) are phase angle plots. ....	116
<b>Figure 7.9.</b> E <sub>corr</sub> of PANI-1/SiO <sub>2</sub> in the deaerated and aerated geothermal solution at 25 °C and 150 °C. ....	117
<b>Figure 7.10.</b> Impedance spectra of PANI-1/SiO <sub>2</sub> in the deaerated and aerated geothermal solution at 25 °C. ....	118
<b>Figure 7.11.</b> FTIR spectra of PANI-1/SiO <sub>2</sub> specimen before exposure (bottom), after exposure test (middle) and after electrochemical test (upper) in the geothermal solution at 150 °C for seven days. ....	119
<b>Figure 7.12.</b> FTIR spectra evolution of PANI-1/SiO <sub>2</sub> specimen after exposed to the deaerated geothermal solution up to 6 months. ....	121



- Figure 7.13.** SEM images in backscattered electron mode and EDX elemental mapping of PANI-1/SiO<sub>2</sub> coated carbon steel cross section (a) before and (b) after exposed to the artificial geothermal water at 150 °C for one month..... 122
- Figure 8.1.** An overview of the key findings and their relevance to possible future work .. 128

# List of Units, Chemicals, and Abbreviation

## Units

° C	degree Celsius
µm	micrometer
a.u.	arbitrary unit
F	Farad
g	gram
gr/mol	gram per mole
GW	Gigawatt
GWe	Gigawatt electrical
km	kilometer
M	Molar
MPa	Megapascal
MWe	Megawatt electrical
mF	microfarad
ml	milliliter
mm	millimeter
mm/a	millimeter per year
mV	millivolt
mV/s	millivolt per second
nm	nanometer
ppb	part per billion
ppm	part per million
ppm/K	part per million per Kelvin
rpm	rotation per minute
V	Volt
wt %	weight percent

## Chemicals

APS	Ammonium Peroxydisulfate
Ag/AgCl	Silver/Silver Chloride
Ar	Argon
As	Arsenic
B	Boron
Br <sup>-</sup>	Bromide ion
C	Carbon
Ca <sup>2+</sup>	Calcium ion
CH <sub>4</sub>	Methane
Cl <sup>-</sup>	Chloride ion
CO <sub>2</sub>	Carbon Dioxide
Cs <sup>+</sup>	Cesium ion

---

DBSA	Dodecylbenzene Sulfonic Acid
F <sup>-</sup>	Fluoride
Fe <sup>2+</sup>	Iron ion
Fe(OH) <sub>2</sub>	Ferrous hydroxide
FEP	Fluorinated Ethylene Propylene
He	Helium
H <sup>+</sup>	Hydrogen ion
H <sub>2</sub>	hydrogen
H <sub>2</sub> S	hydrogen sulphide
H <sub>3</sub> O <sup>+</sup>	Hydronium ion
H <sub>3</sub> PO <sub>4</sub>	Phosphoric acid
HCO <sub>3</sub> <sup>-</sup>	Hydrocarbonate
I <sup>-</sup>	Iodine ion
K <sup>+</sup>	Pottasium ion
KCl	Pottasium Chloride
Li <sup>+</sup>	Lithium ion
M <sup>+</sup>	Metal ion
Mg <sup>2+</sup>	Magnesium ion
MIBK	Methyl Isobutyl Ketone
Mn <sup>2+</sup>	Manganese ion
N <sub>2</sub>	Nitrogen
Na <sup>+</sup>	Sodium ion
NH <sub>3</sub>	Ammonia
Ni	Nickel
Ni/Cr	Nickel/Chromium
PANI	Polyaniline
PANI-EB	Polyaniline Emeraldine Base
PANI-ES	Polyaniline Emeraldine Salt
PE	Polyethylene
PFA	Perfluoroalkoxy Alkanes
PPS	Polyphenylenesulfide
PPY	Polypropylene
Pt	Platinum
PTFE	Polytetrafluoroethylene
Rb <sup>+</sup>	Rubidium ion
SiC	Silicon Carbide
SiO <sub>2</sub>	Silicon Dioxide
SO <sub>4</sub> <sup>2-</sup>	Sulphate ion
TEOS	Tetraethyl orthosilicate
TFE	Tetrafluoroethylene

### Symbols or Formula

$\alpha$ , $\alpha_c$ , $\alpha_{dl}$ , $\alpha_f$	parameter of CPE	dimensionless
A	surface area	cm <sup>2</sup>

## List of Units, Chemicals, and Abbreviation

---

Abs.	Absorbance	a.u.
C, C <sub>c</sub> , C <sub>dl</sub> , C <sub>f</sub>	coating capacitance	F
CR	corrosion rate	mm/a
CPE	Constant Phase Element	s <sup>α</sup> Ω <sup>-1</sup>
D	density	g/cm <sup>3</sup>
E <sup>o</sup>	Standard Cell Potential	V or mV
E <sub>corr</sub>	Free Corrosion Potential	V or mV
EL	elongation	%
Q, Q <sub>c</sub> , Q <sub>dl</sub> , Q <sub>f</sub>	Parameter of CPE	S s <sup>α</sup>
R <sub>ct</sub>	charge transfer resistance	Ω
R <sub>c</sub>	coating resistance	Ω
R <sub>f</sub>	film resistance	Ω
R <sub>s</sub>	solution resistance	Ω
R <sub>po</sub>	resistance within pores	Ω
SHE	Standard Hydrogen Electrode	V or mV
t	time	s
W	Warburg impedance	s <sup>-1/2</sup> Ω <sup>-1</sup>
Z <sub>imag</sub>	impedance imaginary part	Ω
Z <sub>max</sub>	maximum impedance value at the lowest frequency	Ω
Z <sub>real</sub>	impedance real part	Ω
Z	absolute impedance value	Ω

### Indices of α, C, and Q

c	coating
dl	double layer
f	film

### Abbreviation

ATR-FTIR	Attenuated Total Reflection Fourier Transform Infrared
BSE	Back Scattered Electron
CS	Carbon Steel
CVD	Chemical Vapor Deposition
CV	Cyclic Voltammetry
EDX	Energy Dispersive X-Ray
EIS	Electrochemical Impedance Spectroscopy
FFC	Filiform Corrosion
FTIR	Fourier Transform Infrared
GoF	Goodness of Fit
HOMO	highest occupied molecular orbital
LUMO	lowest unoccupied molecular orbital
OCP	Open Circuit Potential
pH	Potential of Hydrogen
SCC	Stress Corrosion Cracking

SEM	Scanning Electron Microscope
UV-Vis	Ultraviolet and Visible Light
XRD	X-ray diffraction



# Chapter 1. Introduction and Motivation

## 1.1. Introduction

The high demand of energy and significant concerns regarding climate change have led to the use of clean and renewable energy. Geothermal energy, as one of the renewable resources, is obtained by extracting the heat stored beneath the earth to produce energy [1]. It is one of the promising solutions to reduce the dependency on fossil fuel due to its consistency, reliability, and low CO<sub>2</sub> emission in the energy production process [2]. In 2016, it was reported that geothermal energy only contributes a small proportion of the world's primary energy consumption, however, the technology development might accelerate due to the increased climate change concerns [1]. Bertani (2003), Stefansson (2005), and Tester et al (2005) estimated in their reports that the global accessible electrical potential ranges from 35 to 200 GW [11], which is about 16 times higher than the generated capacity achieved in 2015 [12]. This shows that there is still huge potential in developing geothermal energy. Many countries have put efforts to develop and utilize geothermal energy resources, especially those with high potential geothermal generating capacity, such as United States, Philippines, Indonesia, Turkey, Mexico, and New Zealand [1].

Despite its promising features, geothermal energy has the most aggressive environment from a corrosion viewpoint, posing major threats for geothermal power plants influenced by temperature, pressure, fluid flows, and the presence of many elements in their corrosive salt forms. The condition in each geothermal well may vary greatly, depending on the location and depth of the geothermal well. Deep geothermal fluid usually contains chloride ions (Cl<sup>-</sup>), sodium ions (Na<sup>+</sup>), and calcium ions (Ca<sup>2+</sup>), various amounts of dissolved gases, such as carbon dioxide (CO<sub>2</sub>), hydrogen sulfide (H<sub>2</sub>S), nitrogen (N<sub>2</sub>) and methane (CH<sub>4</sub>), as well as lower amounts of helium (He), hydrogen (H<sub>2</sub>), and argon (Ar) [13, 14]. In addition, the elemental content in the geothermal water is influenced by several parameters, such as gas-pressure equilibrium, temperature, other ions present in the solution, and residence time of ions [15]. Due to the variety of physicochemical characteristics, corrosion studies for geothermal applications should be conducted by exposing the desired materials in the particular geothermal brine using a simulated geothermal water in the laboratory or preferably, on-site.

Depending on the geothermal fluid and the materials used in the geothermal powerplants, corrosion problems include uniform corrosion, pitting corrosion, stress corrosion cracking, and crevice corrosion. To overcome these problems, a regular maintenance procedure should be performed when a cheaper type of material, e.g., carbon steel, is used. Another option is by implementing high quality materials, which are usually more expensive, as part of the geothermal installation to obtain a longer lifetime of operation [6].

Different metallic materials, i.e. low alloyed steels, stainless steels, and Ni-based alloys [6-10], have been studied using exposure tests and electrochemical measurement to identify suitable materials for geothermal application that meet construction requirements. Stainless and duplex steels are prone to pitting and crevice corrosion with a limitation to certain geothermal brines, and carbon steel can be utilized in a non-saline environment with moderate pH, with a

consideration on the wall thickness with respect to its corrosion rate, which is usually set to 0.3 mm/year [10]. However, in a more aggressive environment, carbon steel may undergo pitting corrosion which can be dangerous for a powerplant. To ensure the safety and longevity of geothermal powerplants, it is important to develop corrosion protection strategies, such as coatings and inhibitors.

Coating systems in geothermal application have been the focus of much research [16–18]. Studies regarding coatings in geothermal environments in the US have been developed by Reeber (1980), using a wide variety of materials, i.e. Teflon (TFE, FEP, PFA), ceramic fused basalt, vinyl ester, fused powdered epoxy, phenolic epoxy, baked phenolic, and plastic zinc [16]. Recently, an investigation using epoxy primer with proprietary components, acrylic primer, epoxy primer, high temperature silicone enamel, high heat zinc modified primer, CVD material, and CVD multilayer silicone coating, was also conducted in the Philippines geothermal fluid [18]. In addition, some polymer coatings were also investigated using polyphenylenesulfide (PPS) and polytetrafluoroethylene (PTFE)-blended PPS [17], polyethylene (PE), and polypropylene (PPy).

The use of conducting polymers, e.g., polyaniline, polypropylene, and polythiophene, as an anticorrosion coating system became popular due to their interesting redox properties [19–22]. In its conductive state, the polymer stores a large amount of charges at the interface formed with a passive layer on metal, thereby maintaining the stationary potential of coated metal in its passive range. Here, polyaniline (PANI) was chosen because it has been proven to provide corrosion protection in other applications [23–25]. PANI can be synthesized to four different oxidation states, i.e. leucoemeraldine, pernigraniline, emeraldine base and emeraldine salt (conducting form) [19], with some advantages that it is easy to process via chemical and electrochemical polymerization, easy to dope and to de-dope using standard aqueous acid or base depending on the desired counter anions, has high resistance to environmental degradation, and due to its economic feasibility [22].

As mentioned before, materials for geothermal application do not only require corrosion resistance but also thermal resistance to operate in the geothermal environment with a temperature of up to about 300 °C. In terms of potentials in geothermal energy, Indonesia stands out with an estimated preserved energy of 29 GWe [3]. Geothermal wells in Sibayak (North Sumatera), Indonesia, belonging to young stratovolcanoes have operating temperatures varying from 36 °C at the near ground surface to 310 °C at the bottom of the well [4, 5]. According to the geothermal fluid classification [26, 27], the liquid-dominated Sibayak fluid has the corrosivity of type II with acidic and saline properties, therefore, creates an aggressive environment that is conducive to corrosion of the powerplant infrastructure.

To enhance the thermal resistance of materials, some pigments are used as a filler or reinforcement in the composite material, e.g. silicon dioxide, titanium dioxide, zirconium dioxide particles. In this research, silicon dioxide was used to enhance the performance of coatings, because it is abundant in nature, can be extracted easily, and can be optimized as a material for advanced technologies [28–30]. Several silicon dioxide phases (e.g. quartz, cristobalite, and tridymite) can be formed naturally or by certain treatments, for example, by



varying the temperature and pressure. The organic/inorganic material has been extensively studied due to its interesting properties, combining the advantages of inorganic material (e.g. rigidity, thermal stability) and organic polymer (e.g. flexibility, dielectric, ductility, and processability). The formation of organic/inorganic material in certain composition and synthesis method can improve the material properties.

In this research, carbon steel was used in the experiments and protective coatings were developed by PANI and silicon dioxide added to the coating. The effect of influencing factors on carbon steel corrosion were subsequently discussed to understand the interaction of carbon steel and the geothermal medium. The effect of each coating component addition on the coatings is also further discussed in this thesis to give an overall future research direction for a coating system based on polyaniline/silicon dioxide for geothermal application.

## 1.2. Motivation of Study

Indonesia, as one of the countries located in the ring of fire, stands out in terms of the amount of preserved geothermal energy resources. The utilization of geothermal energy in Indonesia as a renewable energy has been growing and advancing. By 2018, Indonesia accelerated geothermal energy production from 5% of utilization in 2015 to 11%, and was the second largest energy producer after the United States [31]. Having many volcanoes, geothermal systems in Indonesia are mostly classified as volcanic geothermal systems. These systems have a heat and mass transfer system involving heat transfer from the top concealed magmatic intrusions to the surface [5]. To understand the corrosion mechanism of carbon steel and develop a protective coating system on carbon steel, this work used artificial geothermal water to simulate the geothermal brine found in Sibayak, Indonesia.

Corrosion processes in the geothermal environment were observed and explored to improve the planning, construction and maintenance of a geothermal power plant. Studies related to material selection for the geothermal environment were conducted to determine the type of material suitable for geothermal use. This study was conducted to provide a cheaper alternative to the expensive high alloyed materials suggested by Keserovic et al [7], by protecting carbon steel using coatings. Some coatings have been investigated for some time, and the research regarding coatings for geothermal applications is still actively progressing in an effort to develop new materials and provide more options for corrosion protection in geothermal applications.

## 1.3. Research Objectives

Key questions of interest to academia and industries in the field of corrosion in geothermal applications are:

- *What are the most critical influencing factors that affect corrosion behavior of carbon steel in geothermal application?*
- *Is there any cheaper alternative to high alloyed material that can yield good corrosion resistance and thermal stability in the geothermal environment?*
- *What is the potential of protecting carbon steel using coating materials for future development of construction material in geothermal application?*

To address these key questions, research objectives were set to provide a comprehensive understanding of the corrosion of carbon steel in geothermal application and the development of a coating system for geothermal application as follows:

1. Identify and analyze the corrosion processes of carbon steel in geothermal water with different influencing factors, i.e. pH, temperatures, and different dissolved gas content.
2. Develop a coating system for an application at high temperatures (up to 150 °C) and in the corrosive environment (1,500mg/l Cl<sup>-</sup>).
3. A comparative study of the polyaniline containing coating with different types of dopant using conventional coating application by spray method and electrochemical deposition.
4. Corrosion study of polyaniline/silicon dioxide containing coating in artificial geothermal water.

### 1.4. Thesis Structure

This work provides a further understanding of carbon steel corrosion in a geothermal environment, and the development of polyaniline/silicon dioxide coating system for corrosion protection of carbon steel in geothermal application. The thesis comprises eight chapters as follows:

**Chapter 1** outlines the introduction, study rationale, research objectives and thesis structure. **Chapter 2** provides a comprehensive literature review related to the experimental research, grouped into geothermal energy, corrosion in geothermal environment, material synthesis and properties in the coating components, and the proposed protection mechanism of carbon steel. **Chapter 3** demonstrates the experimental setups and methodologies, including the properties of the investigated material, the synthesis routes and the material characterization of the tested specimens, the experimental condition and composition of the investigated geothermal water, the evaluation techniques and the test setups. The evaluation techniques are elaborated to the exposure test, microstructural and surface analysis, and the electrochemical test. The theoretical background and practice are discussed in this section. **Chapter 4, 5, 6, and 7** provide the experimental results and discussion. **Chapter 4** focuses on the corrosion behavior of carbon steel in artificial geothermal water, discussing the influencing factors in the experiment, such as temperature, dissolved oxygen, and pH. This chapter also outlines the limitation of the experimental condition used for the coated specimens. **Chapter 5** discusses the electrochemical deposition of PANI on carbon steel and its corrosion behavior in the artificial geothermal water, outlining the advantages and disadvantages of using electrochemically deposited PANI for the geothermal application based on the study findings. **Chapter 6** outlines the synthesis and characterization of polyaniline and silicon dioxide as pigments and the individual influence on the properties of the coating system. The experimental results include the characterization of different types of coatings before and after exposure to artificial geothermal water for seven days. **Chapter 7** describes the experimental results of the exposure test and electrochemical test of polyaniline/silicon dioxide coating in the geothermal environment, discussing the protection mechanism of coated carbon steel on exposure to the geothermal medium. **Chapter 8** provides a summary of the findings of each chapter, explains the novel aspects of this work, and proposes the possible future outlook and recommendation for further relevance in the industrial application.

# Chapter 2. Literature Review and State of the Art

To fully understand the motivation and state of the art behind this work, a literature review was conducted regarding geothermal energy, corrosion in geothermal environment, synthesis and properties of coatings components (carbon steel, alkyd, polyaniline, and silicon dioxide), and the possible corrosion protection mechanism of carbon steel by applying conducting polymer/inorganic particles in organic coatings.

## 2.1. Geothermal Energy

The high demand for energy all around the world and the significant concerns regarding environmental and climate change necessitate efforts on using clean and renewable energy. Geothermal energy is one of the promising alternative solutions to replace conventional energy resources because of its consistency, reliability, and low carbon dioxide emission as compared to fossil fuel energy resources [2, 32, 33]. The utilization of geothermal energy in general and in Indonesia, along with the basic technology and its challenges will be discussed in the following sections.

### 2.1.1. Utilization of Geothermal Energy

The utilization of geothermal energy is classified into two categories, i.e. direct uses and electric energy production. For generating electric energy, a geothermal power plant usually has a planned lifetime of 30 years [34]. Between 2010 and 2015, the geothermal capacity worldwide has increased by 1.7 GWe, reaching the total installed capacity of 12.1 GWe, as shown in Figure 2.1 [35, 36]. Many countries aim to develop and to utilize geothermal energy resources as renewable energy resources, especially those with high potential of geothermal generating capacity, such as the United States, Indonesia, Philippines, Turkey, and New Zealand [31].

In recent years, global geothermal generation capacity grew at a rate of 3 to 4% annually, driven by economic growth and increasing fossil fuel prices. Between January 2015 and December 2018, some committed projects added almost 2,000 MWe, equating to almost 16% capacity increase, due to new capacities installed in Indonesia (636 MWe), Turkey (298 MWe), and Kenya (255 MWe) [1, 31].

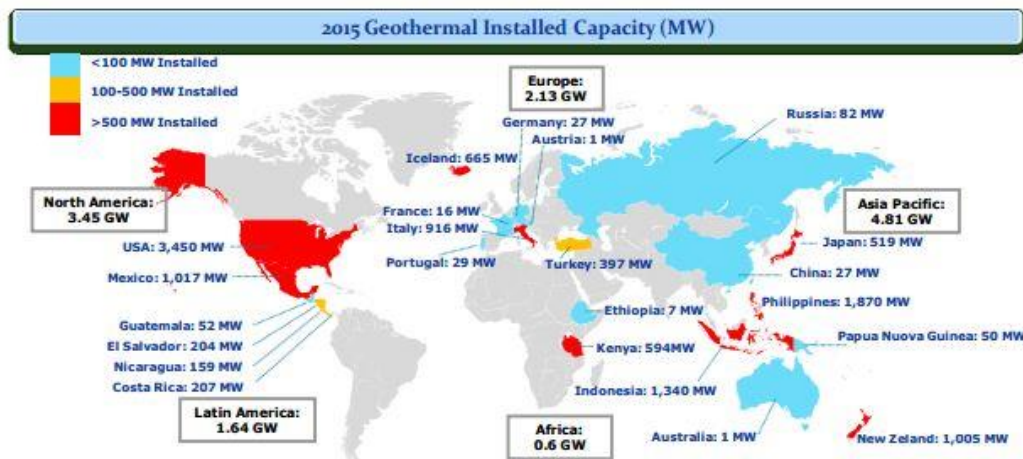


Figure 2.1. Global geothermal capacity in 2015 equating to 12.1 GWe [41]

### 2.1.2. Geothermal Energy in Indonesia

Located in the “ring of fire”, Indonesia has the highest geothermal potential in the world, with 40% of the potential global hotspots. However, most of the energy resources used within the country are fossil fuel, which will become extinct at some point. Therefore, the country has been pushing toward improving geothermal energy production to use renewable and cleaner energy resources. Indeed, by 2018, Indonesia had the second largest geothermal generating capacity, reaching 1,925 MWe, and the country is developing new installations [31, 37].

With the presence of numerous volcanoes, as shown in Figure 2.2, Indonesia is dominated by volcanic geothermal systems which utilize heat from the top of concealed magmatic intrusion to the surface. There are three categories of volcanic systems hosting geothermal plants in Indonesia, i.e. young stratovolcanoes, a set of older stratovolcanoes which are partly eroded, and a few volcanoes supporting the peripheral geothermal systems or transferring hot fluids to large fault zones (graben-volcanism) [5]. This research focuses on the geothermal brine found in Sibayak, Indonesia, which is grouped into young stratovolcanoes. Sibayak is the only known exploited reservoir located beneath the summit area of a stratovolcano [5].



**Figure 2.2.** World map showing the lithospheric plate boundaries (red dots = active volcanoes) [38]

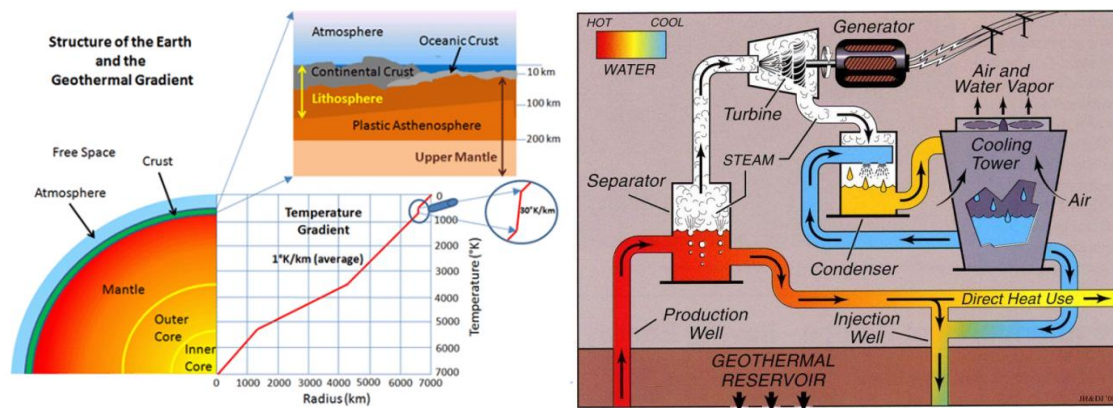
### 2.1.3. Basic Technology and Challenges of Geothermal Energy

Geothermal energy is based on the use of heat stored inside the earth. The structure of earth consists of the core, mantle, and crust as shown in Figure 2.3 (left), which has a temperature gradient of approximately 25-30 °C/km [39, 40], reaching the core of the earth with a temperature of 6,650 °C [41]. However, there are several locations with temperature gradients up to ten times beyond the average temperature gradient covering 10% of the earth surface. These locations are called “*geothermal hotspots*”, where most of the geothermal fields are established [35]. The temperature gradient in geothermal resources is strongly related to the regional heat flow through the crust, the hydrothermal activity, the permeability of the rock, residual heat in extinct volcanic centers [42], and the thickness of crust. In the thicker crust, the temperature gradient of geothermal resources can be as low as 16 °C/km, whereas in the thin crust, it can exceed 90 °C/km [43].

A geothermal reservoir consists of a liquid-dominated phase, vapor-dominated phase, or transitional phase. The reservoir in a liquid-dominated geothermal system contains water in all the channel ways and interstitial pores [44], with the pressure and temperature increasing

naturally with depth. Meanwhile, in a vapor-dominated geothermal system, the pressure and temperature are constant near the maximum enthalpy of “dry” steam, which is about 240 °C and 3.3 MPa. In this geothermal system, the steam is located in the open cracks, fractures and faults, and the intergranular pore space is filled with liquid [44].

Figure 2.3 (right) shows the basic technology utilization in electricity generation, where construction materials, such as pipelines and heat exchangers, are exposed to a different temperature, pressure, and geothermal water, having different physicochemical compositions depending on the stage of the system. The non-gaseous impurities of geothermal fluid are important in the water-phase corrosion, whereas gaseous impurities, such as oxygen, CO<sub>2</sub>, or H<sub>2</sub>S, are critical for steam-phase, condensed-phase, and atmospheric corrosion [26].



**Figure 2.3.** Structure of the earth and geothermal gradient (left) and basic technology and utilization of a geothermal power plant (right) [45]

Armstead [27] reported some processes in geothermal power plants that are prone to corrosion, which are as follows:

- (a) At the two-phase pipeline before the separator where water, steam and possibly some solid/rock particles are present
- (b) In steam pipes, where initial contamination with ‘carry-over’ brine from the separation process is gradually diluted by condensed steam
- (c) At the entrance to the turbine where the steam is almost dry or with slight super-heat
- (d) At the exhaust from the turbine where the steam is very wet
- (e) In the condenser where circulating water and air are both present
- (f) In the gas extraction circuit where air, gas, water, and vapor are present
- (g) In the circulating water circuit where gases may be released, and flashing water and gases are discharged from drains
- (h) In some systems, the brine undergoes downstream processing either through multiple stage separation or passed through heat exchangers; acids are often added to minimize silica scaling [46]
- (i) Cooling the brine in thermal ponds or sumps before re-injection where the resulting fluid is highly oxygenated and saline

## 2.2. Corrosion in the Geothermal Environment

Due to the complexity of the physicochemical properties in some geothermal environments, there are some challenges in geothermal technology depending on the

temperature, pressure, and chemical composition of brines [2]. One challenging aspect of technological development is the durability of construction materials, as materials exposed to geothermal fluids may undergo a severe environment, and are susceptible to corrosion and scaling [6, 47, 48]. Corrosion and degradation of materials occurs as a result of interaction between constituent elements of the material and the surrounding environment [49]. The following sections discuss the details of the chemistry of geothermal brines, the corrosion types often found in the geothermal medium and its effects on carbon steel surface or coatings. Furthermore, the influencing factors that trigger corrosion in the system will also be discussed.

### 2.2.1. Chemistry of the Geothermal Environment

It is necessary to understand the properties of the geothermal medium to understand the corrosion processes that may occur during the utilization of construction materials in a geothermal application. The geothermal fluid has complex possible physicochemical conditions due to variations of temperature, pressure, gas content, heat source, rock type, permeability, hydrothermal age, and fluid source (pH, salinity, and alkalinity level) [40]. Some common species found in geothermal fluids are:

- a. Anions:  $\text{Cl}^-$ ,  $\text{HCO}_3^-$ ,  $\text{CO}_3^{2-}$ ,  $\text{SO}_4^{2-}$ ,  $\text{Br}^-$ ,  $\text{F}^-$ ,  $\text{I}^-$
- b. Cations:  $\text{Na}^+$ ,  $\text{K}^+$ ,  $\text{Li}^+$ ,  $\text{NH}_4^+$ ,  $\text{Ca}^{2+}$ ,  $\text{Mg}^{2+}$ ,  $\text{Rb}^+$ ,  $\text{Cs}^+$ ,  $\text{Mn}^{2+}$ ,  $\text{Fe}^{2+}$
- c. Neutral species:  $\text{SiO}_2$ , As, B, Noble glass
- d. Dissolved gases:  $\text{CO}_2$ ,  $\text{H}_2\text{S}$ ,  $\text{N}_2$ ,  $\text{CH}_4$ , He,  $\text{H}_2$ ,  $\text{C}_2^+$ , Ar,  $\text{NH}_3$

However, some key species have the most crucial effects on the corrosivity of geothermal fluids, such as oxygen (usually from near ground surface contamination), hydrogen ion concentration (or pH), chloride ion ( $\text{Cl}^-$ ), hydrogen sulfide ( $\text{H}_2\text{S}$ ), carbon dioxide ( $\text{CO}_2$ ), carbonate ( $\text{CO}_3^{2-}$ ), and bicarbonate ( $\text{HCO}_3^-$ ) ions, ammonia ( $\text{NH}_3$ ), ammonium ion ( $\text{NH}_4^+$ ) and sulfate ion ( $\text{SO}_4^{2-}$ ). These key species are important in the corrosivity classification system, so the term total key species (TKS) was proposed and used along with the term total dissolved solids (TDS). The TKS is the sum in parts per million (mg/kg) of chloride, sulfate, carbon dioxide, bicarbonate, carbonate, total sulfide species, and total ammonia species [26]. Liquid-dominated systems usually contain chloride, sulfate, and bicarbonate, with only minor weight contributions from ammonia and sulfides. For vapor-dominated systems, the term TKS has little significance on the corrosivity, rather it is more important to define the volume percent of non-condensable gases in the steam [26]. Miller et al. suggested a corrosivity classification system of geothermal fluids [50], which was summarized by Nogara et al. [26], as shown in Table 2.1.

**Table 2.1.** Corrosivity Classification Systems of Geothermal Fluid [26, 50]

No	Type of geothermal fluid	Class	TKS ppm	Chloride % to TKS	pH	Vol. of gas in steam %	Temp °C	Total Alkalinity (CaCO <sub>3</sub> in ppm)
1	hyper-saline geothermal fluids	I	>100,000	19	<5, 5-6	<2.5	199-326	-
2	acidic liquid-dominated geothermal fluids	II-A	1,000-60,000	15-99	3-5	N/E	N/E	-
		II-B	500-40,000	20-99	<3	N/E	N/E	-
3	high salinity neutral pH geothermal fluids	III	10,000-20,000	45-99	5-6, >6	N/E	149-300	-
4	liquid-dominated systems with neutral pH, moderately saline geothermal fluids	IV	500-10,000	45-99	>5	<2.5	121-280	-
5	low temperature, low salinity, neutral to alkaline pH geothermal fluids	V-A	<5,000	3-72	6.7-7.6	N/A	49-96	207-1239
		V-B	<5,000	3-72	7.8-9.85	N/A	120-205	<210
6	vapor-dominated geothermal reservoirs	VI-A	<1	N/A	N/A	<5	160-250	-
		VI-B	-	-	-	-	-	-
		VI-C	-	-	-	-	-	-

N/A: not applicable, N/E: not established, - : no information

In addition to the various chemical compositions described in the corrosivity classification system, temperature is also a significant factor that exhibits a more aggressive environment. The geothermal enthalpy may affect ion mobility and the volume of gas in steam and dissolved gas in the solution, which subsequently influences the corrosion of the construction materials. The classification of geothermal brines enthalpy resources based on the temperature range of the fluid is shown in Table 2.2.

**Table 2.2.** Geothermal Brines Enthalpy Resources Classification [51-54]

Enthalpy resources	Muffler and Cataldi	Hochstein	Benderitter and Cormy	Haenel et al.
<b>Low</b>	<90	<125	<100	≤150
<b>Medium</b>	90-150	125-225	100-200	-
<b>High</b>	>150	>225	>200	>150

According to the corrosivity classification systems, the investigated geothermal system (Sibayak, Indonesia) is classified into the acidic liquid-dominated geothermal fluids type II-A, and this research uses a range of temperature for medium enthalpy resources (temperature up to 150 °C). Therefore, the discussion in this thesis will be limited to these particular parameters.

### 2.2.2. Types of Corrosion and Coating Degradation

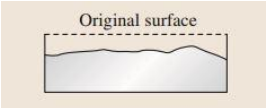

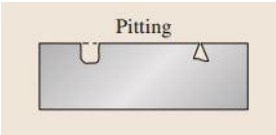

Corrosion is an interaction between materials and the environment, resulting in changes of the material properties. Due to a corrosion reaction, a material can lose its pleasant appearance and thickness, change its thermal and mechanical properties, or form a new compound on its surface.



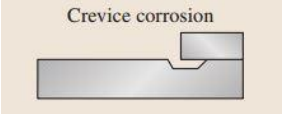

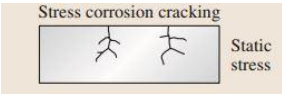



Materials can be grouped into metals, polymers, and ceramics, where transport of mass across the interface to the environment can be broadly considered as electrochemical, chemical, or physical. Electrochemical corrosion involves the release of ions to the environment and movement of electrons within the material. Thus, this mechanism can occur only if the environment contains ions and the material can conduct electrons [55].

One example of an electrochemical mechanism is the simple corrosion of metals in aqueous solutions. Atoms at the surface of the metal enter the solution as metal ions and electrons migrate through the metal to a site where they are consumed by the species in contact with the metal. How a material behaves under a specific condition is strongly related to its thermodynamics and kinetics. There are different types of corrosion depending on the corrosion process. Here, the different types of corrosion that can take place in geothermal applications are described in Table 2.3. Examples of corrosion and coating degradation from geothermal plants are also provided.

**Table 2.3.** Type of Corrosion in Geothermal Environment: descriptions and examples

No	Type of Corrosion	Description
1	<p data-bbox="272 898 555 927">Uniform Corrosion</p>  	<p data-bbox="587 958 1393 1059">Uniform corrosion attacks the metal surface with a uniform distribution; it is not a significant concern as it is possible to estimate the lifetime of material relatively accurately via a simple test [56–58]</p> <p data-bbox="587 1155 1393 1216"><i>Example: Uniform corrosion observed on the wellhead tee of a geothermal well discharging acid-SO<sub>4</sub><sup>2-</sup> chloride type fluid [26]</i></p>
2	<p data-bbox="272 1413 555 1442">Pitting Corrosion</p>  	<p data-bbox="587 1413 1393 1794">Pitting corrosion is a type of localized corrosion in which a pit is formed on the metal surface. The presence of chloride anions in the environment usually triggers metal dissolution, initiating pit formation and is often associated with deterioration of the passive film. Passive film is generally not homogeneous, containing defects and impurities both in the passive film itself and on the metal surface underneath the passive film. This heterogeneity may also be in the form of pores, cracks, imperfections, or inclusions, which allow chloride ions to penetrate through them [57]. After anions penetrate through the film, anodic and cathodic reactions occur in the local sites and continue to grow inward, whereas the bottom of pits is rich in metal M<sup>+</sup> ions due to a large number of anodic reactions [58].</p> <p data-bbox="587 1888 1393 1989"><i>Example: Heavy pitting corrosion damage observed in this last stage gas ejector nozzle made from SS316L caused by accumulation of sulfur deposits [26]</i></p>



3	<p>Crevice Corrosion</p>  	<p>Crevice corrosion is localized corrosion due to crevices in the equipment or under scale deposition. It occurs because of changes in local chemistry, such as oxygen depletion in the crevice, increasing pH due to increased hydrogen concentration [H<sup>+</sup>], increased chloride ions. As the corrosion takes place, oxygen within crevice is consumed, and the cathodic reaction for oxygen reduction cannot be sustained in the crevice area, causing metal dissolution [58]. In addition, the presence of chloride ions and hydrogen ions accelerate metal dissolution.</p> <p><i>Example: Crevice corrosion underneath a galvanized steel guided support of a geothermal pipeline [26]</i></p>
4	<p>Stress Corrosion Cracking</p>  	<p>In the geothermal environment, stress corrosion cracking can happen due to the combination of tensile stress and the presence of a certain chemicals, for instance, chloride ions. In addition, oxygen and increased temperature aggravates the corrosive attack. Common agents inducing the stress corrosion cracking are hydrogen sulfide (H<sub>2</sub>S) and chloride, even though the solubility of chloride in water at high temperature decreases in an open system.</p> <p><i>Example: Stress corrosion cracking (SCC) visible in hardened SS316L stud bolt used inside the geothermal power plant condenser [26]</i></p>
5	<p>Filiform Corrosion and Coating Degradation</p> 	<p>In coated materials, material degradation occurs due to the interaction of the coating and its surrounding medium. When electrolyte, dissolved gases, or ionic species find pathways to pass through the coating, corrosion may occur between the trapped species and the iron surface. Filiform corrosion (FFC) describes filamentary trails of corrosion product forming on organic coated iron (steel) surfaces. Filament heads are electrolyte-filled, containing metal cations and aggressive anions (such as Cl<sup>-</sup>), typically exhibit a low pH toward their leading edge due to cation hydrolysis. Conversely, filament tails are filled with dry, porous, corrosion product.</p> <p><i>Example: Polymeric coating on the surface of the metal which cracked and allowed the corrosive fluid to permeate to the metal surface [26]</i></p>
6	<p>Erosion corrosion</p> 	<p>Erosion corrosion occurs when there is a relative movement between a corrosive fluid and a metallic material [56].</p> <p><i>Example: Erosion corrosion damage on an ER probe cause by the action of acid geothermal fluid moving at high velocity [26]</i></p>
7	<p>Others</p>	<p>Hydrogen embrittlement, intergranular corrosion, dealloying, and microbiology induced corrosion</p>

According to the possible types of corrosion in the geothermal environment, this work focuses on the uniform corrosion and pitting corrosion of carbon steel, and filiform corrosion or coating degradation of the coated specimens.

### 2.2.3. Influencing Factors

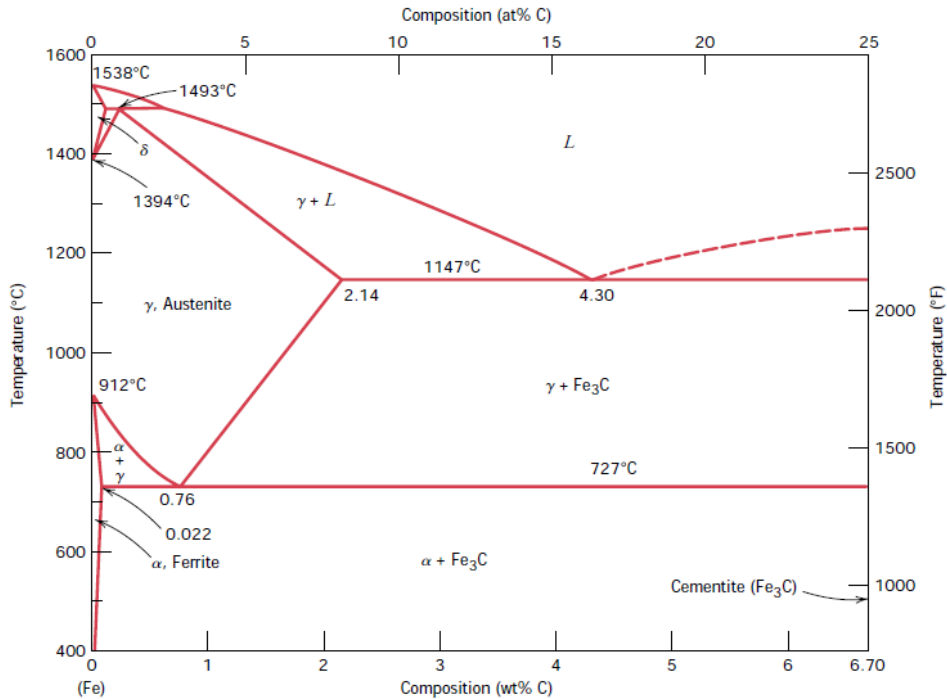
Corrosion is triggered by various factors, categorized as internal and external influencing factors. The internal factors are related to the properties of materials, such as chemical composition, imperfections, and structures, whereas external factors are related to the operation condition and properties of the surrounding environment, such as the chemical composition, temperature, pressure, fluid velocity, acidity, presence of oxygen, presence of dissolved salts.

#### *2.2.3.1. Internal Influencing Factors*

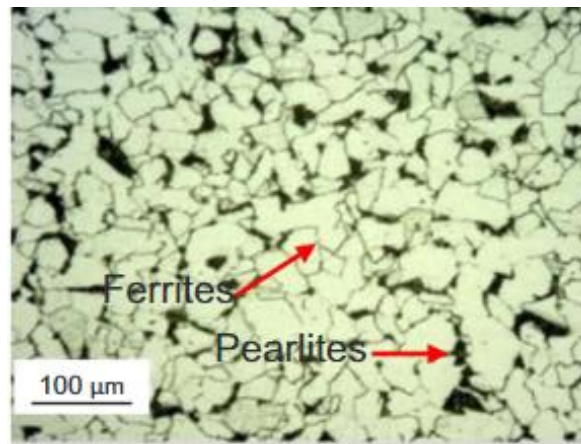
To avoid corrosion and material degradation in construction, it is important to consider material selection in the planning stage. In order to select suitable materials, it is necessary to understand the material properties including its chemical composition and microstructures, which is also mentioned here as internal influencing factors, e.g. chemical composition, imperfections, and structures.

According to the chemical composition, metal is generally grouped into ferrous and non-ferrous alloys. Ferrous alloys are primarily consisted of iron as the elemental constituent, whereas a non-ferrous alloy system consists of a base metal other than iron or a combination of several metals with a specific characteristic that the alloy group shares. Examples of non-ferrous alloys are copper, aluminum, magnesium, and titanium alloys, refractory metals, noble metals, and miscellaneous alloys, including nickel, lead, tin, zirconium, and zinc as the base metals [49].

For many geothermal power plants, carbon steel is used as the component of pipelines [59]. Carbon steel is classified as low carbon, medium carbon, and high carbon depending on the carbon composition. In practice, all steels and cast irons contain less than 6.70 wt% carbon, at this concentration, the intermediate compound iron carbide or cementite ( $\text{Fe}_3\text{C}$ ) is formed. Thus, Figure 2.4 represents Fe –  $\text{Fe}_3\text{C}$ , where 6.70 wt% C (pure graphite) corresponds to 100 wt%  $\text{Fe}_3\text{C}$ . This study used low carbon steel St37 containing less than 0.3 wt% of carbon, with a general microstructure of ferrite and pearlite constituents, as shown in Figure 2.5. Medium carbon steel contains between 0.3–0.6 wt% of carbon, whereas high carbon steel contains 0.6–1.4 wt% of carbon [60].



**Figure 2.4.** Iron-iron carbide phase diagram [49, 61]



**Figure 2.5.** Microstructure of low alloy carbon steel St37 [62]

### 2.2.3.2. External Influencing Factors

#### Temperature

In general, temperature is a parameter that affects any chemical reaction. The dependency of the rate of chemical reaction on the temperature is exponential, as explained by the Arrhenius equation. The geothermal environment has various operational temperatures depending on the resource enthalpy as discussed in Table 2.2. Temperature will also induce the high mobility of ions in the aqueous solution, resulting in a more aggressive environment.

#### Pressure

In conjunction with temperature, initial partial pressure maintains the phase of a system either in a liquid or gas phase. This factor is a decisive influence on the corrosion type that may occur. In a liquid-phase system, aggressive ionic species contribute more to the corrosion

processes, whereas the content of condensed gas is more significant to influence the corrosion processes of a gas phase system.

### Acidity

In the acidic solution, substances release  $H^+$  cations in aqueous solution. As  $H^+$  cannot stand alone without any electron, it reacts with water forming  $H_3O^+$ . Iron, chromium, and manganese corrode rapidly in an acidic solution with a pH less than 4 and in alkaline solutions with a pH above 13.5 at temperatures above 80 °C. At neutral pH (pH = 6–8), iron also corrodes but with a considerably slower rate [57].

Some geothermal waters containing dissolved  $CO_2$  yield a lower pH, which tends to increase the corrosion rate or breakdown the passive layer causing pitting corrosion, crevice corrosion, or SCC [63, 64].

### Dissolved oxygen

In general, oxygen has a great influencing role in the corrosion reaction because oxygen takes part in the cathodic reaction. When oxygen is absent from the system, nearly no corrosion reaction will take place [57]. In the thermal water medium, 30 ppb of oxygen lead to an increased corrosion rate of up to four times on carbon steel [63], while the presence of oxygen in concentrations higher than 50 ppb causes serious pitting corrosion [63]. In the combination with  $Cl^-$  and high temperature, less than 100 ppb oxygen can cause chloride SCC [63]. However, oxygen is usually not present in geothermal brines.

### Dissolved salts

The presence of other species in the system, such as various dissolved salts, will affect the corrosion rate of steels. There are four different classifications of salts depending on how they react with metals, i.e. acidic and alkali salts, deposited salts on the surface and provide a protection, and neutral salts [57].

The presence of chloride ions is common in geothermal brines, which can inhibit the formation of a passive layer or locally breakdown the layer, resulting in a severe localized corrosion including pitting corrosion, crevice corrosion, and SCC [64, 65]. Sulfate is a minor constituent of geothermal water, but with 250 ppm concentration in the brines, it may cause pitting corrosion on carbon steel [66].

### Fluid velocity

Velocity has indirect effects on the corrosion rate. However, it controls some decisive parameters that influence corrosion rate. At a high rate, fluid velocity causes mechanical damage to materials which is associated with erosion corrosion or cavitation erosion. As any other influencing factor may affect corrosion, the effects of fluid velocity on different metals varies widely, and sometimes the effects are conflicting. In general, a little motion of the medium tends to favor uniform corrosion, preventing localized corrosion. However, when the fluid velocity is too high, turbulence may take place, causing non-uniform condition, which in some cases, results in pitting corrosion [67].

With a sufficiently high fluid velocity, oxygen supply will increase and either passivate some alloys or accelerate uniform corrosion on carbon steel, depending on the type of metals. At extremely high velocity, erosion may remove the protective film or corrosion products from the metal layer continuing the corrosion reaction with the initial corrosion rate [67].

### 2.3. Material Properties and Coating Components

The geothermal powerplant consists of different constructional components, i.e. steel casings, screens, and heat exchangers, which require a high corrosion resistance property. The geothermal plant engineering and materials used in the construction are often expensive, consequently, the operation maintenance cost in some cases can be more expensive [32]. As a high corrosion resistance material is necessary, metallic materials (particularly steels) are commonly used as construction materials [68, 69]. As this study focuses on the protective coatings applied to carbon steel, this subsection will specifically discuss carbon steel and the components of the developed protective coatings, i.e. alkyd binder, polyaniline, and silicon dioxide.

#### 2.3.1. Carbon Steel

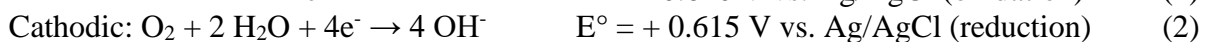
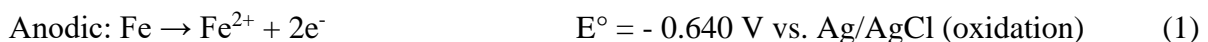
Carbon steel is widely used in many areas and can be classified into three groups depending on its carbon content as mentioned previously, i.e. low carbon steel, medium carbon steel, and high carbon steel. Low carbon steels contain less than 0.3 wt% carbon and have microstructures of ferrite and pearlite constituents, so they are relatively soft and weak but with superior ductility, toughness, and strength compared to ferritic and austenitic stainless steels [66]. Furthermore, carbon steels are machinable, weldable, and have the least production cost of all steels [49]. Typical applications of low carbon steel are as pipelines, structural and sheet steels, structural steels for buildings and bridges. They generally have yield strength of 275 MPa, tensile strength between 415 and 550 MPa, and ductility of 25 % EL [49].

Carbon steel exposure in aqueous solution along with dissolved oxygen in the solution will induce corrosion, mainly due to metal dissolution. Accordingly, corrosion products tend to form uniformly on the metal surface, with the composition correlating to the steel composition and the surrounding medium. In the early phase of exposure, a porous layer of corrosion products is formed on the metal surface, causing the more active surface to react with the surrounding medium, thereby the corrosion rate will be substantially high. In the later stage, the corrosion rate of carbon steel can either increase or decrease, depending on the compactness of the corrosion product [70, 71]. ,

##### *2.3.1.1. Corrosion Reactions of Carbon Steel*

###### Corrosion in neutral aqueous solution

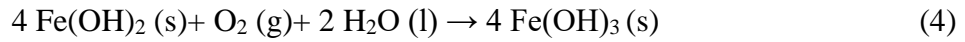
The corrosion reaction of iron in neutral aqueous solution involves metal dissolution in the anodic site as a result of oxidation, whereas oxygen reduction occurs at the cathodic site:



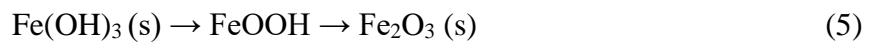
The corrosion reaction forms ferrous II hydroxide,  $\text{Fe(OH)}_2$ , from the oxidation reaction product, ferrous iron  $\text{Fe}^{2+}$ , and the reduction reaction product, hydroxyl anion  $\text{OH}^-$ :



Due to the instability of  $\text{Fe(OH)}_2$ , it is promptly oxidized to the red-brown ferric III hydroxide,  $\text{Fe(OH)}_3$  which is thermodynamically unstable:

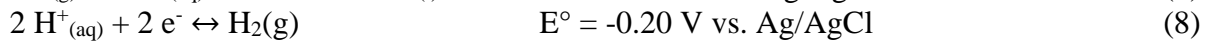
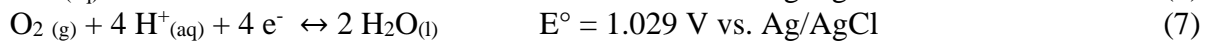
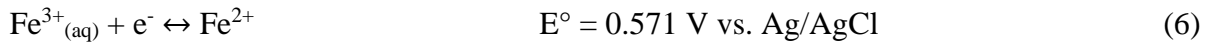


Ferric III hydroxide then forms ferric III oxide ( $\text{Fe}_2\text{O}_3$ ), with intermediate products of dehydrated ferric oxy-hydroxides [52]:



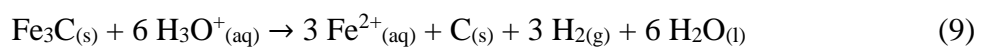
#### Corrosion in acidic aqueous solution

When exposed to an acidic aqueous solution, carbon steel reacts mostly with the proton  $\text{H}^+$ . Due to the heterogeneity of constituent components in the carbon steel, different phases may have a variety of electrical potential in contact with acid. The iron phase is relatively more anodic to the iron carbide ( $\text{FeC}$ ), with free electrons from the anodic site tending to flow to the cathodic site and require more positive species which can receive them, such as  $\text{H}^+$  cations, dissolved  $\text{O}_2$ , and  $\text{Fe}^{3+}$  cations (which can be formed when  $\text{Fe}^{2+}$  cation is oxidized by the dissolved oxygen). The possible cathodic reactions that may occur on the carbon steel surface when exposed to an acidic solution are [55]:



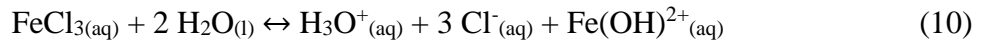
These cathodic reactions are more positive than the electric potential of iron dissolution  $E^\circ = -0.44 \text{ V}$  vs. standard hydrogen electrode (SHE). As the requirement of the corrosion reaction is that  $E^\circ_{\text{cathodic}} > E^\circ_{\text{anodic}}$ , these three possible cathodic reactions may happen simultaneously. Although oxygen reduction exhibits the most positive electrical potential, followed by the reduction of ferric ions, the reduction of hydronium cations is the most prevalent cathodic process in the case of carbon steel exposure to acidic medium. This process can be observed by the hydrogen gas evolution.

Another phenomenon that can be observed during carbon steel corrosion in the acidic medium is the deposition of black powder on the carbon steel surface, indicating the presence of carbon powder, due to the following reaction:



Corrosion in the presence of other species and dissolved salts, e.g. chloride ions

The presence of different species in water and the chemical composition may affect the corrosion rate of metals. Acidic and alkali salts are hydrolyzed salts which form acidic or alkali solution, either increasing or decreasing the pH of the solution, respectively. For example [57]:



Other similar cases to ferric chloride are in the presence of calcium chloride ( $\text{CaCl}_2$ ), magnesium chloride ( $\text{MgCl}_2$ ), ammonium chloride ( $\text{NH}_4\text{Cl}$ ), sodium dihydrophosphate ( $\text{NaH}_2\text{PO}_4$ ), and aluminum sulfate ( $\text{Al}(\text{SO}_4)_3$ ).

In geothermal applications, carbon steel commonly suffers from uniform corrosion, pitting corrosion, or SCC, depending on various concentrations of dissolved salts, chemicals and gases of the brine [66]. Therefore, carbon steel is not suitable for aggressive geothermal brines, although some allowance can be made by using thicker-walled piping [59]. In some cases, carbon steel can withstand the operating condition, but deteriorates once the power plant is shut down for an extended period because of severe internal pitting [66].

*2.3.1.2. Corrosion Products on Carbon Steel: Composition and Morphologies*

There are various possibilities of the forms of iron oxide-hydroxide and iron oxide as shown in Table 2.4 [72], and the most common form of hydroxides are goethite ( $\alpha\text{-FeOOH}$ ) and lepidocrocite ( $\gamma\text{-FeOOH}$ ), and hematite ( $\alpha\text{-Fe}_2\text{O}_3$ ), maghemite ( $\gamma\text{-Fe}_2\text{O}_3$ ), and magnetite ( $\text{Fe}_3\text{O}_4$ ) for iron oxides. The corrosion products can be crystalline or amorphous.

**Table 2.4.** Possible forms of iron oxides [72]

Oxide-hydroxides and hydroxides	Oxides
Goethite $\alpha\text{-FeOOH}$	Hematite $\alpha\text{-Fe}_2\text{O}_3$
Lepidocrocite $\gamma\text{-FeOOH}$	Magnetite $\text{Fe}_3\text{O}_4$
Akaganeite $\beta\text{-FeOOH}$	Maghemite $\gamma\text{-Fe}_2\text{O}_3$
Schwertmannite $\text{Fe}_{16}\text{O}_{16}(\text{OH})_y(\text{SO}_4)_z \cdot n \text{H}_2\text{O}$	$\beta\text{-Fe}_2\text{O}_3$
$\delta\text{-FeOOH}$	$\epsilon\text{-Fe}_2\text{O}_3$
Feroxyhyte $\delta'\text{-FeOOH}$	Wüstite $\text{FeO}$
high pressure $\text{FeOOH}$	
Ferrihydrite $\text{Fe}_5\text{OH}_8 \cdot 4 \text{H}_2\text{O}$	
Bernalite $\text{Fe}(\text{OH})_3$	
$\text{Fe}(\text{OH})_2$	
Green Rusts $\text{Fe}^{\text{III}}_x\text{Fe}^{\text{II}}_y(\text{OH})_{3x+2y-z}(\text{A}^-)_z$ ; $\text{A}^- = \text{Cl}^-; \frac{1}{2}\text{SO}_4^{2-}$	

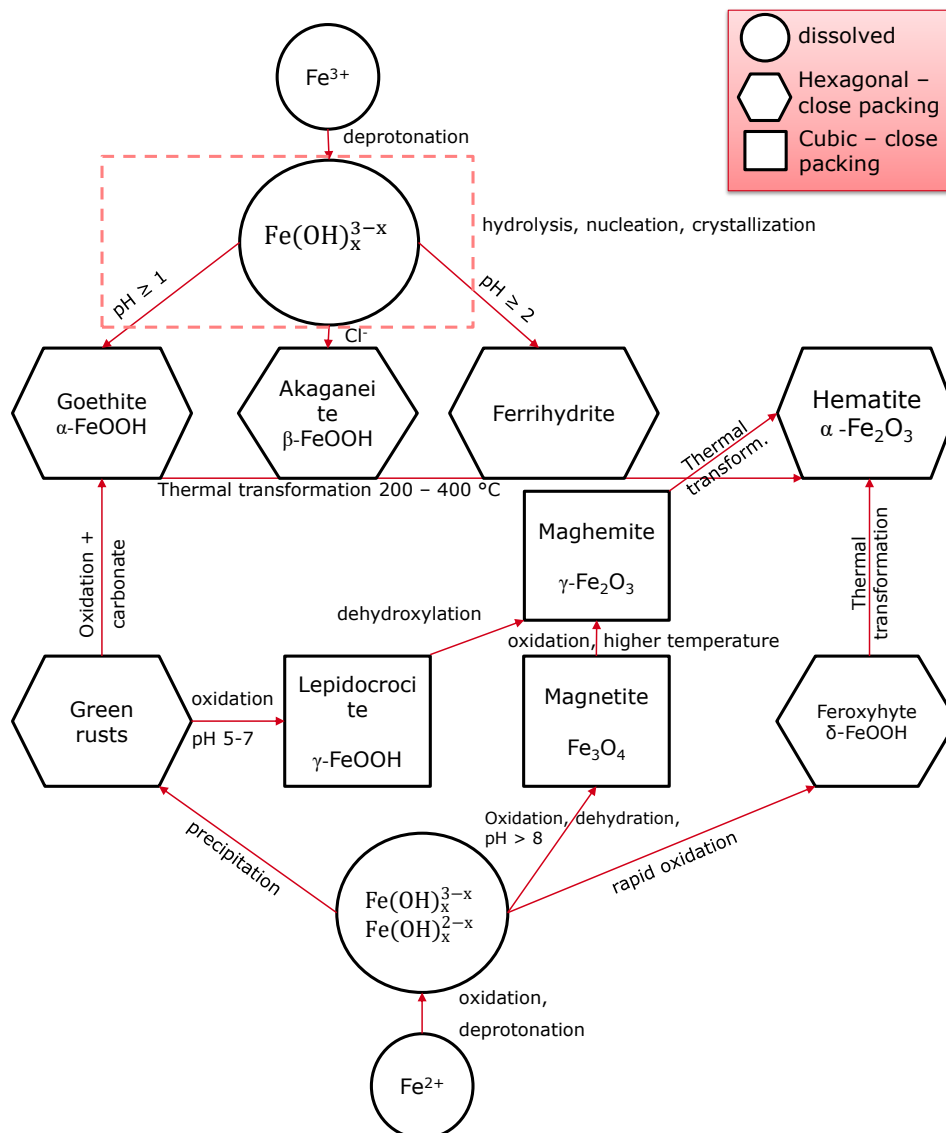
Depending on the influencing factors and the experimental conditions, corrosion products may result in different compositions of iron oxides. Several common iron oxides observed in different experimental conditions are presented in Table 2.5. The different composition of iron oxide is strongly related to the transformation of  $\text{Fe}^{2+}$  or  $\text{Fe}^{3+}$  ions when they react with proton or oxygen, which leads to a certain corrosion product, as shown in Figure 2.6.



**Table 2.5.** Composition of resulting corrosion products in different conditions [72]

Type of corrosion	Conditions	Composition of the corrosion products <sup>a)</sup>
Electrochemical	Stagnant pure water with enough O <sub>2</sub>	Gt, Lp
	Boiling water in low O <sub>2</sub> and/or acid	Mt
	Hot oxygenated water	Mt, Lp, GR
	Seawater	Mt, Lp, Gt, Ak
Atmospheric	Temperature and tropical environments	Lp, Gt (Mt)
	High SO <sub>2</sub>	Gt predominates
	High Cl <sup>-</sup>	Ak predominates
Passive Layer	Anodic polarization in KOH/NaOH, H <sub>2</sub> SO <sub>4</sub>	Mt, Hm
	Borate buffer with Fe <sup>2+</sup>	Lp
	Concentrated HNO <sub>3</sub>	Spinel
Thermal	Air, room temperature	Mt, Mh
	Air, 250–550°C	Mt, Hm
	Air, 600°C	Wu, Mt, Hm

a) Gt: goethite, Lp: lepidocrocite, Ak: akaganeite, Hm: hematite, Mh: Maghemite, Mt: magnetite, Wu: wüstite, GR: green rust, ( ): trace

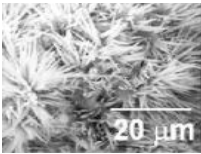
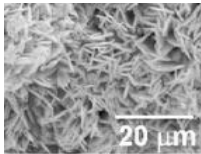
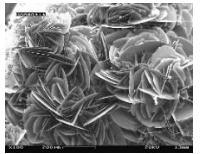
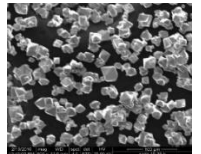
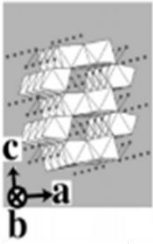
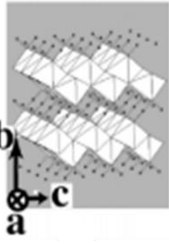
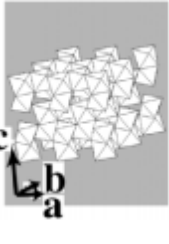
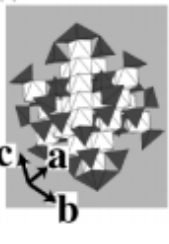


**Figure 2.6.** Transformation pathways of iron oxide from Fe<sup>2+</sup> and Fe<sup>3+</sup> [72]



As summarized in Table 2.4, Table 2.5, and Figure 2.6, the types of corrosion products depend on the types of steels and the environment. To investigate the corrosion behavior of steels in the geothermal environment, the testing condition was set to 150 °C in aqueous solution, with and without oxygen. Based on the intended parameters, four types of corrosion products might be expected, i.e., goethite, lepidocrocite, hematite, and magnetite. Further details on the crystal structures and properties of these corrosion products are summarized in Table 2.6.

**Table 2.6.** Crystal structures and properties of the possible corrosion products discussed in this thesis [72–74].

Crystal	Possible Corrosion Products			
<b>Mineral</b>	Goethite	Lepidocrocite	Hematite	Magnetite
<b>Composition</b>	$\alpha$ -FeOOH	$\gamma$ -FeOOH	$\alpha$ -Fe <sub>2</sub> O <sub>3</sub>	Fe <sub>3</sub> O <sub>4</sub>
<b>Category</b>	Oxyhydroxide	Oxyhydroxide	Oxide	Oxide
<b>Physical color</b>	brownish black, yellow-brown, reddish brown	Deep red, red-brown	Steel-gray to black in crystals and massively crystalline ores	Grayish black or iron black
<b>System</b>	Orthorhombic	Orthorhombic	Trigonal	Cubic
<b>Morphology</b>	Needle-like / hair-like	Plate-like	Plate-like	Octahedral
<b>Structure</b>				
				
<b>Density (g/cm<sup>3</sup>)</b>	~4.3	~4.1	~5.26	~5.2

The oxyhydroxide structures are described using FeO<sub>6</sub> octahedral units; small circles represent hydrogen atoms

### 2.3.2. Protective Coatings

Corrosion prevention is one important aspect to determine the type of materials for geothermal application. Extensive research of material selection to determine the performance of different steels has been conducted as one of the corrosion prevention methods in geothermal applications [8-10, 75, 76]. Corrosion protection can be achieved using different strategies, for example, by controlling the fluid flow, using other materials (plastics, elastomers, and composites), applying protective coatings for steel corrosion control, engineering cathodic protection systems, or introducing corrosion inhibitors [70]. Other corrosion prevention methods are also available along with their advantages and disadvantages, as detailed in Table 2.7. [77].

**Table 2.7.** Corrosion prevention methods

Method	Examples	Advantages	Disadvantages
<b>Altering the environment</b>	Changing process, humidity, temperature, use of inhibitors	Simple changes, lower cost, usually adaptable to the existing facility	May not completely eliminate the problems
<b>Corrosion resistant material</b>	Copper, nickel, chromium, molybdenum alloyed with iron or steel, titanium	Long lifespan, applicable for certain case	High initial costs
<b>Cathodic protection</b>	Ship hulls underwater, underground pipelines	Simplicity, applicable in the presence of a good electrolyte	Limited use in damp or dry areas; immersion is required
<b>Barriers</b>	Brick linings, protective coatings, plastic sheeting, monolithic toppings	Most effective and versatile, reasonable cost	Careful analysis of corrosion problems is necessary; proper surface preparation and application are important
<b>Overdesign</b>	Heavier structural parts or thicker plates than the requirement		Higher initial costs, ineffective, increased weight

In geothermal applications, several protective coatings have been developed as an alternative to suppress the costs of building the geothermal power plants without neglecting its safety and performance [18, 78]; this strategy was selected for this thesis.

As mentioned in Table 2.7, barriers or coatings are the most effective method for protecting carbon steel. However, the utilization of coatings must be carried out carefully, as the substrate may contain defects or trapped impurities that influence the performance of the coatings. In addition, surface preparation and pretreatment methods are likely to be essential for coating system performance [79].

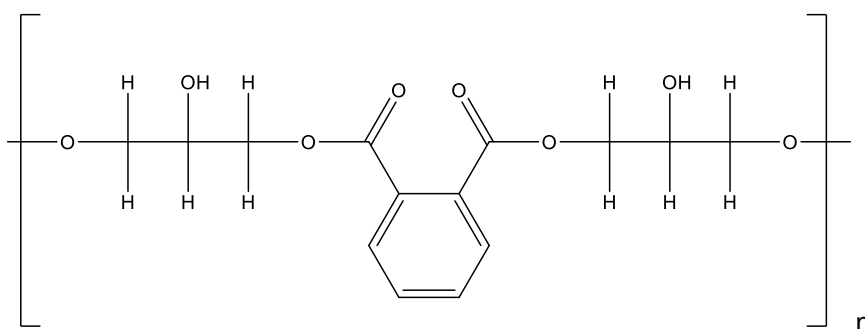
A coating system consists of several important constituents, i.e. binder, pigments, and solvent. In this research, alkyd resin was used as a binder, polyaniline and silicon dioxide as pigments and methyl isobutyl ketone as the solvent. It is important to have good adhesion between coatings and metal substrate, as when deadhesion takes place underneath the coatings, corrosion will follow on the interface between the coatings and metal. If adhesion can be maintained during the immersion service, corrosion protection of the metallic material can be achieved. In most cases, adhesion can be optimized using the secondary valency bonding with metals. Some coatings which are rich in polar groups (hydroxyls or carboxylic acid groups) on their molecules have good adhesion with metals (epoxies, alkyds, and polyesters) [80], whereas polymers bearing polar groups tend to be hydrophilic and attract water into the coatings [70].

### *Alkyds*

Alkyds have been used commercially since 1927 and are easy to apply. They are relatively inexpensive compared to other types of organic coatings and can be modified to both solvent-borne or waterborne coatings [81]. Alkyds cannot tolerate alkali conditions, so are not

suitable for zinc surfaces or in any alkaline condition, e.g. in concrete. They are not suitable for immersion service because they lose adhesion to the substrate during immersion in water, therefore it is very important to choose effective anticorrosion pigments for this class of coating.

Alkyds are thermoplastic polyester resin. The main acid component of alkyd is phthalic acid or its anhydride, and the main alcohol component is glycerol. By polycondensation of alcohol (polyol), these components form an ester, continuing to react with multiple alcohol and acid groups to form a crosslinked polymer, as shown in Figure 2.7 [82].

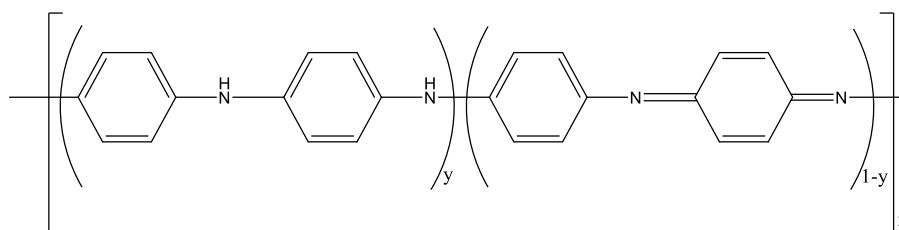


**Figure 2.7.** An example of a simplified chemical formulation of alkyd [82]

### 2.3.3. Polyaniline

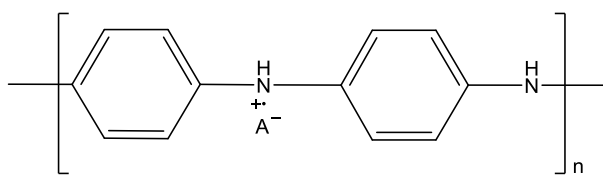
Polyaniline was developed when F. F. Runge (1834) and C. J. Fritzsche (1840) tried to isolate aniline and observed a blue color in the acidic medium caused by oxidation [22]. The name aniline was proposed by Fritzsche and means indigo color. Due to its interesting color, researchers have been trying to understand the mechanism of polyaniline formation to develop useful dyes for textiles. Polyaniline is widely known as a conducting polymer material and has many applications, such as batteries, supercapacitor, fuel cell, actuators, sensors, membranes, LED, corrosion protection, and photovoltaics [22, 83].

As a conducting polymer material, polyaniline is attractive because it is easy to synthesize, has an interesting reversible reduction-oxidation and pH switching properties, low price of monomer, and is environmentally stable. Figure 2.8 shows the general polymeric structure of polyaniline, containing three oxidation states of polyaniline, i.e. leucoemeraldine (fully reduced,  $y = 0$ ), emeraldine (half-oxidized,  $y = 0.5$ ), and pernigraniline (fully oxidized,  $y = 1$ ) [22].



**Figure 2.8.** General polymeric structure of polyaniline [22]

Polyaniline in the form of emeraldine has two distinct electronic properties, i.e. emeraldine base (non-conductive) and emeraldine salt (conductive). Emeraldine salt is formed when polyaniline is doped by anion in acidic medium, with a polymeric structure as shown in Figure 2.9 [22].



**Figure 2.9.** Polymeric structure of emeraldine salt [22]

Along with the formation of polyaniline, a fascinating color transformation of each oxidation state may take place: leucoemeraldine tends to generate a yellow to light green color, emeraldine a green color, and pernigraniline is blue to violet. The color transformation of polyaniline can be an advantage as an initial indication of its properties.

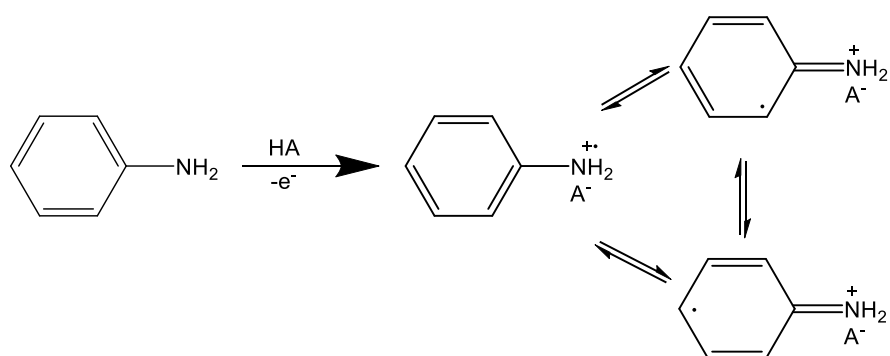
### 2.3.3.1. Polyaniline Synthesis

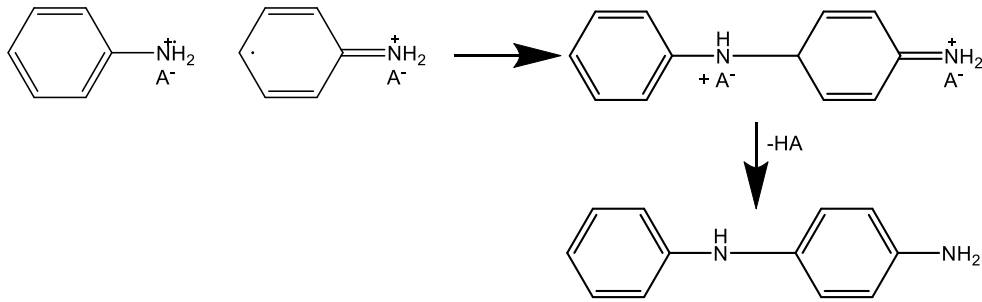
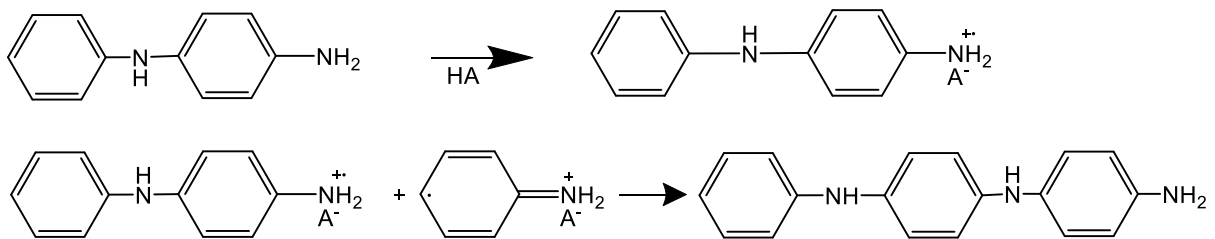
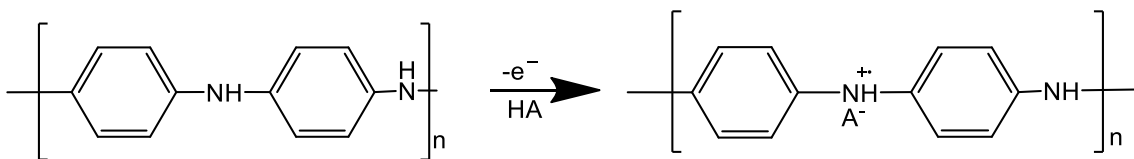
Polyaniline can be synthesized via different routes, i.e. electrochemical polymerization, chemical polymerization, photochemically initiated polymerization, enzyme-catalyzed polymerization, and polymerization employing electron acceptors. The following section presents the synthesis of polyaniline via electrochemical and chemical polymerization, which were utilized in this work.

#### Electrochemical polymerization

As described by Wallace (2009), there are several steps in the mechanism of electrochemical polymerization, i.e. monomer oxidation, radical coupling and rearomatization, chain propagation, oxidation and doping of polymer, as depicted in Figure 2.10 [22].

#### Step 1: aniline oxidation



Step 2: radical coupling and rearomatizationStep 3: chain propagationStep 4: oxidation and doping of PANI

**Figure 2.10.** Polymerization steps of polyaniline via electrochemical polymerization [22]

There are some influencing factors in the electrochemical polymerization process [22], which are related to the electrode materials, concentration and properties of dopant, solvent, temperature, and the monomer type.

a. Electrode materials

The properties of electrode materials play an important role in determining the amount and properties of polyaniline deposited on the surface. It is also necessary to understand the possible chemical or electrochemical behavior of the electrode in the polymerization medium.

b. Concentration and properties of dopant

Common dopant use in polymerization is strong aqueous acids, e.g. sulfuric acid, hydrochloric acid, phosphoric acid, and other strong acids with a pH lower than 2. The concentration and the nature of dopants affect the formation of polyaniline in many aspects, such as morphology, conductivity, pH switching characteristics, and the growth of the polymeric chain.

## c. Temperature

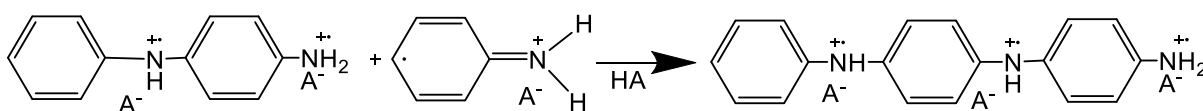
Although it is commonly performed at room temperature, some experiments were conducted at various temperatures.

## Chemical Polymerization

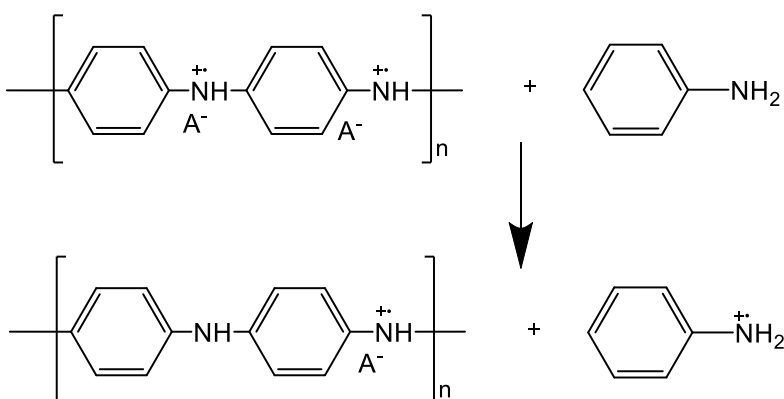
Wallace (2009) also described several steps in the mechanism of chemical polymerization initiated by the oxidation of the monomer, followed by radical coupling and rearomatization as described in electrochemical polymerization, but then undergo the different steps as shown in Figure 2.11 [84].

Step 1 and 2: similar to electrochemical polymerization

Step 3: chain propagation



Step 3: reduction from pernigraniline to emeraldine



**Figure 2.11.** Polymerization steps of polyaniline via chemical polymerization [22]

Factors in the chemical polymerization process

## a. Polymerization temperature

Polymerization via chemical polymerization is strongly related to the temperature and polymerization duration. Polymerization at room temperature will result in low molecular weight and formation of significant defects, for example, an undesirable branching due to ortho-coupling [22]. Polymerization is usually performed between 1–5 °C to produce polyaniline with molecular weight of approximately 30,000–60,000 g/mol. Research at lower temperatures (-30 to -40 °C) has also been conducted, resulting in higher molecular weight polyaniline, approximately 100,000 g/mol.

## b. Concentration and properties of dopant

The duration of the polymerization reaction time affects the morphology of polyaniline. (for example HClO<sub>4</sub>, longer polymerization, more compact). Typically, the pH used in is

0–2, with a pH 4–6 resulting in inconsistency of emeraldine salt formation, subsequently giving a lower molecular weight and lower electrical conductivity.

c. Properties of oxidant

Possible oxidant agents used in chemical polymerization are ammonium peroxodisulfate  $(\text{NH}_4)_2\text{S}_2\text{O}_8$ , ceric ammonium sulfate  $\text{Ce}(\text{SO}_4)_2$ , potassium dichromate  $\text{K}_2\text{Cr}_2\text{O}_7$ , hydrogen peroxide  $\text{H}_2\text{O}_2$ ,  $\text{FeCl}_3$ . Optimal conductivities of polyaniline via chemical polymerization are obtained when using APS as oxidant ( $E^\circ = 1.94 \text{ V}$ ), whereas the others are 1.72, 1.23, 1.78, 0.77 V (vs SHE).

### 2.3.3.2. Corrosion Protection Mechanism

The effect of polyaniline use for corrosion control has been studied with various parameters, such as different types of polyaniline oxidation state, synthesis method, the use of top coat, the type of metal substrate and its preparation, different corrosion media, and the test method [85], resulting in a quite complex hypothesis regarding the protection mechanism. Consequently, many proposed mechanisms have been developed.

In general, the proposed protection mechanisms were developed with different approaches, such as barrier protection, anodic protection, controlled inhibitor release, cathodic protection, corrosion inhibition, dislocation of oxygen reduction, and the synergistic effect. In this section, several possible mechanisms are elaborated.

#### Barrier Protection

The use of polyaniline for corrosion control has been proposed to allow water and oxygen penetration but restrict the access of some corrosive species. However, it was proven by several researchers that there is an indication of active protection instead of a simple barrier protection. Research that support this mechanism are summarized in Table 2.8.

**Table 2.8.** Relevant references supporting the protection mechanism of conducting polymer via barrier protection

No.	Author and Year	Key Findings	Ref
1	Beck (1988)	Electrochemically deposited polyaniline on steel with a thickness of above 1 $\mu\text{m}$ can prevent corrosion	[86]
2	Wessling (1994)	Polyaniline (Versicon) dispersed to coat the steel surface, in which the corrosion current is lower than that of uncoated carbon steel	[87]
3	Mac Diarmid (1996)	Polyaniline in emeraldine base form was applied to the stainless steel surface; an increase of $E_{\text{corr}}$ of 550 mV vs. SCE was observed	[88]

#### Anodic Protection

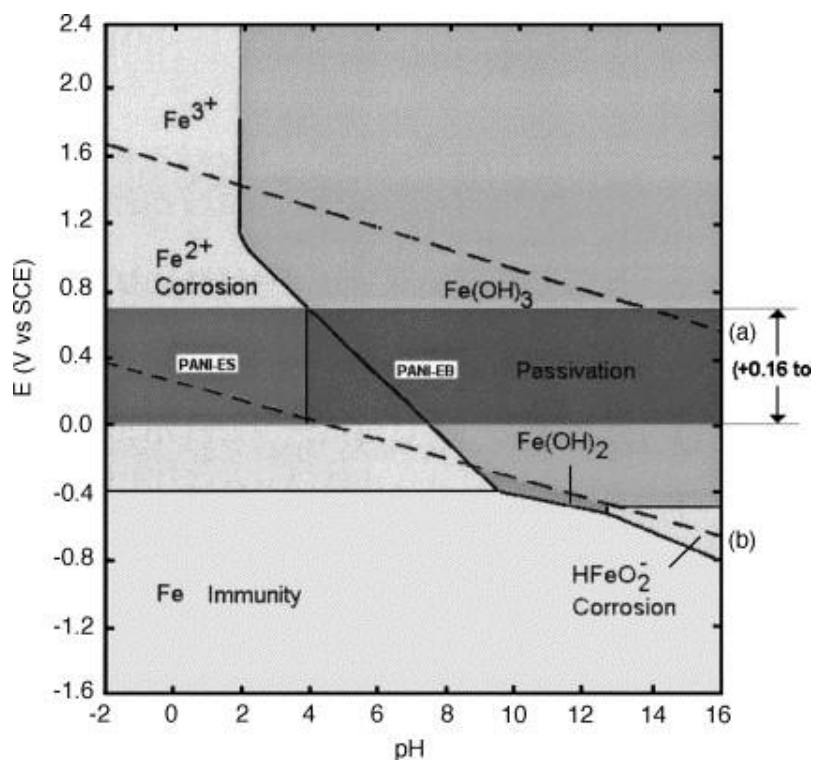
Anodic protection is a technique for corrosion control where the metal substrate is designed to act as an anode by maintaining the potential of metal substrate in its passive region. This technique usually results in the shift of the potential in the anodic direction, or also known as ennoblement. Examples of polyaniline use as anodic protection as detailed in Table 2.9.

**Table 2.9.** Relevant references supporting the protection mechanism of conducting polymer via anodic protection

No.	Author and Year	Key Findings	Ref
1	Tallman, et al. (2002)	Polyaniline coated steel has a redox potential of 0.4–1.0 V vs. SHE, which is higher than that of uncoated carbon steel -0.62 V vs. SHE	[89]
2	De Berry (1985)	De Berry first applied polyaniline on stainless steel [90], which has since been successfully deposited via several electrochemical techniques, i.e. potentiostatic, galvanostatic, or cyclic voltammetry [91, 92], to replace hazardous coatings	[90]
3	Wessling (1996), Lu (1995)	When the doped polyaniline is in contact with steel, the steel undergoes a rapid oxidation at the polyaniline-steel interface, resulting in the formation of $\gamma$ -Fe <sub>2</sub> O <sub>3</sub>	[25, 93]

Schauer et al. investigated the protection of iron against corrosion using polyaniline primer. The first essential phase of corrosion protection is the conversion of original iron oxides, followed by the active corrosion protection caused by the conductive polyaniline form, which occurs because there is a separation of the partial cathodic and anodic corrosion processes. The third phase is the action caused by a non-conductive form of polyaniline [94].

Figure 2.12 shows the Pourbaix diagram of steel in water, and polyaniline in the form of emeraldine salt (PANI-ES) and emeraldine base (PANI-EB), which are superimposed with the stable region of steel [95].

**Figure 2.12.** Pourbaix diagram of polyaniline in different oxidation states [95]



### Controlled Inhibitor Release

When there is a defect on the polyaniline coated carbon steel, the coating-metal interface forms a galvanic cell. The coating will act as a cathode and the metal will act as the anode, which drives the reduction of the coating and the formation of metal-dopant complex. Some research is shown in Table 2.10 below.

**Table 2.10.** Relevant references supporting the protection mechanism of conducting polymer via controlled inhibitor release

No.	Author and Year	Key Findings	Ref
1	Kendig and Warren (2003)	The counter anion of polyaniline with the corrosion inhibiting properties is released in the polymeric matrix, therefore, the selection of anion is important, and might influence the corrosion rate	[96]
2	Kinlen et al. (2002)	Phosphonate doped is better than sulphonate doped	[97]
3	Rohwerder and Michalik (2007)	The conducting polymer coating will fail when a large defects exist. Fast breakdown of the coating can be induced by cation transport, resulting in the reduction of the conducting polymer. It is important to note that the electrochemical activity of the conducting polymer is more substantial than the electrical conductivity in affecting the corrosion protection.	[98]

### Cathodic Protection

There are two types of galvanic protection techniques, i.e. galvanic anodes, and impressed current (Table 2.11). Here, polyaniline coating was used as a galvanic anode, because it is attached to the metal, or connected. The protection comes from the electrochemical cell created between the galvanic anode and the metal which is more noble.

**Table 2.11.** Relevant references supporting the protection mechanism of conducting polymer via cathodic protection

No.	Author and Year	Key Findings	Ref
1	Elkais et al. (2013)	Switching zone	[99]
2	Dun Nguyen et al. (2004)	Local effect was observed; small defects were passivated, whereas large defects continue to corrode, with various oxidation degrees of polyaniline coexisting and participating in both the cathodic process and the anodic passivation of metal	[100]

### Corrosion Inhibition

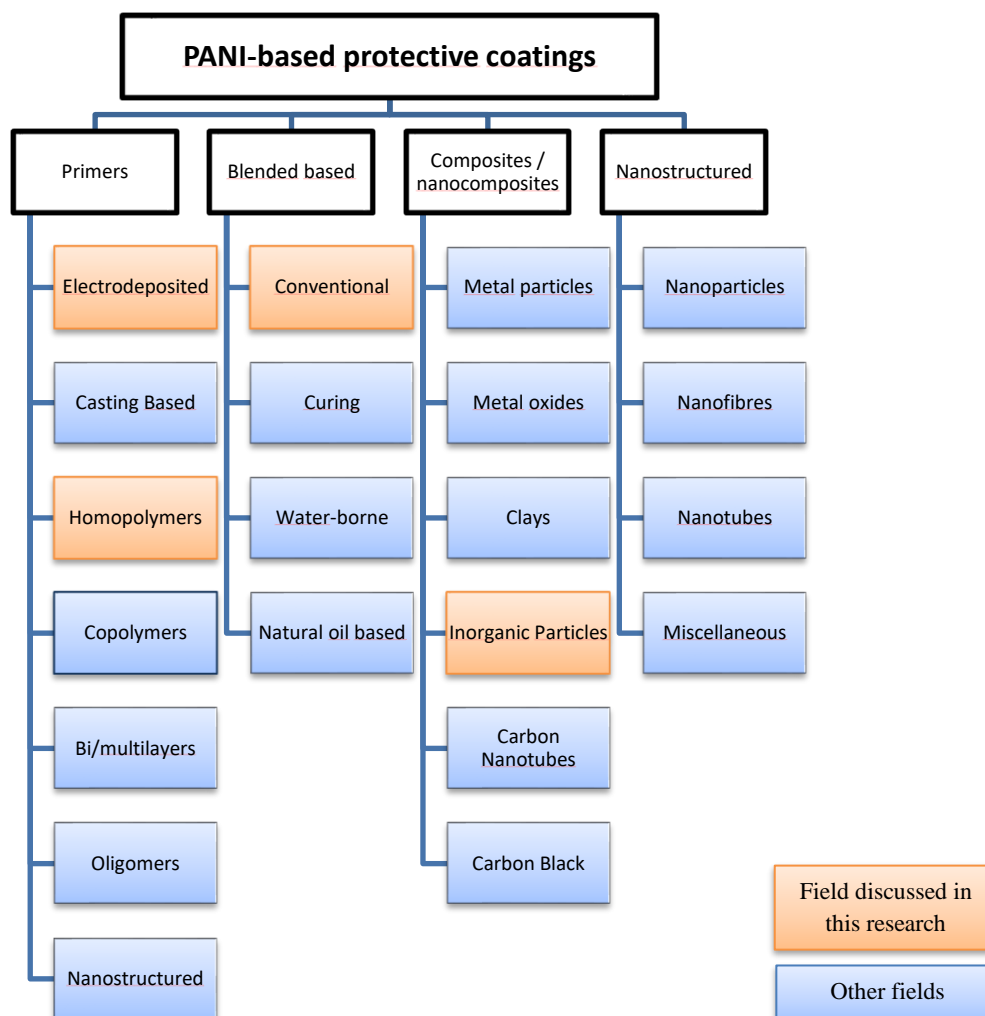
Adsorption of monomers on the surface endorses adhesion (Table 2.12). The most powerful inhibitors are usually organic compounds with  $\pi$ -bonds, thus, there is a tendency of aniline and its derivatives to adsorb on the metal surface. The adhesion of organic molecules to the metallic surface consequently reduces the rate of corrosion.

**Table 2.12.** Relevant references supporting the protection mechanism of conducting polymer via corrosion inhibition

No.	Author and Year	Key Findings	Ref
1	Sathiyarayanan et al. (1992)	Coexistence of delocalized $\pi$ -electrons and the quaternary ammonium nitrogen in the polymer was observed to promote strong adsorption on the iron surface	[101]
2	Iroh and Su (2000)	In case of polypyrrole (PPy), double bonds and the polar -NH group in the ring causes strong adsorption	[102]

### 2.3.3.3. Polyaniline Coating Application

To understand the standpoint of this study, a scheme of polyaniline-based protective coatings has been redrawn as shown in Figure 2.13 [85], with the orange color indicating the aspect discussed in this thesis. It is evident that the research field on conducting polymers as anticorrosion coatings is growing widely. This research explores polyaniline-based protective coatings produced via electrochemical deposition (electrodeposited) and conventional coating application procedure. It is also based on homopolymers and further developed in conjunction with inorganic particles to be utilized in a high temperature and high pressure environment.

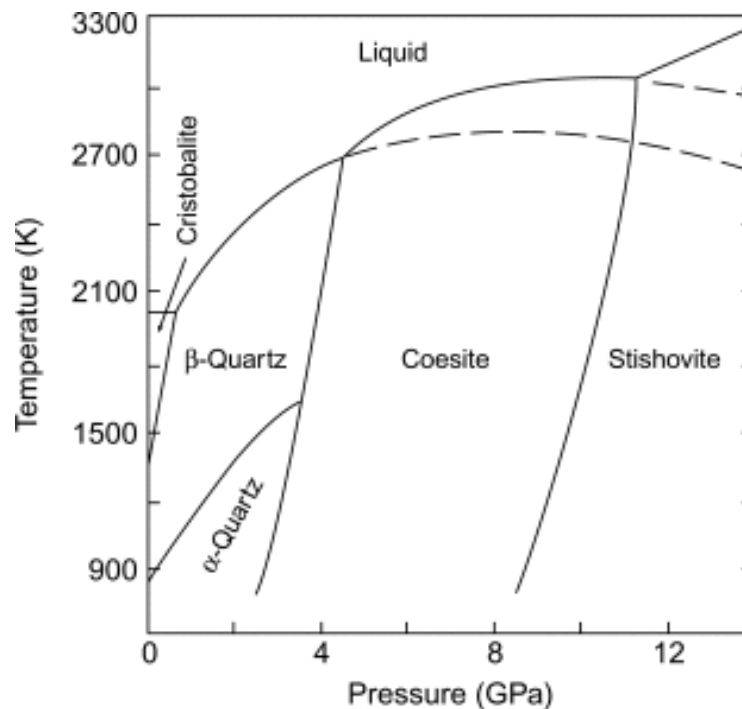
**Figure 2.13.** Various schemes of polyaniline-based protective coatings (adapted from [85])

#### 2.3.4. Silicon Dioxide

Silica ( $\text{SiO}_2$ ) is one of the most common oxides on earth, with an average abundance of about 37 wt% [103]. It is widely used in many applications, such as for the construction industry, as precursors of glass and silicone, microchips, and semiconductors. Figure 2.14 shows the phase diagram of silicon dioxide in which pure silicon dioxide forms stable polymorphs at different temperatures and pressure [103]. There are three different phases of silicon dioxide which exist at normal pressure, i.e. quartz, tridymite, and cristobalite.

Quartz is one of the most common forms of silicon dioxide, with a melting temperature of 1400 °C at ambient pressure [104]. In addition, silicon dioxide has a relatively low thermal expansion coefficient of 8-14 ppm/K [105] which is matched to that of carbon steel, i.e. 12 ppm/K [106]. The thermal expansion coefficient is a crucial parameter for application of coatings at a higher temperature. The substrate and coatings, including the matrix and fillers, should have a compatible thermal expansion coefficient to avoid differential thermal contraction and stresses upon cooling and heating. Therefore, quartz is a suitable candidate as a filler in the coating to enhance the thermal stability for geothermal application.

Silica-based hybrid coatings have been developed as multifunctional coatings for a wide variety of applications, from cultural heritage to aircraft protection. Silica is often utilized to improve anticorrosion properties of coatings on low alloyed steels. Dalbin et al. proposed a new silica-based coating procedure by immersing the galvanized steel in the deposition bath consisting of nanometric silica particles/sodium metasilicate mixture. By electrochemical impedance spectroscopy (EIS) measurement in the  $\text{Na}_2\text{SO}_4$  electrolyte and salt spray test, they found that silica-based coating has almost as good protection comparable to that of chromate coating, although some localized corrosion was identified after the salt spray test [107]. Santana et al. synthesized and characterized a hybrid organic-inorganic coating based on silica to improve the corrosion resistance of carbon steel. A bilayer hybrid silica sol gel was applied on carbon steel AISI 1010, in which the outer layer contained cerium salt as inhibitors and the inner layer with silica nanoparticles without cerium salt. Surface pretreatment of carbon steel was performed by phosphating to enhance the adhesion between the coating and the metal surface [108]. Based on the existing research, there is still a room for improvement and to understand better the role of silica as fillers or additives in the organic polymeric matrix on their corrosion protection behavior.

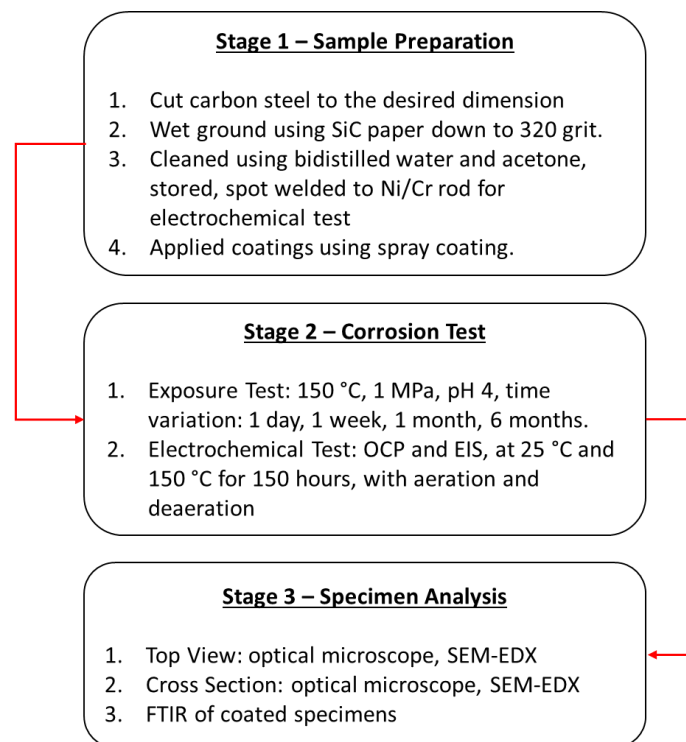


**Figure 2.14.** Phase diagram of silicon dioxide in high temperature and high pressure, according to the calculations of Swamy et al. [109]. Tridymite is not shown, the dashed curves represent the metastable extensions of the melting curves of quartz and coesite.

In the geothermal environment, silica is also often found in geothermal brines, in which dissolved silica is generally controlled by the equilibrium of quartz. The silica content in geothermal water may exhibit scaling on geothermal pipelines which leads to a problem in the pipeline circulation. As a result, silica is often separated from the geothermal water, being obtained as a side product of geothermal site exploration [110]. Considering that silica might be locally available as a raw material, it is one of the most versatile options to develop protective coatings for geothermal applications at a reasonable cost.

# Chapter 3. Methodology and Experimental Techniques: Theory and Practice

This chapter focuses on and describes the methodologies of the experimental work and the related theory behind each of the techniques, as well as discussing the materials used throughout this research. During this study, a number of practical techniques were used to determine the corrosion rate of carbon steel in different conditions, synthesis and formulation of the coating system to develop a suitable coating system and investigate the corrosion resistance of coated carbon steel in artificial geothermal water. A general overview of the experimental steps is presented in Figure 3.1.



**Figure 3.1.** Overview of the experimental procedure

## 3.1. Investigated Material

In this study, carbon steel was used as the common material in the geothermal components as it is vital to understand the corrosion mechanism of carbon steel when exposed to artificial geothermal water. In addition, uncoated carbon steel was used as a control to compare the performance of the developed coated carbon steel. This subsection elaborates the details of each component that comprise the investigated coating system for carbon steel protection for geothermal application, such as the alkyd-based binder, polyaniline, and silicon dioxide.

### 3.1.1. Carbon Steel

Specimens used as the base material to investigate the coating system were made of carbon steel St37 (German name), or S235 JR according to EN 10025-2 which was characterized using spark optical emission spectroscopy to determine the elemental composition, as shown in Table 3.1. Prior to the experiments, specimens were ground using SiC paper to a size of 320 grit, then rinsed with bi-distilled water, and acetone.

**Table 3.1.** Elemental composition of carbon steel based on arc/spark emission spectroscopy

Element	Fe	Mn	Cu	C	Cr	Si	Ni
Composition (%)	99.28	0.3085	0.0789	0.0697	0.0564	0.049	0.0448

Element	Al	S	P	Sn	Ti	V	Ca
Composition (%)	0.0325	0.0229	0.0115	0.0023	0.0013	0.0012	0.0005

Element	B	N	Mo	Co	W	Nb	Ta	Pb
Composition (%)	0.0002	>0.0240	<0.01	<0.01	<0.01	<0.005	<0.002	<0.001

### 3.1.2. Coating System

The investigated coating system consisted of several elements, i.e. alkyd-based binder, polyaniline and silicon dioxide as pigments. To apply the coating on the carbon steel substrate, methyl iso butyl ketone (MIBK) was used as a solvent. Pigments used in this coating system were synthesized as described in the following sections.

#### 3.1.2.1. Alkyd-Based Binder

A commercial marine coating from PT Bintang Energi in Indonesia was used, which is an alkyd-based marine coating containing  $\text{CaCO}_3$ . The formulation of the investigated coating was 10 g of the total mixture of binder and pigments dissolved in 5 ml MIBK and mixed using an orbital shaker at 225 rpm for 30 minutes. Pigments of PANI and  $\text{SiO}_2$  were added to the binder and solvent.

#### 3.1.2.2. Polyaniline

Polyaniline particles were prepared by two methods, chemical polymerization and electrochemical polymerization. Here, the chemical polymerization is elaborated to produce polyaniline pigments using  $\text{H}_3\text{PO}_4$  and DBSA as dopants. Polyaniline particles were characterized using FTIR, UV-Vis, and SEM.

#### Polyaniline-phosphoric acid

To synthesize polyaniline, 0.2 M aniline was dissolved in 1.2 M phosphoric acid (200 ml) and preserved for 2 hours at 5 °C, before the dropwise addition of the oxidation agent, 0.25 M ammonium peroxodisulfate (APS), while stirring to obtain a homogeneous solution. Subsequently, the solution was kept in the climate chamber in a stagnant condition at 5 °C for 12 hours for polymerization. The polyaniline was filtered and cleaned using bi-distilled water and acetone until the pH of the filtrate reached 7, then vacuum-dried to form a fine powder.

### Polyaniline - DBSA

First, 0.1 M aniline was dissolved in 0.07 M dodecylbenzene sulfonic acid (DBSA) in a total volume of 100 ml by slow stirring for 30 minutes, and cooled to 5°C before the dropwise addition of 0.1 M APS while stirring. The color of the solution changed from dark yellow to dark green. Polymerization was conducted for 12 hours with constant stirring. Polyaniline was then cleaned using bi-distilled water and acetone until the pH reached 7, and vacuum-dried to form a fine powder.

#### 3.1.2.3. Silicon Dioxide

Silica powder was obtained from natural sand in the coastal area of Indonesia and pretreated using a planetary ball mill for 2 hours with a zirconia ball, then leached with 2 M HCl. Silica sand powder was washed using bi-distilled water until the pH reached 7, then dried in an oven at 105 °C for 24 hours [111]. The morphology and chemical composition of silicon dioxide were analyzed using SEM and XRD.

## 3.2. Coating Application and Characterization

As mentioned previously, the effect of polyaniline within the coatings can be investigated using several methods, as shown in Figure 2.13. Here, in addition to the complex coating using paint blended pigments, an electrochemical deposition of polyaniline was also performed on carbon steel as detailed below.

### 3.2.1. Electrochemical Deposition

Electrochemical deposition was conducted via a three-electrode system (Gamry potentiostat Reference 600), with carbon steel as the working electrode, Pt as the counter electrode, and Ag/AgCl as the reference electrode. Cyclic voltammetry was performed in 200 ml of electrolyte: 0.1 M oxalic acid and 0.05 M aniline, or 0.3 M oxalic acid and 0.1 M aniline. Cyclic voltammetry was conducted by sweeping the potential from 0.6–1.5 V, with the scan rate of 10 mV/s. After depositing the polyaniline layer, the specimens were cleaned using bi-distilled water and acetone.

### 3.2.2. Polyaniline/Silica Composite Coating

Coatings were applied on the surface of carbon steel that were ground to 320-grit SiC paper by gravity feed double action air brush BELKITS, using a standard needle and nozzle diameter of 0.25–0.3 mm. The air brush was used with an air pressure of 2.5 bar. Specimens were then left in a dust-free area to dry.

The formulation of the investigated coatings was calculated using the weight percent formula by dissolving 10 g of the coating component in 5 ml MIBK and mixing by an orbital shaker for 30 minutes at 225 rpm. The coating formulation is described in Table 3.2 and was chosen to optimize the composition of the coating components suitable for geothermal applications.

**Table 3.2.** Coatings type description and its formulation with the different types of PANI presented in brackets

No	Specimens	Binder (wt%)	PANI (wt%)	SiO <sub>2</sub> (wt%)
1	Binder	100	-	-
2	SiO <sub>2</sub>	85	-	15
3	PANI-1 (PANI/H <sub>3</sub> PO <sub>4</sub> )	98	2	-
4	PANI-2 (PANI/DBSA)	98	2	-
5	PANI-1/SiO <sub>2</sub> (PANI/H <sub>3</sub> PO <sub>4</sub> )	83	2	15
6	PANI-2/SiO <sub>2</sub> (PANI/DBSA)	83	2	15

### 3.3. Experimental Conditions

The electrolyte used in the experiment was artificial geothermal water simulating the geothermal brine at the Sibayak site [4, 7], with a chemical composition as shown in Table 3.3. All experiments were performed at 150 °C with a total pressure of 1 MPa in an under Argon environment, or also mentioned as deaerated conditions to investigate the corrosion behavior of carbon steel and coated carbon steel in the artificial geothermal water. Preliminary studies were conducted using uncoated carbon steel at various temperatures, dissolved gases, and pH to confirm the most significant influencing factors. The For these reasons, experiments for carbon steel specimens were conducted at 25 °C, 70 °C, and 150 °C, with additional experiments at 150 °C in acidic (pH 4), and neutral (pH 7) solutions, whereas for the coated carbon steel, the effect of temperature was observed at 25 °C and 150 °C in a solution pH of 4.

To understand the role of dissolved oxygen in the system, the aerated condition was achieved with oxygen containing solution, followed by pressurizing the autoclave using Ar. In the deaerated condition, the solution was saturated by Ar by 30-minute purging, followed by autoclave pressurizing by Ar. An additional testing of carbon steel in CO<sub>2</sub> environment was also performed for the preliminary test of carbon steel exposure.

**Table 3.3.** Chemical Composition of Artificial Geothermal Water

Cond.	Cl <sup>-</sup>	SO <sub>4</sub> <sup>2-</sup>	HCO <sub>3</sub> <sup>-</sup>	Ca <sup>2+</sup>	K <sup>+</sup>	Na <sup>+</sup>	pH <sub>25°C</sub>	σ (mS/cm)
mg/l	1,500	20	15	200	250	600	4	4.90

### 3.4. Evaluation Techniques

Evaluation is generally performed by exposure and electrochemical test. The exposure test involves the determination of the corrosion rate of carbon steel, microscopic study of specimens by optical and scanning electron microscope, and additional spectroscopy methods using FTIR, UV-Vis, or XRD. Electrochemical studies include the open circuit potential and EIS measurements for a short period (0–24 hours), and longer measurements extended to seven days.

#### 3.4.1. Exposure Test

Exposure tests were performed to simulate real conditions without applying any external disturbance. To estimate the corrosion rate of carbon steel, the weight loss method was used according to the ASTM G1-03 “Standard Practice for Preparing, Cleaning, and Evaluating Corrosion Test Specimens”. The experiment was performed by weighing the freshly ground



specimens and the exposed specimens on an analytical laboratory scale with a precision of  $10^{-3}$  g. The dimension of specimens was measured using a digital caliper.

The corrosion rate was calculated according to ASTM G31 “Standard Practice for Laboratory Immersion Corrosion Testing of Metals”, based on the exposure test using the following equation:

$$\text{Corrosion rate} = \frac{(K \times W)}{(A \times T \times D)} \quad (11)$$

Where, CR: corrosion rate in mm/year, K: a constant ( $8.76 \times 10^4$ ), T: time of exposure in hours, A: area in  $\text{cm}^2$ , W: mass loss in g, D: density in  $\text{g}/\text{cm}^3$ .

### 3.4.2. Microscopic Study

The microscopic study was used to observe the specimens before and after the exposure test. To confirm the mechanistic study by in-situ electrochemical test; visual observation, optical microscope and SEM images were used to describe the specimens.

#### 3.4.2.1. Optical Microscope

An optical microscope was used to investigate the surface of carbon steel and coatings. The surface images of particular localized area of carbon steel or coatings were recorded by an AxioPlan 2 imaging microscope with Zeiss AxioCam HRc camera (Carl Zeiss, Jena, Germany).

#### 3.4.2.2. Scanning Electron Microscopy (SEM)

SEM with different magnifications and measurement modes was utilized, i.e. secondary electron and back scattered electron, using SEM VEGA3 TESCAN, equipped with back scattered electron (BSE) detector, in-lens detector, and electron dispersive X-Ray spectroscopy (EDX). SEM images with a higher magnification were obtained using Zeiss Gemini SEM. Secondary electron mode was used to investigate the material morphology and topography, and BSE mode to observe the contrast of elemental distribution depending on the mass of each constituent element, with a brighter color exhibiting the heavier elements than the darker color. EDX was used to identify the elemental mapping of the investigated area.

The surfaces of carbon steel and polyaniline coated carbon steel were investigated without any additional preparation, because they have sufficient electrical conductivity. The coated carbon steel specimens were prepared by carbon sputtering to enhance the conductivity prior to the measurement. This preparation was also done for the cross section specimens, in which the specimens were embedded in epoxy resin. The morphology of the polyaniline and  $\text{SiO}_2$  particles was also observed using SEM. The polyaniline particles were prepared by dropping the suspension of polyaniline-ethanol mixture on a metallic substrate to avoid agglomeration.

### 3.4.3. Spectroscopy Methods

To characterize the coated specimens at the molecular level, vibrational spectroscopy methods were applied, such as ATR-FTIR and UV-Vis spectroscopy. UV-Vis spectroscopy was only used to characterize polyaniline particles. In addition, XRD was used to characterize the phase of  $\text{SiO}_2$  particles.

### 3.4.2.3. ATR-FTIR

Further analysis of the particles was also performed by Fourier transform infrared (FTIR) spectroscopy using a Thermofischer FTIR Nicolet 6700 instrument. The technique used in the experiment was Attenuated Total Reflectance (ATR), using diamond as the substrate, applied in the mid infrared range (4000–400  $\text{cm}^{-1}$ ), using 32 scans with a resolution of 4  $\text{cm}^{-1}$ . To analyze the infrared spectra, mid infrared region (4000–400  $\text{cm}^{-1}$ ) was divided into four main groups: X-H stretching region (4000– 500  $\text{cm}^{-1}$ ), triple bond region (2500–2000  $\text{cm}^{-1}$ ), double bond region (2000–1500  $\text{cm}^{-1}$ ), and finger print region (1500–600  $\text{cm}^{-1}$ ) [112].

### 3.4.2.4. UV-Visible Light Spectroscopy

To investigate the electronic transitional state, polyaniline was characterized using UV-Vis Spectrolab. Polyaniline particles were dispersed in bi-distilled water and the spectra were measured over the wavelength range 320–850 nm. Since polyaniline presents as emeraldine salt or emeraldine base, the oxidation states can be distinguished by UV-Vis spectroscopy.

### 3.4.4. X-Ray Diffractometry

$\text{SiO}_2$  particles were characterized using XRD RIGAKU Ultima IV, with an angular range of 5–65°, step size 0.02°, and Cu-K $\alpha$  radiation. Diffraction data were analyzed using Crystal Impact Match!3 to confirm the constituent phase of silicon dioxide.

### 3.4.5. Thermogravimetry Analysis (TGA)

To analyze the influence of  $\text{SiO}_2$  particles on the  $\text{SiO}_2$ -alkyd coating system, different compositions of  $\text{SiO}_2$  (5 wt%, 10 wt%, 15 wt%, and 20 wt%) were blended into the alkyd binder. The  $\text{SiO}_2$ -alkyd coating system was then compared to the TGA curve of the singular coating component, i.e.,  $\text{SiO}_2$  and alkyd binder. The mass loss of the samples was recorded using TGA Mettler Toledo TGA-SDTA 851e. Samples (10–11 mg) were prepared and placed in the alumina crucible, with experiments performed under  $\text{N}_2$  atmosphere with a starting temperature at 25°C (conditioned for 5 minutes), then increased to 500°C, with a heating rate of 10°C/minute.

### 3.4.6. Electrochemical Measurement

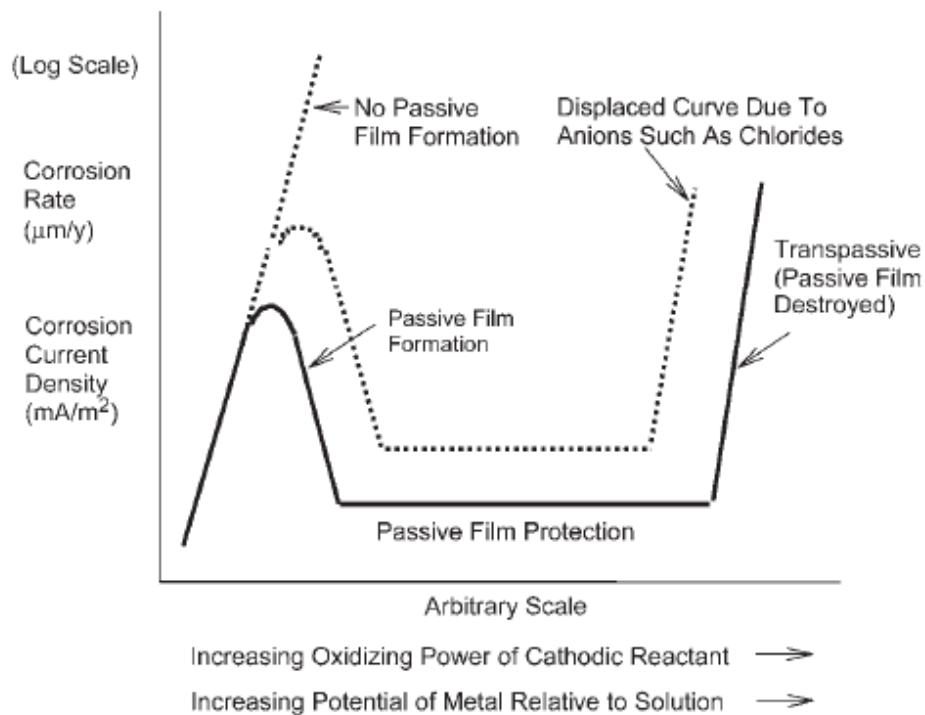
To investigate the corrosion mechanism of carbon steel and the coated carbon steel, electrochemical measurements were conducted in a three-electrode system using potentiostat Gamry Reference 600. The system consisted of the tested materials (carbon steel, and coated carbon steel) as a working electrode, Ti/TiO $_2$  net counter electrode, and Ag/AgCl in 3M KCl-saturated solution as reference electrode. In an attempt to evaluate and understand the corrosion processes electrochemically, the basic corrosion was presented along with the electrochemical techniques, such as open circuit potential (OCP) and EIS. As EIS is the central method in this thesis, both theory and practice are described in detail in section 3.4.6.3. In addition, electrochemical measurement in an autoclave is also described in section 3.4.6.4 to provide an insight regarding the detail for an electrochemical set-up for an application above 100 °C.

#### 3.4.6.1. Basic Corrosion

As discussed to a certain extent in Chapter 2, metals corrode when the species in solution supports a cathodic reaction (i.e., accepting electrons released at the corrosion sites where metal

ions are dissolved into the solution). The cathodic reactant, also known as an oxidizing agent, oxidizes the metal resulting in electron transfer from the metal to the cathodic reactant. Consequently, the cathodic reactant is reduced. When the cathodic reactant half-cell potential is more positive and the concentration is high, the higher the oxidizing power of the environment, in which there is a higher tendency for corrosion to occur. However, some metals can form protective corrosion product films, which decrease the corrosion rate by several orders of magnitude. This phenomenon is described as a passivation of metal. Despite the expectation that the material will be more active in an increasingly aggressive environment, it shows passive behavior, which is represented by a schematic plot of corrosion rate as a function of oxidizing power of environment (Figure 3.2). The shape and position of the curve depends on the type of materials or alloys, pH, temperature, and other ionic species, such as chloride ions.

To utilize a certain type of materials in the corrosive medium, material selection should be directed to the metals or alloys which have an ability to form a passive protective film, such as high alloyed steels. Another approach is by adjusting the environmental conditions which favor a passive film formation on the metal surface [55]. Carbon steel has no ability to form a protective passive layer, resulting in the increase of corrosion rate with respect to the increasing oxidizing conditions. Therefore, to use this type of material, the wall thickness of carbon steel pipelines should be calculated with respect to the predicted corrosion rate or corrosion protection strategy should be applied to protect carbon steel from corrosion.



**Figure 3.2.** Schematic representation of the effect of increasing oxidizing power of the environment on the corrosion of an active-passive type alloy, such as stainless steel, where the x-axis represents the applied potential, and y-axis is the current density in logarithmic scale [55].

Based on Figure 3.2, different electrochemical methods can be applied to investigate the corrosion behavior of materials under a certain environment, such as via free corrosion potential monitoring, potentiostatic or potentiodynamic polarization, linear sweep voltammetry, and EIS.

### 3.4.6.2. Open Circuit Potential

Open circuit potential (OCP), also known as free corrosion potential ( $E_{\text{corr}}$ ), refers to the corrosion potential in the absence of an external electrical current flowing to or from the metal surface (EN ISO 8044). As it involves no external currents flowing,  $E_{\text{corr}}$  is measured with an undisturbed surface reaction when the specimen is in equilibrium. It normally occurs between two device terminals when detached from a circuit. It is the potential of a working electrode compared to the reference electrode when there is no current or potential existing in the cell.

### 3.4.6.3. Electrochemical Impedance Spectroscopy

Electrochemical impedance spectroscopy (EIS) is an approach using a perturbation of the electrochemical cell under investigation with a small magnitude of alternating signal to observe the response in which the system follows the perturbation at a steady state [113]. EIS is often used to investigate physical phenomena of materials relative to their chemical properties.

In a linear system, the current response of a sinusoidal potential will be also sinusoidal at the same frequency but with a phase shift. To measure the impedance of a system, an alternating signal is applied around the free corrosion potential (with a small perturbation of 5-10 mV), which can be expressed as [114]:

$$E(t) = E_0 \sin(\omega t) \quad (12)$$

where  $E_t$  is the potential at time  $t$ ,  $E_0$  is the amplitude of the signal, and  $\omega$  is the radial frequency. The radial frequency is directly related to frequency ( $f$ ) [114]:

$$\omega = 2\pi f \quad (13)$$

In a linear system, the applied potential yields a current response,  $I_t$ , which is shifted in phase ( $\rho$ ) and has an amplitude of  $I_0$ :

$$I(t) = I_0 \sin(\omega t + \phi) \quad (14)$$

Ohm's Law defines resistance as a ratio between voltage  $E$  and current  $I$ . Analogous to that, the impedance of a system can be calculated as follows [114]:

$$Z = \frac{E(t)}{I(t)} = \frac{E_0 \sin(\omega t)}{I_0 \sin(\omega t + \phi)} = Z_0 \frac{\sin(\omega t)}{\sin(\omega t + \phi)} \quad (15)$$

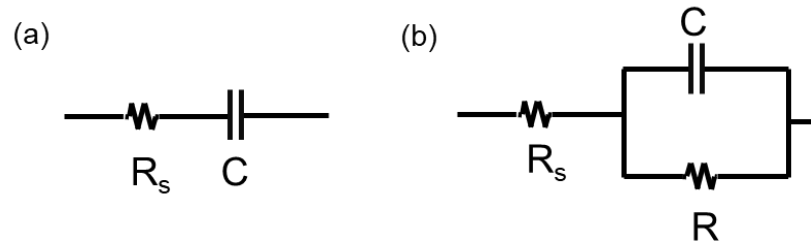
The impedance can be expressed in terms of magnitude  $Z_0$  and a phase shift  $\phi$ . By using Eulers relationship, this equation can be simplified and represented as a complex number [114]:

$$Z(\omega) = Z_0 \exp(j\phi) = Z_0(\cos \phi + j \sin \phi) \quad (16)$$

According to equation (16), the impedance  $Z(\omega)$  is composed of a real and imaginary part, which can be plotted with the real part as the x-axis and the imaginary part as y-axis, which is known as a Nyquist plot.

#### Equivalent circuit

EIS data is fitted to the appropriate equivalent circuit using a non-linear least square algorithm, starting from the proposed values of the equivalent electrical circuit models [115]. The circuit elements applied in the equivalent circuit are common electrical elements in which a meaningful physical characteristic should be extracted, i.e. resistors, capacitors, and inductors. Two examples are presented in Figure 3.3 representing a blocking system and a reacting system. A blocking system consists of two electrical circuits, which is a solution resistance ( $R_s$ ) in series with capacitor (C, also mentioned as  $C_{dl}$ ,  $C_c$ , or  $C_f$ ). This electrical equivalent circuit theoretically represents an ideal isolating coating, comprising a pure capacitive coating with a very high impedance [115]. A Randles cell is used to represent a reacting system, since it is the most common cell model. It includes a solution resistance ( $R_s$ ), a double layer capacitor (C or  $C_{dl}$ ), and a charge transfer or polarization resistance (R or  $R_{ct}$ ). This equivalent circuit is used for a simple reacting system, where a working electrode is uniformly accessible to electrolyte, and only a single reaction occurs. This type of equivalent electrical circuit is generally used to investigate the corrosion behavior of an active metal in an electrolyte.



**Figure 3.3.** Electrical circuit of (a) a blocking system consisting of  $R_s$  in series with C and (b) a Randles cell consisting of  $R_s$ , C, and R [114]

Due to the complex physical mechanism of a system, other electrical elements are also used, e.g. constant phase element (CPE) and Warburg impedance (W). CPE is often attributed to an imperfect capacitor, due to a frequency dispersion. This frequency dispersion might be distributed along the electrode surface or perpendicular to the electrode surface (normal distribution). Normal distribution can be expected in systems such as oxide films and organic coatings. Along the electrode surface, the investigated system might have surface heterogeneity, or local surface reactivity that leads to the frequency dispersion.

The impedance of a film-covered electrode with CPE behavior can be expressed in terms of solution resistance  $R_s$ , the parallel resistance, and CPE parameters Q and  $\alpha$ , as:

$$Z = R_e + \frac{R}{1+(j\omega)^\alpha RQ} \quad (17)$$

When  $\alpha = 1$ , the system is described by a single time constant, and the parameter Q has a unit of capacitance ( $s/\Omega$ ), when  $\alpha \neq 1$ , Q has a unit of  $s^\alpha/\Omega$ . For  $\alpha = 0.5$ , CPE no longer

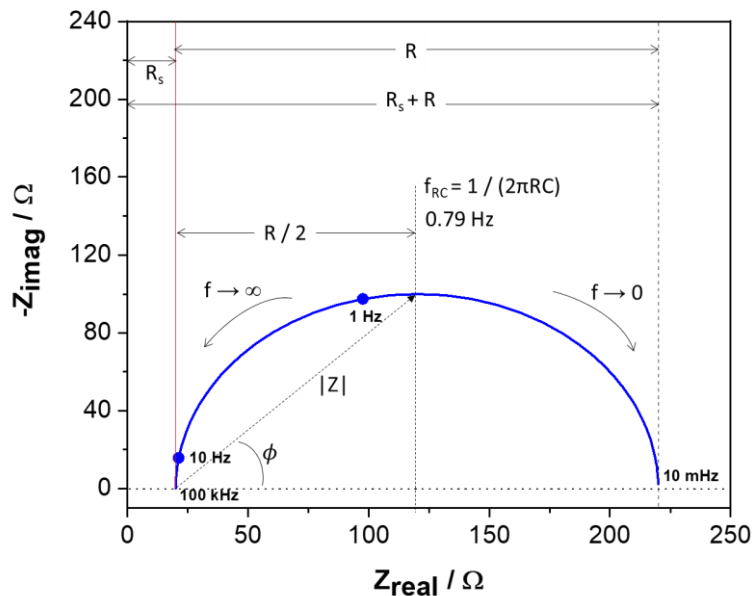
represents a capacitor, but a Warburg impedance. Warburg impedance is related to a diffusion process on the electrode and can be applied to the electrical equivalent circuit when there is an absorption/desorption on the surface of the investigated system. For  $\alpha = 0$ , CPE has the same unit as resistor. The following equation is then used to extract the capacitance from CPE value:

$$C = Q^{1/\alpha} \left( \frac{R_s R}{R_s + R} \right)^{(1-\alpha)/\alpha} \quad (18)$$

### Data interpretation

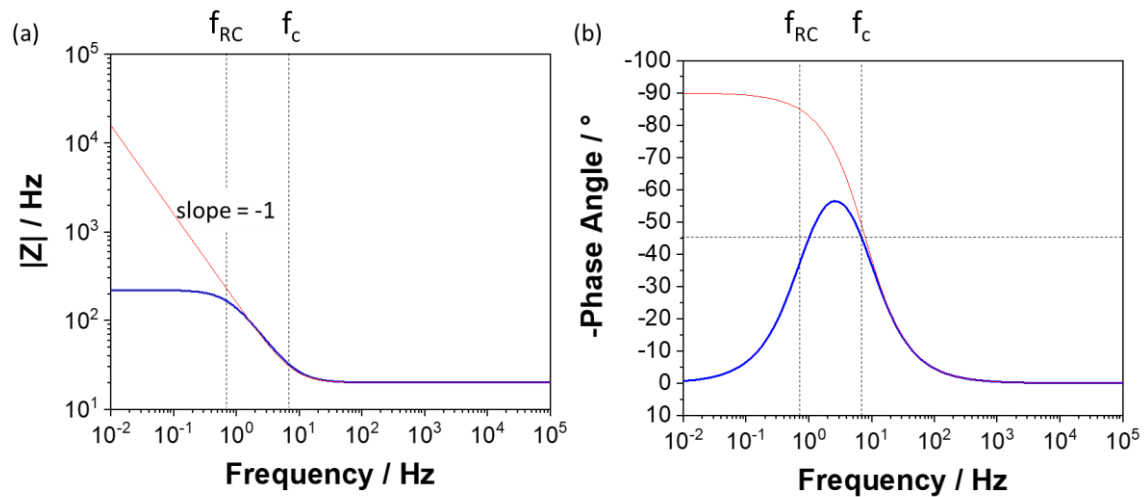
The Nyquist plot is a way to present the EIS measurement, which shows  $Z_{\text{real}}$  vs.  $-Z_{\text{imag}}$  for different values of frequencies, as shown in Figure 3.4. In this data presentation, the information about frequency is shown implicitly. At any data point, frequency is represented by the angle of vector of x- and y- axes, with low frequency data on the right side, while high frequency data are represented on the left side. The Nyquist plot is a favorable data representation because the shape of the curve provides insight into possible mechanisms or the investigated phenomena. If the shape of the curve is a perfect semicircle, the impedance response is related to a single activation-energy-controlled process [114]. The semicircle is also mentioned as “time constant”. For some electrochemical impedance data, it is also possible to find several time-constants.

The Nyquist plot shown in Figure 3.4 is a simulated impedance spectrum according to the equivalent electrical circuit of Figure 3.3, in which the red lines correspond to the blocking circuit, and blue lines to the reactive circuit. The characteristic frequency is also noted here,  $f_{RC}$ , related to the frequency at the maximum  $-Z_{\text{imag}}$ . For a blocking circuit, the real part of impedance is equal to  $R_s$  for all frequencies.



**Figure 3.4.** Impedance-plane or Nyquist plot of impedance data for  $R_s = 20 \Omega$ ,  $R = 200 \Omega$ , and  $C = 1 \text{ mF}$  simulated by Gamry Echem Analyst. The blocking system (Figure 3.3a) is represented by the red lines, and the reactive system (Figure 3.3b) is represented by the blue lines (adapted from [114])

The Bode plot is a data representation of impedance spectra which is more functional than the Nyquist plot in terms of representing the frequency, as shown in Figure 3.5. The log frequency is plotted as the x-axis against the absolute value of impedance  $|Z|$  as y-axis. This type of Bode plot is also known as Bode magnitude plot (Figure 3.5a). The magnitude tends toward  $R_s$  when the frequency approaches  $\infty$ , and toward  $R_s+R$  as frequency approaches 0. Another type of Bode plot further mentioned in the experimental results is the phase angle plot, where the log frequency is the x-axis, and inversed phase shift the y-axis (Figure 3.5b).



**Figure 3.5.** Bode representation of impedance data for  $R_s = 20 \Omega$ ,  $R = 200 \Omega$ , and  $C = 1 \text{ mF}$  simulated by Gamry Echem Analyst. The blocking system (Figure 3.3a) is represented by the red lines, and the reactive system (Figure 3.3b) is represented by the blue lines. Characteristic frequencies are noted as  $f_{RC} = 1/(2\pi RC)$  and  $f_c = 1/(2\pi R_s C)$ , (a) magnitude and (b) phase angle (adapted from [114])

### *EIS for coated metals*

EIS is a useful technique for a corrosion study of a coated material, because it is based on the small sinusoidal perturbations of the electrode potential as a function of frequency perturbation, to yield the physicochemical properties of the electrode [116]. Electrochemical measurement using a DC-based type technique is not commonly used to study the corrosion on a coated metal, because during a potentiostatic polarization of a polymeric-coated metal, the potential drop across the coating layer is much larger than the potential drop across the metal/polymer interface [117].

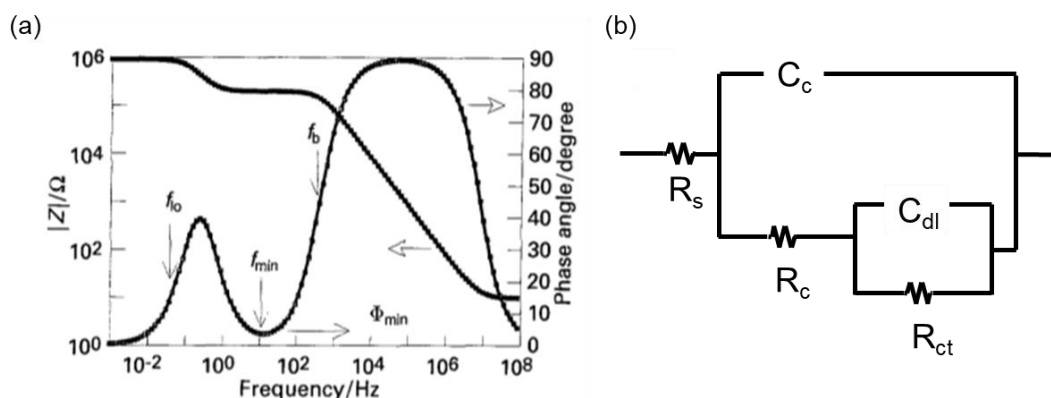
There are several principal processes that are important to investigate during corrosion in a polymeric-coated metal as follows [117]:

- swelling and ion incorporation into the coating and intrinsic defects formation
- onset of localized corrosion
- corrosion propagating underneath the polymeric layer as a result of anodic or cathodic reaction

A typical of Bode plot in coated metals is shown in Figure 3.6a, with a more complex electrical equivalent circuit as shown in Figure 3.6b. By comparing the Bode plot of the EIS data for the coated specimens before and after exposure to electrolytes, some information might be derived from the capacitance value, e.g. water uptake. Water uptake is the most observable phenomenon in metals coated by organic coatings, because the incorporation of polar



molecules, such as water, results in the increase of dielectric constant of the entire coating system.



**Figure 3.6.** Theoretical impedance spectra of degraded polymer coated metal shown in (a) Bode plot [118], and (b) the related equivalent electrical circuit [118]

EIS measurement is influenced by several factors, e.g., the system under investigation, the goal of measurement, and the instrumentation capabilities. Therefore, some measurement parameters need to be optimized for a meaningful result, e.g. frequency range, linearity, modulation techniques, and oscilloscope. The limitations of the instrumentation could also contribute to the error structures, which should be compromised to minimize bias errors, minimize stochastic errors, and maximize the information content of resulting spectrum [119].

#### 3.4.6.4. Electrochemical Measurement in an Autoclave

Electrochemical tests performed in water-based environment are powerful tools to determine corrosion rates and corrosion processes. Electrochemical measurement in high temperature aqueous solution is technologically required to understand the kinetics and thermodynamic properties in some applications, such as nuclear technology, fossil fuel and geothermal applications, and fuel cell. This methodology is useful to conduct a material selection, and to recommend material limitation in certain conditions. However, there are many temperature dependent electrode processes which can affect the measurement accuracy, such as standard electrode potentials, activity coefficients, Debye-Hückel equation (and its extensions) constants, conductance measurements, equilibrium constants, and diffusion activation constants [120]. There are however, research efforts in this area which have suggested various measurement techniques for electrochemical study, from thermally jacketed systems to the more advanced autoclave system [121, 122].

The isothermal system is important for thermodynamic data, but not for kinetic studies. To have an isothermal system, experiments are usually conducted in autoclaves, especially for the application with a temperature range above boiling point. For a temperature near boiling point, another option is available by using double walled cells or water-jacketed cell. In addition, another experimental set-up using an electronic heat gun was also developed by Cole [121]. Herein, the experimental set-up was set using autoclaves for 150°C, and a heat jacketed cell for temperatures below 100°C, as described in section 3.5.

According to the electrode materials, reference electrodes for high temperature and pressure application are classified into two groups: primary reference electrode, and secondary reference electrode. Primary reference electrodes consist of electrodes containing cationic or



anionic species in equilibrium with their ions in the solution, and electrons in the metal phase, for example, SHE,  $M^{n+}/M$  or  $M(OH)_x^{n-}/M$  model redox system. Meanwhile, the secondary reference electrodes have an equilibrium of an element, a compound of that element, and the solution, for example, Ag/AgCl/KCl electrode [123].

Depending on the working principle of the reference electrodes, it is also grouped into internal and external reference electrodes. Internal reference electrode operates at the same temperature and pressure as the rest of the system. However, there are inconsistencies with its stability because of the solubility and hydrolysis of electrode materials. External reference electrodes operate at room temperature and are connected to the electrochemical cell by an electrolyte bridge. The measured pressure can be set to the same pressure as the electrochemical cell. However, if the pressure is not balanced, formation of pressure and thermal gradient across the thermal junction may occur. The gradients give rise to irreversible streaming and thermal diffusion effects which contribute to the measured potential difference, consequently it cannot be used as a thermodynamic standard [123].

Ag/AgCl is the most commonly used reference electrode for electrochemical measurement at high temperature, up to 225°C according to Digby McDonald. It has some advantages, such as low solubility, and is resistant to hydrolysis. However, it has to be carefully treated when used in the hydroxide solutions, because there is a significant hydrolysis of AgX (X is  $Cl^-$  or  $Br^-$ ) to  $Ag_2O$  [123].

#### 3.4.7. Adhesion Test

One of the influential parameters in coating degradation is the adhesion of coatings. To investigate the adhesion of different coatings after exposure, pressure sensitive adhesives were used to observe the physical bonds between the coating layers by applying brief contact and light pressure. The adhesive tape was applied to the exposed specimens within an area of 2 cm × 2 cm. To assess the adhesion test more precisely, the scanned images of the tape after debonding were analyzed using image-J software by adjusting the color threshold to select and calculate the delaminated area.

### 3.5. Test Set-up

To describe the test set-up, the specimen dimension and the testing cells are presented as follows.

#### 3.5.1. Specimens

Two dimensions of specimens were used in this research depending on the testing methodology, i.e. exposure test or electrochemical test. Specimens for the exposure test were prepared having a dimension of 50 mm × 20 mm × 4 mm, and a hole with a diameter of 5 mm. Specimens for electrochemical measurements were prepared with the dimension of 20 mm × 15 mm × 4 mm and spot welded to a Ni/Cr based alloy rod with the diameter of 2 mm, as illustrated in Figure 3.7.

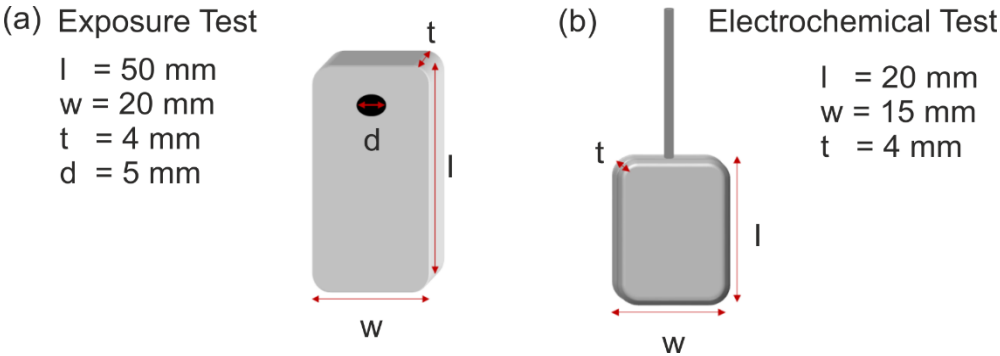


Figure 3.7. Specimen dimensions for (a) exposure test and (b) electrochemistry test

3.5.2. Testing Cell

Exposure tests were conducted as described in section 3.4.1. Below 100 °C, specimens were immersed completely in a glass vessel and mounted using PTFE thread, as illustrated in Figure 3.8. Depending on the experimental condition, the gas inlet was used to purge Ar (for deaerated condition) or CO<sub>2</sub> gas. The system was heated using a heating mantle, connected to a temperature regulator with a precision of ±3 °C. Detailed description of the electrochemical test set-up is presented in Figure 3.9.

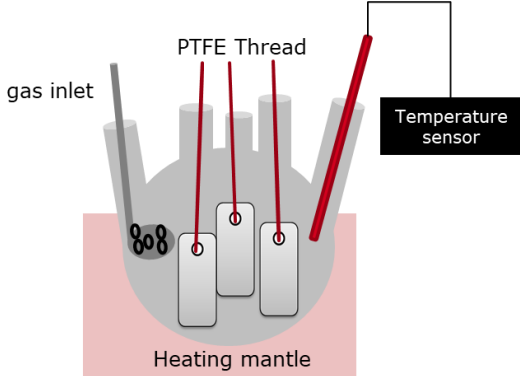


Figure 3.8. Exposure test set-up for lower temperatures, illustration of specimen arrangement inside the glass vessel.

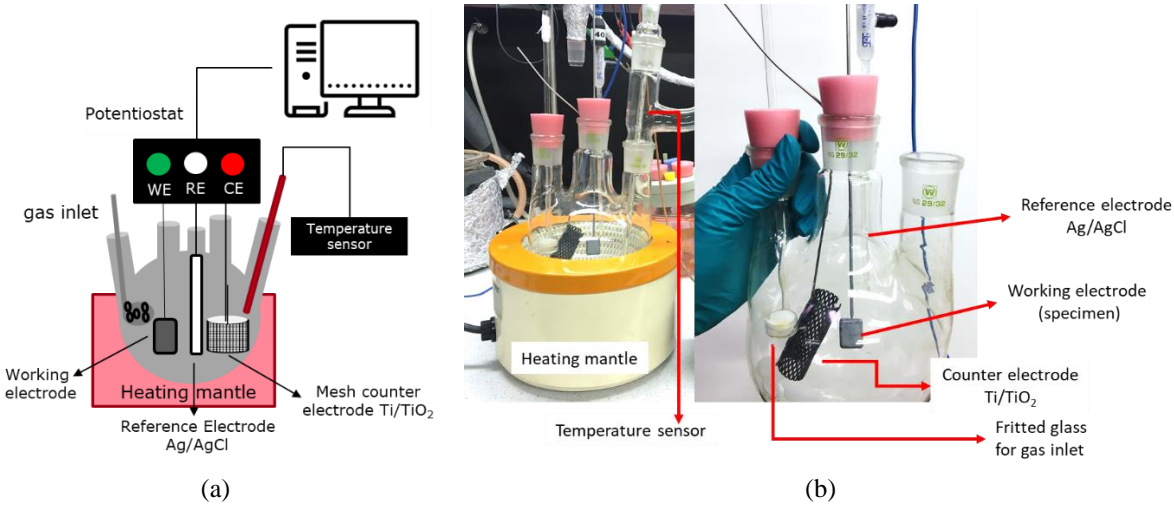
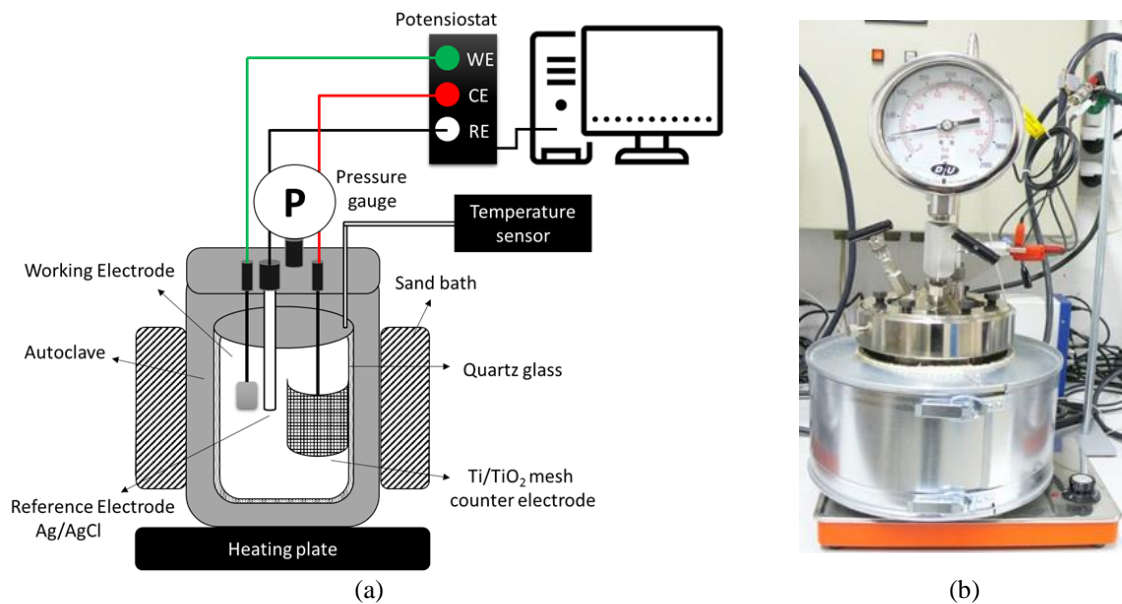


Figure 3.9. Electrochemical test set-up in a glass vessel for lower temperature experiments: (a) illustration and description of test set-up, and (b) image of test set-up and the electrodes arrangement

At temperatures higher than the boiling point (100 °C), the exposure test was conducted using an autoclave, and kept in a climate chamber. Specimens were arranged in an autoclave under the investigated condition, as shown in Figure 3.10. Electrochemical measurements were conducted as described in section 3.4.4., with the test set-up shown in Figure 3.11.



**Figure 3.10.** Exposure test set-up for higher temperatures: (a) illustration of specimen arrangement inside the autoclave, and (b) image of autoclaves



**Figure 3.11.** Electrochemical test set-up in an autoclave for higher temperature experiments up to 150 °C: (a) illustration and description of test set-up, and (b) image of the test set-up



# Chapter 4. Carbon Steel Corrosion in Artificial Geothermal Water

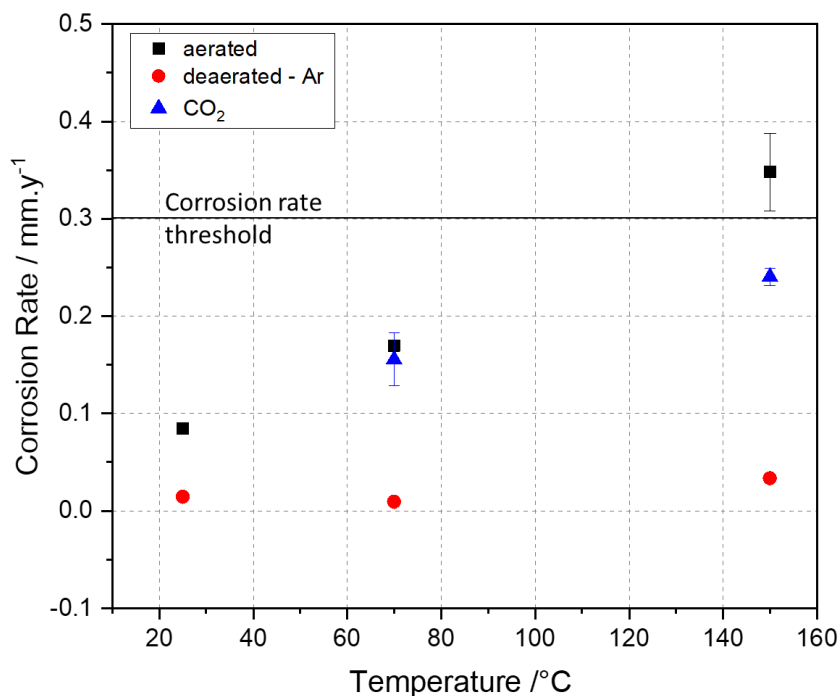
This chapter discusses the carbon steel corrosion in artificial geothermal water simulating the Sibayak geothermal source. Here, different influencing factors of corrosion were explored, i.e. temperature, dissolved oxygen, and pH. Exposure tests, surface analysis, and electrochemical measurements were used to investigate the corrosion mechanism.

## 4.1. Effect of Temperature

Temperature is one of the critical parameters in any chemical reaction governed by Arrhenius equation. In geothermal applications, temperature changes affect different chemical and physical properties, such as pressure, dissolved gases solubility, and electrical conductivity of electrolytes. This subchapter discusses the experimental results of the exposure test, surface analysis, and electrochemical test of carbon steel by varying the temperature.

### 4.1.1. Influence of Dissolved Gases on the Corrosion Rate of Carbon Steel

Corrosion rate determination is commonly performed by measuring the mass loss of materials after exposing them to the corrosive environment, as outlined in the ASTM G1-03 Standard Practice for Preparing, Cleaning, and Evaluating Corrosion Test Specimen. Figure 4.1 shows the corrosion rate as a function of temperature after exposure to the artificial geothermal water for seven days. The values presented here are an average of two measurements, with error bars representing the standard deviation (see Appendix).



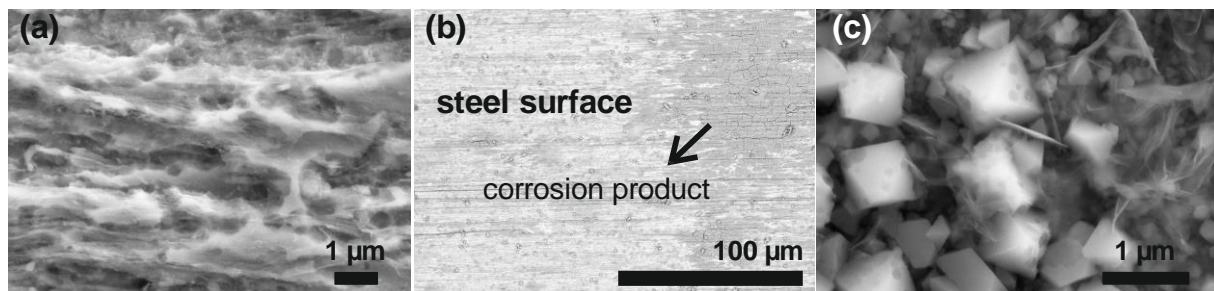
**Figure 4.1.** Corrosion rate of carbon steel as a function of temperature in artificial geothermal water at 25, 70 and 150 °C in different dissolved gas composition. Corrosion rates of specimens exposed to deaerated solution has error values of 0.001 mm/year.

In geothermal applications, the corrosion rate threshold is usually set to 0.3 mm/year to ensure the safety and structural integrity of materials, although it requires the absence of pitting corrosion [10]. The significant effect of increasing temperature was observed in the aerated and CO<sub>2</sub>-containing solution. When dissolved oxygen is present, as simulated by the aerated solution, the corrosion rate significantly increased with temperature, suggesting that dissolved oxygen contributes to the accelerated corrosion reaction. This result is in agreement with other studies that confirmed the presence of oxygen to be the main cause of the corrosion rate increase [63, 124, 125]. In the presence of CO<sub>2</sub>, carbonic acid formed from the reaction of CO<sub>2</sub> and water is corrosive to carbon steel, therefore the formation of corrosion products contributes to the higher corrosion rate observed at 70 and 150 °C. In the deaerated solution, the increase in the corrosion rate due to increasing temperature was much lower compared to the other two conditions. Although the deaerated solution carbon steel appeared suitable for geothermal application because of the negligible corrosion rate, it is important to ensure the absence of pitting corrosion.

#### 4.1.2. Morphological Characterization

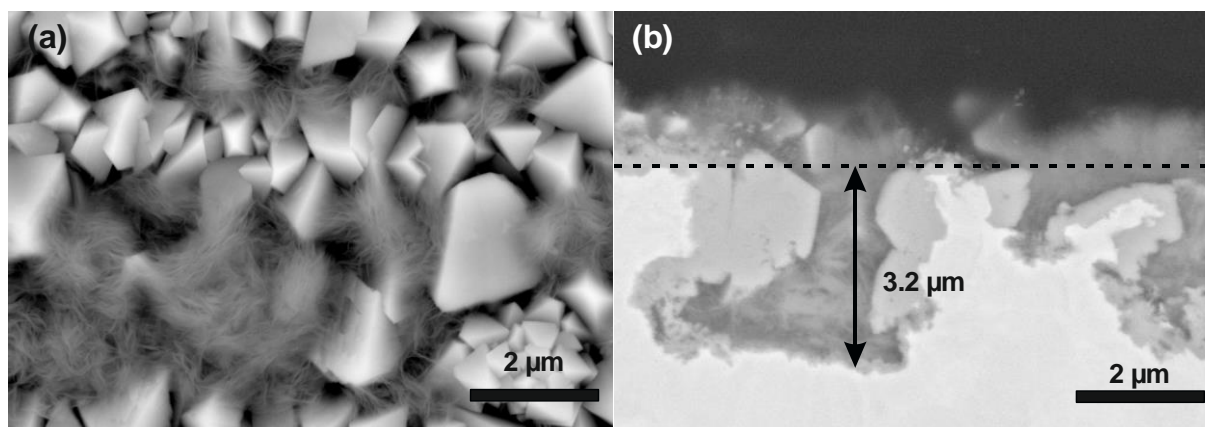
The surface morphology of the carbon steel surface was characterized to investigate the presence of pitting corrosion, the growth of corrosion products, and their properties. Deaerated solution was chosen to understand the interaction of carbon steel with the solution solely, without any influence of other gas components such as oxygen. Unlike in the aerated solution, carbon steel exposed to the deaerated solution showed a very low corrosion rate of 0.014, 0.090, and 0.034 mm/year for 25, 70, and 150 °C, respectively (Figure 4.1).

At 25 °C, there was no significant corrosion product observed visually on the surface. However, the SEM image revealed that carbon steel surface was etched, resulting in a rougher surface (Figure 4.2a). At 70 °C, there was a change of the carbon steel surface color to rainbow-like, due to the reflection of light on a very thin adjacent layer of iron oxide with a nanometer thickness [126]. Figure 4.2b shows that the steel surface was visible, indicated by the brighter area in the SEM image. At 70 °C, the corrosion product layer was very thin and not homogeneous, hence the morphological structure could not be identified by SEM. However, it was protective to the carbon steel structure, as the corrosion rate was lower than that at 25 °C. At 150 °C, two dominating structures were revealed by SEM, a prismatic and hair-like structure. The formation of corrosion products contributes to the uniform corrosion and a higher corrosion rate (Figure 4.2c).



**Figure 4.2.** SEM images of carbon steel exposed in deaerated geothermal solution at (a) 25 °C (b) 70 °C (c) 150 °C

A longer exposure test was performed for 28 days at 150 °C to confirm the suitability of carbon steel use in deaerated solution. The SEM image shows corrosion products of carbon steel with two dominating structures like those observed after seven days of exposure, however with a much smoother morphology (Figure 4.3a). Although there was no pitting corrosion observed after seven days, after 28 days, a sample specimen cross section revealed localized corrosion with a depth of 3 μm (Figure 4.3b). These results showed that in all conditions, carbon steel underwent either pitting corrosion or uniform corrosion, which necessitates a protection strategy to prevent corrosion and material degradation.



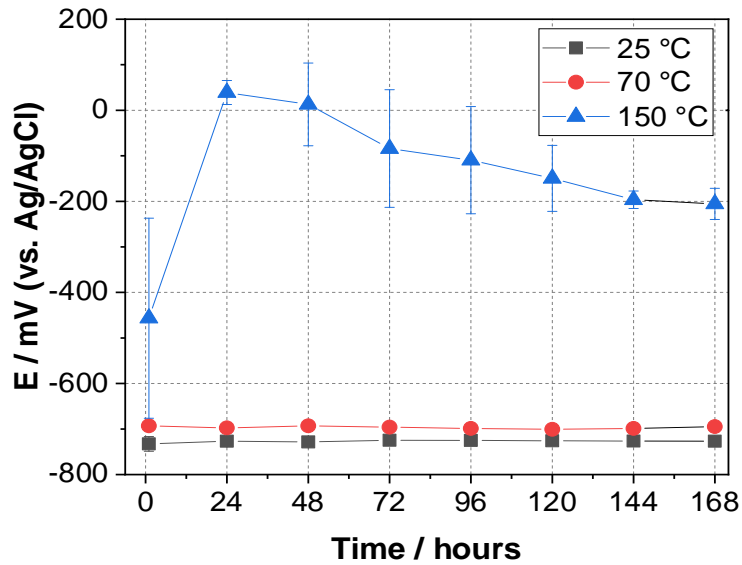
**Figure 4.3.** SEM images of carbon steel exposed to deaerated geothermal solution at 150 °C for 28 days (a) surface morphology (b) cross section

#### 4.1.3. Influence of Temperature on the Electrochemical Behavior of Carbon Steel

To understand the effect of temperature on the corrosion behavior of carbon steel in artificial geothermal water, an electrochemical study in the deaerated condition (under Ar environment) was conducted. This involved monitoring the OCP, also known as free corrosion potential ( $E_{\text{corr}}$ ), and EIS over seven days.

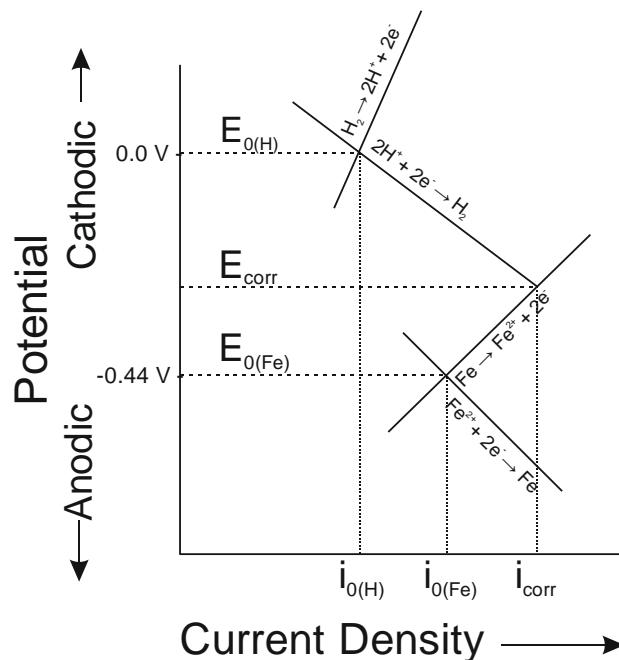
$E_{\text{corr}}$  was measured as a function of time to investigate the spontaneous corrosion reaction in artificial geothermal water (Figure 4.4). The data was recorded after reaching the desired temperature. By selecting datapoints with an interval of 24 hours, the free corrosion potential stability of carbon steel was observed at different temperatures every day. At lower temperatures, i.e. 25 °C and 70 °C, carbon steel has a much lower  $E_{\text{corr}}$  than at 150 °C. The increase of potential to a more positive value suggested an ennoblement of carbon steel electrode potential, which can be caused by the change in physical and chemical properties of the corrosion products formed at 150 °C, as suggested by the surface analysis. As shown by SEM images (Figure 4.2), corrosion products formed a dense layer on the carbon steel surface at 150 °C, whereas at 25 °C there was no corrosion product layer, and at 70 °C, the metallic part of the surface was still visible.





**Figure 4.4.**  $E_{\text{corr}}$  of carbon steel exposed to different temperatures in the artificial geothermal water for seven days.

At 25 °C, there was no significant formation of an oxide layer leading to the continuous contact of the carbon steel surface with the artificial geothermal water, which is an acidic-saline electrolyte. Based on the properties of the electrolyte, electrochemical reactions were supposedly dominated by the iron dissolution and hydrogen evolution. At 25 °C,  $E_{\text{corr}}$  remained stable within -733 mV to -727 mV, which is slightly lower than the free corrosion potential of pure iron in an acidic solution as shown in Figure 4.5. It is noteworthy to mention that the potential shift might be affected by a higher pH value, the chemical composition of the tested geothermal water, the elemental composition of carbon steel, and its microstructure. Therefore, open circuit potential monitoring at 25 °C is important to establish a baseline reference of the free corrosion potential for carbon steel in such artificial geothermal water.

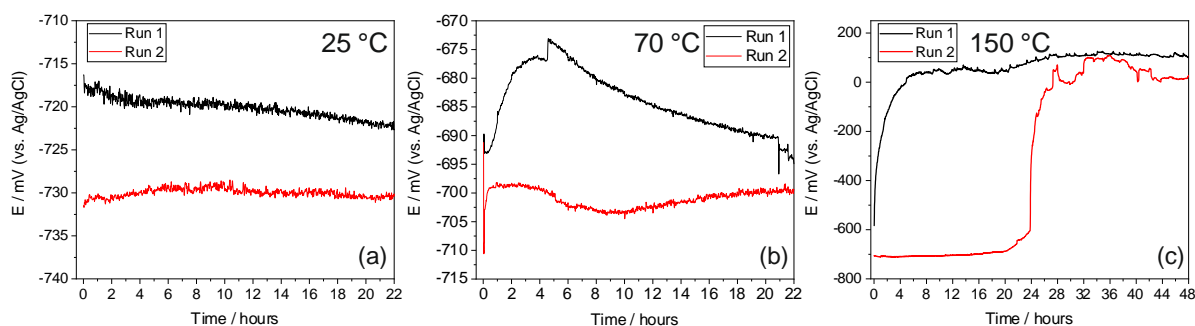


**Figure 4.5.** Corrosion potential of iron with hydrogen evolution at pH 0. Potentials are in SHE [56, 58]



By increasing the temperature to 70 °C, there was an increase of free potential of 25 to 40 mV. Although there is a possibility of  $\text{Fe}(\text{OH})_2$  formation, it might form a defective hydrous film barrier layer between the carbon steel and electrolyte, which is not protective to carbon steel [127, 128]. Since  $\text{Fe}(\text{OH})_2$  was not adherent to the surface, further electrochemical reactions take place with a relatively large active surface. The further increase of temperature to 150 °C resulted in a significant change to the free corrosion potential. Although in acidic medium, hydrogen evolution is the most favorable cathodic reaction, other reactions may also be contributed by metal ion oxidation and corrosion product deposition [56]. An increase of temperature promotes an oxidation of metal ions from  $\text{Fe}^{2+}$  to  $\text{Fe}^{3+}$ , which contributes to the cathodic reaction. In addition, at higher temperature, there is a faster nucleation and growth of iron oxides, corrosion products accumulate and provide a coverage on the surface which then act as a physical barrier layer.

The error bars show the standard deviation of the average corrosion potentials, with the most significant deviation at 150 °C of 220 mV, whereas at 25 °C and 70 °C, there was a maximum potential deviation of 16 mV and 7 mV, respectively. In all three conditions, the maximum potential deviation occurred within the first hour, indicating a difference in corrosion potentials within the initial few hours. To evaluate the free corrosion potential in the first few hours, Figure 4.6 shows  $E_{\text{corr}}$  as a function of time. Comparisons of two datasets for each experiment show that at 25 °C, curves of  $E_{\text{corr}}$  obtained from the first and the second experiments are relatively similar, with a potential difference between the first and second experiment of 12 – 15 mV, whereas at 70 °C,  $E_{\text{corr}}$  reached the same value within 22 hours with a potential difference of 5 – 25 mV. At 150 °C, there was a large deviation in the first few hours until the specimens were exposed for 28 hours, which might be associated with the different rates of iron dissolution, followed by corrosion product formation.



**Figure 4.6.** Open circuit potential of carbon steel exposed to the artificial geothermal water within the first few hours (a) at 25 °C, (b) at 70 °C and (c) at 150 °C

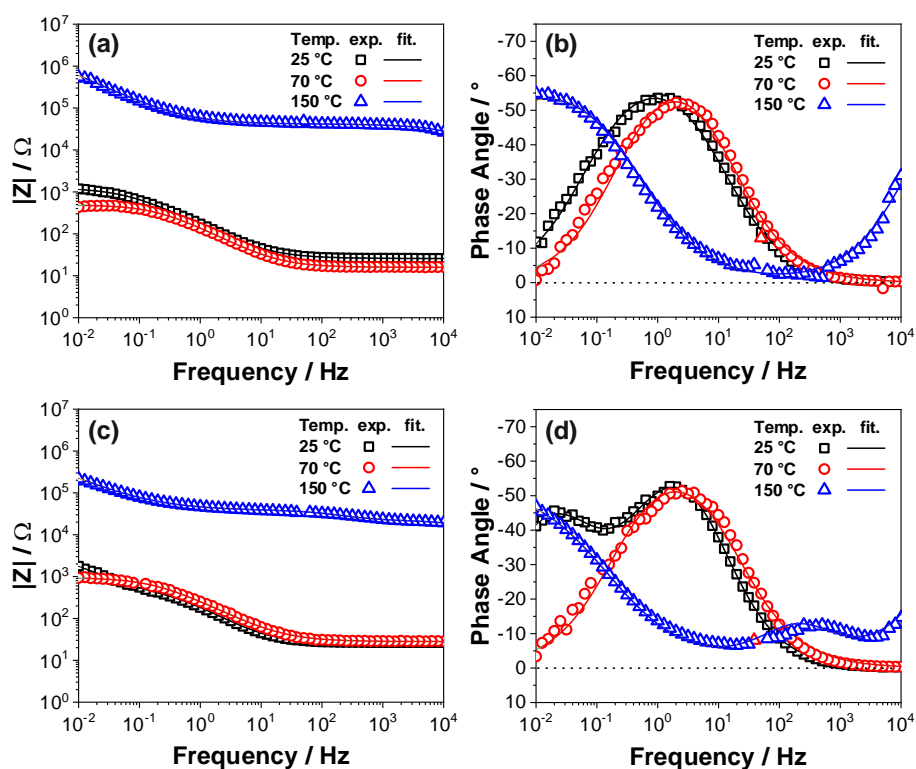
EIS was used to further investigate the effect of temperature on the surface-interface interaction between carbon steel surface, the electrolyte, and the possible corrosion product layer. Two different exposure times were selected to show the effect in the first day and seventh day. Here, EIS was represented by the Bode magnitude plot and phase angle plot to show the total impedance value  $|Z|$  and the corresponding phase angle with respect to frequency.

At any exposure time,  $|Z|$  had the highest value when carbon steel was exposed at 150 °C (Figure 4.7a and Figure 4.7c), whereas at both 25 °C and 70 °C, the  $|Z|$  values remained 2–3 orders of magnitude lower than that at 150 °C. As also shown by the  $E_{\text{corr}}$ , this result indicated that at 150 °C, there was an ennoblement effect which might be associated with the corrosion

product formation. However, after seven days exposure at 150 °C,  $|Z|$  decreased almost 10 times lower than after the first day of exposure, indicating that the corrosion resistance of carbon steel decreased.

After the first day of exposure, the phase angle plot at 25 °C and 70 °C showed a time constant in the medium to low frequency range ( $10^2$ – $10^2$  Hz), as depicted in Fig. 4.7b, which may be associated with the interfacial reaction between the carbon steel surface and the electrolyte. Both phase angle curves have the same maximum phase angle value of  $-55^\circ$ , although there was a shift of its position. At 25 °C, the maximum phase angle value shifted to a lower frequency, indicating that the kinetic of interfacial reaction is slower than that at 70 °C. Unlike at lower temperatures, there were two time-constants detected at 150 °C in the high frequency range ( $>10^4$ – $10^2$  Hz) and medium to low frequency range ( $10^1$ – $10^2$  Hz). The time-constants might be associated with two different physical phenomena: interfacial reaction between the electrolyte and corrosion product, as well as between electrolyte and carbon steel surface through the corrosion product pores. Compared to that at the lower temperature, the phase angle peak was in a much lower frequency range indicating a much slower reaction on the carbon steel surface.

After seven days of exposure, the phase angle plot of carbon steel at 25 °C and 150 °C showed a significant change (Figure 4.7d). At 25 °C, there was a second time constant at a lower frequency range between  $10^{-1}$ – $10^{-2}$  Hz, which may be related to the etched surface observed in the SEM image. At 150 °C, the first time constant at higher frequency has a very low phase angle value of  $-15^\circ$ , indicating resistive behavior, whereas the second time constant has a phase angle value of  $-45^\circ$ , indicating a diffusion control or adsorption at the surface [114].



**Figure 4.7.** EIS of carbon steel in deaerated geothermal solution at different temperatures (a) Bode magnitude plot and (b) phase angle plot of the first day; (c) Bode magnitude plot and (d) phase angle plot of the seventh day

## 4.2. Effect of Dissolved Oxygen

As shown in Figure 4.1, the corrosion rate of carbon steel is not only dependent on temperature, but also on the gas composition involved in the reaction. Here, the effect of dissolved oxygen was studied to consider the risk for oxygen trace intrusion into the geothermal well. In this study, aerated solution was used to simulate the dissolved oxygen, whereas deaerated solution (purged by Ar) was used as a comparison or control experiment.

Surface water usually contains dissolved oxygen, approximately 6–11 ppm, depending on the location [70]. The dissolved oxygen saturation value varies with temperature and salinity. Oxygen has an important role in corrosion because it participates in the cathodic reaction. If the amount of oxygen in the system increases, it will accelerate the corrosion reaction because of its role in cathodic processes. When two sites on carbon steel are exposed to a different concentration of dissolved oxygen  $[O_2]_1$  and  $[O_2]_2$ , these sites have different electric potentials as follows:

$$E = E_1 - E_2 = \frac{RT}{nF} \ln \frac{[O_2]_1}{[O_2]_2} \quad (19)$$

This formula describes the occurrence of corrosion in aerated system that is not necessarily homogeneous. A carbon steel surface with the larger dissolved oxygen concentration will be the cathode and does not corrode. In contrast, the carbon steel surface with the smaller dissolved oxygen concentration acts as an anode, thus corrodes. However, when the oxygen is removed from the system, the oxygen concentration is near zero, and there will be no difference of oxygen concentration at different sites. As a result, corrosion reaction can be suppressed, and is mostly driven by iron dissolution and hydrogen evolution.

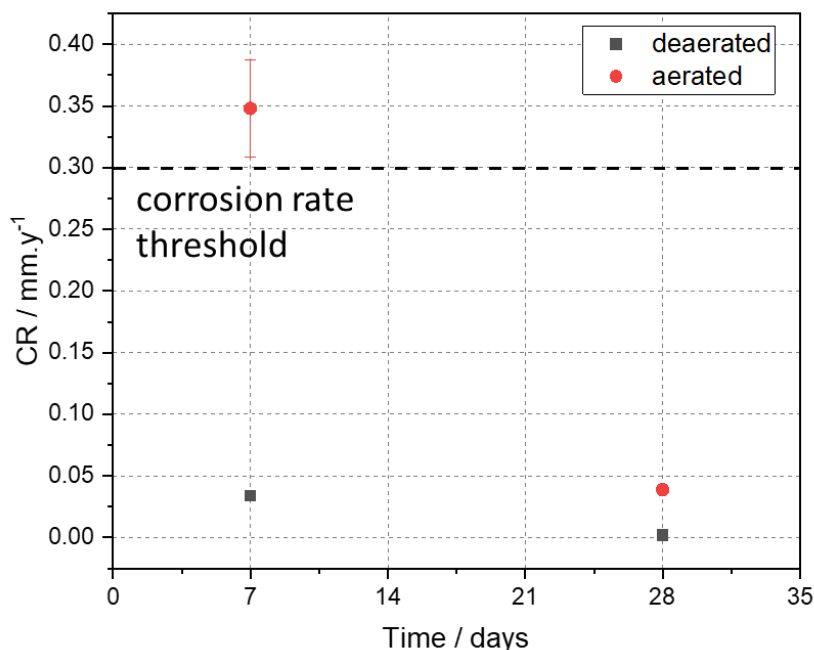
### 4.2.1. Influence of Exposure Time on the Corrosion Rate of Carbon Steel

To investigate the effect of dissolved oxygen on the corrosion rate of carbon steel, exposure tests were performed for 7 and 28 days. As shown in Figure 4.1, the corrosion rate of carbon steel was almost ten times higher in the presence of oxygen after seven days of exposure, due to more iron oxide formation in the presence of oxygen. However, a longer exposure test showed a decrease to even lower than the corrosion rate threshold, i.e. 0.3 mm/year, although still higher than that exposed to the deaerated solution (Figure 4.8). The corrosion rate depends on the electrical conductivity of the solution and the diffusion of ionic species. The decrease of the corrosion rate with a longer exposure time in the presence of dissolved oxygen is associated with the growth of corrosion products which are accumulated on the surface of carbon steel and serve as a barrier to oxygen diffusion [70].

As oxygen was not present in the deaerated solution, other ionic species are responsible for corrosion processes. The diffusion of ionic species is related to the ion mobility, which is related to its molar conductivity, diffusivity, and solvent viscosity.  $H^+$  and  $OH^-$  have the highest ion mobility, several times greater than other ions [129]. As a result, mechanisms which involve the transport and interaction of protons or hydroxyl ions are usually very fast. These mechanisms might also contribute to the formation of a corrosion product layer [129].

In this study, experiments were carried out in stagnant condition, where the pH of the solution increased from 4 to 6 within seven days and remained stable until 28 days. This result indicated that there was a decrease of proton concentration in the solution, as it was consumed

in the early stage short after the carbon steel was in contact with the electrolyte. As the ion mobility of other species are much lower than  $H^+$ , the reaction rate with other species is much lower. In addition, as also shown by SEM image (Fig. 4.2c), the corrosion product layer might block the diffusion of other ions, resulting in a decrease of corrosion rate over time. The values presented here are an average of two or three measurements, with error bars representing the standard deviation (see Appendix).



**Figure 4.8.** Corrosion rate of carbon steel exposed at 150 °C for 7 and 28 days in aerated and deaerated artificial geothermal water. Error bars are between  $10^{-3}$  and  $10^{-6}$  mm/year

#### 4.2.2. Identification of Pitting Corrosion

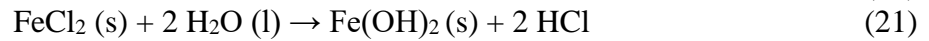
As mentioned before, it is important to identify pitting corrosion before using materials for industrial purposes. Although the corrosion rate of carbon steel is low, Figure 4.9 indicates pitting corrosion of carbon steel exposed to artificial geothermal water, both in the aerated and deaerated solution. By using optical microscope, pitting corrosion was observed after seven days of exposure in the presence of dissolved oxygen (Figure 4.9a). The optical microscope was then used to observe several corrosion pits, where the measurements of 6 pits result in an average depth of  $20 \pm 6 \mu\text{m}$  and diameter of  $4 \pm 1 \mu\text{m}$ . Without dissolved oxygen, there were homogeneous corrosion products on the carbon steel surface and an indication of pitting corrosion where a hole was identified; however, it is to a much lesser degree than that in the aerated solution (Figure 4.9b).

Further analysis was conducted by preparing the cross section of specimens to confirm the thickness of corrosion product and the depth of pitting corrosion. An example of corrosion pit was measured with a depth of  $11 \mu\text{m}$  after exposed to aerated geothermal solution for only seven days (Figure 4.9c), whereas in the deaerated solution the corrosion pits were observed around  $3 \mu\text{m}$  after 28 days of exposure (Figure 4.9d).

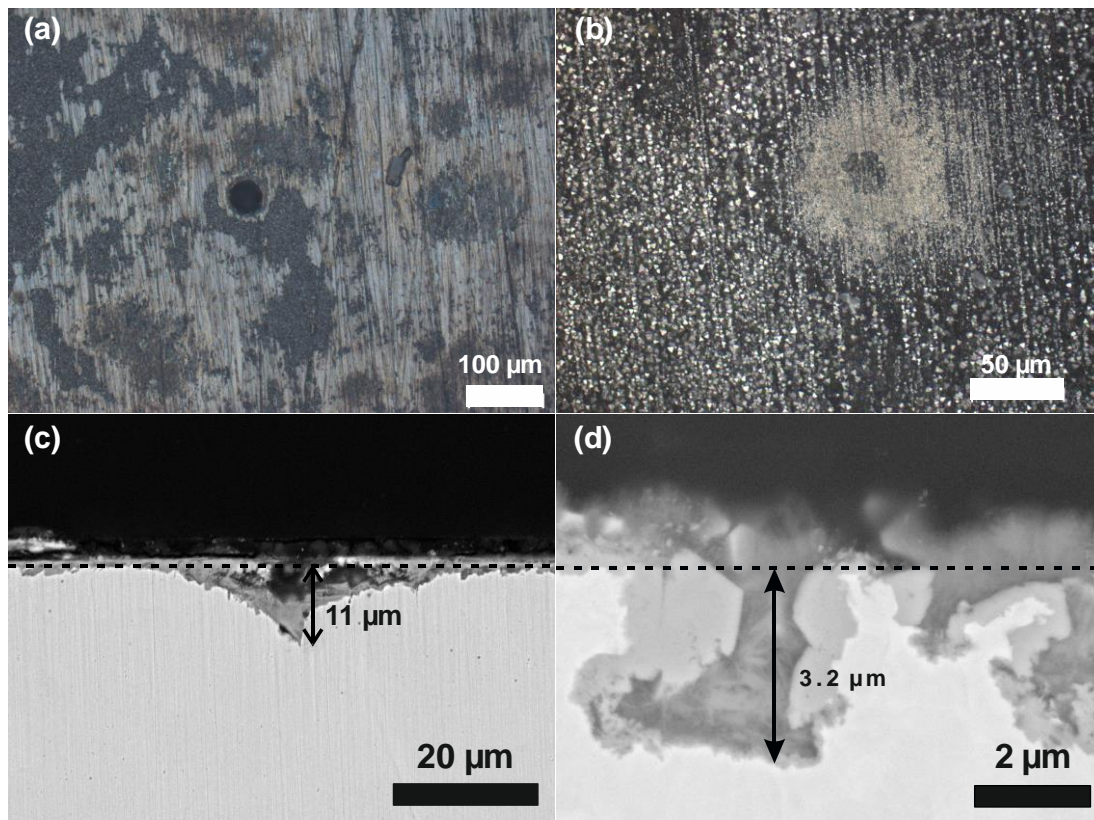
The decreased oxygen content in the solution has a less aggressive effect on carbon steel corrosion. As mentioned in other literature, 2 ppm of dissolved oxygen is considered corrosive at room temperature [70], whereas in the geothermal water, 30 ppb of oxygen causes uniform

corrosion [66]. Oxygen content of above 50 ppb may also cause serious pitting corrosion [63, 66].

Localized corrosion can be related to several influencing factors on the surface, such as the dispersed phases in the microstructure, the physical condition of the surface, or the irregularities caused by deposits or oxide layer. Moreover, it can also be caused by a non-uniform access of ionic species in the medium. Other than dissolved oxygen, chloride ions may also inhibit pitting corrosion on the surface of carbon steel with an imperfect oxide film. Due to their small size and high diffusivity, chloride ions can penetrate through the oxide film, reaching the bare surface of carbon steel [55]. The presence of chloride ions at several certain spots on carbon steel contribute to the electrochemical reaction and grow within the localized depth. The corrosion reaction involving chloride ions can be written as followed:



The formation of HCl from the reaction generates a more aggressive acidic environment inside the pit (locally), therefore the reaction propagates within the pit. In addition,  $\text{SO}_4^{2-}$  ions may also have an inhibiting effect in the chloride-containing solution [130].



**Figure 4.9.** Optical microscope images of the surface appearance of carbon steel after exposure to artificial geothermal water (a) in aerated condition after 7 days, and (b) in deaerated condition after 28 days. SEM images of the cross section (c) in aerated condition after 7 days, and (d) in deaerated condition after 28 days

## 4.2.3. Corrosion Mechanism at Room Temperature

To understand the reaction between carbon steel and electrolyte without any effect of temperature, electrochemical tests were performed at room temperature. When in contact with acidic aqueous solution, carbon steel reacts electrochemically to spontaneously corrode due to the following reactions.

*Deaerated*

In addition to the electrochemical reactions, a chemical reaction may occur between  $\text{Fe}^{2+}$  and water, where  $\text{H}^+$  will contribute again to the cathodic reaction:

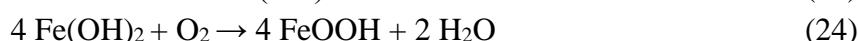


The surface appearance showed that there was no corrosion product layer at 25°C, however the surface of carbon steel became very rough (Figure 4.2a). As the surface was always in contact with the electrolyte, the  $E_{\text{corr}}$  of carbon steel in deaerated condition showed a stable value of -733 mV to -727 mV (Figure 4.10).

In the presence of oxygen,  $E_{\text{corr}}$  showed a more positive value (more cathodic) compared to the deaerated condition. The electrochemical reactions that may contribute to the potential shift to the cathodic direction are as follows:

*Aerated*

In the presence of dissolved oxygen, chemical reactions may occur between  $\text{Fe}^{2+}$ , water, and oxygen, which might result in the formation of  $\text{Fe}(\text{OH})_2$  and  $\text{FeOOH}$ .

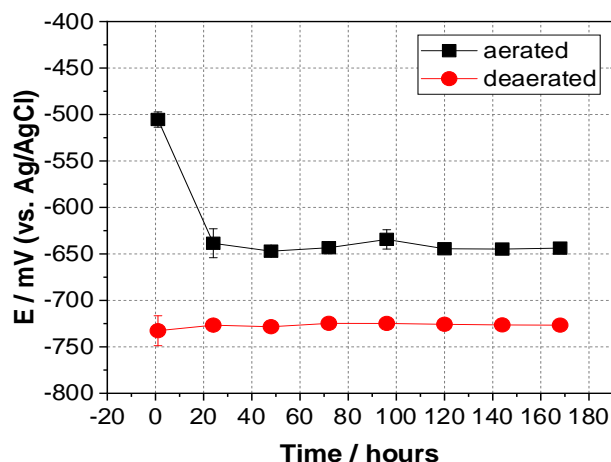


SEM image of the specimen surface is shown in Figure 4.2b where parts of the specimen surface are still visible. Based on the morphologies of corrosion products as summarized in Table 2.6, it is not clear which types of  $\text{Fe}(\text{OH})_2$  or  $\text{FeOOH}$  was formed.

Under the presence of oxygen,  $E_{\text{corr}}$  decreases in the first 24 hours from -484 mV to -616 mV, which then remained stable between -622 mV to -651 mV, about 70 mV higher than in the deaerated solution. The decrease of potential might be associated with a decrease in the electrochemical reaction rate between oxygen and  $\text{H}^+$ , which has a much higher standard electrode potential of  $E^\circ = 1.229 \text{ V vs. SHE}$ . Although not much greater, this electrochemical reaction could contribute to the overall addition of potential in the aerated solution [55]. As the

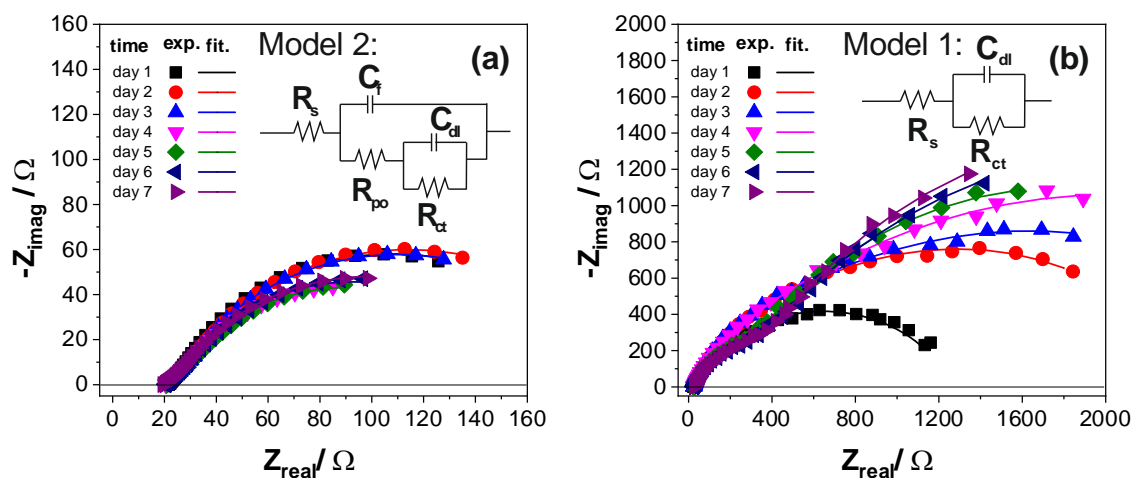


electrochemical reactions reach equilibrium and the amount of oxygen is limited, oxygen promotes formation of lepidocrocite  $\text{FeOOH}$ . Lepidocrocite formation is favorable in a condition with fast oxidation, low temperature, low pH, and the presence of  $\text{Cl}^-$ , which also complies with the aerated condition at  $25\text{ }^\circ\text{C}$  [72].



**Figure 4.10.** OCP of carbon steel in aerated and deaerated artificial geothermal water at  $25\text{ }^\circ\text{C}$ .

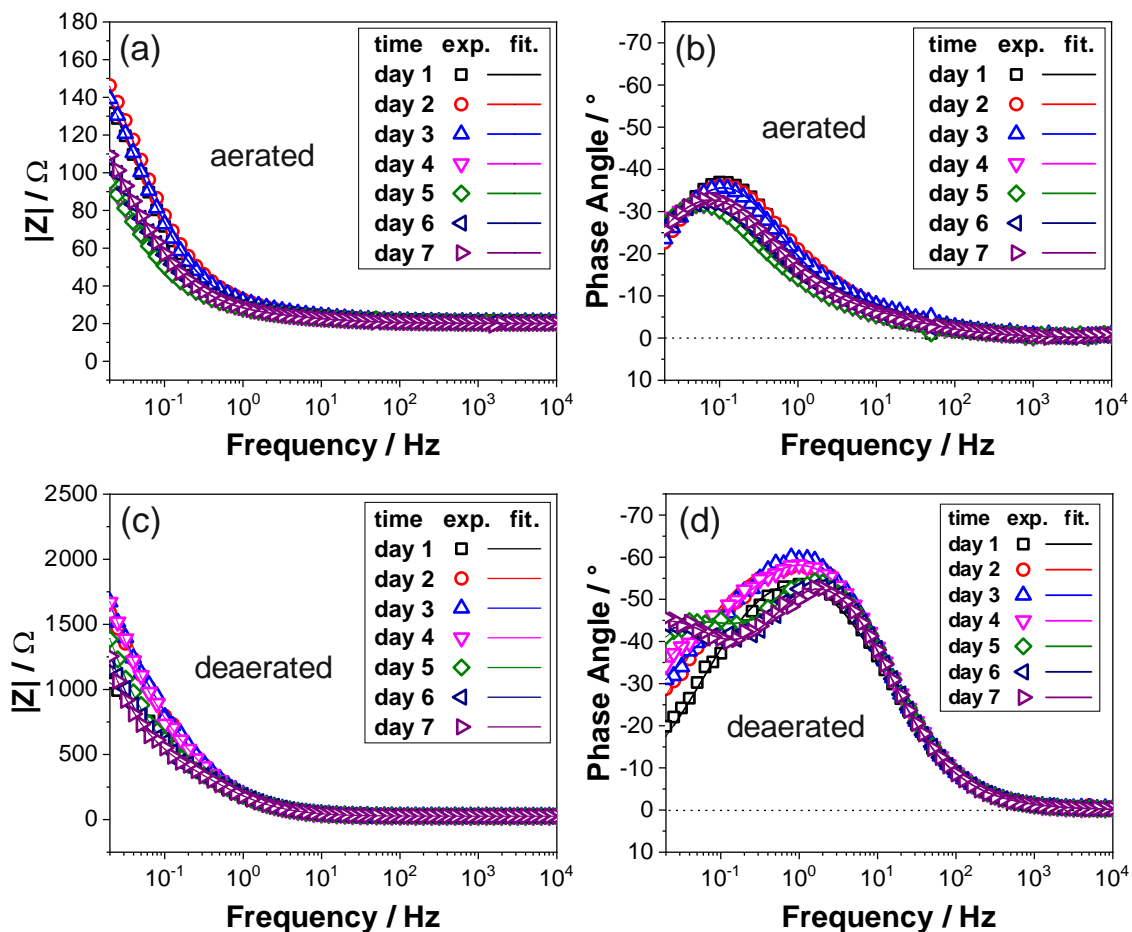
Although  $E_{\text{corr}}$  monitoring revealed a difference in free corrosion potential, there was no significant change with respect to time, except for the first 24 hours in the aerated condition. EIS was used to investigate the surface-interface reaction of carbon steel and electrolyte (Figure 4.11). Nyquist plot was selected to depict the evolution of impedance, both in its real ( $Z_{\text{real}}$ ) and imaginary ( $Z_{\text{imag}}$ ) part with respect to time. The results showed that carbon steel exposed to the deaerated solution (Figure 4.11b) had a much higher impedance (in the range of  $2000\ \Omega$ ) compared to the aerated condition (Figure 4.11a), which is more than ten times lower. This indicates that in the absence of dissolved oxygen, carbon steel has a much higher corrosion resistance. By comparing the Nyquist plot every day, different patterns were observed in the aerated and deaerated solution. In the aerated solution, there was a decrease in the capacitive semicircle after the fourth day of exposure, whereas in the deaerated solution, there was an increase of semicircle after the first day.



**Figure 4.11.** Nyquist plot of carbon steel exposed to artificial geothermal water at room temperature in (a) aerated and (b) deaerated solution

Further EIS analysis was conducted by representing data representation in a Bode magnitude plot and phase angle plot (Figure 4.12). In the aerated solution, the Bode magnitude plot shows that the total impedance value  $|Z|$  was stable during the first three days at around  $160 \Omega$ , then decreased after the fourth day (Fig. 4.12a). Although there was an overlap of Nyquist plots for the first three days, there was a shift of phase angle peak to a lower frequency (Figure 4.12b), indicating an increase of surface coverage by the oxide layer [114, 131].

In the deaerated solution, the Bode magnitude plot showed an increase of total impedance value up to the fourth day of measurement, then decreased gradually (Figure 4.12c). Related to this trend, the phase angle plot shows an increase of phase angle peak up to the fourth day, followed by the appearance of the second time constant at a lower frequency starting on the fifth day of measurement (Figure 4.12d). Compared to the phase angle in the aerated solution, the impedance spectra in the deaerated solution have a lower phase angle, indicating more capacitive behavior. Overall, in the presence of oxygen, carbon steel is highly susceptible to corrosion compared to the condition without oxygen.



**Figure 4.12.** EIS results of carbon steel exposed to artificial geothermal water at  $25^\circ\text{C}$  (a) Bode magnitude plot, and (b) phase angle plot in aerated solution; (c) Bode magnitude plot, and (d) phase angle plot in deaerated solution.

To understand the mechanism of corrosion processes, equivalent electrical circuits were fitted to the impedance data (as inserted in Figure 4.11). Model 1 was used to fit the EIS data in the first two days of deaerated condition, whereas model 2 was used in the deaerated condition for the third to seventh day, and all the EIS data obtained in the aerated condition.  $R_s$



represents the solution resistance,  $R_{ct}$  is the charge transfer resistance, and  $R_{po}$  is the resistance within the pores or film interface, parameter  $Q$  and  $\alpha$  were used as CPE to compensate for heterogeneity on the electrode surface,  $C_{dl}$  is the double layer capacitance and  $C_f$  represents the film capacitance. The fitted data is shown in Table 4.1 and Table 4.2 to provide more detailed and precise information regarding the parameters fitted in the impedance spectra. GoF is goodness of fit which represents the quality of data fitting. The smaller value of GoF indicates a better fitting, where a value higher than  $10^{-4}$  correlates to an error of 1%.

**Table 4.1.** Fitting output of EIS in aerated condition at 25 °C

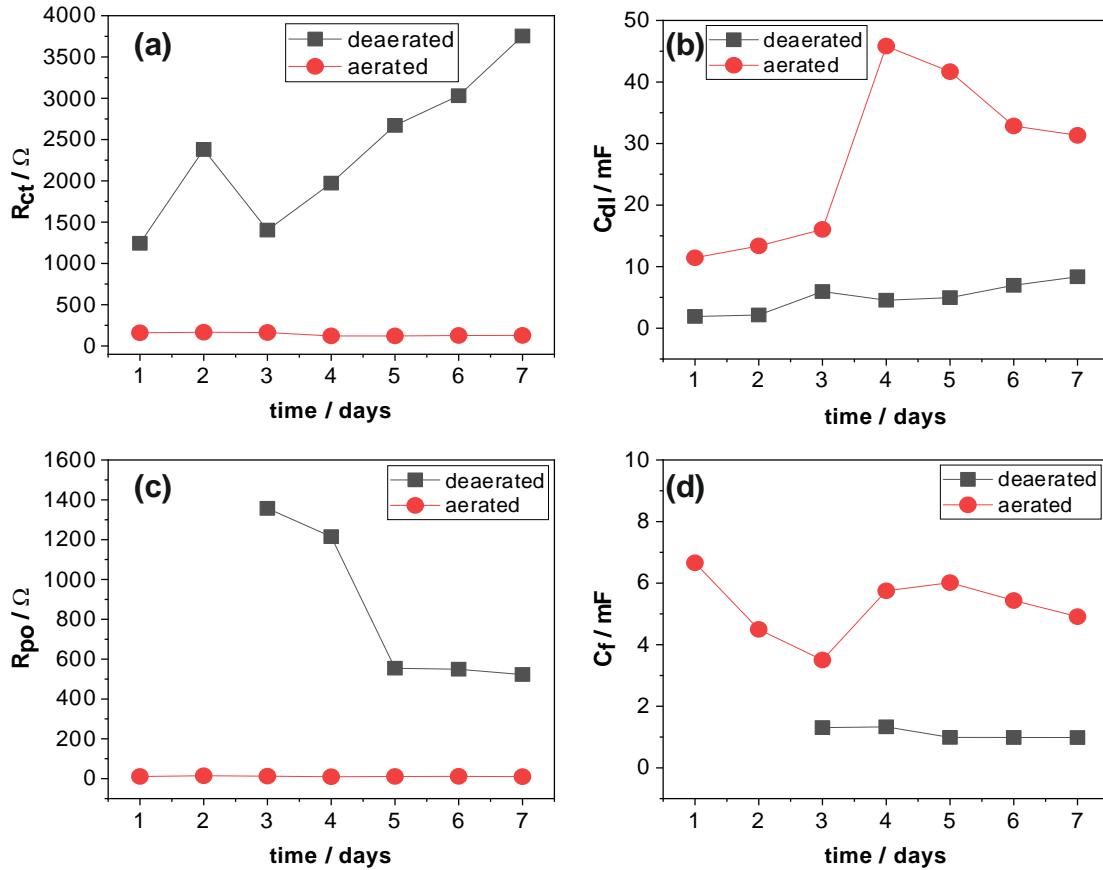
day	$R_s$ ( $\Omega$ )	$R_{ct}$ ( $\Omega$ )	$Q_{dl}$ ( $S s^\alpha$ )	$\alpha_{dl}$	$C_{dl}$ (mF)	$R_{po}$ ( $\Omega$ )	$Q_f$ ( $S s^\alpha$ )	$\alpha_f$	$C_f$ (mF)	GoF
1	22	160	0.010	0.79	12	11	0.013	0.75	7	6.66E-05
2	21	168	0.011	0.79	13	15	0.009	0.73	5	8.05E-05
3	21	164	0.013	0.80	16	12	0.009	0.70	4	1.04E-04
4	21	123	0.030	0.75	46	10	0.012	0.76	6	1.53E-04
5	21	122	0.028	0.76	42	11	0.012	0.76	6	1.21E-04
6	21	128	0.024	0.77	33	11	0.011	0.75	5	1.43E-04
7	20	128	0.023	0.77	31	10	0.010	0.76	5	1.32E-04

**Table 4.2.** Fitting output of EIS in deaerated condition at 25 °C

day	$R_s$ ( $\Omega$ )	$R_{ct}$ ( $\Omega$ )	$Q_{dl}$ ( $S s^\alpha$ )	$\alpha_{dl}$	$C_{dl}$ (mF)	$R_{po}$ ( $\Omega$ )	$Q_f$ ( $S s^\alpha$ )	$\alpha_f$	$C_f$ (mF)	GoF
1	26	1243	0.002	0.75	2	-	-	-	-	0.0007
2	25	2380	0.001	0.76	2	-	-	-	-	0.0018
3	26	1404	0.004	0.79	6	1357	0.0012	0.82	1	0.0002
4	26	1972	0.003	0.78	5	1215	0.0012	0.81	1	0.0002
5	26	2672	0.003	0.79	5	555	0.0011	0.83	1	0.0002
6	26	3031	0.004	0.79	7	550	0.0011	0.83	1	0.0003
7	26	3754	0.004	0.78	8	523	0.0011	0.83	1	0.0002

The values extracted from the fitting were then plotted as a function of time to see the evolution of each parameter until seven days. In aerated solution, both  $R_{ct}$  and  $R_{po}$  show very low values indicating that carbon steel has a very low corrosion resistance, which did not significantly change over time (Figure 4.13a and Figure 4.13c). In the deaerated solution,  $R_{ct}$  increases over time, indicating that there was an increase in the corrosion resistance. This might be associated with the main corrosion reaction driven by hydrogen evolution. The pH measurement showed an increase from 4 to 5.5 within 24 hours, which is related to the decrease of  $H^+$  in the solution, as it is consumed by the carbon steel. The limited supply of  $H^+$  in the solution results in the increased corrosion resistance of carbon steel.

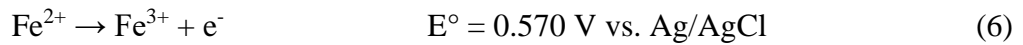
Inversely, both  $C_{dl}$  and  $C_f$  of carbon steel in the deaerated solution show very low values compared to that of the aerated solution (Figure 4.13b and Figure 4.13d). The evolution of  $C_f$  is associated with the change of corrosion product properties.



**Figure 4.13.** EIS fitting parameter as a function of time (a)  $R_{ct}$  (b)  $C_{dl}$  (c)  $R_{po}$  and (d)  $C_f$

#### 4.2.4. Corrosion Mechanism of Carbon Steel at 150 °C

To simulate the real condition, the temperature was set to 150 °C. As mentioned before, carbon steel reacts electrochemically to spontaneously corrode due to the iron dissolution and hydrogen evolution. Additionally, oxidation of  $Fe^{2+}$  to  $Fe^{3+}$  might happen due to the increasing temperature, which contributes to the cathodic reaction:



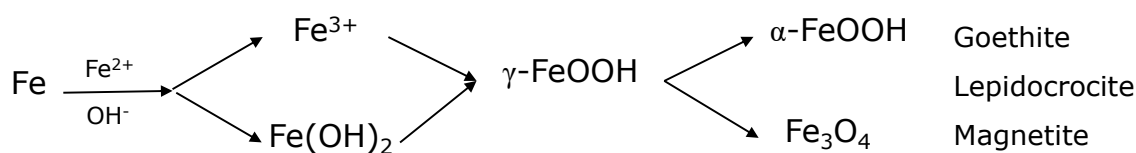
In addition to the electrochemical reactions, a chemical reaction may occur between  $Fe^{2+}$  or  $Fe^{3+}$  and water:



Whereas in the presence of oxygen, the chemical reaction may occur between  $Fe^{2+}$ , water, and oxygen:



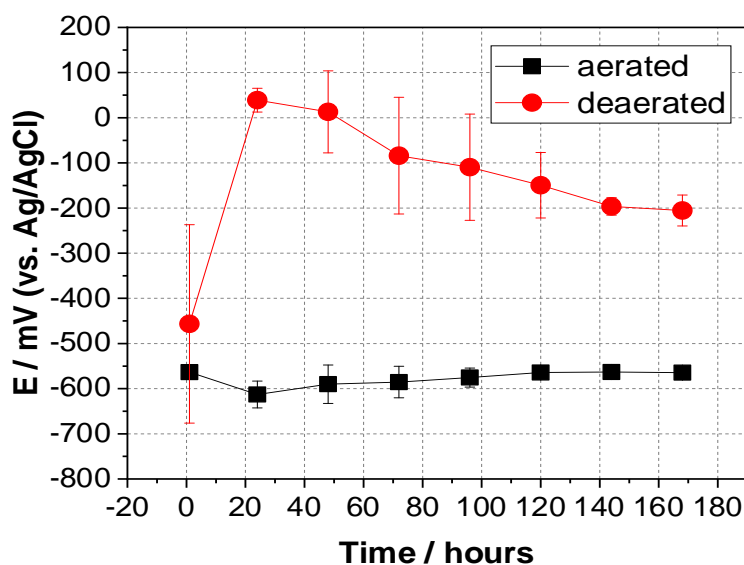
According to the literature, the possible corrosion products are goethite, lepidocrocite, or magnetite [78]:



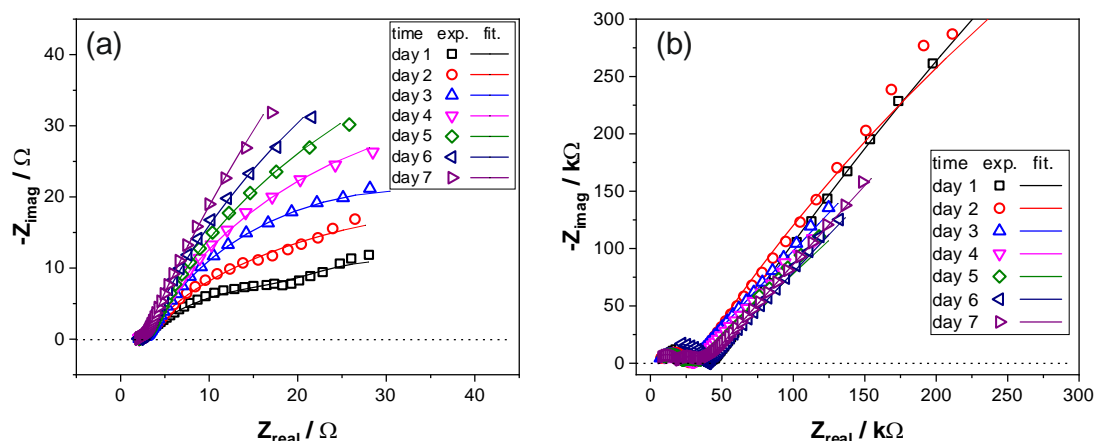
Since the solution contains  $\text{Cl}^-$ , it is suggested that the favored corrosion products formation are lepidocrocite [132] and magnetite [133].

The free corrosion potential was measured as a function of time. At room temperature, the  $E_{\text{corr}}$  of carbon steel in the aerated solution was higher than in the deaerated solution. However, at 150 °C,  $E_{\text{corr}}$  was higher when carbon steel was exposed to the deaerated solution (Figure 4.14). The significant difference in  $E_{\text{corr}}$  influenced by oxygen presence showed a different nature of corrosion products in both conditions. After the first day of exposure in the deaerated solution,  $E_{\text{corr}}$  increased significantly in the first few hours from -457 mV to 39 mV, then the potential gradually decreased over the seven days reaching -206 mV. Compared to the deaerated condition,  $E_{\text{corr}}$  measured in the aerated condition was more stable between -613 mV to -563 mV.

To further investigate the surface-interface interaction at 150 °C, EIS was performed with an interval of 24 hours. As observed by  $E_{\text{corr}}$  monitoring, the Nyquist plots show a significant difference in the range of impedance value recorded, approximately 30  $\Omega$  in the aerated solution (Figure 4.15a) and 300 k $\Omega$  in the deaerated solution (Figure 4.15b). These results showed a significant enhancement in the corrosion resistance when oxygen was removed from the solution. For both conditions, the pattern of Nyquist plots changed with exposure time. For example, in the aerated solution, impedance increased along with time, indicated by the increase of semicircle diameter in the Nyquist plot, whereas in the deaerated solution, impedance seem to decrease over time.



**Figure 4.14.** OCP of carbon steel in aerated and deaerated artificial geothermal water at 150 °C



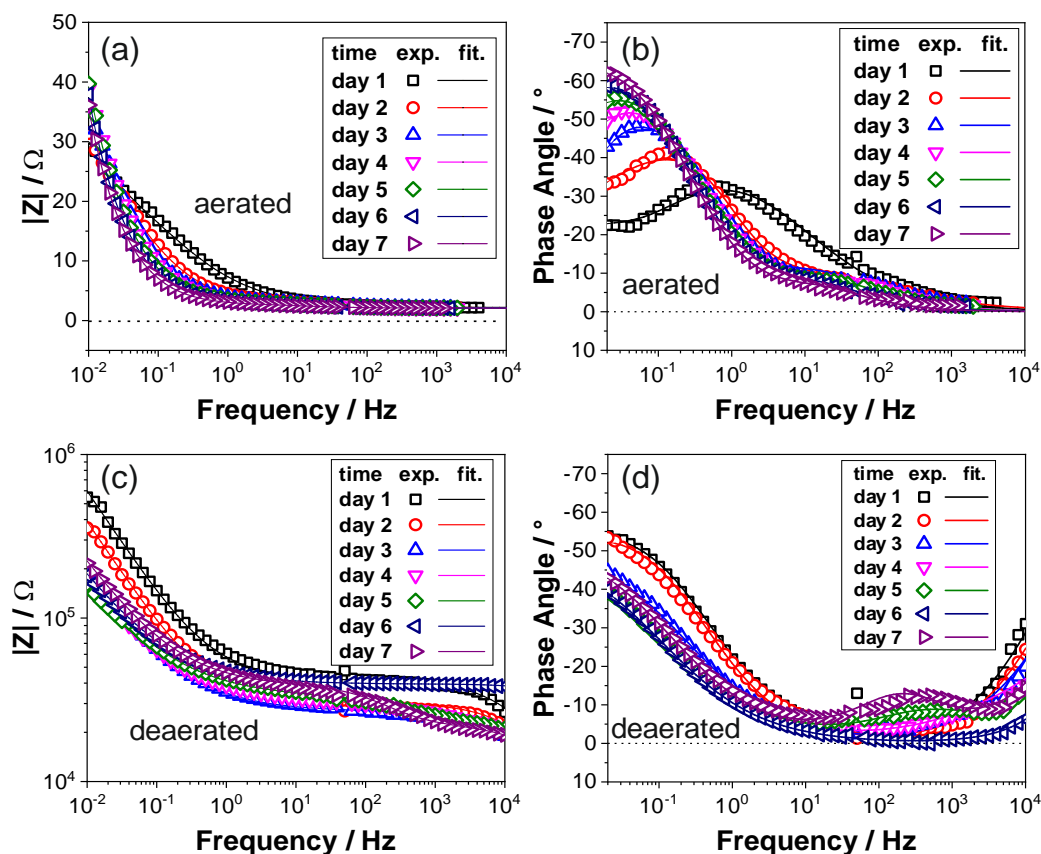
**Figure 4.15.** Nyquist plot of carbon steel exposed to artificial geothermal water at 150 °C (a) in aerated and (b) deaerated solution

To further observe the change of surface-interface interaction over time, Bode magnitude plots and phase angle plots are presented in Figure 4.16. In aerated condition, the total impedance values ranged between 30 – 40  $\Omega$  over seven days (Figure 4.16a), and the peak of phase angle shifted to a lower frequency range and increased gradually (Figure 4.16b). On the first day, the phase angle peak was between 10 Hz – 0.1 Hz, which then shifted to lower than 1 Hz after the second day, indicating that the electrochemical reaction involved is kinetically slower. However, for the next days, the phase angle position remained stable, with an increase in the negative phase angle axis, suggesting an increase in the capacitive behavior, which could be associated with the growth of the corrosion product layer.

In the deaerated solution, Bode magnitude plot shows that  $|Z|$  was between  $10^5$  –  $10^6$   $\Omega$ , indicating passive behavior of carbon steel (Figure 4.16c). However, the absolute impedance value decreased with time, suggesting a decrease in corrosion resistance. With respect to exposure time, the phase angle plot showed an increase of phase angle between  $10^2$  –  $10^1$  Hz, and a decrease of phase angle in the lower frequency region between  $10^0$  –  $10^{-2}$  Hz (Figure 4.16d). Here, there was no significant change in the kinetics of the involved reactions, but a change in the electrical properties of surface and the corresponding corrosion product layer. Fitting of the impedance data were performed using equivalent electrical circuits model 2 as also explained at the room temperature measurements, but in a shorter frequency range of  $10^3$  –  $10^{-2}$  Hz. The results of fitted parameters are shown in the Table 4.3 and 4.4.

Similar to the results at 25 °C, carbon steel has a higher corrosion resistance in the deaerated solution. Figure 4.17a shows a much higher  $R_{ct}$  of the deaerated solution, which is about six orders of magnitude higher than in the presence of oxygen. The value remained stable over seven days of exposure, indicating passive behavior of carbon steel at 150 °C in the absence of oxygen. Figure 4.17d shows a higher value of  $C_f$  in the aerated solution indicating a higher capacitance of the oxide film or corrosion product layer. This might be associated with a higher surface coverage in the presence of oxygen and a higher dielectric constant of the corrosion product.

GoF shows the quality of data fitting, where the value  $10^{-4}$  represents 1% of error, and  $10^{-2}$  represents 10% of error. Although the GoF at a higher temperature measurement is higher than that at room temperature, the error value is below 10 %, representing fairly good fits.



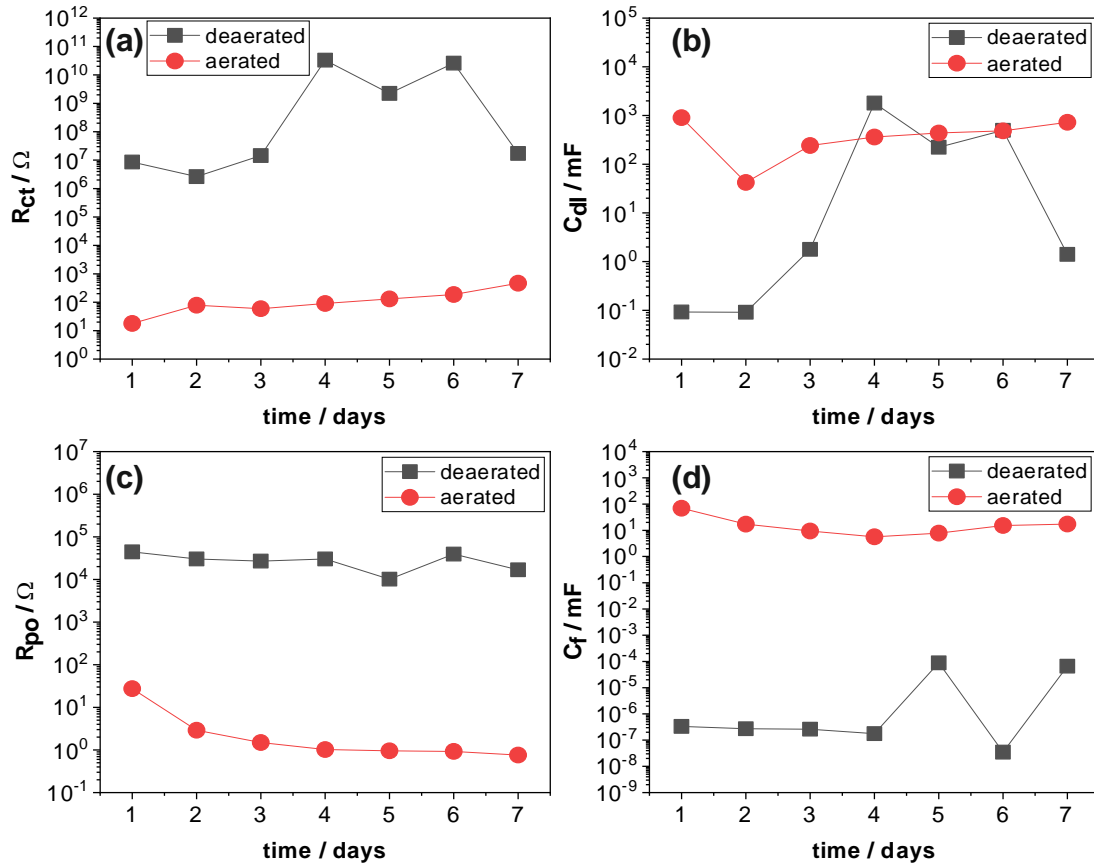
**Figure 4.16.** EIS results of carbon steel exposed to artificial geothermal water at 150 °C (a) Bode magnitude plot, and (b) phase angle plot in aerated solution; (c) Bode magnitude plot, and (d) phase angle plot in deaerated solution.

**Table 4.3.** Fitting output at 150 °C: aerated condition

day	$R_s$ ( $\Omega$ )	$R_{ct}$ ( $\Omega$ )	$Q_{dl}$ ( $S s^a$ )	$\alpha_{dl}$	$C_{dl}$ (mF)	$R_{po}$ ( $\Omega$ )	$Q_f$ ( $S s^a$ )	$\alpha_f$	$C_f$ (mF)	GoF
1	2	18	0.657	0.89	902	27	0.053	0.58	69	0.0007
2	2	78	0.038	0.92	42	3	0.081	0.48	17	0.0003
3	2	59	0.137	0.79	241	1	0.027	0.75	9	0.0007
4	2	90	0.161	0.77	362	1	0.017	0.78	6	0.0001
5	2	131	0.174	0.77	438	1	0.023	0.78	8	0.0001
6	2	187	0.184	0.79	483	1	0.040	0.77	15	0.0001
7	2	466	0.209	0.79	727	1	0.042	0.78	17	0.0002

**Table 4.4.** Fitting output at 150 °C: deaerated condition

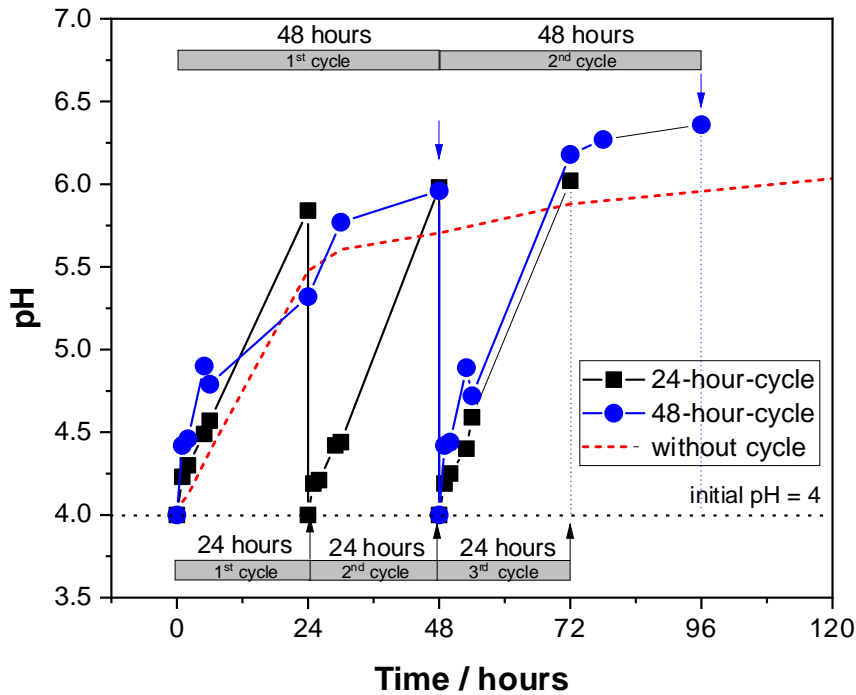
day	$R_s$ ( $\Omega$ )	$R_{ct}$ ( $\Omega$ )	$Q_{dl}$ ( $S s^a$ )	$\alpha_{dl}$	$C_{dl}$ (mF)	$R_{po}$ ( $\Omega$ )	$Q_f$ ( $S s^a$ )	$\alpha_f$	$C_f$ (mF)	GoF
1	2	8.6E+06	1.13E-05	0.68	0.09	4.45E+04	4.20E-08	0.57	3.34E-07	0.0064
2	2	2.6E+06	1.72E-05	0.70	0.09	3.03E+04	5.08E-09	0.75	2.72E-07	0.0091
3	2	1.5E+07	2.98E-05	0.60	1.78	2.70E+04	9.19E-09	0.70	2.62E-07	0.0047
4	2	3.3E+10	3.23E-05	0.56	1801.67	3.02E+04	6.36E-08	0.52	1.77E-07	0.0007
5	2	2.2E+09	3.33E-05	0.56	222.56	1.02E+04	3.53E-07	0.80	8.84E-05	0.0007
6	2	2.6E+10	3.16E-05	0.58	496.83	3.94E+04	1.45E-10	0.89	3.49E-08	0.0001
7	2	1.7E+07	2.68E-05	0.61	1.41	1.69E+04	2.35E-07	0.81	6.61E-05	0.0021



**Figure 4.17.** EIS fitting parameter as a function of time of carbon steel exposed at 150 °C in aerated and deaerated solution, with the parameter of (a)  $R_{ct}$  (b)  $C_{dl}$  (c)  $R_{po}$  (d)  $C_f$

### 4.3. Influence of pH on Carbon Steel Corrosion

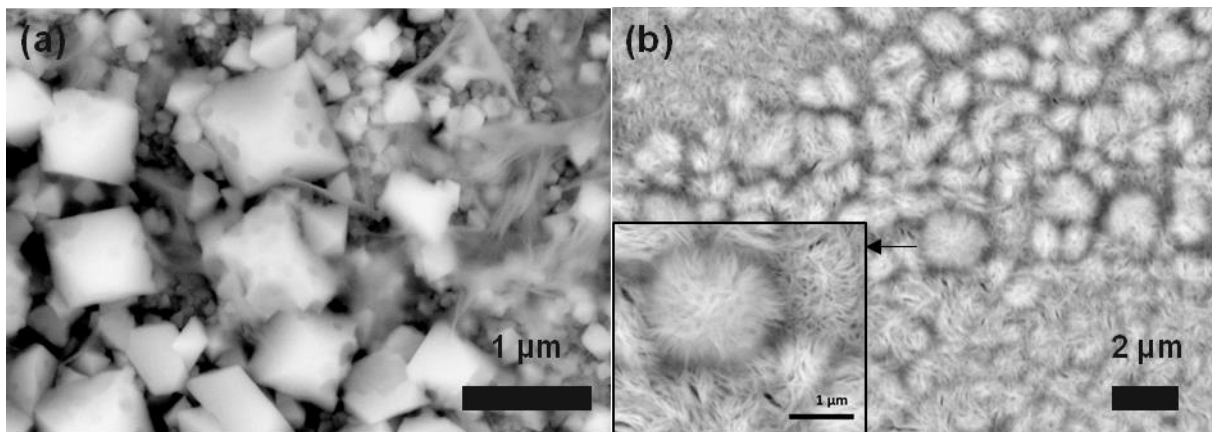
As shown by the electrochemical measurements, the change of corrosion potential in the first few hours in the deaerated solution might be associated with the pH change. The pH measurement showed that after 24 hours,  $H^+$  was consumed in the corrosion processes, leading to an increase of pH to 5.5, reaching pH 6-7 by the end of experiment (Figure 4.18). At room temperature under the aerated condition, pH was measured as a function of time. In addition, the solution was renewed every 24 hours and every 48 hours to simulate the condition where the corroded carbon steel is always in contact with a solution of the same pH. The pH increased significantly in the first two hours from 4 – 5, then gradually increases to 5.7 after 24 hours, and to 6 after 48 hours. In the seven days of exposure, the solution pH remained stable between 6 -7 regardless of the gaseous condition and temperature. By renewing the solution with an initial pH of 4, the solution pH increased faster within the same interval. This result showed that the reaction of iron and  $H^+$  is a fast reaction which was dominating at the beginning of experiments.



**Figure 4.18.** Solution pH at 25 °C in the renewed solution with an interval of 24 and 48 hours

#### 4.3.1. Morphological Characterization

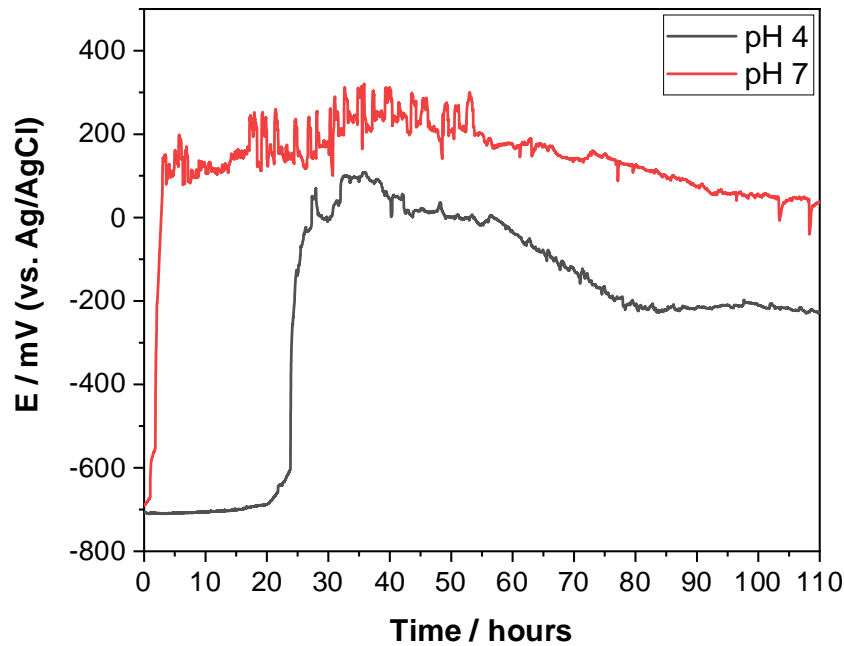
A test solution of pH 7 was used to compare the effect of acidity on carbon steel corrosion. The SEM image shows different formation of corrosion products at pH 4 and pH 7 (Figure 4.19), with only one homogeneous structure observed at pH 7, which was a hair-like structure. This result showed that at a lower pH, the prismatic structure is more favorable. The different resulting oxide layer might also contribute to different corrosion behavior.



**Figure 4.19.** SEM image of carbon steel after exposed at 150 °C for seven days in the solution with (a) pH 4 and (b) pH 7

#### 4.3.2. Influence of pH on Carbon Steel $E_{\text{corr}}$

The open circuit potential was measured to compare the effect of pH on the corrosion reaction. Figure 4.20 shows that  $E_{\text{corr}}$  of carbon steel in the solution with pH 7 is higher than that of pH 4. When the solution has a neutral pH,  $\text{H}^+$  is not readily available to initiate a fast reaction with carbon steel as in the acidic solution. Although it might still be the main reactant responsible for the corrosion reaction, the availability of  $\text{H}^+$  is achieved by the dissociation of water molecule to  $\text{H}^+$  and  $\text{OH}^-$  (hydrolysis). The high temperature might also contribute to a faster hydrolysis in the solution.



**Figure 4.20.** OCP of carbon steel in deaerated artificial geothermal water at 150 °C with pH 4 and 7

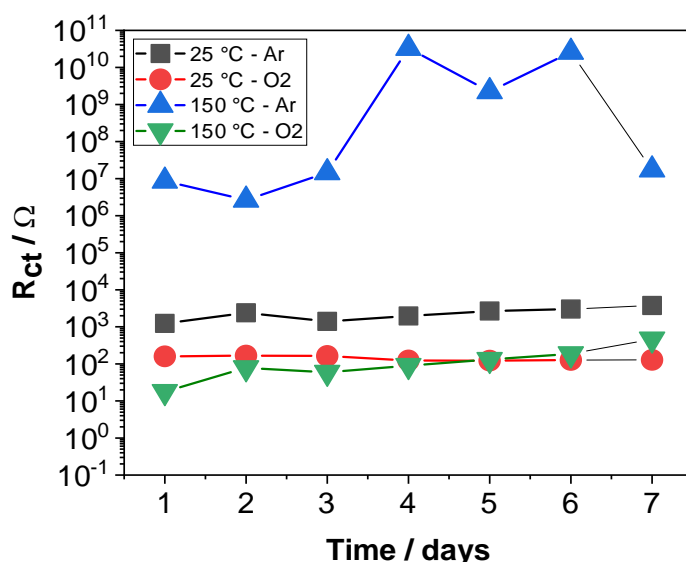
#### 4.4. Summary and Conclusion

To sum up the results of this chapter, several findings were as follows:

1. Corrosion rate of carbon steel in artificial geothermal water depends on the temperature and gaseous condition. At any temperature, the presence of dissolved oxygen caused corrosion rate to increase. For example, after exposure for 7 days at 150 °C, the corrosion rate of carbon steel increased almost ten times higher than that in the absence of dissolved oxygen (in the deaerated solution).
2. Effect of solution at different temperatures: at room temperature, there was no corrosion product formation, but the surface of carbon steel was rougher due to the interaction of carbon steel with  $\text{H}^+$  in the acidic solution. At 70 °C, a very thin layer of corrosion product was formed, although not homogeneously, whereas at 150 °C there were two distinct structures of corrosion products identified by SEM.
3. Pitting corrosion was observed in both the aerated and deaerated solution, although the severity was less in the absence of dissolved oxygen. Carbon steel exposed to the deaerated solution was more corrosion resistant than that in the aerated solution.



4. By using acidic and neutral pH, different corrosion products were observed. In the acidic medium there were prismatic and hair-like structures, whereas in the neutral medium only the hair-like structure was present, indicating that the prismatic structure formation is triggered by the lower pH. However, this result is limited to pH 4 and 7.
5. The free corrosion potential showed different partial electrochemical reactions contributed by iron dissolution, hydrogen evolution, oxygen reduction reaction, and further oxidation of metal ions. The results were discussed in detail for lower temperature (25 °C) and high temperature (150 °C) in aerated and deaerated solution.
6. EIS was used to investigate the corrosion behavior of carbon steel at different temperatures, in absence/presence of oxygen, and at different pH. Figure 4.21 summarized the evolution of corrosion resistance ( $R_{ct}$ ) of carbon steel over time until seven days of exposure.



**Figure 4.21.**  $R_{ct}$  representing corrosion resistance as a function of time.

Carbon steel underwent the most severe corrosion at 150 °C in the presence of oxygen, shown by a high corrosion rate, and low corrosion resistance. In the absence of oxygen, the corrosion rate of carbon steel was lower than the corrosion rate threshold set for geothermal application of 0.3 mm/year, regardless of the temperature. Based on the electrochemical data and morphological characterization, the corrosion attack was more severe for carbon steel at a lower temperature in the oxygen-free solution. When oxygen is present, the corrosion rate of carbon steel increased significantly, with a corrosion rate of 0.34 mm/year at 150 °C. However, regardless of the presence oxygen, pitting corrosion was observed on carbon steel exposed to the artificial geothermal water at 150 °C, which necessitate a protection strategy on carbon steel to ensure the safety of the infrastructure of geothermal powerplants.



# Chapter 5. Electrochemical Deposition of Polyaniline and its Suitability in Geothermal Solution

This chapter focuses on the polyaniline synthesis via electrochemical polymerization and its characterization in artificial geothermal water. Electrochemical polymerization was performed on the working electrode (graphite electrode and carbon steel) to produce a controllable polyaniline layer which was further used to study the surface and interface interaction of each adjacent part of the coating, i.e. carbon steel, polyaniline layer, and the tested electrolyte at room temperature and elevated temperature.

## 5.1. Electrochemical Polymerization of Polyaniline on Graphite Electrode

Electrochemical polymerization offers several advantages compared to chemical polymerization, such as rapid polymerization at room temperature, as well as simultaneous doping with the desired anion by alternating the supporting electrolytes. In addition, it also offers advantages in controlling film thickness, molecular structure and morphology, and an easy application. Moreover, the electrochemical application avoids the solubility problem that has been encountered in applying polyaniline on the metal substrate by casting [85]. Thus, electrochemical polymerization is the method of choice to investigate interaction of pure polyaniline with the artificial geothermal water and its protection mechanism on metal substrate during a corrosion test.

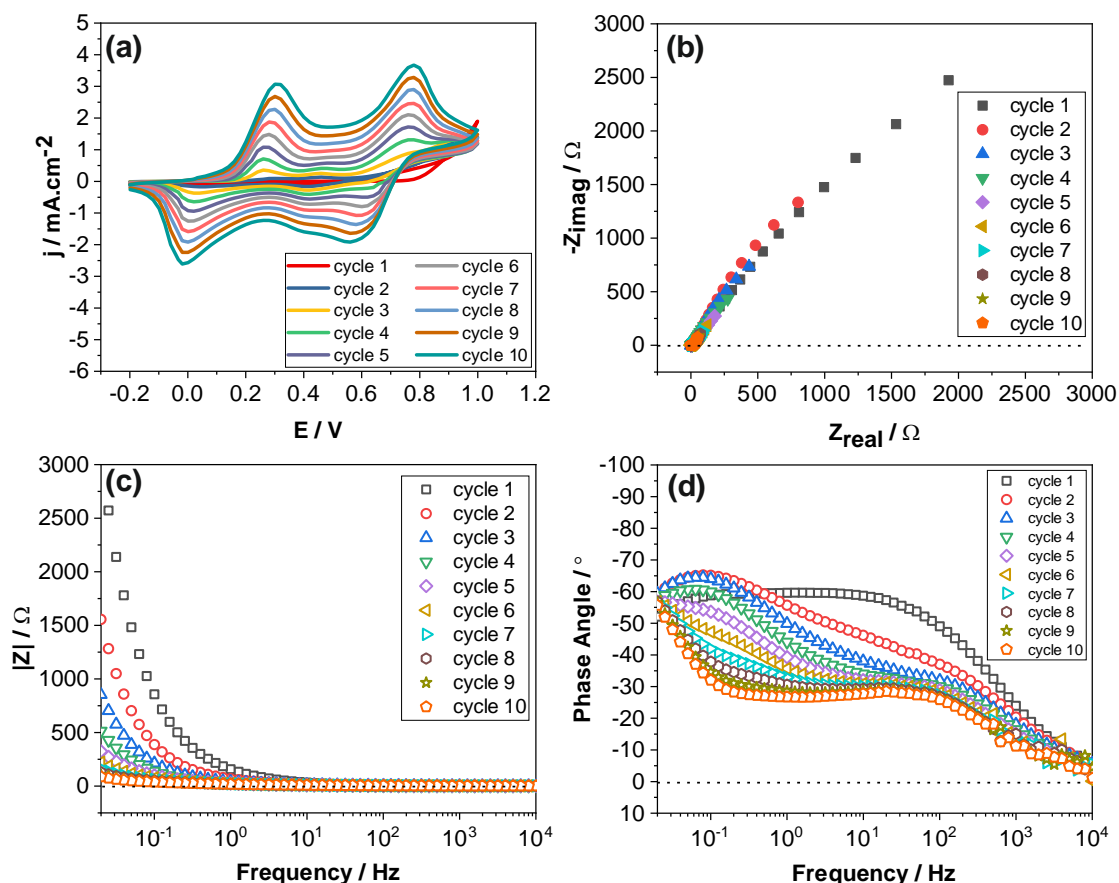
The first step was to synthesize and characterize PANI electrochemically and expose it to the artificial geothermal water at different temperatures. For this purpose, polyaniline was first deposited on a graphite electrode using the same composition as chemically synthesized polyaniline, 0.2 M aniline in 1.2 M phosphoric acid. To understand the standalone interaction of pure PANI without any effects from the metal substrate with artificial geothermal water, graphite electrode was used instead of carbon steel substrate as it is inert and stable in the electrolyte.

Among many available electrochemical deposition methods such as potentiostatic and galvanostatic deposition, cyclic voltammetry was chosen and used in this experiment with a scan rate of 20 mV/s. The potential was applied between two values  $E_1$  and  $E_2$  at a constant sweeping rate, i.e. -0.2 to 1.0 vs Ag/AgCl. As the potential reaches  $E_2$ , the sweep was reversed until reaching  $E_1$ . The current response was recorded as a function of the applied potential, indicating the oxidation or reduction reactions occurred at the corresponding applied potential.

The cyclic voltammogram revealed several redox couple peaks of PANI/ $H_3PO_4$  which increased in current density with cycle number (Figure 5.1a). Two pairs of peaks appear in the cyclic voltammogram, with two oxidation peaks and two reduction peaks (as mentioned in the electrochemical polymerization mechanism of polyaniline in section 2.3.3). The cyclic voltammogram of polyaniline is similar to other studies [22, 134], although minor differences were observed which were influenced by the type of acid used. The type of acids contributes to the properties of polyaniline, e.g. the electrical conductivity, which is strongly related to the size and charge of the dopants, or also mention as counter anions. For example,  $SO_4^{2-}$  is more

difficult to diffuse into the polyaniline chain than  $\text{Cl}^-$  because of its larger radius compared to  $\text{Cl}^-$ . Thus, polyaniline doped with  $\text{HCl}$  exhibits a higher electrical conductivity due to the effective migration of anions into the electrode materials [134].

EIS was applied after each cycle to observe the change of impedance with the cycle number. A short frequency range from  $10^4$  to  $0.02$  Hz was used to maintain the working electrode and the electrolyte in a stable condition before performing the next cycle of cyclic voltammetry. Impedance spectra are presented in three forms of data representation, i.e. Nyquist plot, Bode magnitude plot, and Phase angle plot. The Nyquist plot does not show any significant change in pattern, although decreasing in the  $Z_{\text{real}}$  and  $-Z_{\text{imag}}$  value with respect to the cycle number (Figure 5.1b). At the lowest frequency, the Bode magnitude plot shows a significant decrease in the total impedance value from almost  $3000 \Omega$  at the first cycle to near  $0 \Omega$  at the tenth cycle (Figure 5.1c) indicating that the formation of conductive polyaniline contributes to the lower resistance. The change of impedance might be associated with polyaniline growth, building up a thicker layer which is electrically more conductive after each cycle. The phase angle plot shows different curves at each cycle with a change of slope in each cycle, but the phase angle remained between  $-50^\circ$  to  $-60^\circ$  at the lowest frequency (Figure 5.1d).

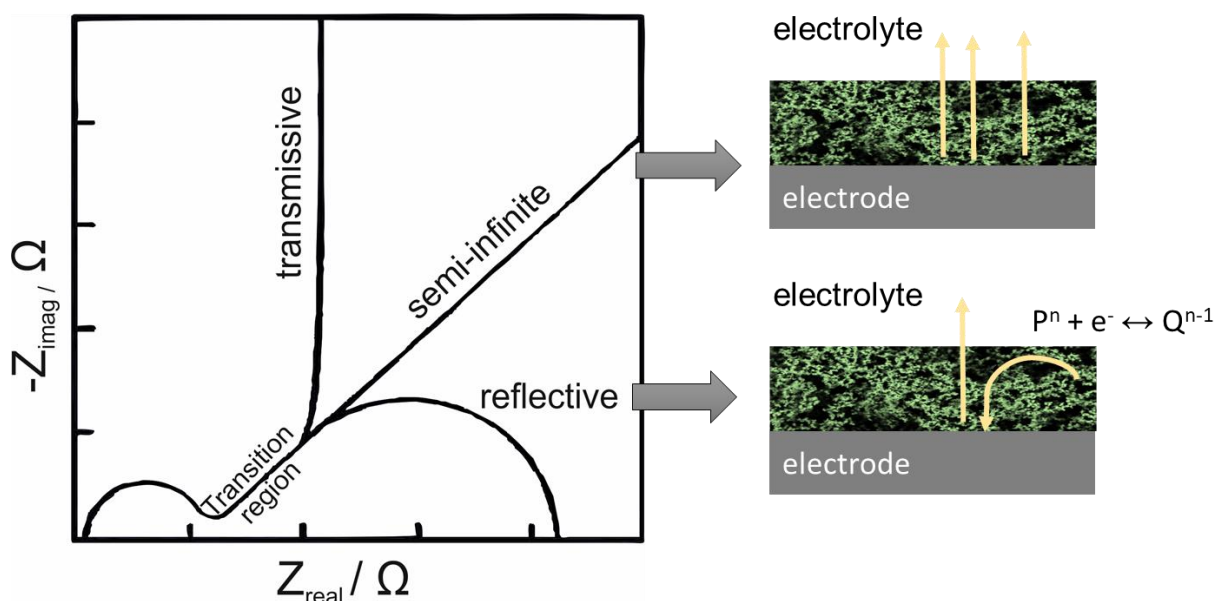


**Figure 5.1.** Electrochemical deposition of PANI/ $\text{H}_3\text{PO}_4$  on a graphite electrode (a) Cyclic voltammogram, 20 mV/s, (potential is vs. Ag/AgCl) (b) Nyquist plot (c) Bode magnitude plot (d) phase angle plot.

To extract well-understood phenomena by interpreting impedance spectra, an appropriate electrical equivalent circuit should be used. Nyquist plot indicates that the equivalent circuit might include a diffusion element, or also known as a Warburg element.

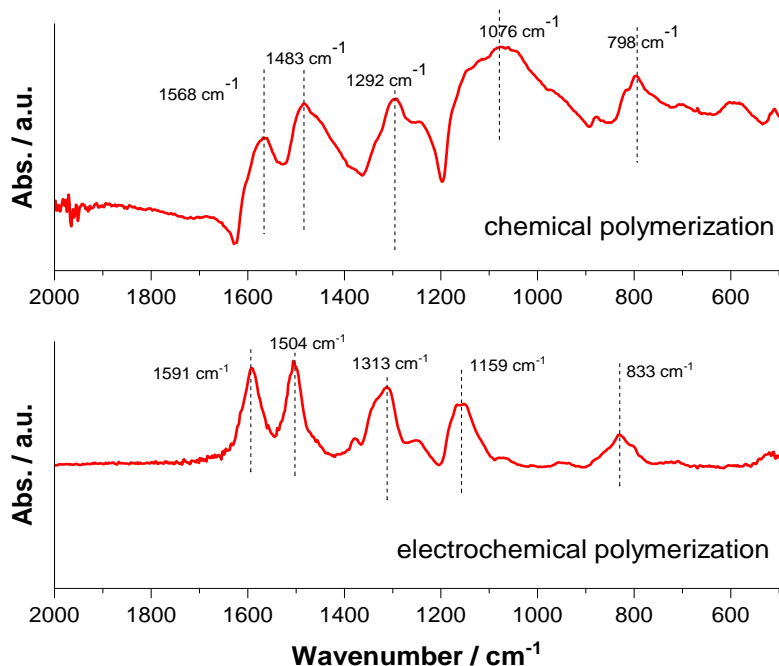
There are several types of diffusion impedance depending on the experimental system, e.g. for a uniformly accessible electrode and for a porous film. To use a diffusion impedance in the impedance data fitting of a porous film or a coated electrode, it is important to consider whether the electroactive species is exchanged between the film and the electrolyte (semi-infinite boundary) or the diffusion occurs within the film without any exchange of electroactive species between the film and the bulk electrolyte (finite boundary), as illustrated in Figure 5.2 [114]. Diffusion impedance, therefore, can have either a finite boundary or a semi-infinite boundary, depending on how the ionic species diffuse from the bulk electrolyte.

Although the Nyquist plot generally shows the  $45^\circ$  tendency, it is not perfect straight and has a curvature, which can be associated with a finite diffusion impedance with reflective boundary condition. The reflective boundary condition shows that there is a surface coverage that blocks the diffusion, but it involves an exchange of electroactive species within the film, due to the growing of polyaniline layer during polymerization. This diffusion process might involve the redox sites on the surface of electrode, where the charge propagates through the polyaniline layer by electron hopping or electric conduction. Consequently, there is a diffusion of the freely moving ions from counterions to the solution. Thus, electrons cross the electrode-polymer boundary and ions can cross the polymer-solution interface.



**Figure 5.2.** Nyquist plot of a porous film with different types of diffusions and the illustration of diffusion in the coated electrode under a semi-infinite boundary and a reflective boundary condition [114].

FTIR was used to characterize the functional groups in the electrochemically polymerized PANI/H<sub>3</sub>PO<sub>4</sub> as compared to that from the chemically synthesized one (Figure 5.3). To identify the difference between specific compound from both synthesis routes and confirm the formation of polyaniline, the fingerprint characteristic region i.e. from 2000 to 500  $\text{cm}^{-1}$  were analyzed. The peaks are identified and assigned to the reference spectra as listed in the Table 5.1. There was a shift in several peaks, which might be associated with the electronic properties or a possible deformation in the molecule.



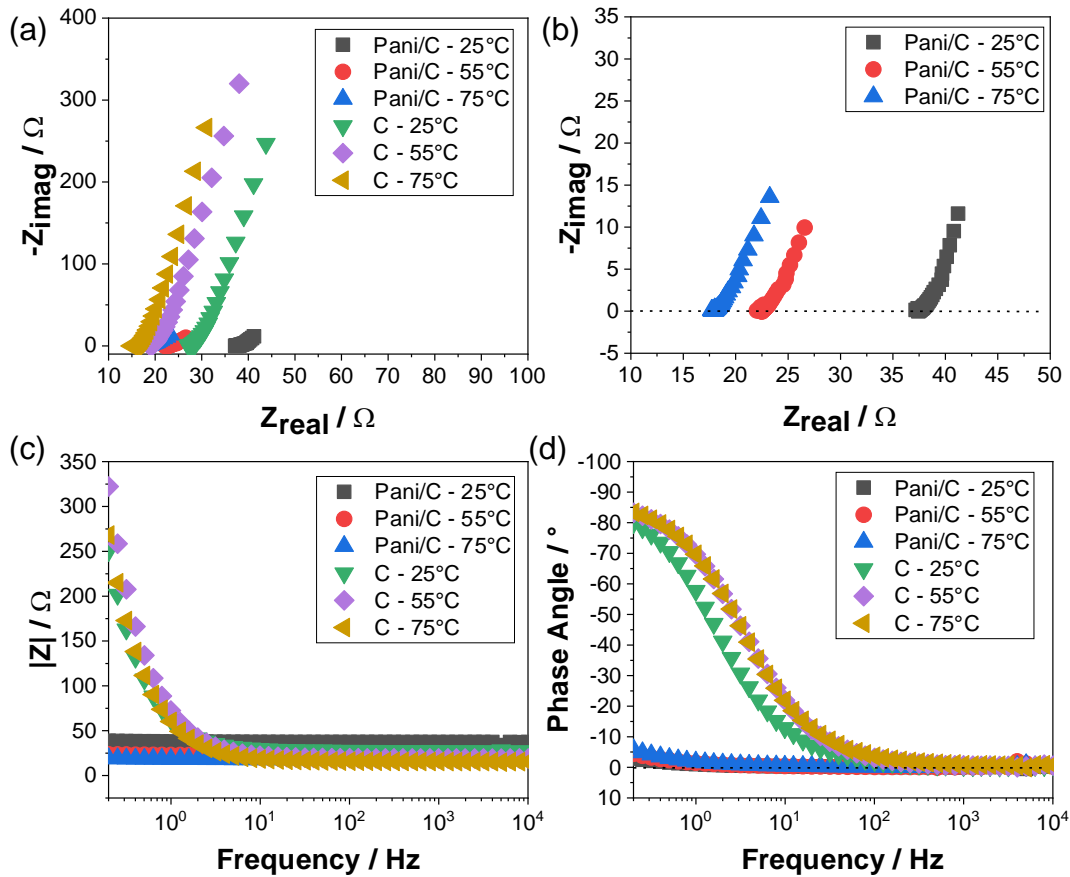
**Figure 5.3.** ATR- FTIR spectra of PANI/H<sub>3</sub>PO<sub>4</sub> synthesized using chemical and electrochemical polymerization

**Table 5.1.** ATR-FTIR spectra assignment of PANI/H<sub>3</sub>PO<sub>4</sub> synthesized using chemical and electrochemical polymerization compared and assigned to the reference [112]

Wavenumber (cm <sup>-1</sup> )			Assignment
Chemical	Electrochemical	Reference[112]	
798	833	850-750	Amine / N-H wagging and twisting
1076	1159	1220-1020	Amine / Aliphatic C-N stretching
1292	1313	1360-1250	Amine / Aromatic C-N stretching
1483	1504	1600-1430	Aromatic / C=C stretching
1568	1591	1600-1430	Aromatic / C=C stretching

## 5.2. Interaction of Polyaniline Coated Graphite with the Geothermal Solution

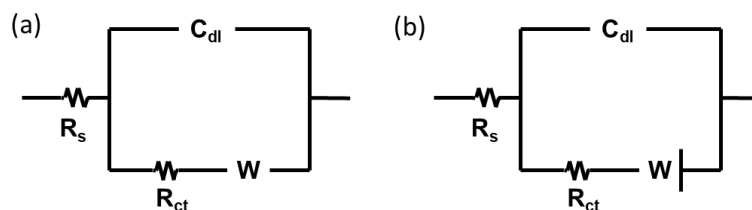
The electrochemical activity of both graphite and polyaniline coated graphite was then investigated in the artificial geothermal water using EIS (Figure 5.4a) after exposed for one hour at 25, 55, and 75 °C. At all temperatures, graphite had a higher impedance than the polyaniline coated graphite indicated by the high  $-Z_{imag}$  value in the Nyquist plot and  $|Z|$  in the Bode magnitude plot. A magnification of Nyquist plot shows that polyaniline coated graphite has a lower impedance value, however there was no significant change in pattern compared to the uncoated graphite. By increasing the temperature, there was a negative shift of impedance spectra (Figure 5.4b), indicating that the solution resistance decreased due to the temperature effect on ion mobility. Without the polyaniline layer, solution resistance was approximately 10  $\Omega$  lower than that in the polyaniline coated graphite, which might be associated with the retarding effect of polyaniline. Polyaniline acts as a permissible charged barrier, which could induce some absorption/desorption effects on the ions of the solution.



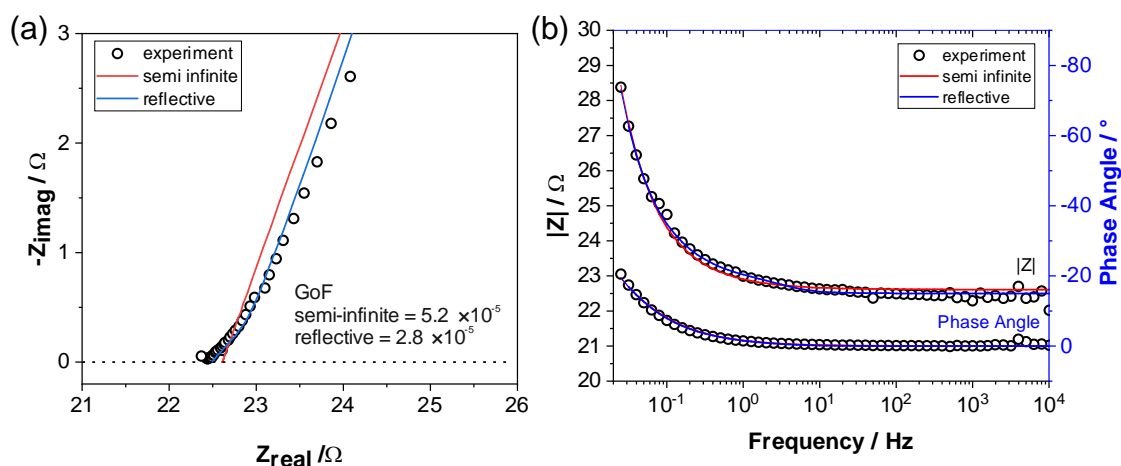
**Figure 5.4.** Impedance spectra of uncoated (written as C) and polyaniline coated graphite electrode (written as PANI/C) at 25, 55, and 75 °C (a) Nyquist plot (b) magnification of Nyquist plot (c) Bode magnitude plot (d) phase angle plot

The Bode magnitude plot shows that the uncoated graphite has a higher resistance compared to the polyaniline coated graphite, with a total impedance value of almost seven times higher than the polyaniline coated graphite (Figure 5.4c), because graphite is inert in this environment. In contrast, polyaniline coated graphite showed very low resistance as acquired after the tenth cycle of polymerization, indicating that polyaniline was conductive. The phase angle plot also shows that uncoated graphite has a phase angle of almost  $-90^\circ$  regardless of the temperature, whereas polyaniline coated graphite has a phase angle of almost  $0^\circ$ .

An example of data fitting using an equivalent electrical circuit containing Warburg impedance (Figure 5.5) is shown in Figure 5.6. Here, two different types of diffusion impedance were applied in conjunction with a Randles circuit, which is based on the semi-infinite boundary and reflective boundary, as previously mentioned. The Nyquist plot show that the reflective diffusion impedance is more suitable than the semi-infinite diffusion impedance, with a goodness of fit (GoF) of  $2.8 \times 10^{-5}$  and  $5.2 \times 10^{-5}$ , respectively. The smaller value of GoF indicates a better fitting, where a value higher than  $10^{-4}$  correlates to an error of 1% [110].



**Figure 5.5.** Equivalent electrical circuit of Randles cell with diffusion, with different types of diffusion element representing (a) semi-infinite diffusion, and (b) reflective finite diffusion



**Figure 5.6.** Impedance spectra of polyaniline coated graphite electrode at 25 °C fitted to the equivalent circuit with semi-infinite and reflective boundary of diffusion element, presented in (a) Nyquist plot, and (b) Bode magnitude and phase angle plot.

Given these points, for short-term exposure tests, the electrochemical properties of polyaniline adjacent to an inert material do not change when exposed to the artificial geothermal water at 25 – 75 °C. The impedance data interpretation shows that there is an exchange of electroactive species within the polyaniline layer, instead of a simple exchange between the film and the bulk electrolyte, which suggest that the redox properties of polyaniline might have a retarding effect for the ionic species of electrolyte to the electrode surface.

### 5.3. Electrochemical Polymerization of Polyaniline on Carbon Steel

To study the interaction of PANI-carbon steel and the geothermal solution, electrochemical deposition was performed directly on the carbon steel surface. Polyaniline deposition on carbon steel has been found to be challenging because it requires the use of acidic medium which is usually corrosive to carbon steel. In this section, several parameters governing the deposition of polyaniline on carbon steel surface are discussed, such as the type of acids, potential window, monomer to acid composition, and the cycle number.

#### 5.3.1. Choosing the Medium for Polymerization

As mentioned in Chapter 2, to perform electrochemical deposition of polyaniline on an electrode, an acidic medium is required. At higher pH, polyaniline will be formed with a lower molecular weight, lower electrical conductivity, and inconsistent properties. The selection of acids becomes important as it plays a role in the properties and characteristics of the end-product



of polyaniline. Polyaniline in its conductive form is doped by counter anion associated with the acidic medium, which was proven to influence its physical properties, e.g. thermal properties, electrical conductivity, and rigidity [135]. On the other hand, carbon steel is prone to uniform and localized corrosion, especially in the presence of different ionic species, e.g.  $\text{Cl}^-$ ,  $\text{Br}^-$ ,  $\text{I}^-$ , and  $\text{SO}_4^{2-}$  [129]. Therefore, to lower the risk of carbon steel corrosion induced by ionic species from the acids in the end-product of polyaniline, HCl and  $\text{H}_2\text{SO}_4$  are avoided both in the chemical and electrochemical polymerizations. Accordingly, electrochemical deposition of polyaniline on carbon steel is challenging because sulfuric acid, hydrochloric acid, nitric acid, or other inorganic acids are corrosive to carbon steel. Using these media, there are at least two simultaneous reactions that strongly take place, i.e. a corrosion process happens between carbon steel and the polymerization medium, and polyaniline formation on carbon steel surface [20, 91]. In many failure cases, corrosion reaction on carbon steel appears stronger, and inhibits the polyaniline formation, or resulting in an incomplete oxidation reaction of the monomer.

According to previous studies, organic acid is a promising medium to deposit polyaniline directly on the carbon steel surface. Different organic acids were used in chemical polymerization, e.g. acetic acid, citric acid, tartaric acid, and oxalic acid [136]. Sazou et al., reported the effect of different aqueous solutions on polyaniline formation on mild steel. Among of the investigated acids, oxalic acid induced polyaniline showed redox couple peaks during electrochemical deposition, indicating a stable and complete formation of polyaniline film, whereas other aqueous solutions result in different electrochemical behavior, such as the oxidation of aniline without the appearance of polyaniline redox couple [137]. Oxalic acid also showed that the resulting polyaniline synthesized in this medium has the highest electrical conductivity, thermally activated behavior [136], and a good adhesion with the carbon steel substrate [91, 137]. The increased conductivity is attributed to the increase of charge transfer efficiency between the polymeric chain and the counter anion. It is also important to note that there might be molecular rearrangement upon heating, which makes the molecular conformation favorable for electron delocalization.

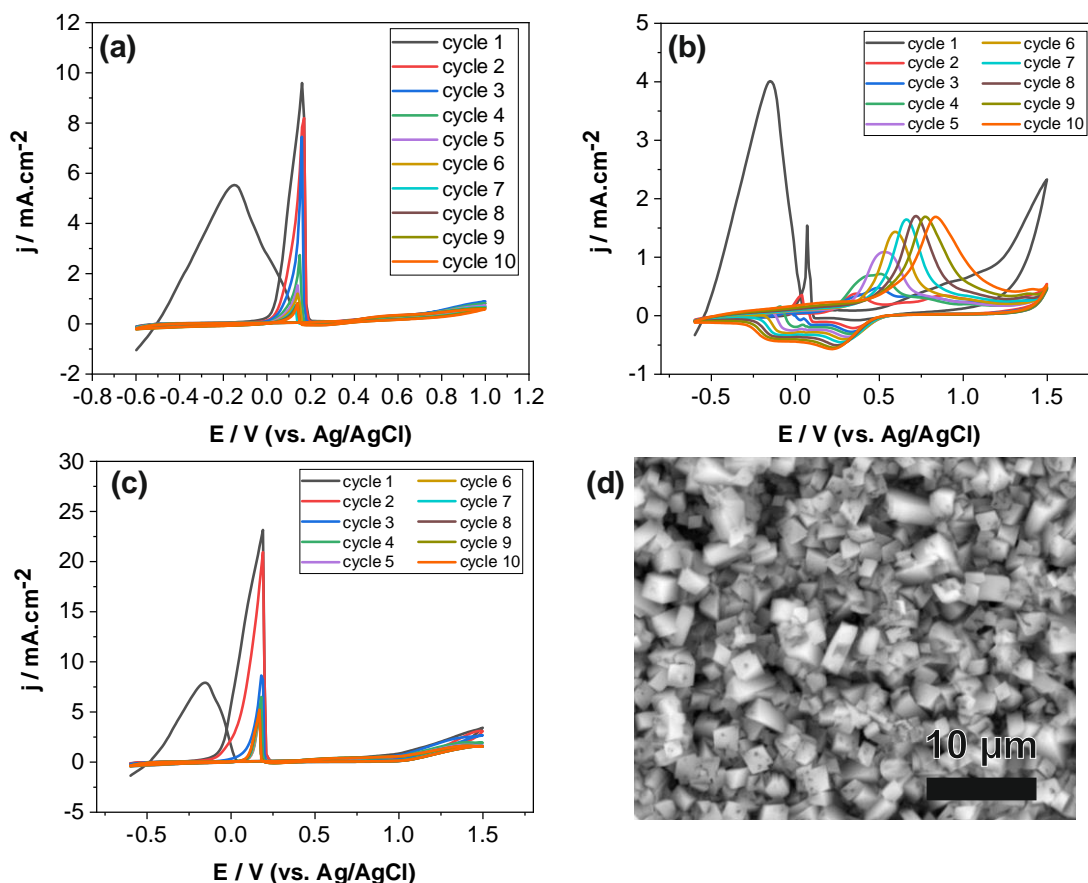
Based on the above discussed advantages of using oxalic acid, herein this study uses oxalic acid as a medium to deposit polyaniline on carbon steel electrochemically.

### 5.3.2. Optimization of Potential Range

A suitable potential range for electrochemical deposition using cyclic voltammetry should be selected based on the oxidation potential of the monomer and should avoid the electro-dissolution of substrate. Aniline, as the monomer, has a standard oxidation potential  $E^\circ$  of 0.9 V to 1.2 V vs. Ag/AgCl [22, 85]. However, it also depends on the type of acid and substrate used as the medium. For instance, Figure 5.1 shows that aniline oxidation potential was around 0.8 V vs. Ag/AgCl, which lead to the chosen potential range of -0.2 to 1.0 V. Here, two different potential ranges were used: -0.6 V to 1.0 V (Figure 5.7a), and -0.6 V to 1.5 V (Figure 5.7b).

On the forward scan of the first cycle, there was an anodic peak at -0.15 V associated with the iron dissolution in the medium (Figure 5.7a and b). By extending the potential window up to 1.5 V, there was an increase of current at the end of the first forward scan (Figure 5.7b), which apparently was not observed in Figure 5.7a, indicating that the aniline oxidation potential is higher than 1.0 V vs. Ag/AgCl. Compared to the electrochemical deposition of polyaniline

on a graphite electrode, the applied potential to oxidize aniline is much higher. Although a higher applied potential is evidently required, it has also drawbacks concerning the possibility of overoxidation. The effect of overoxidation is however still debatable, as it could further crosslink the polymer, or initiate the opening of polymeric chain [138, 139].



**Figure 5.7.** Cyclic voltammogram of polyaniline/oxalate deposition on carbon steel with a scan rate of 10 mV/s (a) in 0.05 M aniline + 0.1 M oxalic acid, from -0.6 to 1.0 V (b) in 0.05 M aniline + 0.1 M oxalic acid, from -0.6 to 1.5 V vs. Ag/AgCl (c) in 0.1 M oxalic acid, from -0.6 to 1.5 V vs. Ag/AgCl, and (d) the corresponding SEM image after CV with experimental parameters (c).

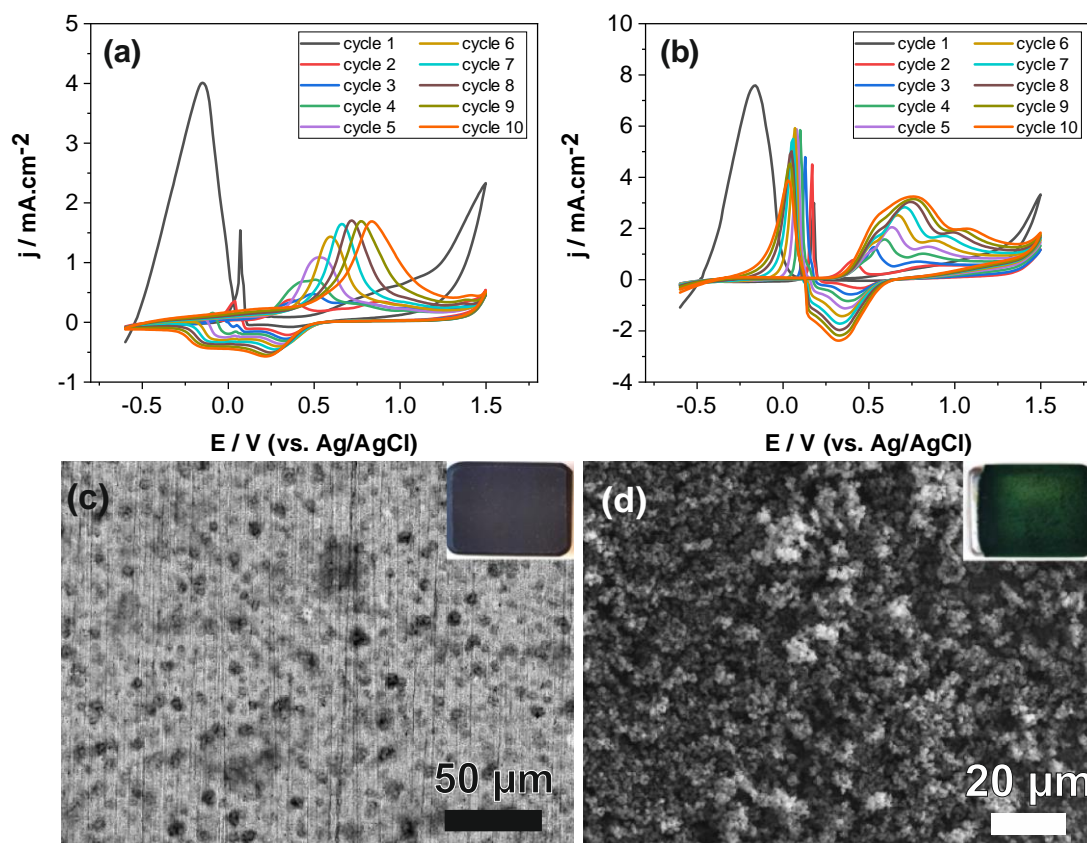
As a control experiment, cyclic voltammetry was applied on carbon steel in 0.1 M oxalic acid without the presence of monomer to assess the redox peaks associated with the reaction between oxalic acid and carbon steel (Figure 5.7c). In the first cycle, the same peak also appears at -0.15 V as observed in the solution with aniline, which is associated with iron dissolution. In the presence of aniline, there was a sharp peak identified at the backward scan at 0.07 V indicating the reactivation of iron oxalate caused by reduction reaction of  $\text{Fe}^{3+}$  to  $\text{Fe}^{2+}$ . This peak was also observed in the oxalic acid medium at 0.19 V and remained at the same potential with lower current density in the second cycle, and stable after the 5<sup>th</sup> cycle (Figure 5.7c). The corresponding surface image of carbon steel after the cyclic voltammetry in oxalic acid medium was acquired by SEM (Figure 5.7d), showing homogeneous formation of iron oxalate. Although iron dissolution peaks appear with almost similar current density in all conditions, the peak of iron oxalate reactivation is dependent on oxalic acid concentration, and whether the monomer is oxidized.

### 5.3.3. Effect of Aniline to Oxalic Acid Ratio

To reveal the effect of monomer/acid ratio and optimize the surface characteristics of the polyaniline coated carbon steel, two different compositions were used in the electrochemical deposition: 0.05 M aniline in 0.1 M oxalic acid (later on mentioned as PANI/oxalate-1), and 0.1 M aniline in 0.3 M oxalic acid (later on mentioned as PANI/oxalate-2). As revealed in the previous section, the optimized potential range for electrochemical deposition is between -0.6 to 1.5 V vs. Ag/AgCl, which is then used here to deposit polyaniline with different monomer to acid ratios. For both compositions, a green color of the electrode was observed at the end of polymerization, which indicates the polyaniline formation in emeraldine state, with a structure as mentioned in Section 2.3.3 [22, 140]. After cleaning thoroughly using water and acetone, it was evident that the deposited layer was stable and adherent to the carbon steel surface.

Although both compositions result in homogeneous and intact layers of polyaniline on carbon steel, the cyclic voltammogram shows different patterns and peak position. Iron dissolution peak, as the first reaction occurs in both solutions, appears at the same potential at -0.15 V followed by monomer oxidation in the first forward scan between 1.2 to 1.5 V. The backward scan shows a sharp characteristic peak of iron oxalate reactivation at around 0.20 V, as also observed in the cyclic voltammogram of carbon steel in oxalic acid (Figure 5.7c). This peak, however, disappears after the first cycle of PANI/oxalate-1 (Figure 5.8a). Whereas at a higher concentration of oxalic acid and aniline as in PANI/oxalate-2, the peak of iron oxalate reactivation is observed at a higher current density for all cycles (Figure 5.8b). These results suggest the importance of iron oxalate reactivation on the continuity of polyaniline formation and growth.

The characteristic peaks of polyaniline are also different, where two oxidation peaks are observed in PANI/oxalate-2, whereas only one oxidation peak is distinctly shown in PANI/oxalate-1. Further characterization using SEM was performed, in which the SEM image shows that polyaniline did not completely cover the entire surface of carbon steel for the composition of PANI/oxalate-1 (Figure 5.8c). On the other hand, the SEM image of PANI/oxalate-2 surface reveals that polyaniline was homogeneously formed and covered the metal surface (Figure 5.8d). Thus, PANI/oxalate-2 was further used to investigate the interaction of polyaniline with the artificial geothermal water.



**Figure 5.8.** Electrochemical deposition using cyclic voltammetry with 10 cycles (a) PANI/oxalate-1 with pores still visible (b) PANI/oxalate-2 (c) SEM image of (a), and; (d) SEM image of (b).

#### 5.3.4. Optimization of Cycle Number

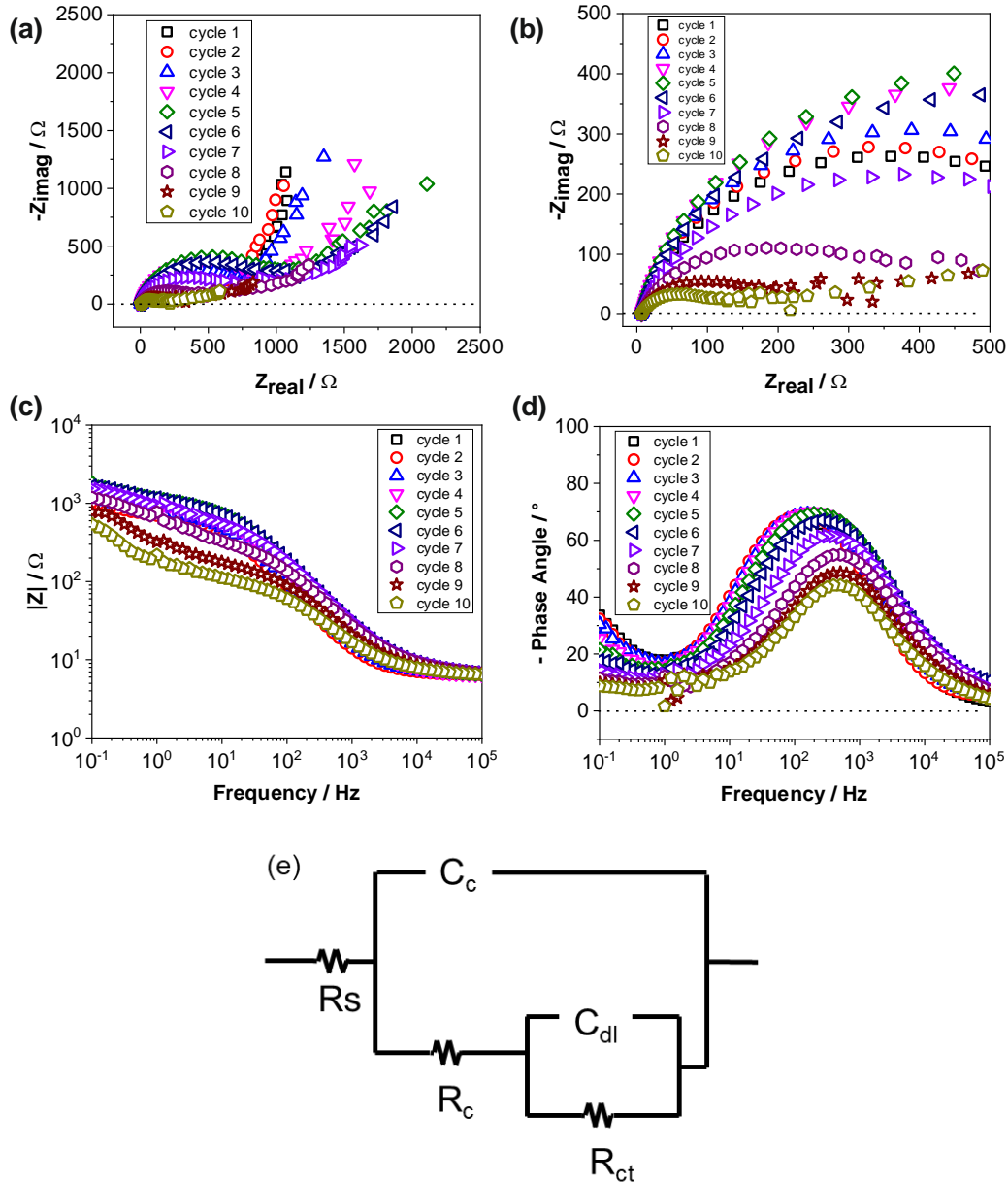
Different cycle numbers were used to investigate the optimum polyaniline structure. To trace the development of electrochemical behavior of polyaniline in each cycle, EIS was applied immediately after each cycle. Unlike the impedance spectra of polyaniline deposition on graphite (Figure 5.1), the impedance spectra show different behavior on the polymerization process, because it involves an active material as the metal substrate. The Nyquist plot shows that in general there are two distinct parts of the curve, which is a capacitive semicircle, followed by a positive slope (Figure 5.9a).

Based on the changing patterns of the Nyquist plot, the whole polymerization process can be divided into two parts, i.e. from the 1<sup>st</sup> to the 5<sup>th</sup> cycle, in which the capacitive semicircle at higher frequency is gradually increase, and from the 5<sup>th</sup> to the 10<sup>th</sup> cycle, where the capacitive semicircle decreases significantly (Figure 5.9b). Both parts of the process, however, share the same characteristic: a decrease of the slope at lower frequencies (Figure 5.9a).

To investigate the absolute impedance value and phase angle with respect to frequency more explicitly, Bode magnitude plot and phase angle plot representation are presented in Figure 5.9c and Figure 5.9d, respectively. The Bode magnitude plot shows that the overall impedance for any cycle number remains around  $10^3 \Omega$ . However, the curves are decreasing from the 6<sup>th</sup> to the 10<sup>th</sup> cycle, indicating a lower resistance on the surface. Phase angle plot shows overlapping curves from cycle 1 to 4 with a peak at  $-70^\circ$  in the mid frequency region (Figure 5.9d). At low frequencies, the phase angle shift to  $-40^\circ$  is related to a diffusion process. From the 5<sup>th</sup> cycle onwards, the peak of phase angle is decreasing which might be associated

with the doping of counter anions from the solution and the increase of polyaniline electrical conductivity.

The Nyquist plot shows that at any cycle number, the slope of the curve at low frequency decreases, which might indicate the change of polyaniline layer properties. In the initial stage, there is more exchange of electroactive species between the film and the electrolyte. Thereupon, the slope of curve at low frequency further decreases indicating the contribution of electrochemical activity within the polyaniline layer, as suggested in Figure 5.2.



**Figure 5.9.** EIS during the polymerization for 10 cycles with an interval of 1 cycle (a) Nyquist plot (b) magnified Nyquist plot between 0-500  $\Omega$  (c) Bode magnitude plot, (d) phase angle plot, and (e) equivalent electrical circuit

Impedance spectra were then fitted to the equivalent circuit with  $R_s$  is solution resistance,  $R_c$  is the coating resistance, and  $R_{ct}$  is charge transfer resistance. Constant Phase Element (CPE) was used instead of a perfect capacitor because of the frequency dispersion or the local surface distribution of reactivity. Here, CPE parameters consist of  $Q$  and  $\alpha$ , which are

representative of a physical system. When  $\alpha = 1$ ,  $Q$  is equal to the perfect capacitor, whereas when  $\alpha = 0$ ,  $Q$  has a value of a perfect resistor. Thus, it is important to note that  $\alpha$  should be between 0.75 and 1.00 to represent capacitance. In this case,  $Q_c$  and  $\alpha_c$  represent the capacitive behavior of the polyaniline layer, whereas  $Q_{dl}$  and  $\alpha_{dl}$  represent the charge transfer resistance. Impedance spectra from 1<sup>st</sup> to 6<sup>th</sup> cycle were fitted to the equivalent circuit in Figure 5.9a, and then presented in Table 5.2. Impedance measured after the 7<sup>th</sup> cycle is no longer satisfactorily fitted to the proposed equivalent circuit, mostly due to some additional processes occurred at the lower frequency. One possibility is that the structure of polyaniline is porous as revealed by SEM (Figure 5.8d), and this might complicate the extraction of physical parameters from the impedance spectra.

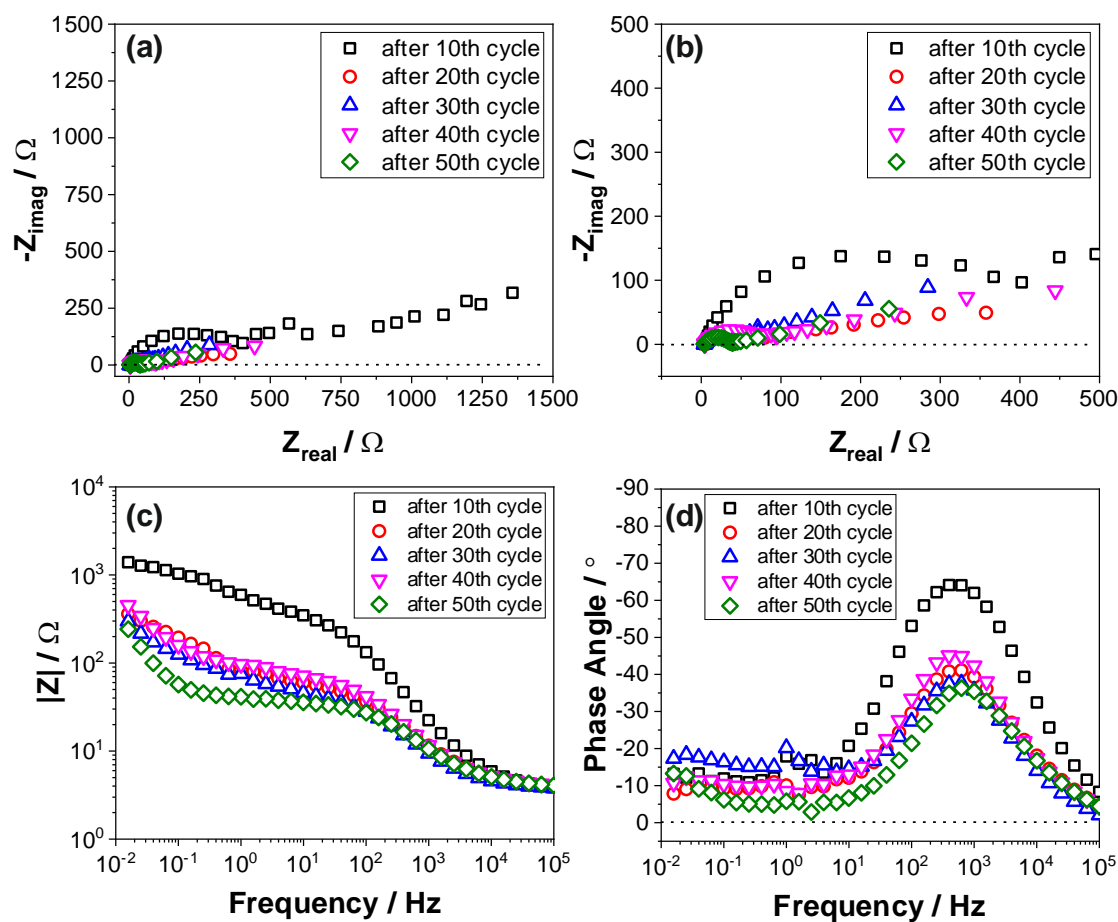
As shown in Table 5.2, the fitting results satisfactorily present that  $\alpha_c$  is between 0.84 and 0.88. On the other hand,  $\alpha_{dl}$  is between 0.49 and 0.73 which might be associated with diffusion processes.

**Table 5.2.** Fitting output of EIS data obtained during the polyaniline deposition on carbon steel

Cycle	$R_s$ ( $\Omega$ )	$R_c$ ( $\Omega$ )	$Q_c$	$\alpha_c$	$R_{ct}$ ( $\Omega$ )	$Q_{dl}$	$\alpha_{dl}$	GoF
1	7	683	4.00E-05	0.86	1.99E+08	0.0019	0.68	1.46E-03
2	6	674	4.14E-05	0.88	4.18E+08	0.0023	0.73	7.74E-04
3	6	735	3.48E-05	0.87	8.74E+06	0.0019	0.68	9.40E-04
4	7	912	2.62E-05	0.87	1.26E+07	0.0016	0.58	1.53E-03
5	7	1021	2.30E-05	0.86	5.67E+03	0.0014	0.59	1.94E-03
6	7	954	2.25E-05	0.84	6.99E+03	0.0014	0.49	3.20E-03
7-10	----- Not applicable -----							

GoF : Goodness of Fit

To further optimize the cycle number and observe the possible progress of the polymerization process, EIS was applied from the 10<sup>th</sup> to the 50<sup>th</sup> cycle with an interval of 10 cycles in a separate experiment. The results show much lower impedance of polyaniline compared to that measured within the first 10 cycles. The Nyquist plot shows a decrease of impedance with the number of cycle (Figure 5.10a and b). The Bode magnitude plot presents a significant decrease of total impedance value after the 20<sup>th</sup> cycle. This value remained stable until the 50<sup>th</sup> cycle (Figure 5.10c). A decrease of phase angle peak was also observed from the 10<sup>th</sup> to the 20<sup>th</sup> cycle, which remained stable with a phase angle of  $-45^\circ$  (Figure 5.10d). Although the cyclic voltammogram after 50 cycles showed different behavior than that obtained after 10 cycles, the electrochemical behavior of polyaniline on carbon steel is relatively the same, as confirmed by all data representations of impedance spectra.

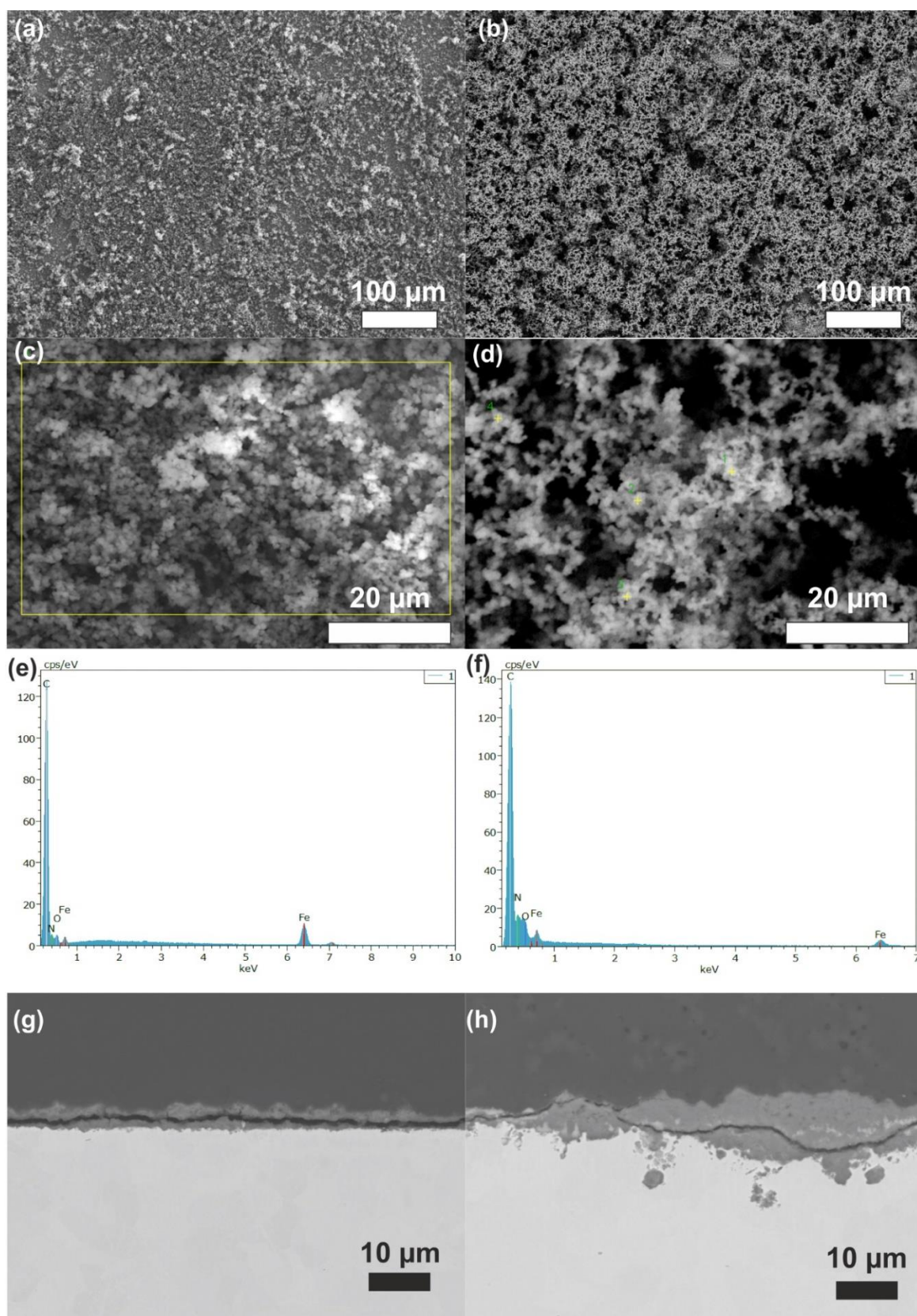


**Figure 5.10.** EIS during the polymerization between 10<sup>th</sup> – 50<sup>th</sup> cycles with an interval of 10 cycles (a) Nyquist plot, (b) magnified Nyquist plot, (c) Bode magnitude plot, and (d) phase angle plot.

Surface characterization was performed after the electrochemical deposition of polyaniline of carbon steel after 10 and 50 cycles. SEM images of the surface show that after 10 CV cycles polyaniline was homogeneously formed (Figure 5.11a). A further polymerization with 50 cycles resulted in the growth of polymeric chains, however, with higher porosity than that observed after 10 cycles (Figure 5.11b). A higher magnification of SEM images show that polyaniline was formed as interconnected particles with a size below the micrometric scale (Figure 5.11c). After polarizing for 50 cycles, polyaniline continued growing (Figure 5.11d)

EDX spectra revealed that the elemental composition of the selected surface consisted of Fe, C, O, and N after 10 and 50 cycles (Figure 5.11e and f). The elements C, O, and N correspond to oxalate-doped polyaniline, whereas Fe might be associated with the carbon steel as the substrate since the EDX spectrum is usually attained at 1 – 3  $\mu\text{m}$  below the analyzed surface [141]. The cross section image shows that after 10 cycles, polyaniline layer thickness was about 7  $\mu\text{m}$  (Figure 5.11g). An increase of cycle number to 50, although results in a thicker polyaniline layer, does cause localized corrosion, which might be due to the overoxidation since the applied potential is relatively high. Furthermore, the characteristic porous layer of polyaniline allows the acidic medium to attack the metal surface. Based on these results, further experiments were conducted using 10 cycles of CV.





**Figure 5.11.** Characterization of polyaniline/oxalate coated carbon steel after 10 cycles (a,c,e,g) and after 50 cycles (b, d, f, h). Higher SEM magnification presenting the morphology of polyaniline/oxalate (c and d). The EDX spectra (e and f) show the elemental composition of (c and d), respectively. Cross sectional images are also presented (g and h).

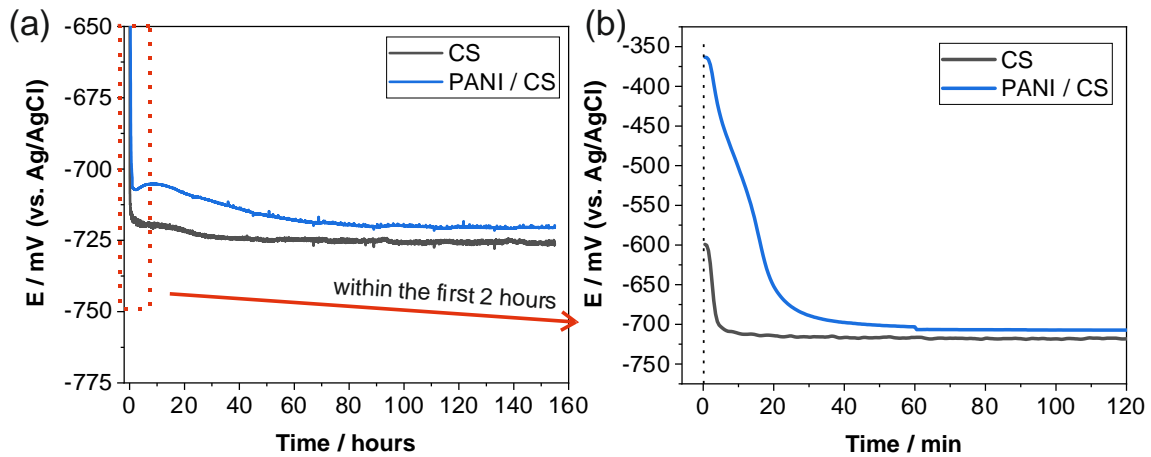


#### 5.4. Electrochemical Behavior of PANI-coated Carbon Steel in the Geothermal Solution

Electrochemical measurements were performed at room temperature and 150 °C to observe the electrochemical behavior of carbon steel and polyaniline coated carbon steel in the artificial geothermal water with and without the effect of high temperature. Polyaniline coated carbon steel was synthesized using the composition of PANI/oxalate-2, with 10 cycles of CV, which is hereafter mentioned as PANI/CS. The measurements include OCP and EIS, followed by surface analysis using SEM-EDX.

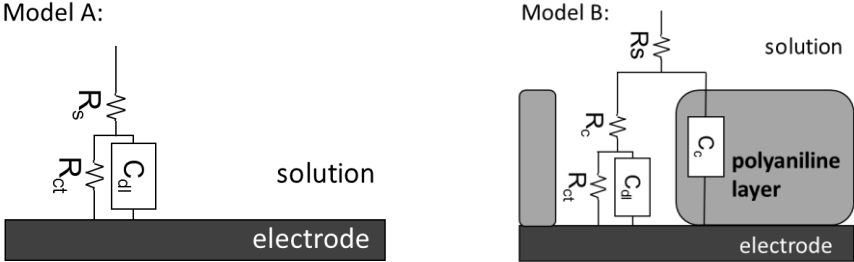
##### 5.4.1. Electrochemical Test at Room Temperature

$E_{\text{corr}}$  was measured at room temperature to investigate the free corrosion potential of polyaniline coated carbon steel in the artificial geothermal water. All experiments were performed in an Ar-saturated solution to avoid the anodic reaction caused by oxygen. In the initial stage of the reaction, PANI/CS has a higher potential of -250 mV than that of carbon steel (-600 mV). However, the free corrosion potential decreases significantly within 30 minutes after the first contact of specimens with the electrolyte.  $E_{\text{corr}}$  was stable for all specimens after 1 hour of exposure, which is about 20 mV more positive than the carbon steel free corrosion potential (Figure 5.12b).

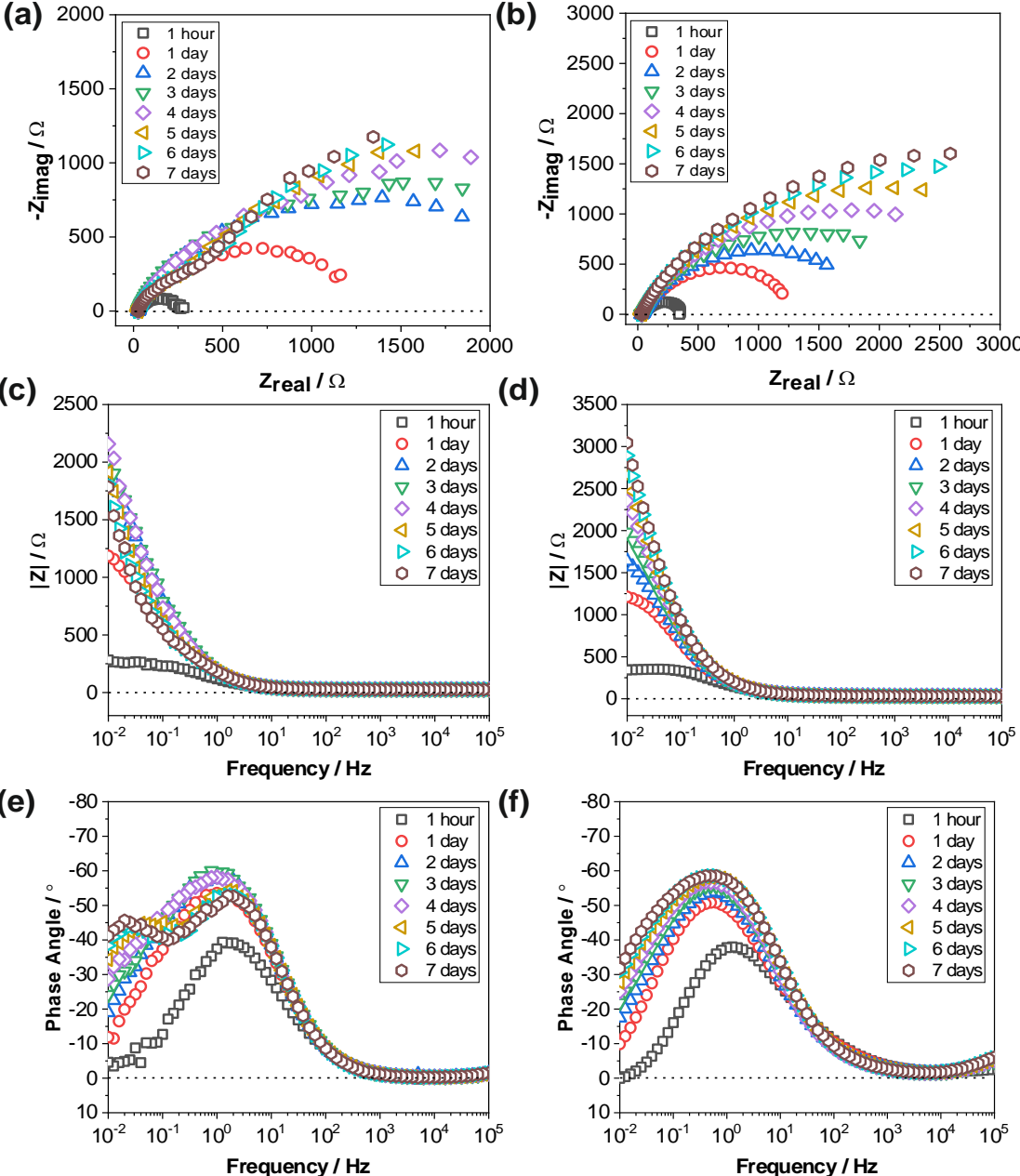


**Figure 5.12.**  $E_{\text{corr}}$  of carbon steel (CS) and PANI/CS in artificial geothermal water at room temperature (a) 0 – 7 days, and (b) 0 – 2 hours.

To further observe the surface-interface interaction between the uncoated or coated carbon steel and the artificial geothermal water for seven days, EIS was applied after 1 hour and after each day of exposure. The Nyquist plot of PANI/CS has a different pattern compared to that of carbon steel starting from the 4<sup>th</sup> day.



**Figure 5.13.** Equivalent electrical circuit for EIS data fitting of carbon steel and coated carbon steel (PANI/CS) in the artificial geothermal water at 25 °C



**Figure 5.14.** Impedance spectra after the specimen was exposed to artificial geothermal water at room temperature. Nyquist plot of (a) carbon steel, (b) PANI/CS; Bode magnitude plot of (c) carbon steel, (d) PANI/CS; phase angle plot of (e) carbon steel, (f) PANI/CS

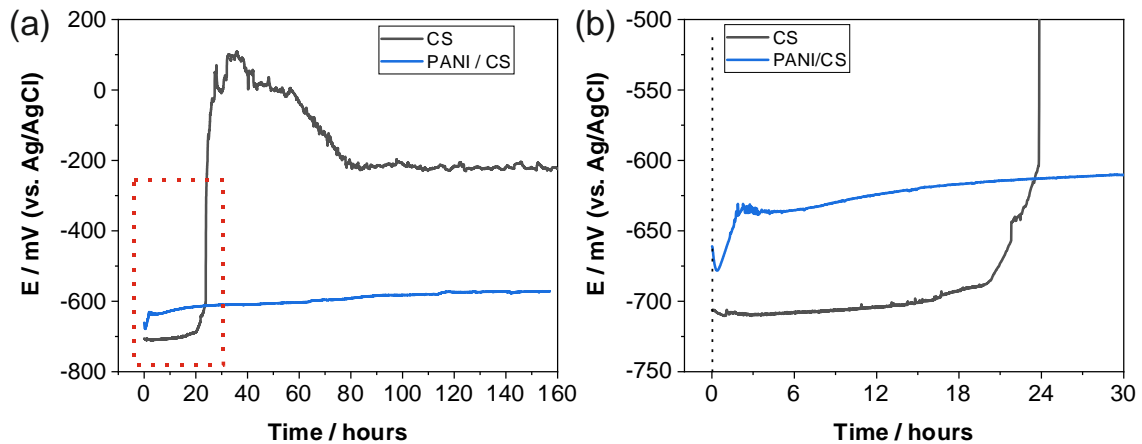
**Table 5.3.** Fitting output of impedance spectra of the PANI/CS exposed to the artificial geothermal water at room temperature.

Day	Model	$R_s$	$R_{ct}$	$Q_{dl}$	$\alpha_{dl}$	$R_c$	$Q_c$	$\alpha_c$	GoF
1	B	33	1307	0.0009	0.77	35.86	0.0007	0.76	1.74E-04
2	B	33	1932	0.0006	0.78	21.12	0.0010	0.72	5.22E-05
3	A	34	2513	0.0015	0.74				3.40E-04
4	A	34	3108	0.0014	0.74				2.85E-04
5	A	31	3708	0.0014	0.74				3.89E-04
6	A	31	4192	0.0014	0.74				4.12E-04
7	A	32	4604	0.0014	0.74				4.23E-04

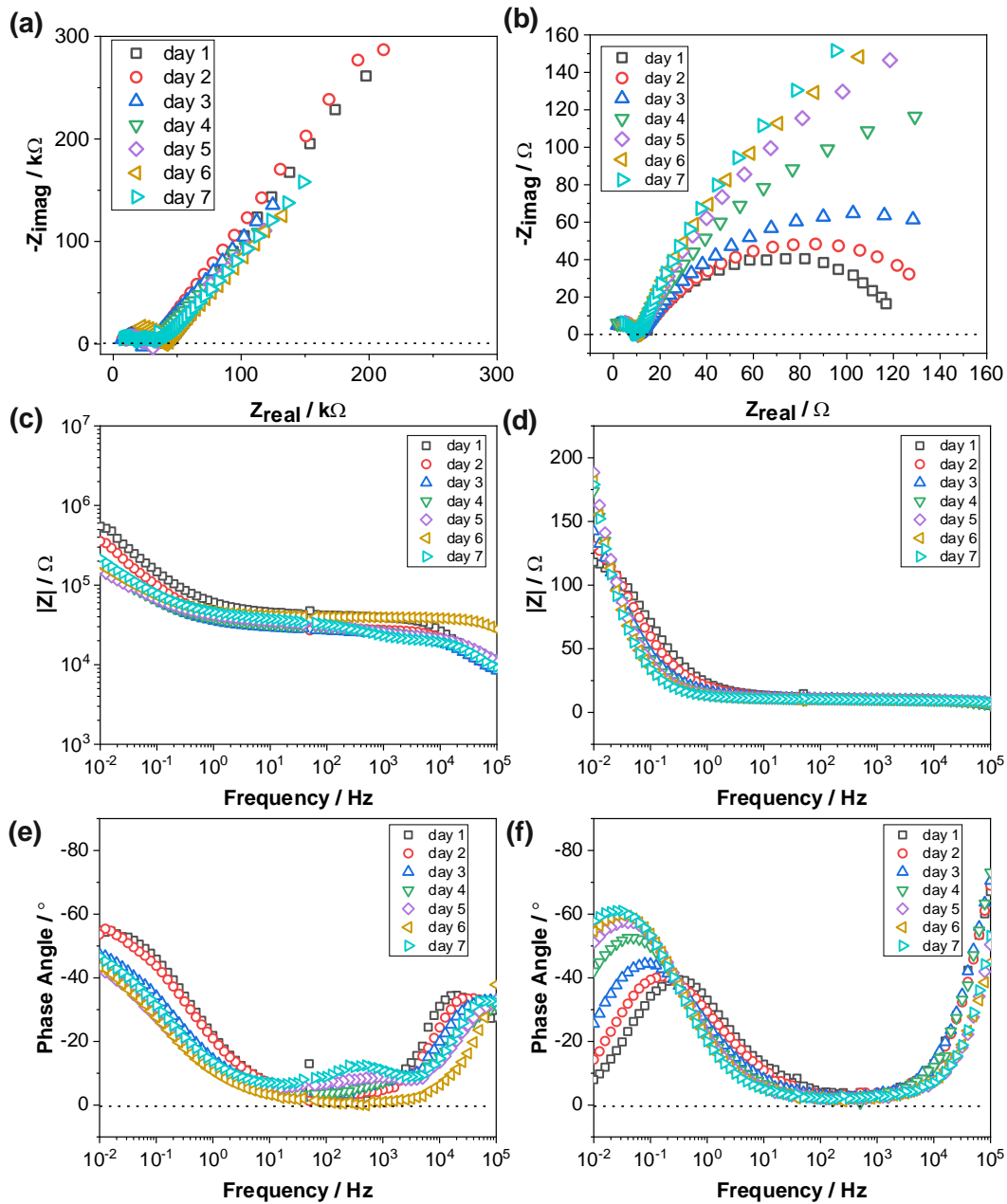
GoF : Goodness of Fit

#### 5.4.2. Electrochemical Test at 150 °C

$E_{corr}$  was measured at 150 °C to investigate the free corrosion potential of polyaniline coated carbon steel in the artificial geothermal water at higher temperature. During seven days of exposure,  $E_{corr}$  of carbon steel shows a much higher potential compared to PANI/CS after about 24 hours indicating that carbon steel is more passive than PANI/CS (Fig. 5.12a). Within the first 24 hours carbon steel has a lower free corrosion potential, which might be associated with the iron dissolution. However, carbon steel then corroded uniformly, forming a corrosion product layer which has a quasi-passive behavior. On the other hand,  $E_{corr}$  of PANI/CS is stable during the immersion, which requires further analysis using surface characterization and EIS.


**Figure 5.15.**  $E_{corr}$  of carbon steel (CS) and PANI/CS in artificial geothermal water at 150 °C (a) 0 – 7 days (b) 0 – 30 hours.

Impedance spectra show that polyaniline coated carbon steel exposed to the artificial geothermal water at 150 °C has low corrosion resistance. Compared to the impedance spectra measured at room temperature, the impedance value is about 20 times lower, indicating that polyaniline coated carbon steel is not suitable for use at 150 °C.

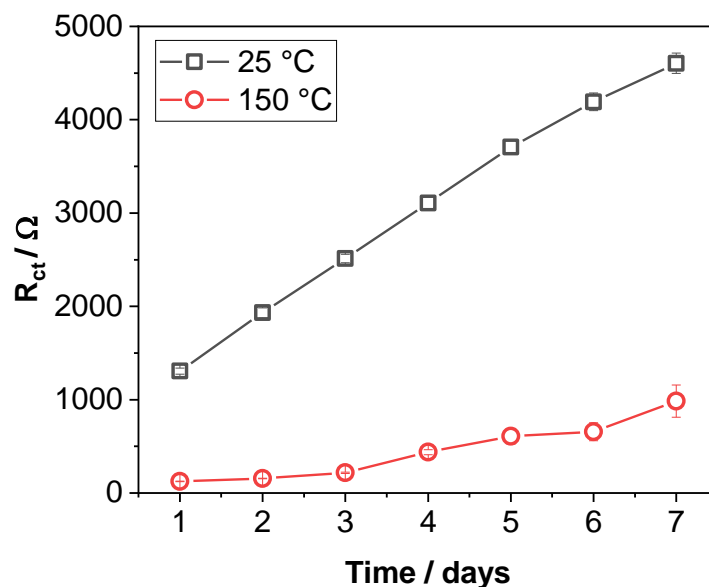


**Figure 5.16.** Impedance spectra after specimen was exposed to the artificial geothermal water at 150 °C: Nyquist plot of (a) carbon steel, and (b) PANI/CS; Bode magnitude plot of (c) carbon steel, and (d) PANI/CS; phase angle plot of (e) carbon steel, and (f) PANI/CS

**Table 5.4.** Fitting output of impedance spectra of PANI/CS exposed to the artificial geothermal water at 150 °C.

Day	Model	$R_s$	$R_{ct}$	$Q_{dl}$	$\alpha_{dl}$	$R_c$	$Q_c$	$\alpha_c$	GoF
1	A	11.3	125.2	0.016	0.72				1.83E-03
2	A	11.3	156.2	0.022	0.70				4.60E-04
3	A	10.9	217.2	0.031	0.71				5.19E-04
4	A	11.0	438.0	0.038	0.74				4.35E-04
5	B	10.1	608.2	0.034	0.79	1.556	0.0076	0.76	3.34E-04
6	B	10.1	656.1	0.030	0.80	2.365	0.0175	0.83	4.78E-05
7	B	9.5	984.7	0.046	0.80	1.394	0.0030	0.76	2.62E-04

GoF : Goodness of Fit

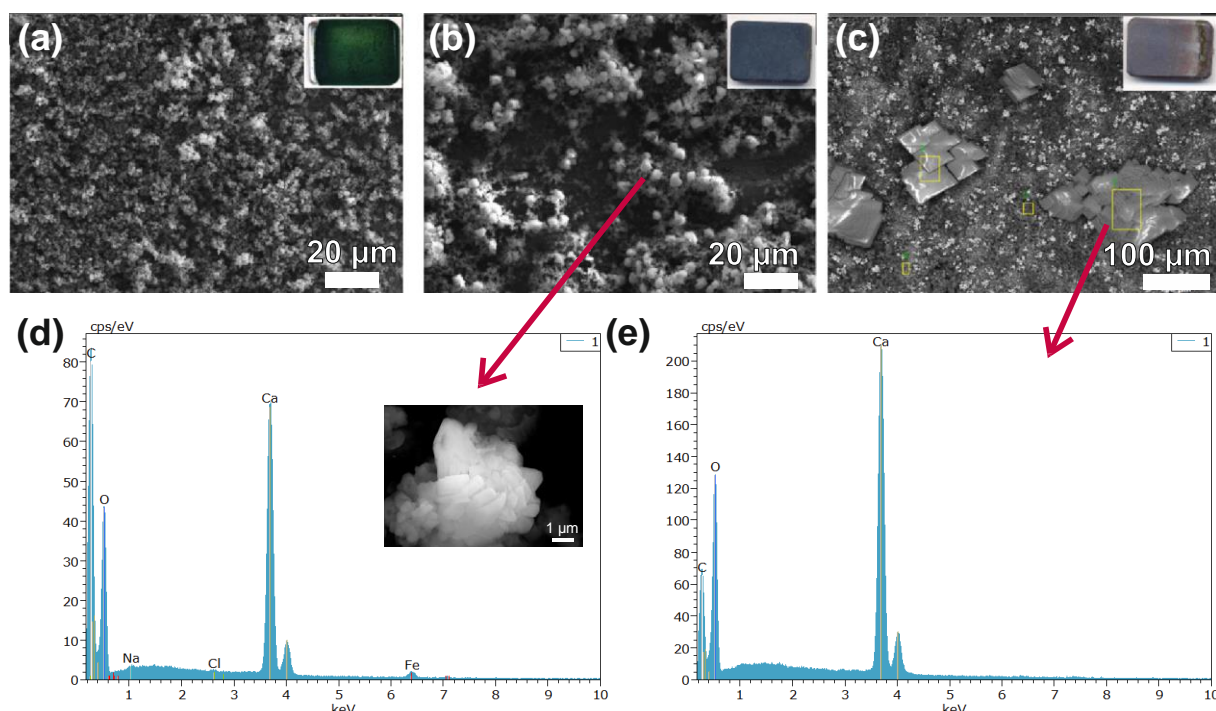


**Figure 5.17.**  $R_{ct}$  of PANI/CS as a function of time at room temperature and at 150 °C. Error bars indicate the error value of  $R_{ct}$  from the fitting of impedance spectra.

#### 5.4.3. Surface Morphological Characterization

By visually assessing the surface of specimens after being exposed to the artificial geothermal water, the color of the polyaniline layer on carbon steel was darker than at the initial condition (as inserted in Figure 5.18). SEM images revealed that after exposed to the artificial geothermal water at room temperature, the morphological structure of polyaniline slightly changed (Figure 5.18b), compared to the initial condition (Figure 5.18a), in which some particles were deposited on the surface. After exposed at 150 °C, there were larger particles deposited on the surface (Figure 5.18c).

To identify the particles observed by SEM and the transformation of polyaniline morphological structure after the exposure test, EDX analysis was performed. As mentioned previously, the EDX spectra of PANI/CS at the initial condition revealed that the constituent elements of PANI/CS specimen are Fe, C, N, and O, which is attributed to the pure oxalate-doped polyaniline, with Fe as the substrate (Figure 5.11e). After exposed to the artificial geothermal water at room temperature for seven days, there was a small amount of Na and Cl detected, and a significant amount of Ca (Figure 5.18d). At 150 °C, larger particles were deposited on the surface with the identified elements of Ca, C, and O (Figure 5.18e). This suggests that there is an intrusion of ionic species of the artificial geothermal water, e.g.  $\text{Na}^+$ ,  $\text{Ca}^{2+}$ , and  $\text{Cl}^-$  into the polyaniline layer, regardless the temperature. At a higher temperature, however, the contact between polyaniline layer and the artificial geothermal water leads to a formation of  $\text{CaCO}_3$ .



**Figure 5.18.** SEM images of polyaniline/CS (a) at initial condition (b) after exposed to room temperature (c) after exposed to 150 °C. EDX of polyaniline/CS after exposed to the geothermal water (d) at room temperature (e) at 150 °C.

## 5.5. Conclusion

Based on the experimental results, the EIS fitting results of polyaniline on graphite electrode indicated that there is an exchange of electroactive species within the polyaniline layer, instead of a simple exchange through the layer with the bulk electrolyte, which is the artificial geothermal water. The effect of the reaction between polyaniline coated carbon steel and the artificial geothermal water was revealed by SEM-EDX analysis of the specimen's surface after exposure for seven days at 25 °C and 150 °C, where Ca was detected in both conditions. This suggests that there is an interaction of ionic species, such as  $\text{Cl}^-$ ,  $\text{Na}^+$ ,  $\text{Ca}^{2+}$  from the artificial geothermal water to the PANI/CS, regardless of the temperature. The morphological structure of PANI/CS after exposed at room temperature is homogeneous and does not show any indication of corrosion. The polyaniline layer has a porous structure as observed by SEM image and suggested by EIS data interpretation. The porous structure allows the electrolyte to penetrate through the layer. Based on these observations, the protection mechanism of polyaniline is not solely as the physical barrier layer, but rather associated with the redox mediated properties of polyaniline which selectively allow the ionic species intrusion from the electrolyte into the polyaniline layer.

At a higher temperature,  $\text{Ca}^{2+}$  further reacted and formed larger particles of  $\text{CaCO}_3$ , which may cause a scaling problem in real conditions, usually caused by  $\text{CaCO}_3$  and  $\text{CaCl}_2$  deposition on the surface. In addition, it is thermally not stable as presented by the visual observation and SEM image. Based on these results, another approach to utilize polyaniline with a better functionality was chosen and investigated by dispersing polyaniline in alkyd based polymeric matrix.

# Chapter 6. Synthesis and Characterization of Polyaniline and Silicon Dioxide Composite Coatings

The alkyd-based primer coating, also mentioned as binder, has been used as the main polymeric matrix on carbon steel in marine industrial applications. Before modified by the additional active pigments, this binder was used as a standalone coating material and was exposed to geothermal water to reveal its role in corrosion process. In this chapter, polyaniline and silicon dioxide were synthesized, and used as pigments added into the alkyd-binder to produce a binary component coating on carbon steel. Silicon dioxide was obtained from the natural sand in Indonesia, as the locally available resource, which was then purified and used as pigments. The coating systems, i.e. PANI-alkyd and SiO<sub>2</sub>-alkyd, were then tested in the artificial geothermal water to investigate the suitability and functionality of polyaniline and silicon dioxide as anticorrosion pigments.

## 6.1. Alkyd-Based Matrix

### 6.1.1. Chemical and Morphological Characterization

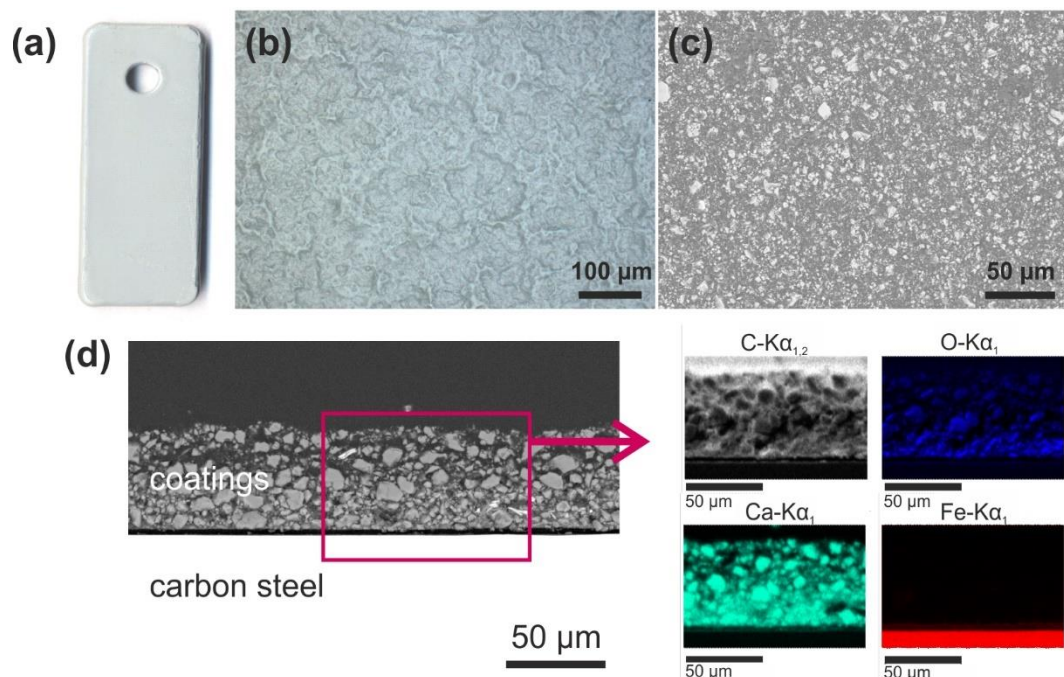
The polymeric matrix used in these experiments was based on an alkyd coating which is locally available in Indonesia. As discussed in subchapter 2.3.2, alkyd-based coating has a good adhesion behavior with a metal substrate. However, nowadays it is mostly utilized for corrosion protection in atmospheric conditions instead of in immersion condition because it is susceptible to degradation when in contact with water [81]. Since alkyd is one of the most applicable coating in the class of organic coating which offers an easy application and is affordable compared to other polymeric matrices, a modification of alkyd was implemented to improve its physical and chemical properties for protection of carbon steel in the geothermal application.

Morphological characterization of commercial alkyd as single coating layer on carbon steel was performed by macro/microscopic photography and SEM as presented in (Figure 6.1a-c), followed by elemental analysis using EDX on the cross-sectioned specimen (Figure 6.1d). To reveal the functional groups FTIR analysis was conducted and presented in Figure 6.2.

It is evident from the SEM image of the cross section under the BSE mode that the alkyd coating layer comprises of heavier elemental components represented by the brighter area, surrounded by the polymer matrix as the darker area. To further analyze the elemental distribution of the filler within the coating, a cross section of a representative specimen was made by embedding the specimen in epoxy resin. The filler distributed homogeneously within the coating, with a wide range of particle sizes in the micrometer scale. The elemental mapping using EDX shows that Ca was predominant, suggesting a common compound used as filler, i.e. CaCO<sub>3</sub>. It is common to have CaCO<sub>3</sub> as filler in the coating to lower the production cost of coatings, and this type of filler is also known as extender [77]. CaCO<sub>3</sub> pigments have a low oil



absorptions and low specific gravity, which allow them to take up a larger volume without using much binder [142].

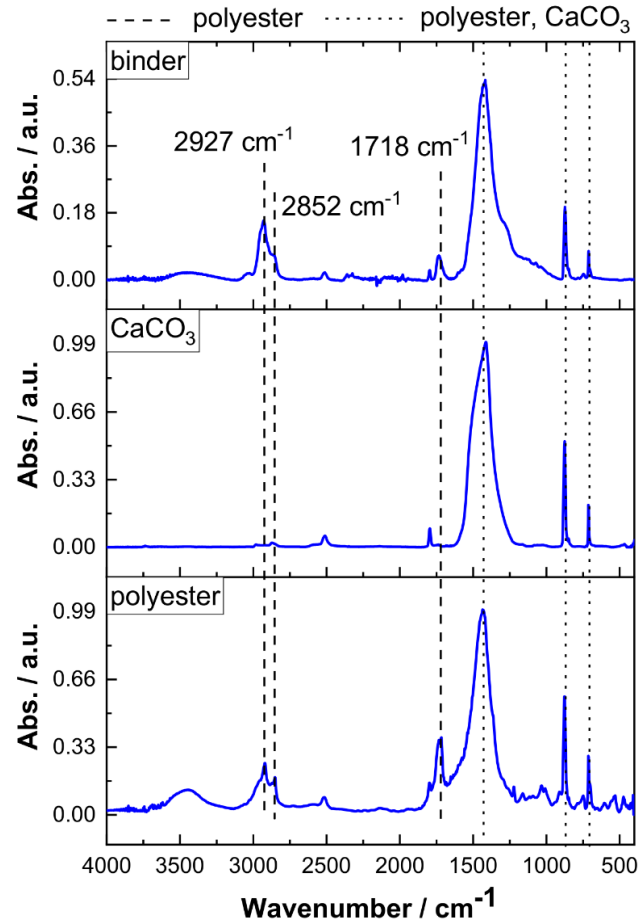


**Figure 6.1.** Characterization of alkyd binder as the primer and its application on carbon steel (a) macrophoto (b) optical microscope (c) SEM with BSE mode, and (d) SEM-EDX of the cross section.

To confirm the functional group of the polymeric matrix and the type of filler in the coating, the specimen was analyzed using ATR-FTIR. Alkyd binder is polyester modified by the addition of fatty acids, usually derived from polyols and a dicarboxylic acid and/or carboxylic acid anhydride. Based on the above elemental identification of  $\text{CaCO}_3$  as the main filler in the coatings, FTIR spectra of the alkyd coating were compared with the reference spectra of  $\text{CaCO}_3$  and thermoplastic polyester elastomer obtained from the FTIR spectra library of Omnic Software, showing good agreement in peak position and intensity (Figure 6.2).

Peaks of polyester might originate from esters and carboxylic acid, where the possible absorption peak assignment is listed in Table 6.1. At  $3440\text{ cm}^{-1}$  there is a broad peak which is associated with the hydroxyl group. Other characteristic peaks of alkyds are at  $2927$ ,  $2852$ , and  $1465\text{ cm}^{-1}$ , which are related to (C-H)  $\text{CH}_2$  asymmetric and symmetric stretching, and bending, respectively [143]. At around  $1718\text{ cm}^{-1}$ , there is a strong peak associated with C=O stretching. Additionally, alkyd has absorption peaks around  $1256$  and  $1120\text{ cm}^{-1}$  due to C-O stretching of ester. Since the alkyd-based binder is containing  $\text{CaCO}_3$ , there are some combinational peaks of alkyd and  $\text{CaCO}_3$ . However, three peaks of polyester do not overlap with the  $\text{CaCO}_3$  absorption peaks which can be used to specify the degradation of the binder, i.e. at  $2927$ ,  $2852$ , and  $1718\text{ cm}^{-1}$ .





**Figure 6.2.** FTIR spectrum of alkyd coating compared to the reference spectra of  $\text{CaCO}_3$  and polyester.

**Table 6.1.** FTIR peak assignment to the functional group of esters [112, 143].

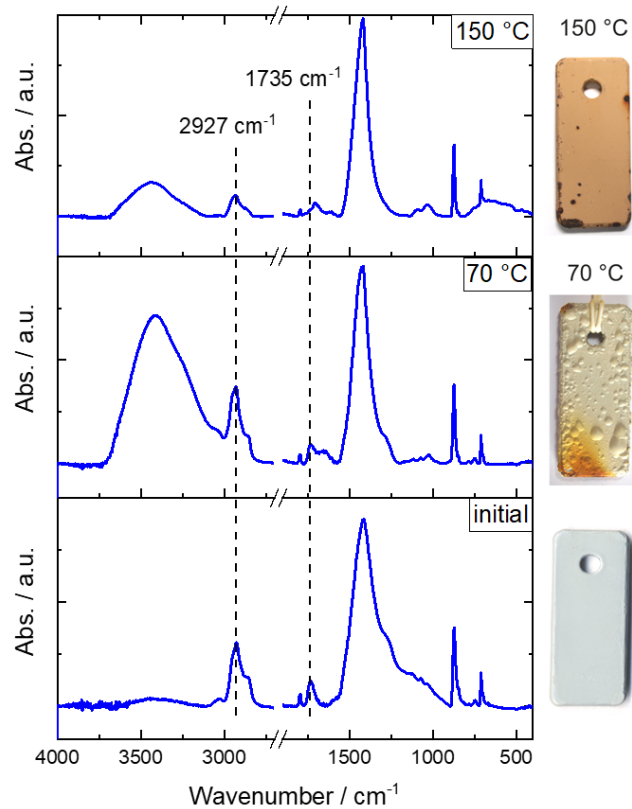
Assignment	Wavenumber ( $\text{cm}^{-1}$ )		
	Reference	Polyester Ref.	Binder
(C-H) $\text{CH}_2$ asymmetric stretch	$2926 \pm 10$	2934	2927
(C-H) $\text{CH}_2$ symmetric stretch	$2855 \pm 10$	2849	2852
Aromatic C=O stretching	1730 – 1705	1716	1718
$\text{CH}_2$ scissors	$1455 \pm 10$	1469	1465
Aromatic C-O stretching	1310 – 1250	1270	1256
Aliphatic C-O stretching	1300 – 1100	1270, 1249, 1122	1256, 1120

### 6.1.2. Exposure Test in the Artificial Geothermal Water at Different Temperatures

In general, temperature may affect the properties of coatings due to the change in the thermal stress balance between coating and substrate, the mechanical properties of coatings, and the barrier properties of the coatings [81]. To study the suitability of alkyd-based coatings for the artificial geothermal water at different temperatures, the alkyd-coated carbon steel specimens were exposed to 70 °C and 150 °C in aerated artificial geothermal water. After 7 days, at 70 °C, blister formation resulting in filiform corrosion was observed as shown in Figure 6.3. Whereas at 150 °C, there were some black spots observed on the surface of the coatings. Furthermore, there was a possible chemical degradation indicated by the discoloration of specimen.

The FTIR spectra of binder before and after exposure at 70 °C and 150 °C for 7 days are also shown in Figure 6.3. There was an increase of a broad peak between 3100 – 3700  $\text{cm}^{-1}$ ,

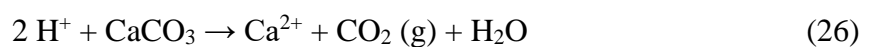
indicating O-H stretching bond of water. As the coating was used for immersion purpose, there is water uptake for both specimens exposed to 70 °C and 150 °C. The water absorption within the coating may lead to the coatings failure because it remains located within microcracks, microvoids, and local delamination sites [144]. There is also a significant difference observed at 1735 and 2927 cm<sup>-1</sup>, indicating the change of the C=O stretching and C–O stretching. This characteristic peak was observed at the initial condition and at 70 °C, which reduces after the exposure at 150 °C, thus evidently shows that the degradation was more severe at a higher temperature.



**Figure 6.3.** FTIR spectra of binder before and after exposed to the aerated geothermal solution at 70 °C and 150 °C, and the corresponding images of specimens.

Blistering is a sign of failure in the coating-substrate system. It occurs when water or ions penetrate through the coating and accumulate at the coating-metal interface. There are two types of blistering, i.e. alkaline and neutral blistering [81]. Alkaline blistering occurs when cations migrate to the cathodic area at the coating-metal interface via coating defects, including pores and scratches, whereas neutral blistering usually occurs in the neutral or weak acidic medium.

Here, the coating system has CaCO<sub>3</sub> as filler which reacts with the acidic solution, leading to the release of CO<sub>2</sub> as a gas phase:



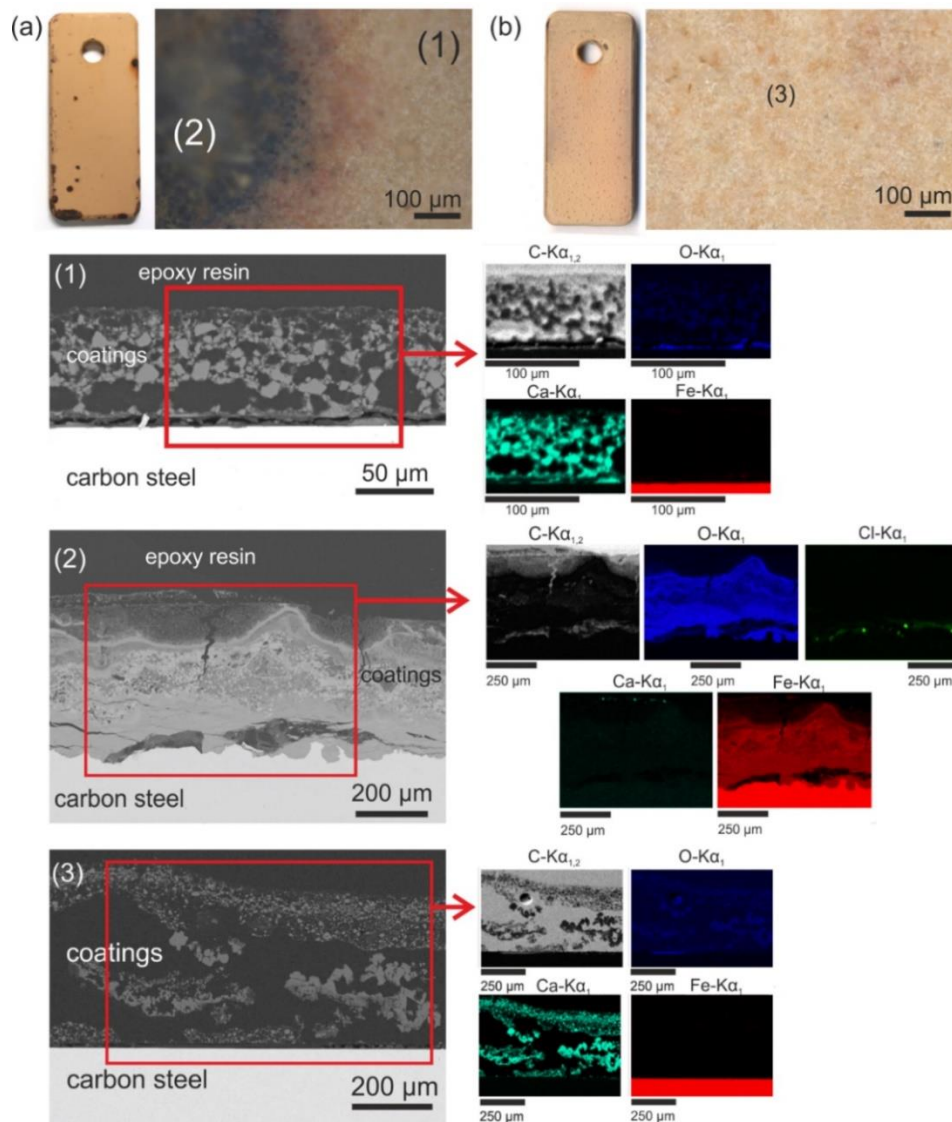
Water absorption to the metal substrate will induce corrosion, as mentioned in equation (23):



## 6.1.3. Alkyd Coating Stability in the Oxygen-Containing Solution at 150 °C

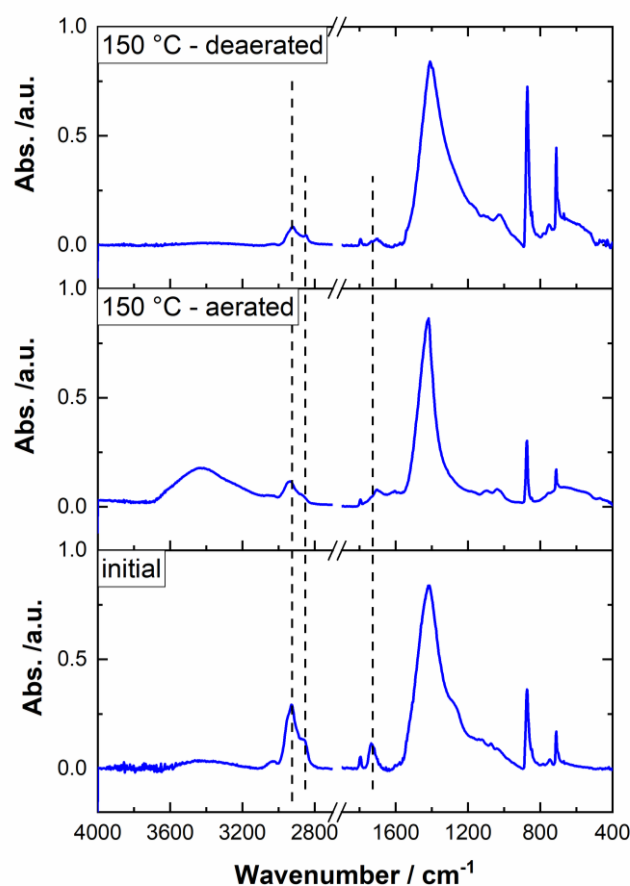
The specimens were exposed to the deaerated solution at 150 °C to distinguish the degradation caused by the oxygen content of the solution. The macroscopic images show that in the deaerated solution, there were no black spots identified, albeit there were some blisters on the surface (Figure 6.4).

BSE images of the cross sections showed that there are different structures of coating components in different areas. Element mapping of the remaining intact coating area after exposed to the aerated solution (1) shows that the substrate is protected from corrosion, and the fillers are still occupying the coating, although not as dense as in initial condition (Figure 6.1d). The darker/black section of the coating after exposed to the aerated solution (2) shows that the section with defect is iron oxide, with small intrusion/diffusion of Cl between the substrate and the oxide. Under the absence of oxygen (deaerated solution), the remaining intact coating (3) is protective to carbon steel substrate, although there is a tendency of the filler to migrate to the surface of coatings.



**Figure 6.4.** Characterization of alkyd-based coatings using macro-photo and optical microscope: (a) after exposed to the aerated geothermal solution at 150 °C for 7 days (b) after exposed to the deaerated geothermal solution at 150 °C for 7 days. Back-scattered electron images and EDX elemental mapping of the cross sections were used to identify the element distribution within the selected areas (1), (2), and (3).

The peak at  $1735\text{ cm}^{-1}$  of C=O stretching shifted after the exposure at  $150\text{ }^{\circ}\text{C}$  for 7 days. Another peak at  $2927\text{ cm}^{-1}$  of C-H stretching which has lower absorption intensity after the exposure at  $150\text{ }^{\circ}\text{C}$  for 7 days both in aerated and deaerated solution (Figure 6.5). Thus, FTIR spectra suggest that the chemical degradation of the coating is mainly caused by the temperature, rather than the aeration. However, the optical microscope and SEM images revealed that in the aerated condition there is a degradation at random points on the surface, which might be associated with the differential aeration on the surface. Beside these alkyd characteristic peaks, the OH peak at  $3400\text{ cm}^{-1}$  increases in the case of the specimen that exposed to aerated solution, suggesting that the water adsorption occurred favorably in aerated conditions. As the result, the metal under the water might not have access to oxygen compared to the adjacent surface, a local electrochemical cell was formed where the oxygen-rich blister is more cathodic [145].

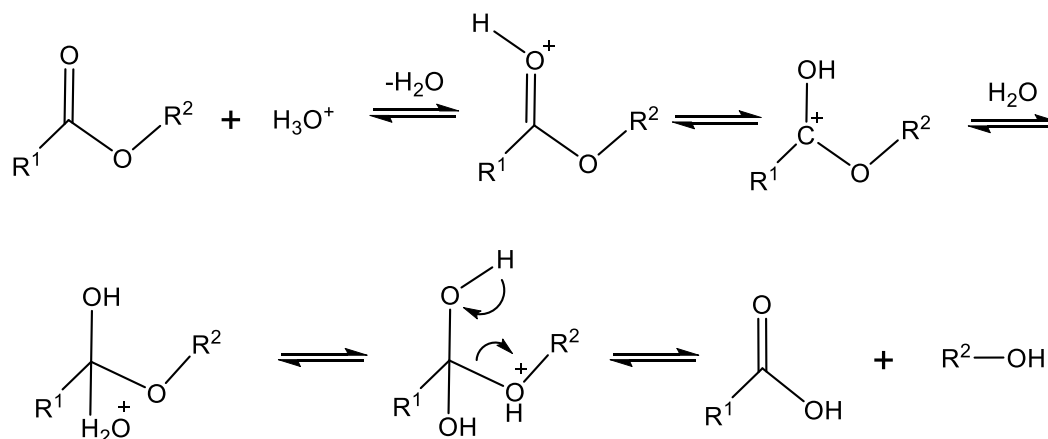


**Figure 6.5.** FTIR spectra of binder before (bottom) and after (upper) exposed to the deaerated and aerated geothermal solution at  $150\text{ }^{\circ}\text{C}$ .

Polymer degradation is the physical and/or chemical changes during the usage of the material, which lead to the loss of some useful properties [146]. Some common processes that lead to these changes are thermal, thermoxidative, light- or radiation-induced, and chemodegradation in the aggressive medium [146], e.g., a variety of chain-radical, ionic, or molecular reactions. In order to suppress or slow down polymer degradation, some chemical and physical changes/modifications need to be implemented.

The characterization results of alkyd-based coatings after exposed to the artificial geothermal water show several significant influencing parameters that play a role in the

degradation processes, such as chemical, thermal, and thermoxidative degradation. Chemical degradation in the coating might be associated with the reaction of the alkyd-coated specimen with the electrolyte. In general, the ester group in the alkyd binder will undergo hydrolysis when it is in contact with acid or base, possibly continuing at a very slow rate at a neutral pH. Since the electrolyte has a pH of 4, there is a possibility of alkyd binder degradation by acid catalyzed ester hydrolysis, with a mechanism presented in Figure 6.6. A fast reaction in the initial stage might contribute to the macromolecular degradation, which slows down when the electrolyte is neutralized. After seven days of, the artificial geothermal water had an almost neutral pH of 6.5.

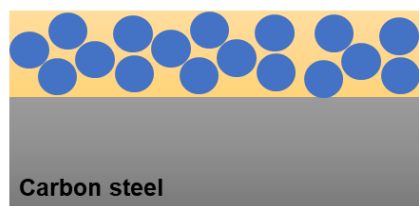


**Figure 6.6.** Mechanism of acid catalyzed hydrolysis of ester [147]

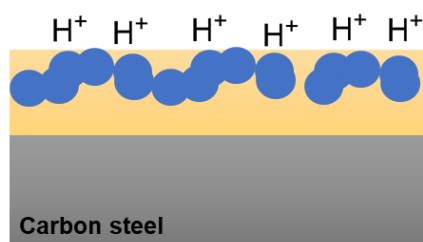
In addition to the chemical degradation, thermal degradation is another concern in this research, since the coated specimen will be used for high temperature purpose. By comparing macroscopic images of specimens after being exposed to 70 °C and 150 °C, it was observed that there was a discoloration of specimens after being exposed at 70 °C and 150 °C when compared to the initial condition. Based on the FTIR spectra, the thermal degradation is also confirmed to occur at a higher temperature than at 70 °C, as shown in Figure 6.4.

When oxygen is present in the solution, there is a possibility of thermoxidative degradation, which is a combination of degradation caused by the temperature and the presence of oxygen as revealed by SEM-EDX of cross sections in Figure 6.4. After the coating-breakdown, there is a possibility that some ionic species (e.g.  $\text{Cl}^-$ ) migrate and react with the carbon steel substrate. A schematic degradation process of alkyd-based coating is presented in Figure 6.7. Alkyd-based coating containing  $\text{CaCO}_3$  is not suitable for use at 150 °C with or without the presence of oxygen, unless it is modified with a stabilizing agent.

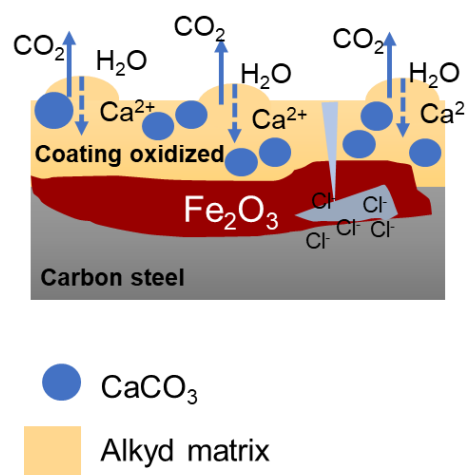
1) **Initial condition:** binder containing alkyd matrix and  $\text{CaCO}_3$  fillers



2) **Interaction with matrix and filler:** acid catalyzed hydrolysis of matrix, and fillers are floating to near surface



3) **Blistering:** reaction between  $\text{H}^+$  and  $\text{CaCO}_3$  might lead to blisters and coating breakdown because of the release of  $\text{CO}_2$



**Figure 6.7.** Illustration of degradation processes of alkyd as a polymeric matrix coating on carbon steel in the geothermal solution.

By comparing the FTIR spectra of binder exposed to  $150\text{ }^\circ\text{C}$  in the aerated and deaerated solution, and assessing the three characteristic peaks of alkyd, it can be concluded that the binder is chemically unstable for a high temperature operation both in aerated and deaerated solution. This finding is also supported by the cross-sectional analysis of the specimens at  $150\text{ }^\circ\text{C}$ . To avoid the blistering and coating breakdown due to the reaction between the electrolyte and coating which happened locally, polyaniline was added to the coating system.

## 6.2. Polyaniline

In Chapter 5, electrochemical polymerization was discussed as it has a controllable behavior in terms of its synthesis. However, as concluded in Chapter 5, polyaniline coated carbon steel alone is not sufficient to prevent corrosion in artificial geothermal water at  $150\text{ }^\circ\text{C}$ , although it slows down the ionic species to be directly in contact with the carbon steel surface. Furthermore, it is inconvenient and technically difficult to produce polyaniline via electrochemical deposition in a large-scale surface such as pipelines, which then motivates the use of chemically synthesized polyaniline in a paint blended system [85]. To further optimize the functionality of polyaniline for corrosion protection in geothermal application using chemically synthesized polyaniline, two acids were chosen due to the lowest risk of corrosion on carbon steel related to their counter anions, i.e. phosphoric acid ( $\text{H}_3\text{PO}_4$ ) and dodecylbenzenesulfonic acid (DBSA). The coating was then characterized and evaluated by exposing the specimens to the geothermal solution.

### 6.2.1. Polyaniline Synthesis and Characterization

Phosphoric acid was chosen as the polymerization medium as being one of the inorganic acids having the lowest risk of exhibiting corrosion reactions with carbon steel compared to other inorganic acids, e.g., sulfuric acid, and hydrochloric acid. When exposed to the electrolyte, there is a possibility that the polymeric matrix undergoes breakdown and the counter anions originating from the acidic media used in the polymerization, i.e. phosphate or sulfonate, release from PANI pigments. The release of counter anions may lead to their migration to the metal substrate. Phosphate anions offer an advantage, as they might provide passivation locally on the nearest  $\text{Fe}^{2+}$  ions releasing metal surface, whereas chloride and sulfate are aggressive and usually responsible for pitting corrosion on carbon steel. Phosphate is often used for a conversion coating on various steels. Conversion coating refers to the formation of a coating on a ferrous or non-ferrous metal surfaces due to a controlled chemical or electrochemical attack [148]. Phosphate-based coating systems have been used for corrosion protection in different applications [149-152].

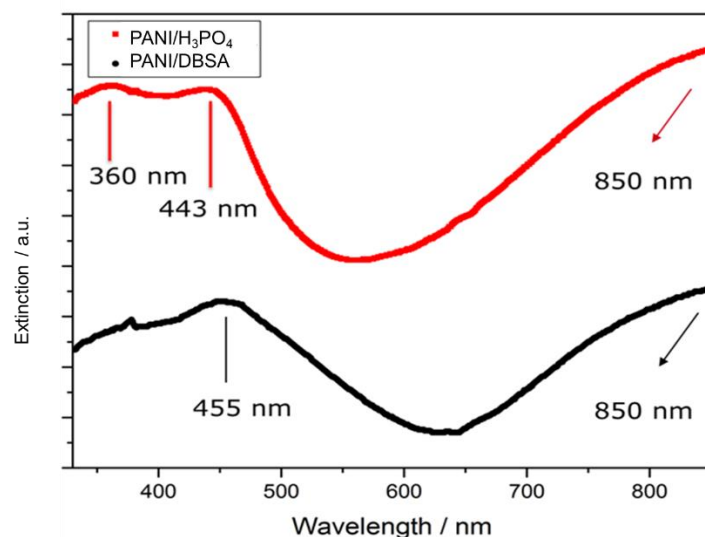
Alternatively, DBSA can also be used to synthesize polyaniline, since it is an organic acid which has surfactant behavior due to the long molecular tail. Another advantage of using DBSA is that organic sulfonic acid dopant can induce more processable polyaniline [153, 154], especially for dispersion in the polymeric matrix. PANI/DBSA was also proven to have a higher thermal resistance compared to other inorganic acid doped polyaniline [153].

Chemical polymerization has a slightly different mechanism than the electrochemical polymerization, as already mentioned in Chapter 2. During the synthesis using phosphoric acid, the solution color turned from colorless to blue after Ammonium Peroxydisulfate (APS) was added, indicating the fast-initial formation of polyaniline in the oxidation state of emeraldine base. By the end of the polymerization, the solution is green, indicating the oxidation state of emeraldine salt.

Han et al first reported the use of micellar solution DBSA in producing polyaniline to obtain conductive nanoparticles with enhanced thermal stability and processability [155]. As a doping agent, DBSA provides additional behavior as surfactant, which induces better dispersibility of PANI in other polymeric matrix [156]. During the synthesis, aniline was added to DBSA, resulting in a white solution, which then turned to dark yellow after APS addition indicating the initial formation of polyaniline in the oxidation state of leucoemeraldine. By the end of the polymerization, the solution is green, identified as polyaniline in the oxidation state of emeraldine salt.

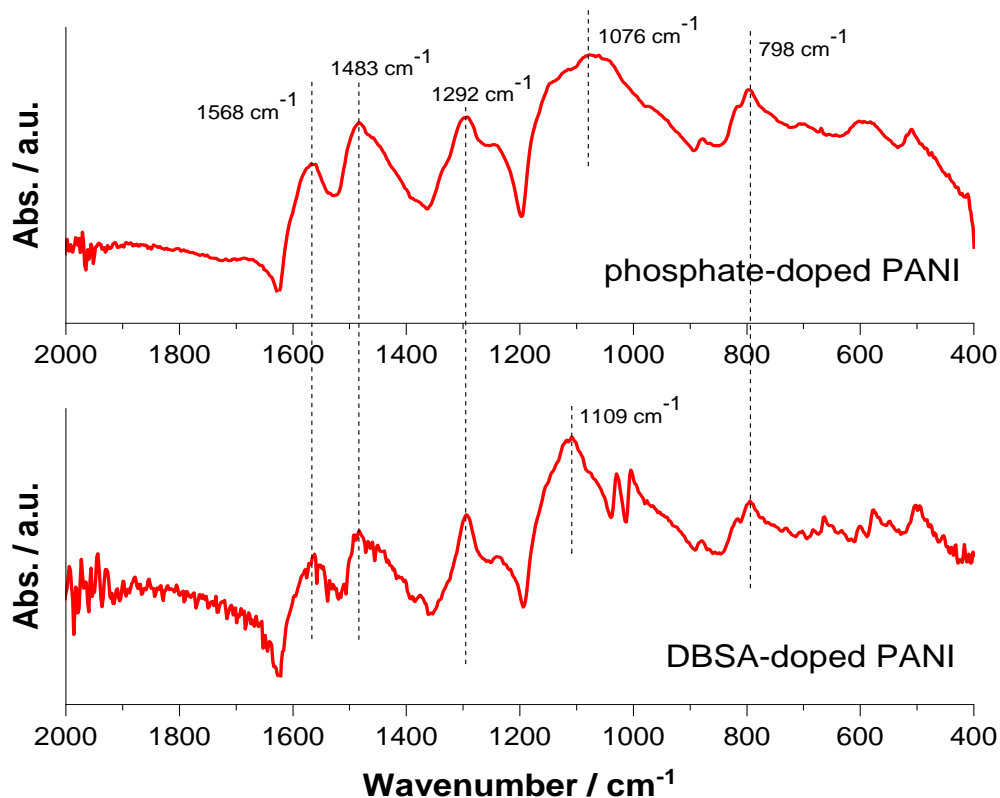
UV-Vis spectroscopy was used to analyze the electronic transition of the polyaniline molecules. Figure 6.8 shows that the dominant absorption peaks of PANI/ $\text{H}_3\text{PO}_4$  were at 360, 443, and 850 nm, whereas PANI/DBSA were dominated by peaks with wavelength of 455 and 850 nm. The absorption peak at 360 nm has been attributed to the transition of electrons from the highest occupied molecular orbital (HOMO) to the lowest occupied molecular orbital (LUMO), which corresponds to  $\pi$ - $\pi^*$  transition in the benzenoid structure [157]. Absorption peaks in both PANI/ $\text{H}_3\text{PO}_4$  and PANI/DBSA at 443 and 455 nm, as well as broad peaks at around 850 nm are often attributed to the transition of polaron- $\pi$  and  $\pi^*$ -polaron, respectively [158, 159].





**Figure 6.8.** Characterization of phosphate-doped PANI and DBSA-doped PANI using UV-Vis spectroscopy [160].

FTIR spectroscopy was used to confirm the formation of synthesized polyaniline by assigning the characteristic peaks from the corresponding functional groups (Figure 6.9). Details of FTIR peak assignment are described in Table 6.2. The functional groups of the formed polyaniline compounds were mostly assigned to the aromatic compound with C=C, and amine group C-N and N-H, which represent polyaniline chemical structure.



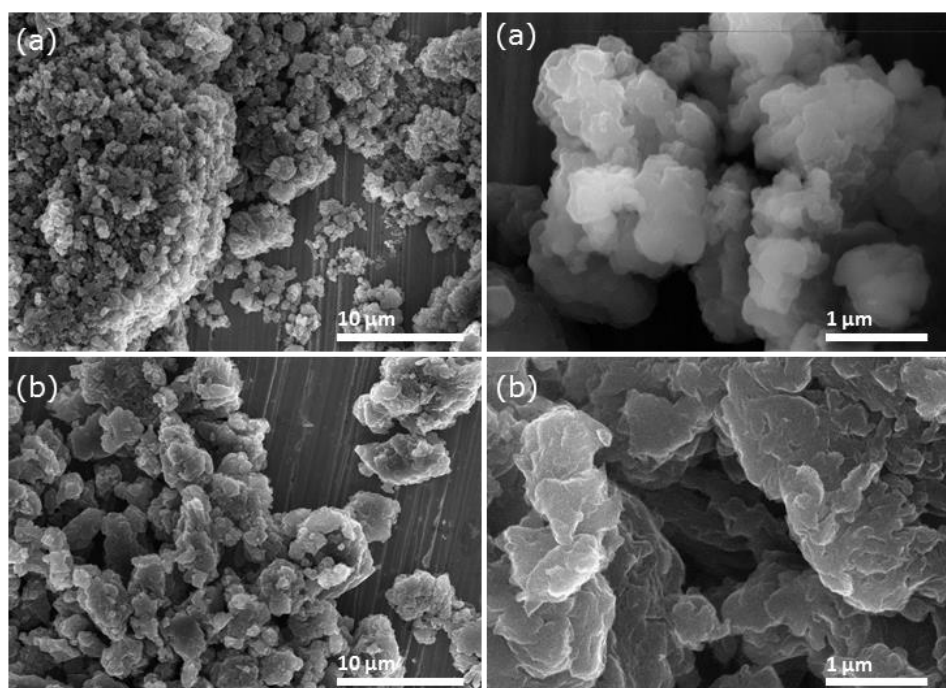
**Figure 6.9.** Characterization of phosphate-doped PANI and DBSA-doped PANI using FTIR spectroscopy



**Table 6.2.** Peak assignment for FTIR spectra of chemically synthesized polyaniline [112]

Wavenumber (cm <sup>-1</sup> )			Assignment
PANI-H <sub>3</sub> PO <sub>4</sub>	PANI-DBSA	Reference	
798	795	850-750	Amine / N-H wagging and twisting
1076	1109	1220-1020	Amine / Aliphatic C-N stretching
1292	1294	1360-1250	Amine / Aromatic C-N stretching
1483	1483	1600-1430	Aromatic / C=C stretching
1568	1554, 1572	1600-1430	Aromatic / C=C stretching

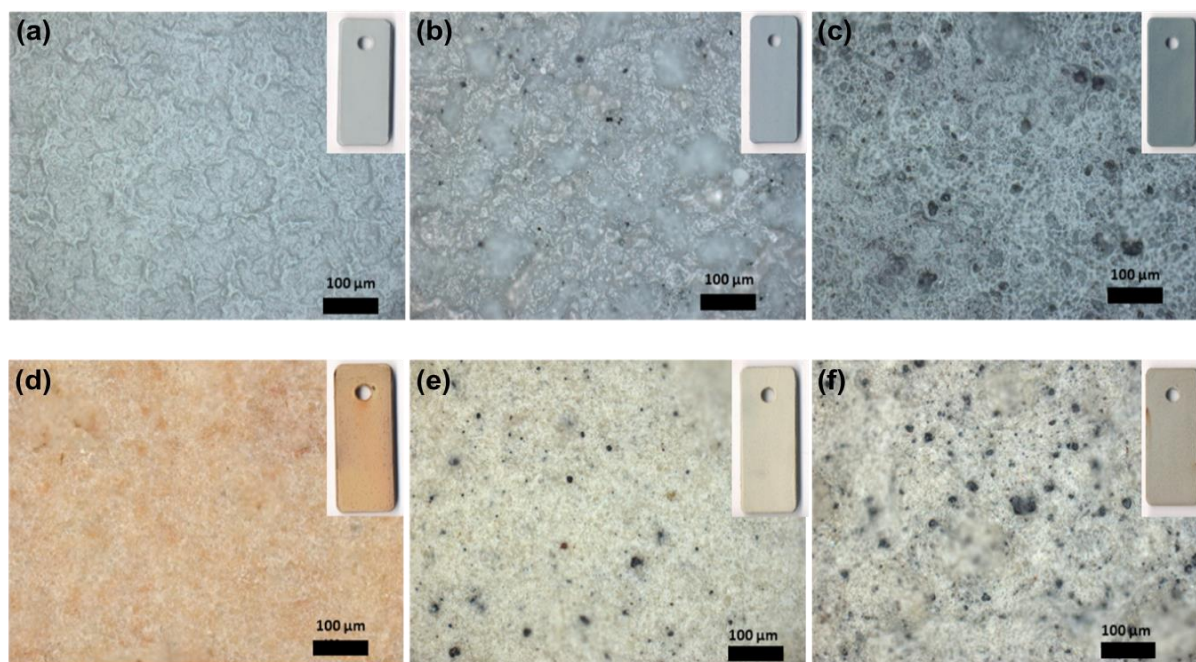
The SEM images show the aggregation of fine polyaniline powder, both in the case of phosphate-doped and DBSA-doped polyaniline, as shown in Figure 6.10. The SEM images were presented in a higher magnification to show an approximation of polyaniline particle size and morphology. Phosphate-doped polyaniline had a nearly round shape of around 1  $\mu\text{m}$ , while DBSA doped polyaniline was formed in a continuous structure. This is mainly attributed to the effect of solvents/counter ions during the growth of PANI.

**Figure 6.10.** SEM images of chemically synthesized polyaniline with (a) H<sub>3</sub>PO<sub>4</sub> dopant and with (b) DBSA dopant [160]

### 6.2.2. The Effect of Polyaniline Addition

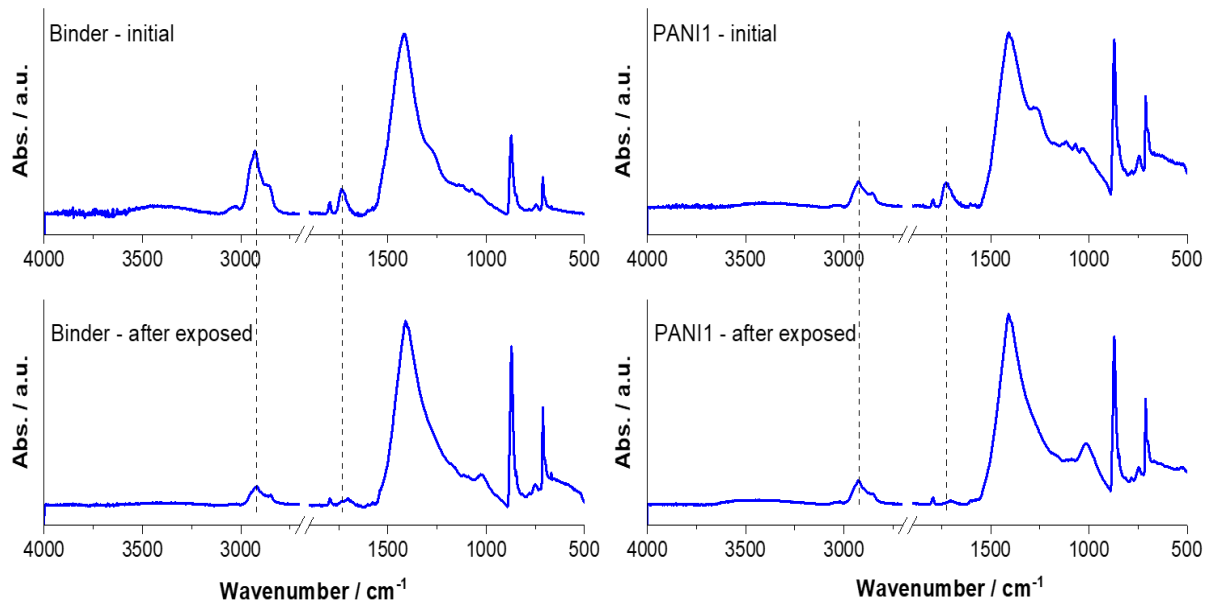
To inhibit the chemical degradation of alkyd coating caused by the reaction with the geothermal solution, polyaniline particles were dispersed in the alkyd-based matrix and tested at 150 °C. Different compositions of polyaniline have been investigated resulting in the optimum use of polyaniline composition within the range of 1-5 wt% [92, 161]. Previous findings emphasize that, although polyaniline has anticorrosive behavior, the increase of polyaniline composition within another polymeric matrix triggered a more vigorous corrosion on the steel [98]. This might be associated with the reaction between the counter anions along the conducting polymer chain with metals [98]. Thus, herein 2 wt% of as-prepared PANI was dispersed homogeneously in the alkyd-based binder before coated on carbon steel specimens.

Two types of polyaniline were used in the composite coatings, in which the coated carbon steel specimens are hereafter referred to as PANI-1 (with 2 wt% of phosphate-doped polyaniline) and PANI-2 (with 2 wt% of DBSA-doped polyaniline), as also described in subchapter 3.2.2. As shown in Fig. 6.10, after exposed to the deaerated artificial geothermal water at 150 °C for seven days, both types of coatings were intact on the substrate, without any blisters on the coating surface. However, there was a discoloration of coatings, indicating that there was still a chemical degradation during the exposure test. Based on the macroscopic and microscopic images, there was no significant difference between PANI-1 and PANI-2.



**Figure 6.11.** Optical microscope images of chemically synthesized polyaniline blended in alkyd-based matrix at the initial condition: (a) without pigment (b) PANI-1 (c) PANI-2. After exposed to the geothermal solution at 150 °C for 7 days: (d) without pigment (e) PANI-1 (f) PANI-2.

To confirm the functional group of coatings containing polyaniline before and after the exposure to the artificial geothermal water at 150 °C, FTIR spectra are presented in Figure 6.11. Unlike the FTIR spectra of binder after exposed to the geothermal water, there is no significant change in the absorption peak at 2921  $\text{cm}^{-1}$  which is C-H stretching. There is, however, a decrease at 1716  $\text{cm}^{-1}$  related to C=O stretch, suggesting that the coating modified with polyaniline addition is degraded at a slower rate than that of the alkyd-binder.



**Figure 6.12.** FTIR spectra of PANI-1 before and after exposed to the deaerated geothermal solution at 150 °C compared to that of the binder.

Based on the experimental results, after adding polyaniline to the coating, there is no blisters that might lead to coating degradation. In addition, the FTIR spectra revealed that the reduction of the absorption peak at around  $2921\text{ cm}^{-1}$  which is related to C-H stretching is less than that of the binder, suggesting that the coating degrades at a slower rate than that of the binder. However, the reason for degradation might be associated with the low thermal resistance of both PANI and alkyd, since they are polymer-based materials. The addition of  $\text{SiO}_2$  as thermal resistance enhancer was proposed.

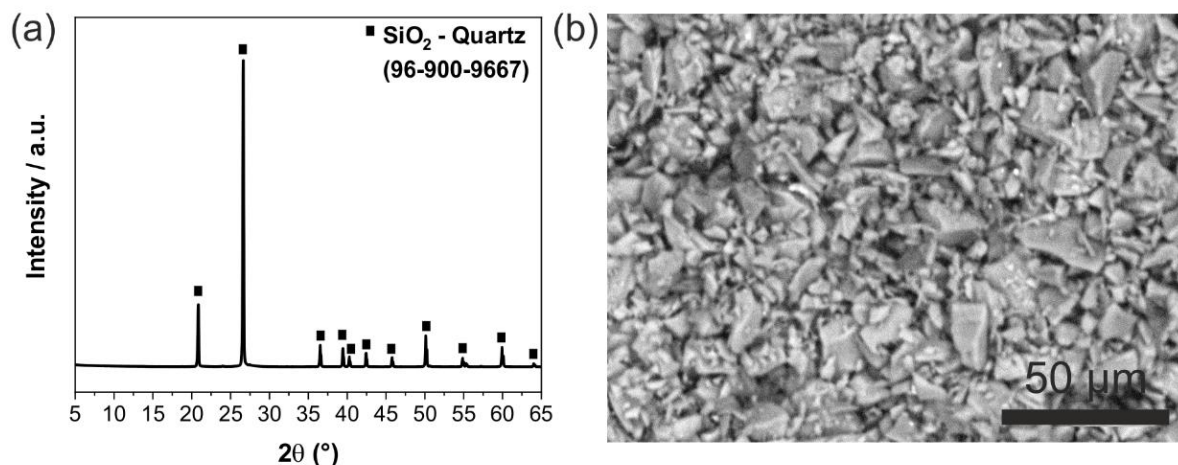
### 6.3. Silicon Dioxide Filled Alkyd Coating

To enhance the thermal resistance of coating, a ceramic-based material was considered. Silicon dioxide was chosen because it has a temperature stability of up to  $1400\text{ °C}$ , and it is resistant to many chemicals. As also mentioned in subchapter 2.3.4., silicon dioxide is abundant in nature, and might be found as a side product of the scaling in geothermal sites. The silicon dioxide used in this research was also obtained from the locally available resource in Indonesia. Considering all these aspects, silicon dioxide has the desired properties and cost efficiency.

#### 6.3.1. Silicon Dioxide Characterization

Silicon dioxide was extracted from natural sand, originating from a beach in Bancar, East Java, Indonesia, and treated as described in subchapter 3.1.2.3. A comparison of the silicon dioxide purity is discussed elsewhere, in which the silicon dioxide used here has a purity of 98.7 % with 1.3 % impurities of  $\text{CaCO}_3$  [111].

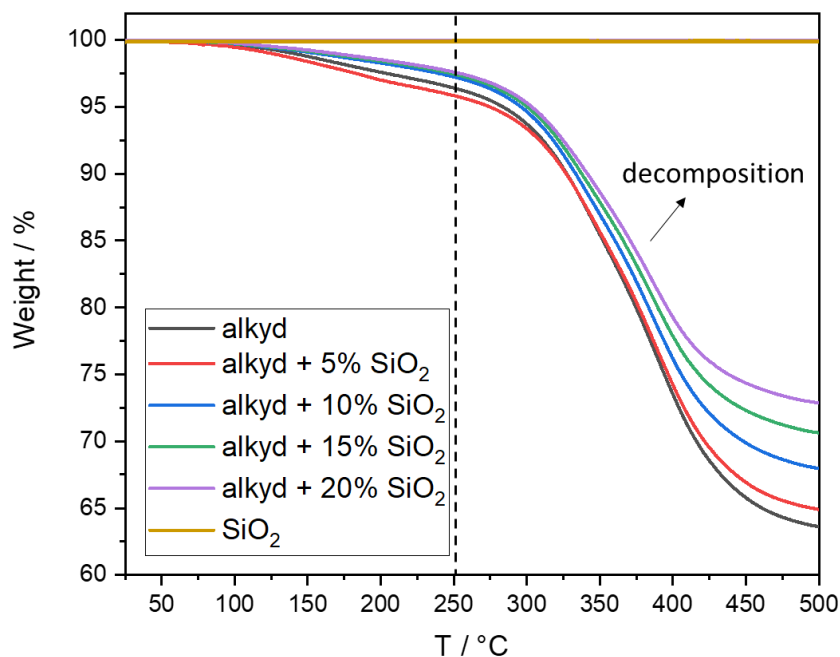
Silicon dioxide particles were characterized using XRD and SEM to identify the particle morphology, compositional phase, and its crystallinity. XRD data show that silicon dioxide is crystalline quartz, which was matched to the COD 96-900-9667 (Figure 6.13a). SEM image revealed a particle size of under  $100\text{ }\mu\text{m}$  (Figure 6.13b).



**Figure 6.13.** Characterization of SiO<sub>2</sub> particles (a) XRD and (b) SEM

To investigate the effect of SiO<sub>2</sub> composition to the thermal resistance of the SiO<sub>2</sub>-alkyd coating system without any chemical influence with the solution, SiO<sub>2</sub> was blended in the alkyd matrix with various amount, i.e., 5 wt%, 10 wt%, 15 wt%, and 20 wt%, and tested using thermogravimetry analysis. Figure 6.14 revealed that SiO<sub>2</sub> powder is stable in the temperature range of 25 – 500 °C, with mass loss of lower than 0.1%. On the other hand, alkyd coating has two steps of mass loss, i.e., a gradual mass decrease from about 70 °C until about 250 °C, and a steep mass decrease until 500 °C. The step decrease in the second temperature region between 250 °C to 500 °C might be associated with the decomposition of the alkyd coating, resulting in the remaining coating mass of 63% at 500 °C. When SiO<sub>2</sub> is added to the alkyd, the mass losses of specimens at 500 °C were less than the alkyd coating without SiO<sub>2</sub>.

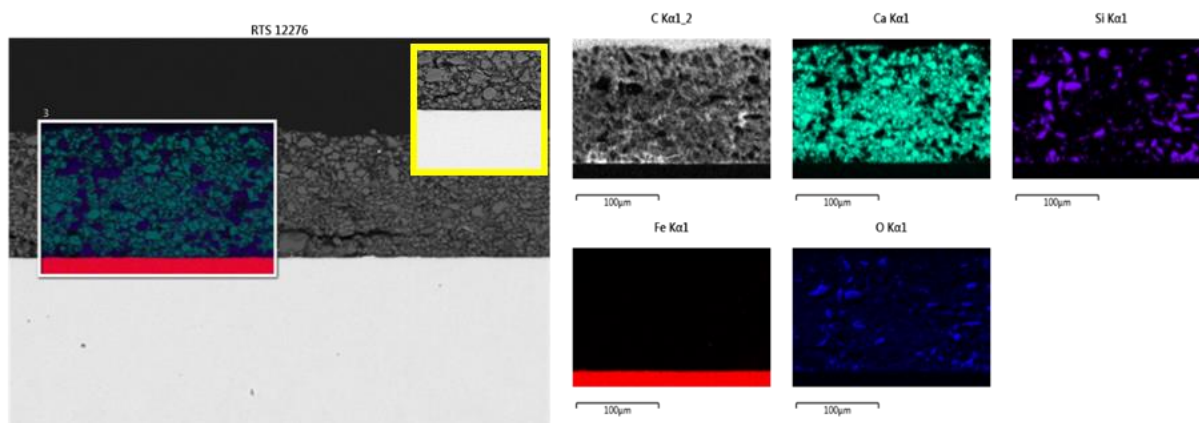
To evaluate the thermal resistance of the coating at the temperature range which represents a geothermal application, the gradual mass decrease at below 250 °C was observed. The addition of 5 wt% SiO<sub>2</sub> results in a greater decrease of mass than the unmodified alkyd. However, when the amount of SiO<sub>2</sub> is increased to 10 wt%, the TGA data shows that the thermal resistance of the coating system is improved. There is, however, no significant difference between the composition of SiO<sub>2</sub> between 10-20 wt%. Thus, 15 wt% of SiO<sub>2</sub> was used to modify the coating system for a further testing purpose.



**Figure 6.14.** Thermogravimetry analysis of alkyd-SiO<sub>2</sub> coating system with various SiO<sub>2</sub> composition from 0 – 20 wt% of SiO<sub>2</sub> under N<sub>2</sub> atmosphere. Temperature ranges from 25 – 500 °C with a temperature gradient of 10 °C/min.

### 6.3.2. The Effect of Silicon Dioxide Addition

To apply the silicon dioxide particles to the coatings, silicon dioxide was dispersed in the solvent (MIBK) which was then blended with the alkyd-based binder using an orbital shaker. The SEM image and EDX analysis of the specimen cross section show that silicon dioxide particles are dispersed homogeneously within the coating (Figure 6.15).

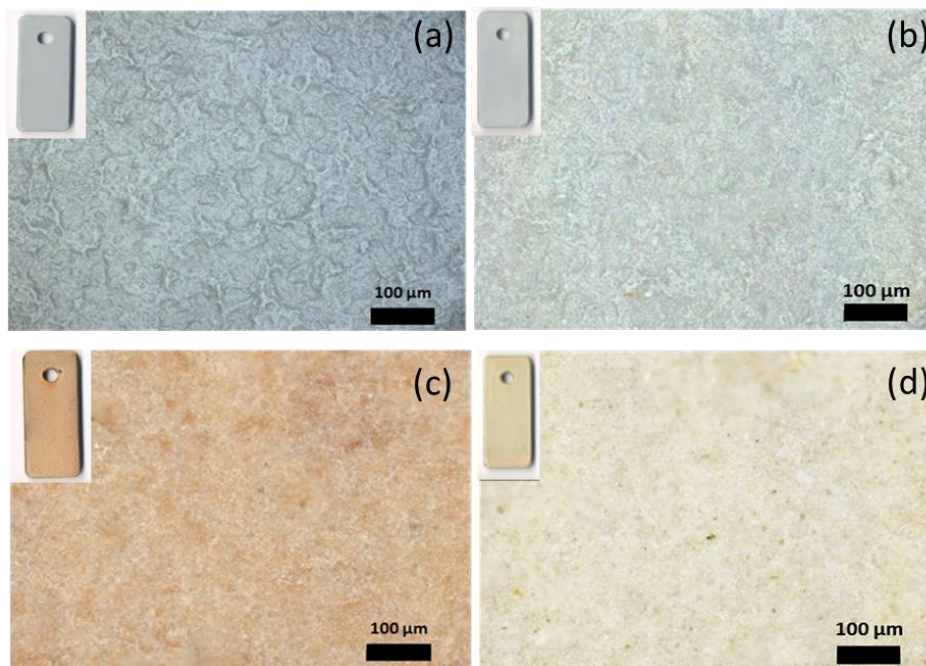


**Figure 6.15.** EDX elemental mapping of the silicon dioxide composite coating cross section at the initial condition.

The specimens were then exposed to the artificial geothermal water at 150 °C for seven days, which led to the discoloration of specimens as compared to the initial condition, as shown in Figure 6.16. Although there is discoloration of the specimens, optical microscopic images show that there is less blistering compared to the specimens of alkyd binder without any addition of silicon dioxide. Silicon dioxide is stable at high temperature, which was proposed

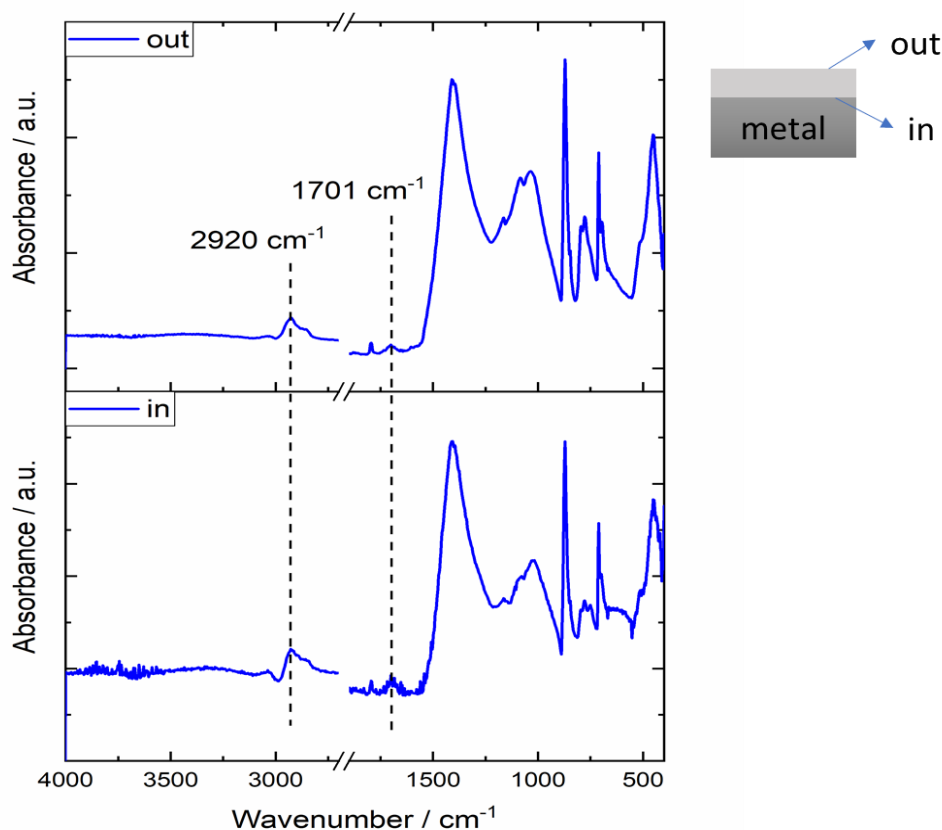


to enhance the resistance to thermal degradation. However, when the chemical degradation continues, the effect of silicon dioxide alone to inhibit the degradation is not sufficient.



**Figure 6.16.** Optical microscope images of coatings (a) without silicon dioxide (b) with silicon dioxide (c) without silicon dioxide after exposure, and (d) with silicon dioxide after exposure in the geothermal solution at 150 °C for 7 days.

Although there were no blisters identified after adding silicon dioxide particles to the coating system, the coating can be entirely delaminated and detached from the metal surface. The side which was attached to the metal (in) was then compared to the side which was exposed to the solution (out) using FTIR to observe the chemical properties (Figure 6.17). The FTIR spectra indicated that there was still degradation of the organic part of the coating, which was observed at around 2920 and 1701  $\text{cm}^{-1}$ , corresponding to the C-H stretching and C=O stretching, respectively. However, the inorganic part shows the same pattern, indicating that  $\text{SiO}_2$  was dispersed homogeneously and there was no indication that  $\text{SiO}_2$  might flow to the outer part of the coating.



**Figure 6.17.** FTIR spectra of SiO<sub>2</sub> containing coating after exposed to the artificial geothermal water at 150 °C for seven days.

#### 6.4. Conclusion

It has been shown that there is synergistic polymer degradation contributed by chemical and thermal degradation. In the presence of oxygen, the alkyd-based binder was further degraded due to thermoxidative degradation. Besides oxidative degradation, the degradation might also be associated with the hydrolysis of alkyds, which was further catalyzed by the acidic nature of the geothermal solution, however, reduced with time due to neutralization (pH increased to 6.5). Chemical analysis and morphological characterization showed an improvement of coatings by the addition of polyaniline or silicon dioxide to the alkyd binder. However, each individual system of PANI-alkyd or SiO<sub>2</sub>-alkyd has its advantages and disadvantages which can be mitigated by combining the pigments.





# Chapter 7. Corrosion Study of Polyaniline/Silicon Dioxide Modified Alkyd Coating

Different types of coatings including a single component (PANI or SiO<sub>2</sub>) modified alkyd binder and a binary component PANI/SiO<sub>2</sub> modified alkyd binder were characterized and developed to improve the durability of coatings for a long-term use. Morphological and chemical analyses were performed, in which the most optimized combination was selected and tested for up to 6 months to investigate the coating durability.

## 7.1. Combinational Properties of Pigments

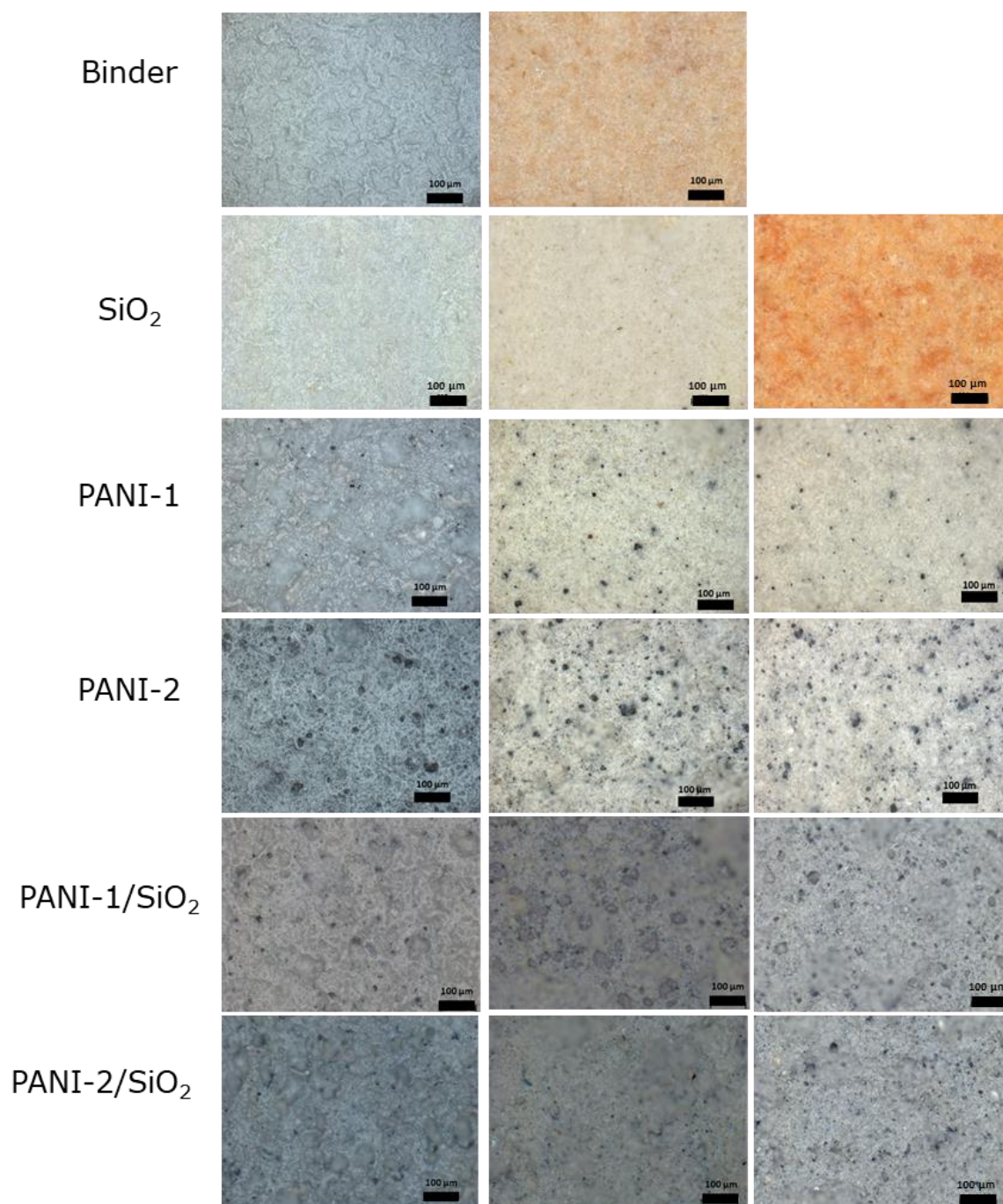
### 7.1.1. Morphological and Chemical Analysis

As discussed in the previous chapter, the individual component (PANI or SiO<sub>2</sub>) addition to the alkyd binder contributes to a slow down of the degradation of coatings when exposed to artificial geothermal water at 150°C. Both doping types of polyaniline pigments were then combined with silicon dioxide in the alkyd binder, coated on carbon steels and exposed to artificial geothermal water at 150°C for seven days. PANI-1/SiO<sub>2</sub> represents the coating with the addition of 2 wt% phosphate-doped PANI and 15 wt % silicon dioxide. To reveal the effect of the dopant, PANI-2/SiO<sub>2</sub> was made with the addition of 2 wt% DBSA-doped polyaniline and 15 wt% silicon dioxide.

Exposure tests were performed on the six types of coatings, with and without pigments, for 7 days and 28 days. Optical microscopic images show that there is clear discoloration on the binder coated specimen after 7 days of exposure (Figure 7.1); some blisters were also observed as discussed in Chapter 6. By adding SiO<sub>2</sub> particles to the alkyd binder, SiO<sub>2</sub>-alkyd coating underwent a lower degree of discoloration compared to that of the alkyd binder only coating after 7 days which, however, became stronger after 28 days of exposure. This indicates that SiO<sub>2</sub> might enhance the corrosion protection on carbon steel and slow down the degradation to a certain extent, which may be associated with the good thermal properties of SiO<sub>2</sub> compared to the polymer matrix in the coating. For a coating system used at a high temperature, it is crucial to have a compatible value of thermal expansion coefficient to avoid differential thermal stresses upon heating and cooling which may lead to microcracks [162, 163]. As mentioned in Chapter 2, SiO<sub>2</sub>-quartz has a thermal expansion of 8–14 ppm/K [105], which is compatible to that of carbon steel of 12 ppm/K [106], whereas alkyd and calcite have a thermal expansion coefficient of 36 and 24 ppm/K [105], respectively. The addition of SiO<sub>2</sub> might help lower the thermal expansion coefficient of the entire coating system, as confirmed by the longer stability of coating compared to that without SiO<sub>2</sub>.

After 28 days of exposure, the color of SiO<sub>2</sub>-containing coating changed to orange/brown, which is associated with rust or iron oxide. This indicates that the electrolyte infiltrated through the coating and reacted with the metal substrate, which might be associated with the porosity or local defects on the coating surface. The SiO<sub>2</sub>-alkyd coating system acts as a physical barrier layer with enhanced stability, albeit SiO<sub>2</sub> did not contribute to the active

corrosion protection. As observed in Figure 7.1, when polyaniline pigments were added, there was no color change after 28 days of exposure test, indicating active corrosion protection on the carbon steel surface.



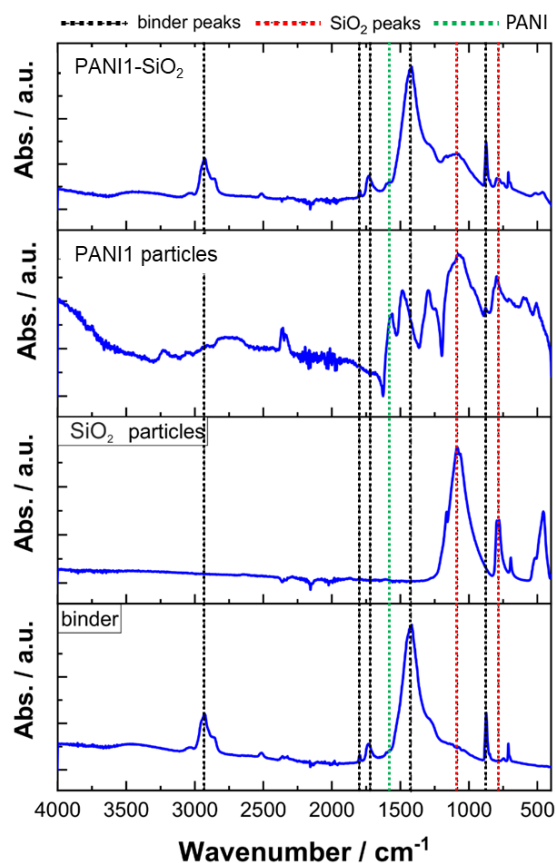
**Figure 7.1.** Optical microscope images of different types of coatings before exposure (left), after exposed to the artificial geothermal water for 7 days at 150 °C (middle), and after 28 days at 150 °C (right).

The optical microscopic images of PANI-1 and PANI-2 reveal that there was also a low degree of discoloration on the surface of coating, which is comparable to the SiO<sub>2</sub>-alkyd coating after 7 days of exposure. This discoloration, however, does not change significantly after 28 days compared to that of the SiO<sub>2</sub>-alkyd coating. The color of specimens remained yellow,

instead of brown/orange, indicating the inhibitive effect of PANI on the corrosion process between the metal and solution, regardless of the dopant types of PANI. Consequently, the formation of iron oxides was not observed, suggesting that the most reactive interaction between the electrolyte and the PANI-alkyd coatings occurred within the first 7 days of exposure. Since the improvement shown by the optical microscopic images of all types of the singular component modified coating is limited, the combinational coating of PANI and SiO<sub>2</sub> was applied on carbon steel.

In comparison to the other types of coatings, PANI-1/SiO<sub>2</sub> and PANI-2/SiO<sub>2</sub> coated specimens did not suffer from severe discoloration after exposure to the geothermal solution at 150°C for seven days, which remained the same until 28 days of exposure (Figure 7.1). As observed in the specimens PANI-1/SiO<sub>2</sub> and PANI-2/SiO<sub>2</sub>, and similarly in the specimens of PANI-1 and PANI-2, the type of dopants used in synthesizing polyaniline does not significantly affect the corrosion behaviors of coatings. Thus, PANI-1/SiO<sub>2</sub> coated specimens were exposed and scratched for further chemical analysis by FTIR spectroscopy to investigate the changes upon corrosion.

By analyzing the FTIR spectra, specific absorption peaks can be identified to reveal the affected functional groups of coatings after exposure to the artificial geothermal water. The first step is to compare the FTIR spectra of PANI-1/SiO<sub>2</sub> modified alkyd coating with the individual spectrum of its constituent component at the initial condition, i.e. phosphate-doped PANI particles, SiO<sub>2</sub> particles, and the alkyd-based binder. As observed in Figure 7.2, there are more combinational/overlapping absorption peaks due to the complexity of the coatings. As discussed in Chapter 6, the characteristic peaks of alkyd-based binder are evident around 2927 cm<sup>-1</sup> and 1718 cm<sup>-1</sup>, which corresponds to C-H stretching and C=O stretching. SiO<sub>2</sub> or quartz, might be identified by the absorption peak at 779 cm<sup>-1</sup>, which does not overlap with other peaks. However, polyaniline peaks mostly overlap with other components. For example, at 1901 cm<sup>-1</sup>, there is a broad peak, which might be associated with -O-Si-O- from silicon dioxide at 1087 cm<sup>-1</sup> and might overlap with the C-N stretching of polyaniline at 1076 cm<sup>-1</sup>. A more detailed peak assignment is listed in Table 7.1.



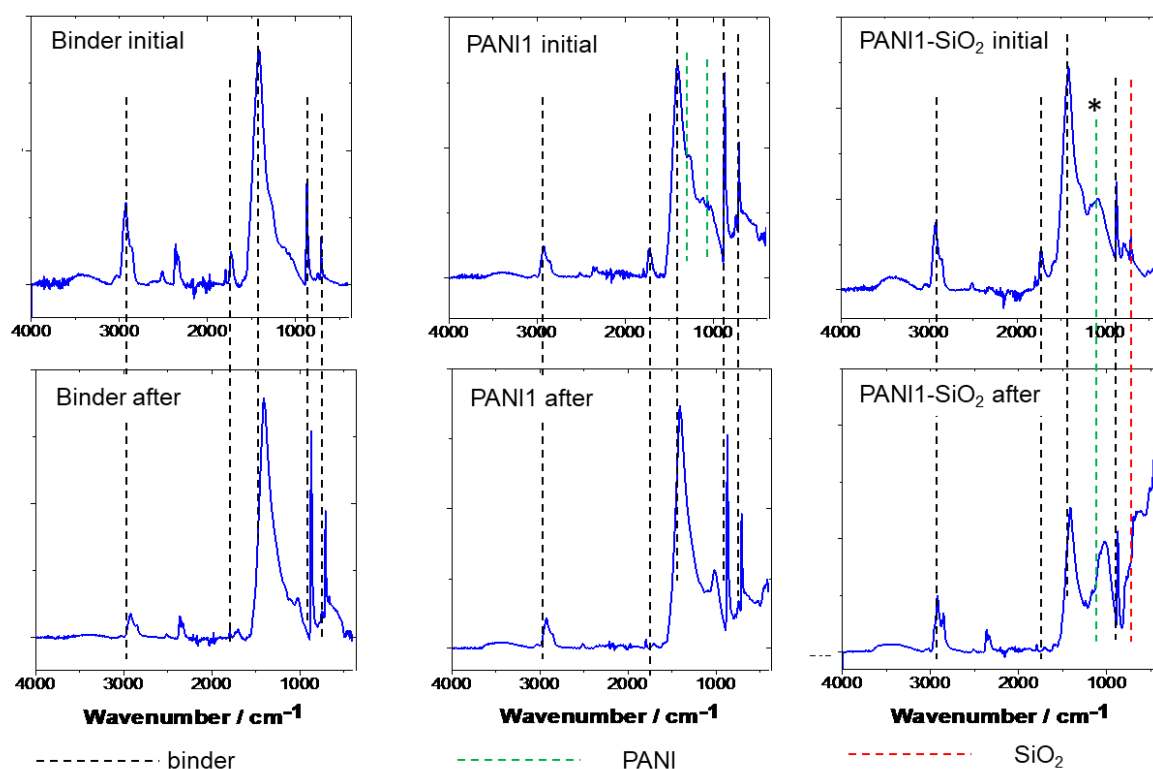
**Figure 7.2.** FTIR spectra of binder, SiO<sub>2</sub> particles, PANI particles, and combinational coating PANI-1/SiO<sub>2</sub> at the initial condition.

**Table 7.1.** Peak position of FTIR spectra and its assignment to the functional group of binder, SiO<sub>2</sub> particles, PANI particles, and combinational coating PANI-1/SiO<sub>2</sub> [112, 143, 164].

Wavenumber (cm <sup>-1</sup> )					Assignment
Binder	SiO <sub>2</sub>	PANI	PANI-1/SiO <sub>2</sub>	Reference	
2927	-	-	2923	2926 ± 10	(C-H) CH <sub>2</sub> asymmetric stretch
2852	-	-	2852	2855 ± 10	(C-H) CH <sub>2</sub> symmetric stretch
1718	-	-	1731	1730 – 1705	Aromatic C=O stretching
1587	-	1568	1589	1600 – 1430	Aromatic C=C stretching
-	-	1483	-	1600 – 1430	Aromatic C=C stretching
1417	-	-	1417	1420	CaCO <sub>3</sub>
-	-	1292	-	1360 – 1250	C-N stretching
1256	-	-	-	1310 – 1250	Aromatic C-O stretching
1256, 1120	-	-	-	1300 – 1100	Aliphatic C-O stretching
-	1087	1076	1091 (broad)	1070, 1220-1020	-O-Si-O-, C-N stretching
875	-	-	875	875	CaCO <sub>3</sub>
-	-	798	-	850 – 750	N-H wagging and twisting
-	779	-	779	779	Symmetric SiO <sub>2</sub> bending
713	-	-	711	712	CaCO <sub>3</sub>

The next step was to compare the FTIR spectra of the exposed PANI-1/SiO<sub>2</sub> to the unexposed one (Figure 7.3). Most of the peaks observed originated from the binder or alkyd matrix since it constitutes more than 85 wt% of the coating composition. Therefore, several peaks were selected and marked to observe the changes between before and after the exposure test. In the PANI-1 coated specimen, additional peaks were assigned to polyaniline, i.e. at 1076 cm<sup>-1</sup> and 1292 cm<sup>-1</sup>, both related to C-N stretching, whereas for the PANI-1/SiO<sub>2</sub> coatings, an additional peak at 779 cm<sup>-1</sup> was assigned to the symmetric SiO<sub>2</sub> bending. There is an overlapping peak of polyaniline and SiO<sub>2</sub> at around 1100 cm<sup>-1</sup> which might be associated with C-N stretching of polyaniline and -O-Si-O- stretching of silicon dioxide.

After exposure to artificial geothermal water for 7 days, the FTIR spectra of all specimens revealed a shifting of the vibration frequency (reciprocal to the wavenumber). The wavenumber shift is a result of an interaction between the electrolytes and coatings, which is strong enough to cause the shift in the wavenumber position.



**Figure 7.3.** FTIR spectra of binder (left), PANI-alkyd (middle), and PANI/SiO<sub>2</sub>-alkyd (right) before and after exposed to the geothermal solution for 7 days at 150 °C. (\* indicating the overlapping peak of PANI and SiO<sub>2</sub>).

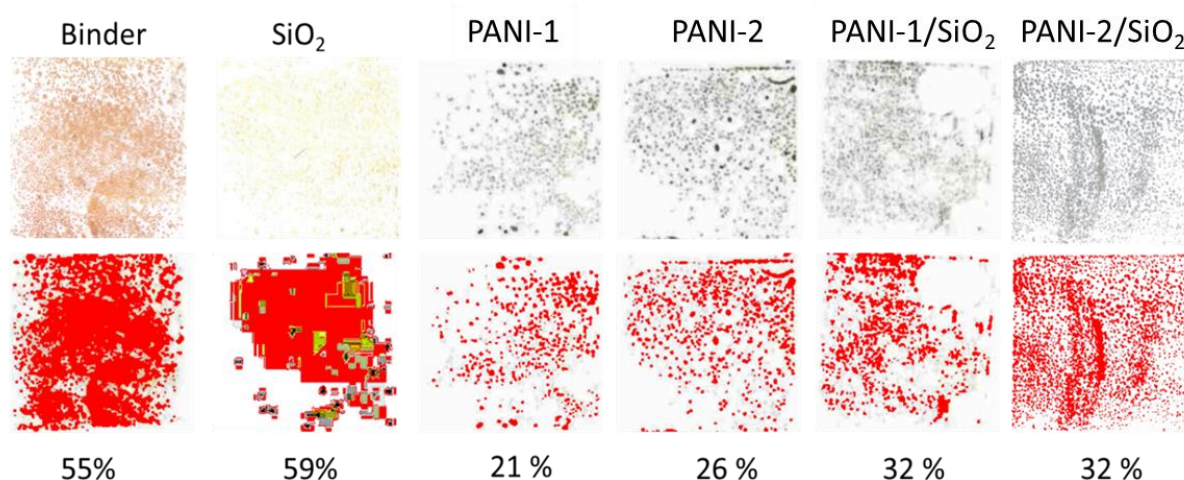
### 7.1.2. Mechanical Testing Using Pressure Sensitive Adhesive

In addition to the optical microscopic images and FTIR analysis, a tape test was used to investigate the adhesion of different types of coatings after the exposure test, as detailed in subchapter 3.4. Pressure sensitive adhesives are useful to form physical bonds with other materials by applying brief contact and light pressure. Bond formation between the tape and coating results from the ability of the polymeric material to flow under light pressure,



establishing good contact area with the substrate [165]. The debonding step was then caused by the deformation of polymer under the stress, which then separated the coating from the metal substrate.

To assess the adhesion test more precisely, the tape after debonding step were scanned and analyzed using image-J software by adjusting the color threshold to select and calculate the delaminated area. This technique supports the image analysis by a semi-quantitative estimation of delaminated area. As shown in Figure 7.4, the tape test indicates that the unmodified binder and SiO<sub>2</sub> modified binder have the least adhesion/cohesion. With the addition of polyaniline particles to the binder, a better adhesion/cohesion was achieved, which then slightly decreased with the addition of silicon dioxide (Figure 7.4). This result might be associated with the fact that the addition of SiO<sub>2</sub> particles to the coating reduces the adhesion-cohesion of coatings.



**Figure 7.4.** Images of detached coatings on a transparent tape, where the experiments performed on the specimens after exposed to the geothermal solution for 7 days at 150 °C (upper). The red areas are the selected area representing the delaminated coating, which then calculated to as a semi-quantitative estimation of the degree of delamination (bottom).

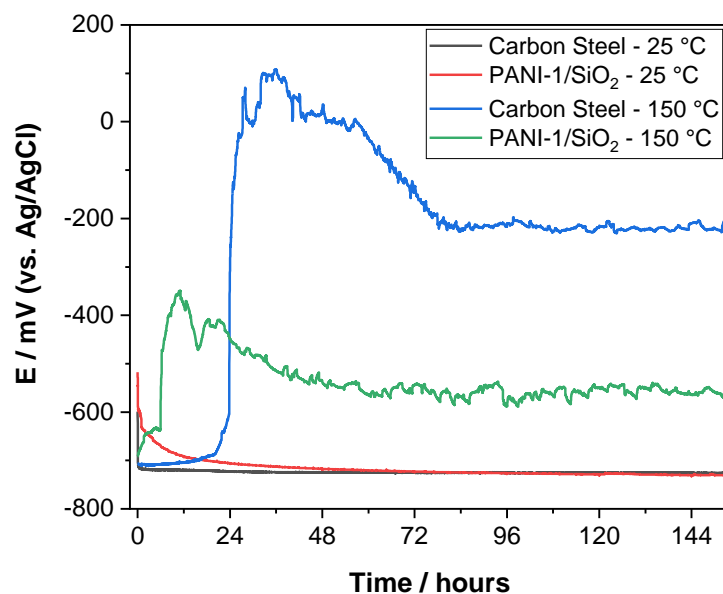
## 7.2. Effect of Temperature on the Corrosion Behavior of Coatings

PANI-1/SiO<sub>2</sub> based coating was then used for further tests. As revealed by the experimental results of carbon steel and polyaniline coated carbon steel via electrochemical deposition, temperature is a crucial parameter and eventually detrimental factor to the coating performance. Thus, the temperature effect was also investigated in this section by electrochemical tests. The tests were conducted at 25 °C and 150 °C to investigate the chemical and electrochemical behaviors of coating in the artificial geothermal water with and without the influence of high temperature.

Figure 7.5 shows that the  $E_{\text{corr}}$  of PANI-1/SiO<sub>2</sub> coating is dependent on temperatures. At 25 °C, its  $E_{\text{corr}}$  decreases from -517 mV to -691 mV within the first 24 hours after exposed to the artificial geothermal water. The  $E_{\text{corr}}$  of PANI-1/SiO<sub>2</sub> is slightly more positive compared to that of carbon steel, having a range of -500 mV to -730 mV, whereas the  $E_{\text{corr}}$  of carbon steel is -720 mV to -750 mV under the same experimental condition. Based on the  $E_{\text{corr}}$  monitoring at room temperature, there was no distinct ennoblement by the free corrosion potential.

At 150 °C,  $E_{\text{corr}}$  of PANI-1/SiO<sub>2</sub> coated specimen increased from -700 to -380 mV on the first day. After 24 hours, the  $E_{\text{corr}}$  slowly reduced and remained stable at about -520 mV

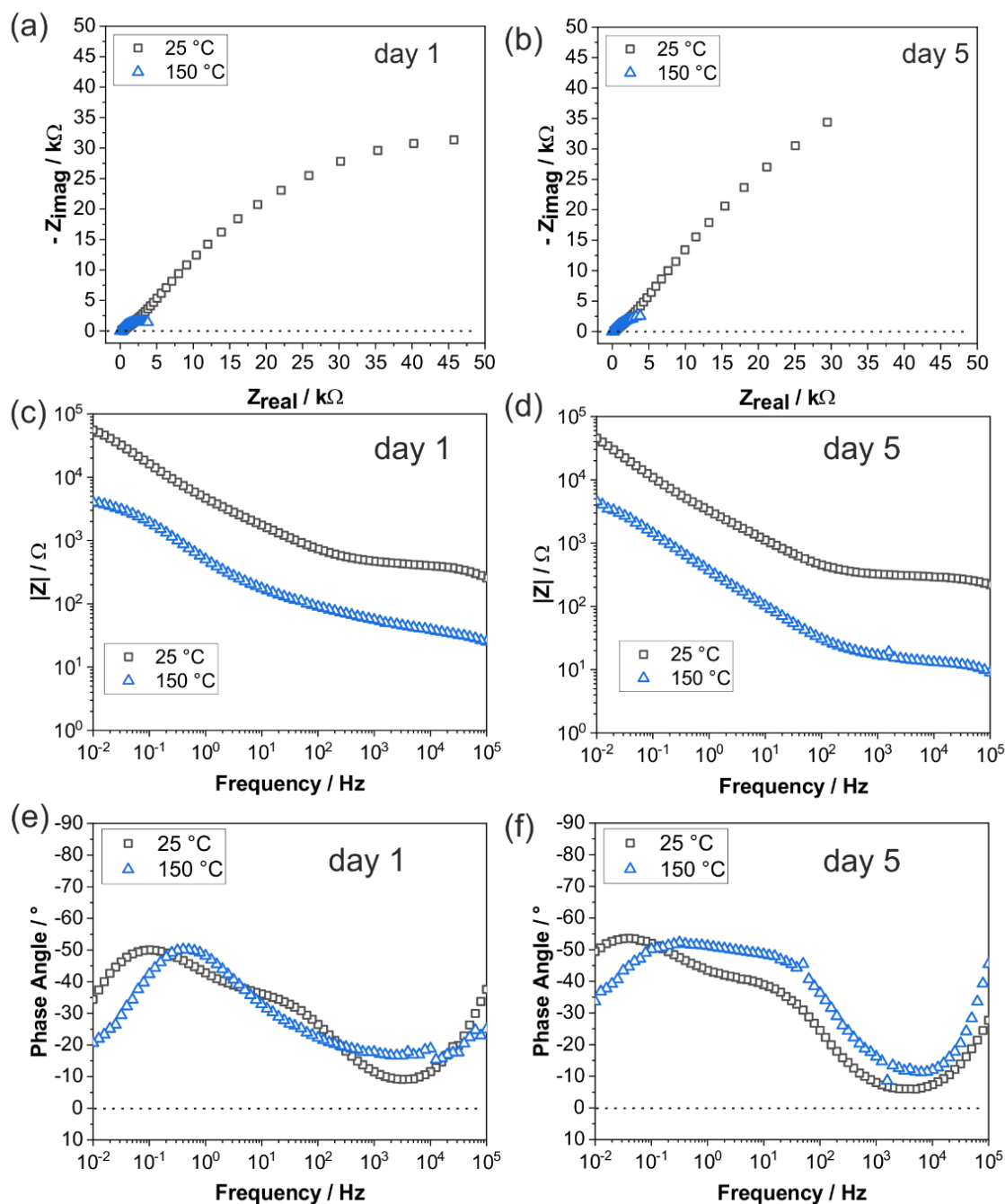
until the end of the experiment, which is in a much lower range compared to carbon steel  $E_{\text{corr}}$  of -670 mV to 100 mV. At 150 °C, carbon steel underwent an active corrosion within the first day, whereby an oxide layer was formed and induced more positive  $E_{\text{corr}}$ , which could also be contributed by the oxidation of  $\text{Fe}^{2+}$  to  $\text{Fe}^{3+}$ . The oxide layer, however, did not completely cover the surface, indicated by the decrease of  $E_{\text{corr}}$ . Unlike at room temperature, there was a significant difference in  $E_{\text{corr}}$  between the coated carbon steel and uncoated carbon steel. As presented in Chapter 5, at 150 °C PANI coated carbon steel (via electrochemical deposition) has an  $E_{\text{corr}}$  of -630 mV when tested in the artificial geothermal water. Thus, these experimental results suggest a cathodic protection of coatings on carbon steel at 150 °C.



**Figure 7.5.**  $E_{\text{corr}}$  of PANI-1/SiO<sub>2</sub> coating in comparison to carbon steel exposed to the artificial geothermal water at 25 and 150 °C.

To further analyze the change of PANI-1/SiO<sub>2</sub> coating at different temperatures, EIS was selected at two different days and plotted in the form of Nyquist, Bode magnitude, and phase angle plots. The impedance spectra of PANI-1/SiO<sub>2</sub> coating share some common patterns with the theoretical impedance spectra of degraded polymer coating, as shown in Figure 3.6. The most useful parameter to compare the coating performance is by observing the maximum impedance at the lowest frequency ( $Z_{\text{max}}$ ) [166]

Figure 7.6 shows that PANI-1/SiO<sub>2</sub> has a higher impedance value at a lower temperature, indicated by the Nyquist and Bode magnitude plot. Bode magnitude plot shows that  $Z_{\text{max}}$  remained in the range of  $10^3 \Omega$  at 150 °C and  $10^4 \Omega$  at 25 °C, showing that the impedance of the coating is about ten times lower when used at high temperature. The absolute impedance value at the lowest frequency, which might be associated with the corrosion resistance, remained stable between the first and fifth day.



**Figure 7.6.** Impedance spectra of PANI-1/SiO<sub>2</sub> coating in the artificial geothermal water at 25 °C and 150 °C after 1 day (a, c, e) and 5 days (b, d, f); the data were presented as (a) and (b) Nyquist plot, (c) and (d) Bode magnitude plot, and (e) and (f) phase angle plot

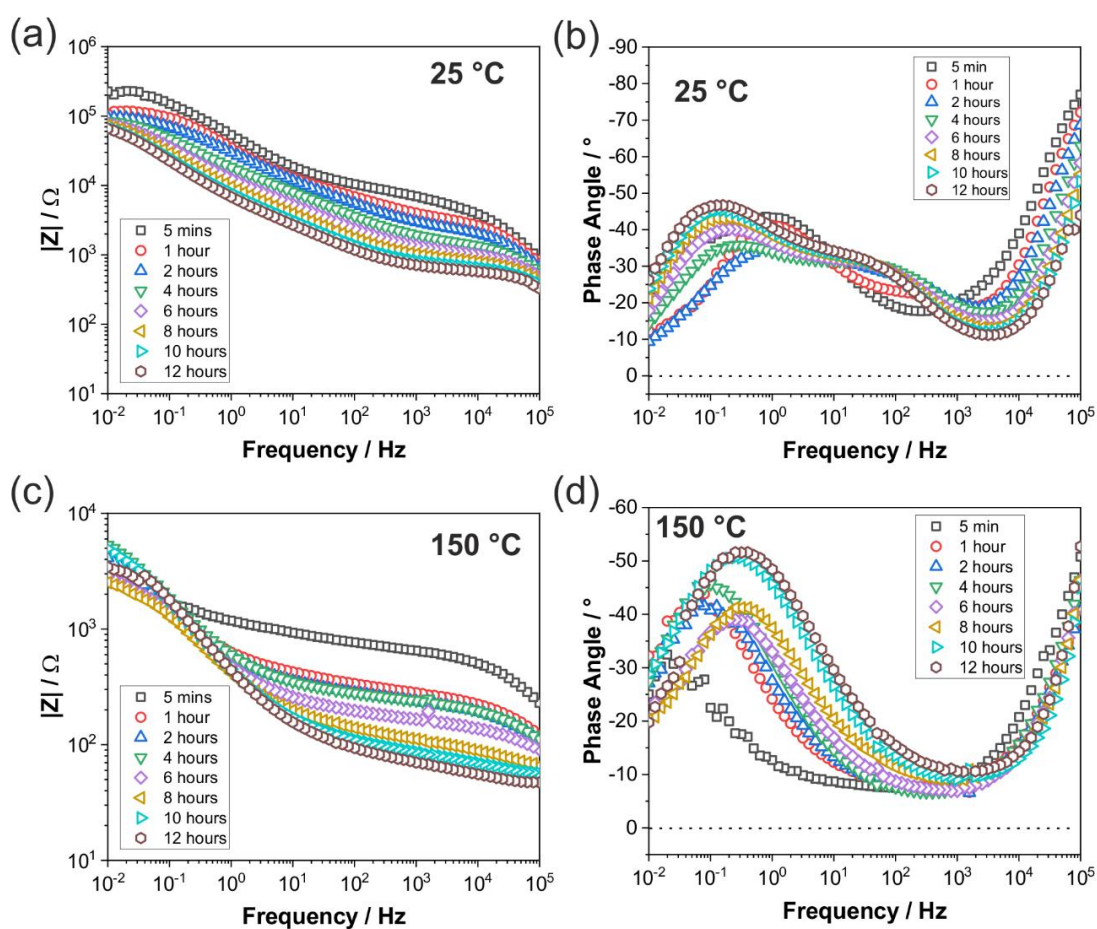
As shown in Figure 7.5, the  $E_{\text{corr}}$  changed significantly within the first few hours, which motivates the monitoring of EIS every 2 hours within the first 12 hours. Figure 7.7 shows that at room temperature, the total impedance value presented by Bode magnitude plot decreases along with time and the phase angle at low frequency is increasing, regardless the temperature, indicating that the coating became less resistive as it is aged in the artificial geothermal water.

To further monitor the changes of PANI-1/SiO<sub>2</sub> coating as a function of time, EIS was recorded every hour within the first day of exposure and every day from 1<sup>st</sup> -7<sup>th</sup> days. Although  $E_{\text{corr}}$  is relatively stable after the first day as shown in Figure 7.5, impedance spectra show the

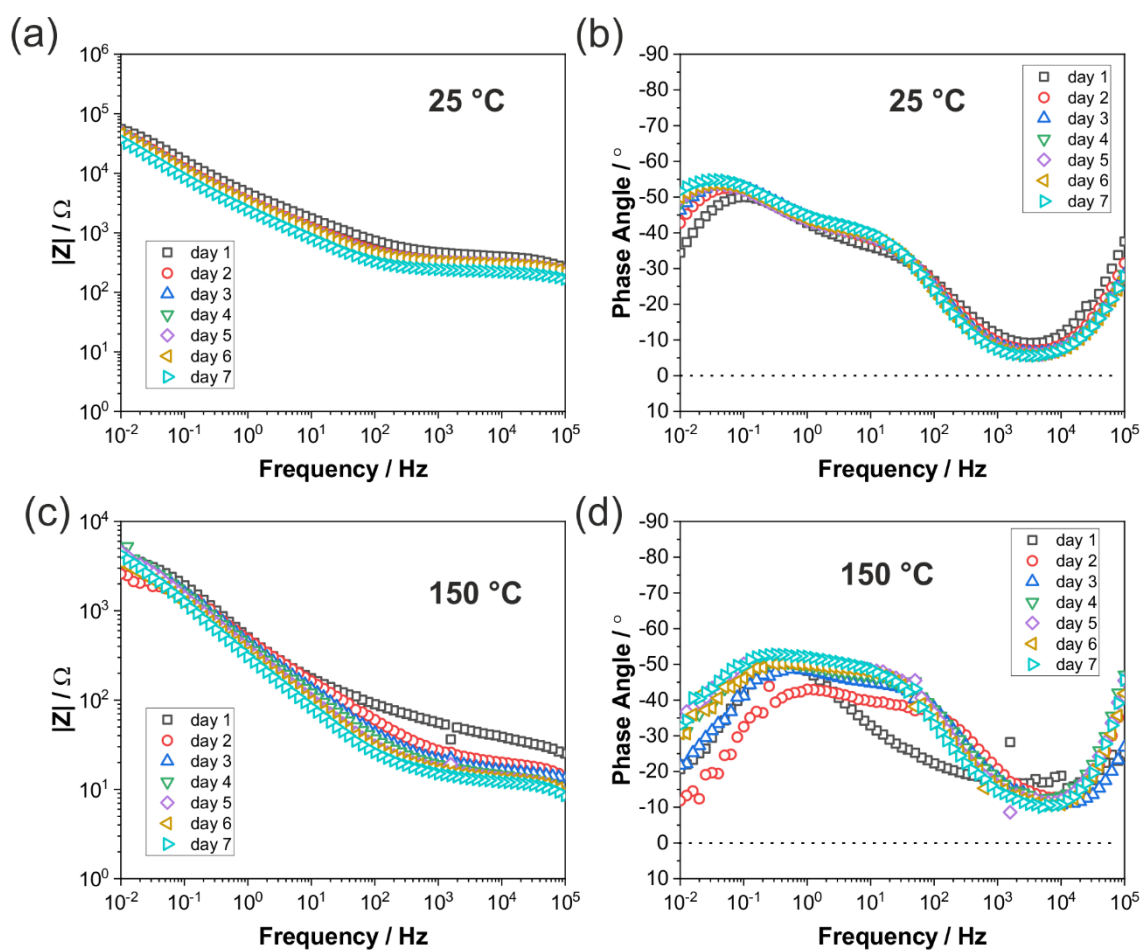


gradual decrease of impedance value at both temperatures. When compared to the early stage monitoring shown by Figure 7.7 (0-12 hours), the decrease of impedance within the first day of exposure occurs at a much higher rate than the decrease of impedance observed between 1 – 7 days (Figure 7.8).

The decrease of the impedance value in coated metal may be associated with the water absorption within the coatings. Stratmann et al reported that the amount of water at the polymer-metal interface was 1.1 mol/L, which is slightly higher than the water concentration in the bulk electrolyte of 0.8 mol/L. They studied the water absorption at metal-polymer interface by investigating alkyd on ZnSe prism coated with 10 nm Fe [144]. Water has a much higher dielectric constant than organic coating, which influences the coating capacitance. It is important to note that although a coating is saturated with water, it can still prevent the electrolyte from reacting with the metal substrate when it adheres tightly to the metal [81].



**Figure 7.7.** Impedance spectra of PANI-1/SiO<sub>2</sub> coating in the artificial geothermal water during the early stage of exposure between 0-12 hours: (a, b) at 25 °C and (c, d) at 150 °C, where (a) and (c) are Bode magnitude plots and (b) and (d) are phase angle plots



**Figure 7.8.** Impedance spectra of PANI-1/SiO<sub>2</sub> coating in the artificial geothermal water between 1 – 7 days: (a, b) at 25 °C and (c, d) at 150 °C, where (a) and (c) are Bode magnitude plots and (b) and (d) are phase angle plots.

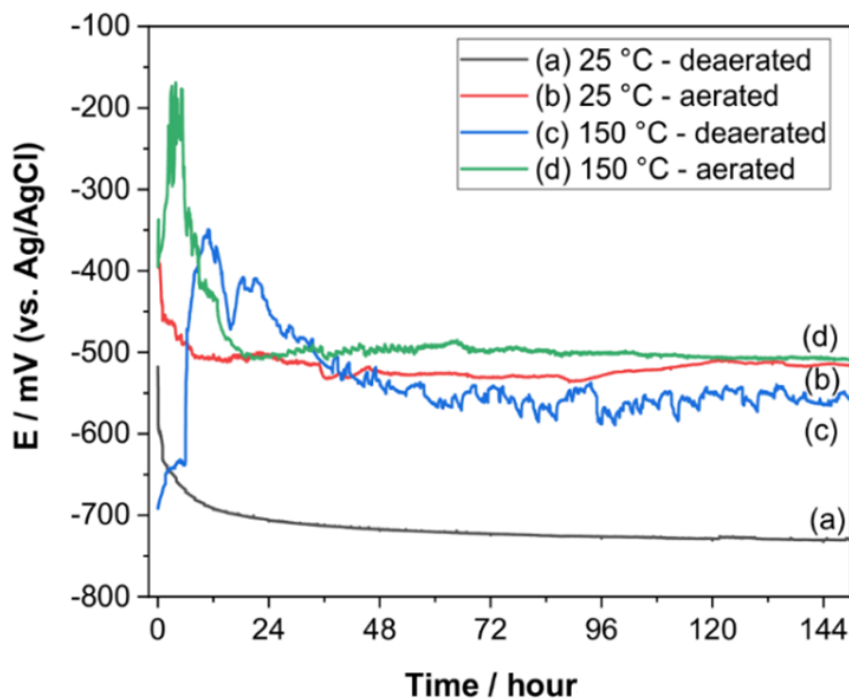
There are several important requirements to utilize organic coating for corrosion protection, such as the permeability of coating to O<sub>2</sub>, H<sub>2</sub>O, and CO<sub>2</sub>, the permeability of coating to the migration of ions, and in conjunction with the mechanical properties. A good protective coating should not have mechanical damage that exposed the metal surface to the testing medium. Ion migration causes electrolytic blister, where blistering is evident by the appearance of pitting which may lead to a coating failure. When the coating is cathodic, the cathodic partial reactions of oxygen reduction reaction (equation 7) or hydrogen evolution in the acidic condition (equation 8) are much less restricted than the anodic part [167].



As indicated by  $E_{\text{corr}}$  monitoring, that the coating has a much lower free corrosion potential than carbon steel, suggesting that the coating provides cathodic protection.

### 7.3. Suitability of Coatings in the Oxygen Containing Solution

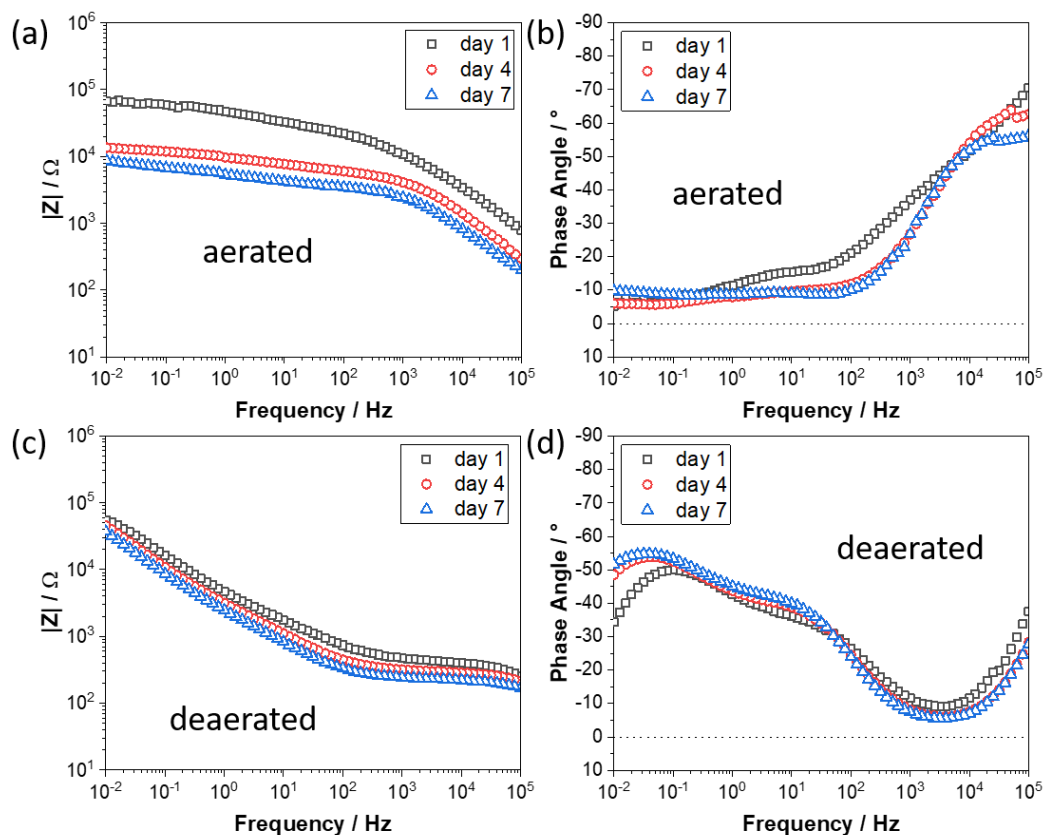
The effect of dissolved oxygen was then also tested in the PANI-1/SiO<sub>2</sub> coating. Figure 7.9 shows the  $E_{\text{corr}}$  of PANI-1/SiO<sub>2</sub> coating at 25 °C and 150 °C in the aerated and deaerated geothermal solution. In general, both experiments share the same data pattern of  $E_{\text{corr}}$  with respect to time, although the values are at different range. At 25 °C, there is a significant potential increase of about 200 mV when the PANI-1/SiO<sub>2</sub> coated specimen is exposed to the aerated geothermal solution. This result is in agreement with the  $E_{\text{corr}}$  of carbon steel under the influence of dissolved oxygen, as shown in Figure 4.10, albeit the  $E_{\text{corr}}$  of carbon steel in the aerated solution is only about 70 mV higher than that measured in the deaerated solution. At 150 °C, the  $E_{\text{corr}}$  of PANI-1/SiO<sub>2</sub> coating in the aerated solution is about 50 mV higher than that measured in the deaerated solution. The presence of oxygen contributes to a more anodic potential of the PANI-1/SiO<sub>2</sub> coating, where the potential difference is more significant at low temperature due to the higher difference of dissolved oxygen concentration. This may also suggest that the PANI-1/SiO<sub>2</sub> coating may inhibit the oxidation of Fe<sup>2+</sup> to Fe<sup>3+</sup> due to the barrier layer properties, even in the presence of oxygen.



**Figure 7.9.**  $E_{\text{corr}}$  of PANI-1/SiO<sub>2</sub> in the deaerated and aerated geothermal solution at 25 °C and 150 °C.

A comparison of EIS at 25 °C is presented in Figure 7.10 in the form of a Bode magnitude plot and phase angle plot. The Bode magnitude plot shows the  $Z_{\text{max}}$  of PANI-1/SiO<sub>2</sub> coating is still decreasing until the 4<sup>th</sup> day, to almost 10 times lower than at the first day in the aerated condition.  $Z_{\text{max}}$  of PANI-1/SiO<sub>2</sub> coating was stable at around  $10^4 - 10^5 \Omega$ , indicating that the degradation is much slower when there is no oxygen present in the solution. Phase angle plots show a different pattern between the measurement performed in the aerated and the deaerated solution, especially in the mid to low frequency region. At the lowest frequency, the PANI-1/SiO<sub>2</sub> coating exposed to the aerated solution has a phase angle of between 0 and -10°, whereas in the deaerated solution, the phase angle was between -30° to -50°, indicating there

might be a more defected area when the coating is exposed to the aerated solution than that exposed to the deaerated solution.



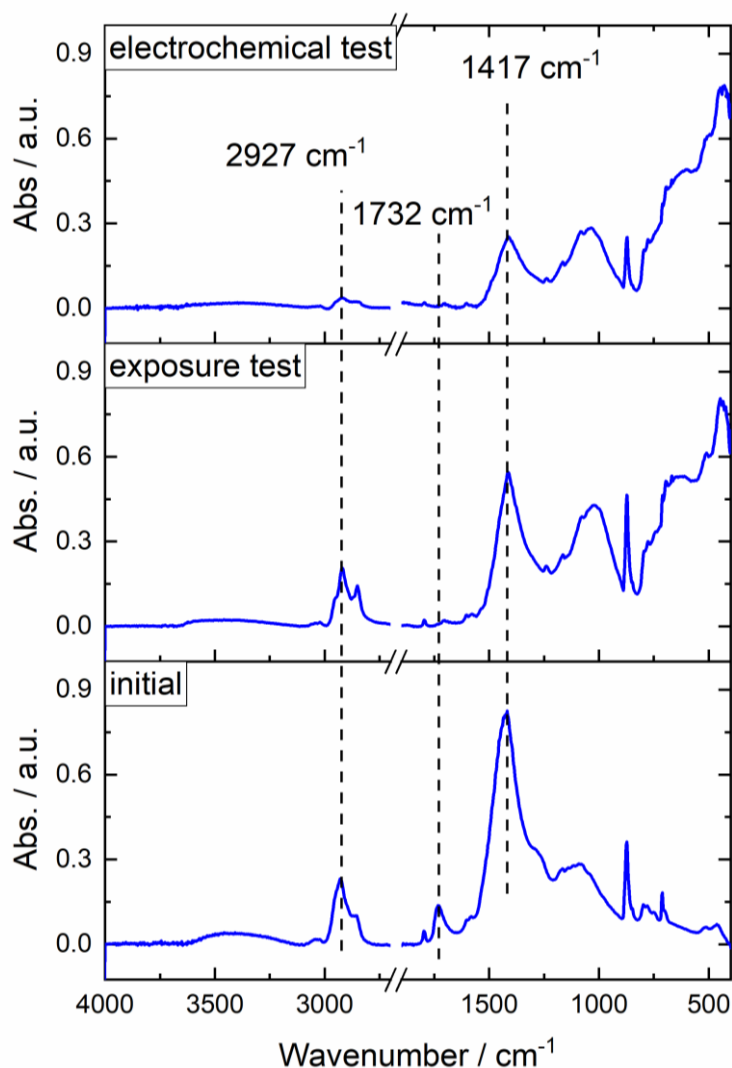
**Figure 7.10.** Impedance spectra of PANI-1/SiO<sub>2</sub> in the deaerated and aerated geothermal solution at 25 °C.

#### 7.4. Compatibility of the Electrochemical Test and Exposure Test at 150 °C

Although electrochemical test is a useful tool to monitor and identify significant electrochemical changes due to the physical and/or chemical changes within the coating, it is a method that utilizes external influence. An additional effect originating from the applied method, therefore, should be identified by comparing the experimental results or the specimens used in these different methods. The specimens after the electrochemical test show that they suffered from a stronger corrosion process compared to the specimens after the exposure test. To further analyze these differences, FTIR spectra were taken from both types of tests and compared to that of the initial state (Figure 7.11).

The peaks of FTIR spectra of specimens after electrochemical and exposure test share similarities, in which the peaks at the lower wavenumber appear with the same pattern and intensity. The peak at 1732 cm<sup>-1</sup> disappears after exposed to the artificial geothermal water at 150 °C for 7 days, using both methods, indicating the functional group of C=O stretching. At 1417 cm<sup>-1</sup>, the absorption peak decreased in both methods, which is associated with the CaCO<sub>3</sub> absorption peak. Other absorption peaks at 2927 and 2850 cm<sup>-1</sup> decrease more in the case of the electrochemical specimen than that of exposure specimen, which is related to the functional group of C-H asymmetric and symmetric stretching, respectively. Thus, a permanent

monitoring using an electrochemical test would affect the coating properties, thereby limiting the use of this technique. Electrochemical test for a monitoring purpose can be used in the early stage of exposure, and this technique should be presented with a comparison to the exposure test results.



**Figure 7.11.** FTIR spectra of PANI-1/SiO<sub>2</sub> specimen before exposure (bottom), after exposure test (middle) and after electrochemical test (upper) in the geothermal solution at 150 °C for seven days.

### 7.5. Durability of Coatings

To evaluate the durability of coatings in the artificial geothermal water, the mass of specimens was measured before and after the exposure to calculate the mass loss. As presented in Table 7.2, there was no significant mass loss over time with a range between 12 to 22 mg up to 6 months of exposure. However, there was no trend in the mass loss data as a function of time. Here, mass loss and mass gain might happen simultaneously, resulting in a change of mass that is more difficult to evaluate. Mass loss can be associated with the degraded coated specimens which then delaminate and detach from the coating to the electrolyte, whereas mass gain originates from water absorption in the coating, which was also discussed in sub chapter 7.2. Thus, the mass loss measurement might indicate a durability of the coating, since the mass changes were small within the different durations of exposure, i.e. below 22 mg.

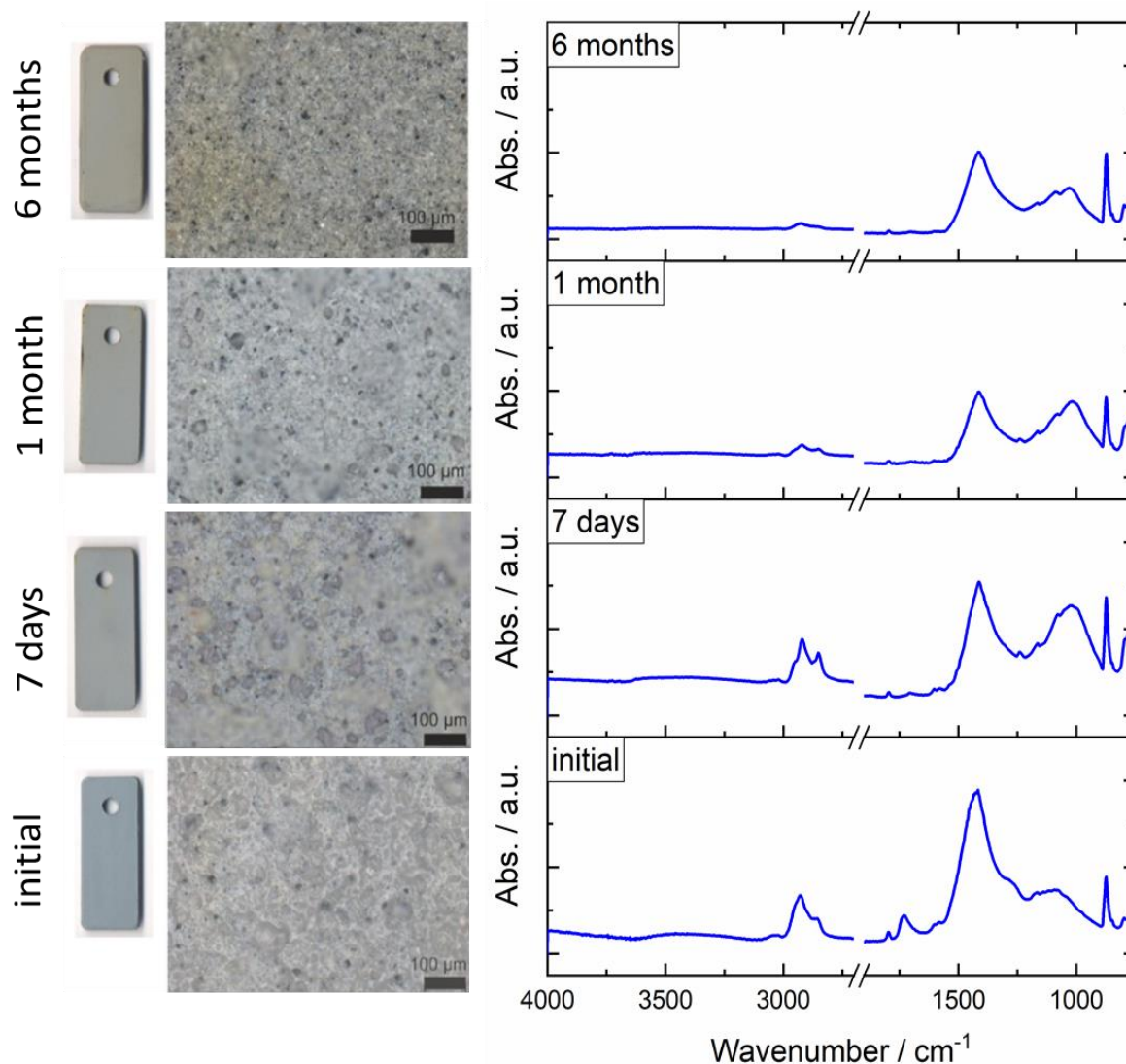
**Table 7.2.** Mass loss of PANI-1/SiO<sub>2</sub> coatings with respect to time

Time (h)	Mass loss (g)			
	Sample 1	Sample 2	Sample 3	Average
24	0.016	0.015	0.013	0.015 ± 0.002
168	0.020	0.019	0.022	0.020 ± 0.002
672	0.014	0.011	0.011	0.012 ± 0.002
4032	0.021	0.024	0.022	0.022 ± 0.002

The macrophotos, optical microscope images, and FTIR spectra show the physical and chemical changes of coatings with immersion time (Figure 7.12). For all specimens, there were no significant physical damage or corrosion on the surface. However, several changes in the IR absorption peaks were evident, indicating that a degradation in the molecular level occurred to a certain extent. For example, C=O stretching of ester at 1725 cm<sup>-1</sup> decreased significantly after seven days of exposure. In addition, C-H asymmetric stretching was still identified at around 2922 cm<sup>-1</sup> after 6 months, although the absorption decreased significantly after only seven days. The same behavior was also observed for the peak of C-H stretching and C=O stretching at 2850 cm<sup>-1</sup> and 1795 cm<sup>-1</sup>, respectively. For these peaks, the significant change was observed between the 7<sup>th</sup> day and 28<sup>th</sup> day of exposure. These changes of absorption peaks show that the polymeric matrix, which is based on alkyd coating was slowly degraded.

The inorganic part of the coatings, which consisted of SiO<sub>2</sub> and CaCO<sub>3</sub> pigments, however, remained intact within the coatings, indicated by the IR absorption peaks as presented in Figure 7.12 and the corresponding IR absorption peak assignment listed in Table 7.3. The polyaniline pigments were also intact, indicated by the dark particles dispersed on the surface, as observed in the optical microscopic images.





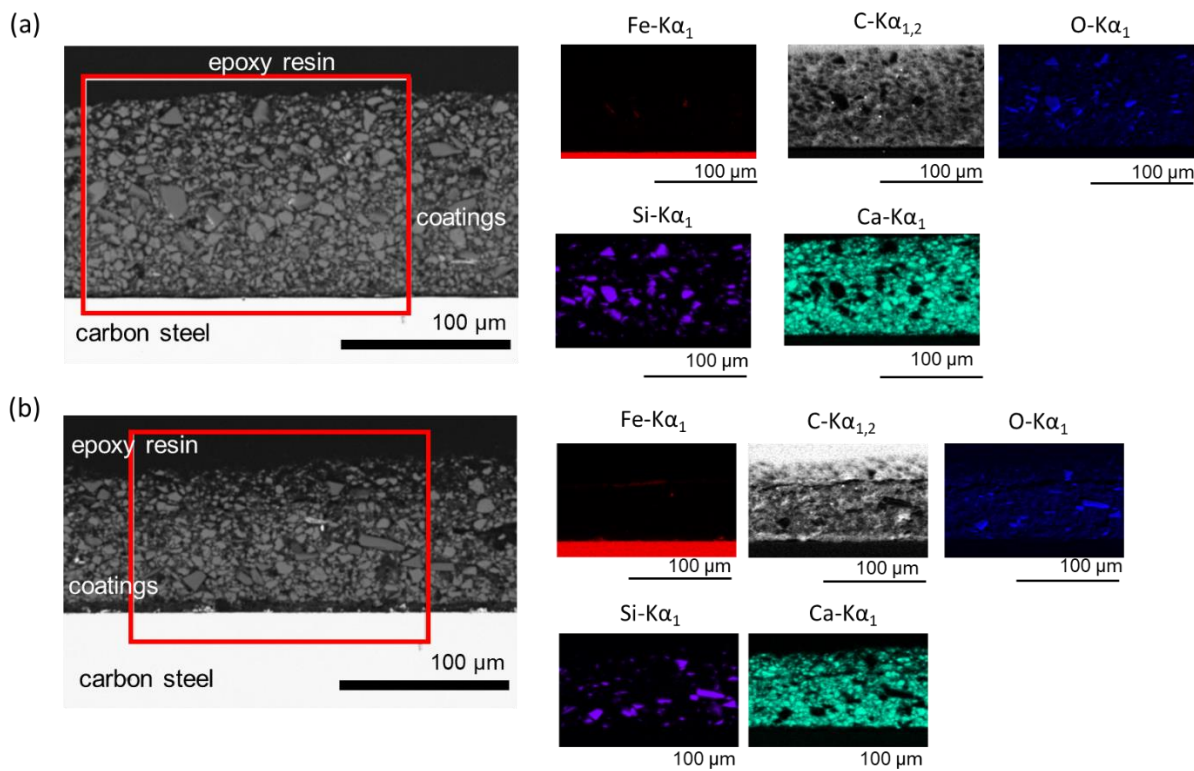
**Figure 7.12.** FTIR spectra evolution of PANI-1/SiO<sub>2</sub> specimen after exposed to the deaerated geothermal solution up to 6 months.

**Table 7.3.** FTIR spectra assignment of PANI-1/SiO<sub>2</sub> coatings after exposed in the artificial geothermal water for different exposure time [112, 143, 164]

Assignment	Wavenumber (cm <sup>-1</sup> )				
	Reference	initial	7 days	1 month	6 months
(C-H) CH <sub>2</sub> asymmetric stretch	2926 ± 10	2923	2916	2922	2927
(C-H) CH <sub>2</sub> symmetric stretch	2855 ± 10	2852	2850	2852	-
C=O stretching	1810 - 1640	1795	1792	1793	-
Aromatic C=O stretching	1730 - 1705	1731	-	-	-
CaCO <sub>3</sub>	1420	1417	1410	1406	1410
-O-Si-O-	1070	1091 <sup>b</sup>	1022	1009	1020
CaCO <sub>3</sub>	875	875	872	872	872
Symmetric SiO <sub>2</sub> bending	779	779	771	777	775

b: broad peak

SEM images of the cross sections revealed that the PANI-1/SiO<sub>2</sub> coating remained intact after exposed in the deaerated geothermal solution at 150 °C for 1 month (Figure 7.13). EDX elemental mapping shows that SiO<sub>2</sub> and CaCO<sub>3</sub> were dense and well-dispersed within the matrix before the exposure test. After exposed to the geothermal solution, there were no significant migration of pigments, as identified by EDX elemental mapping. This result confirms the FTIR spectra, that the inorganic parts of the coatings were stable and intact after exposed to the artificial geothermal water at 150 °C.



**Figure 7.13.** SEM images in backscattered electron mode and EDX elemental mapping of PANI-1/SiO<sub>2</sub> coated carbon steel cross section (a) before and (b) after exposed to the artificial geothermal water at 150 °C for one month.

## 7.6. Conclusion

Throughout the experimental data presented in this chapter, the role of each pigment in the coating toward protecting carbon steel in the geothermal solution was further elucidated. SiO<sub>2</sub>-alkyd coating system was able to prolong the sustainability of coated metals compared to the unmodified alkyd-based coating, albeit only up to 28 days. This improvement might be associated to the contribution of the silicon dioxide thermal expansion coefficient to lower the thermal expansion coefficient of the coating system, which leads to a more compatible thermal expansion coefficient with that of carbon steel. Although thermally enhanced, SiO<sub>2</sub> did not provide any active protection indicated by the change of coating color after 28 days of exposure to the artificial geothermal water to brown/orange associated with the iron oxide. Here, it was confirmed that polyaniline provides active corrosion protection on the carbon steel surface, in which the coating color was not identified as brown/orange after 28 days of exposure test. Thus, a combinational coating PANI-1/SiO<sub>2</sub> was used to improve the coating properties.



The electrochemical test results suggested an indication of cathodic protection, as the  $E_{\text{corr}}$  of PANI-1/SiO<sub>2</sub> remained in a lower potential region compared to the carbon steel potential. The impedance spectra of the combinational coating of PANI-1/SiO<sub>2</sub> show that there was a decrease in impedance of about ten times when the coating was used at 150 °C compared to 25 °C. It was also highlighted that there was a continuous decrease in the absolute impedance value over time, in which the highest decrease was observed within one day of exposure, followed by a slow gradual decrease, which might be associated with water absorption in the coating. The long-term exposure test of the combinational coating of PANI-1/SiO<sub>2</sub> shows that there were no blisters or discoloration of coatings after 6 months exposed to the artificial geothermal water, indicating that this type of coating is a promising candidate for use in the construction material of geothermal powerplants.

Nonetheless, there are several limitations of PANI-1/SiO<sub>2</sub> usage as identified during the experimental tests. The coating performance of PANI-1/SiO<sub>2</sub> decreased when exposed to the oxygen containing solution at 150 °C. Here, further optimization is required to prevent coating degradation caused by thermoxidative reaction, for example by investigating the effect of the ratio of each coating component on the physicochemical properties of the coating system. Another limitation regarding the testing method was also addressed, in which the different testing methods were compared, i.e. electrochemical and exposure test, suggesting that the coating is sensitive to external electrochemical treatment. Thus, an electrochemical investigation should only be used for a short time frame, for example to investigate the electrochemical behavior of the coating in the early stage of exposure or to compare exposed coatings once after a certain time. However, it should always be accompanied by the exposure test.



# Chapter 8. Conclusion and Outlook

This chapter presents the major findings and conclusions drawn by the experimental studies to address the research objectives, in which their relevance to industrial practicalities are also taken into account. Furthermore, the novel aspects of the work are elaborated with respect to their importance, leading to some ideas regarding recommendations for future work toward corrosion protection in the geothermal environment.

## 8.1. Conclusion

Exploring the problems and understanding the main influencing factors behind the corrosion mechanism of carbon steel for use in geothermal applications are important steps to develop a corrosion protection strategy. When possible, a corrosion prediction model in the geothermal power plant is a powerful tool to estimate the longevity of the powerplant, consequently to manage the maintenance of a powerplant.

Based on the available knowledge in the literature, a major problem of understanding the main influencing factors of corrosion on carbon steel in a specific geothermal location is the lack of consistency in terms of the geothermal water composition, the operating temperature and pressure, the pH, and the content of dissolved gas in the solution. As each geothermal resource has its unique physical and chemical properties, the results of a corrosion study in a specific geothermal location cannot be generalized for all geothermal applications. To overcome these limitations and challenges, which might be viewed as a major gap, the first research objective was to identify and analyze the corrosion processes of carbon steel in Sibayak based on artificial geothermal water with different influencing factors, i.e. temperature, oxygen content, and pH, which was discussed in detail in Chapter 4.

Carbon steel underwent the most severe corrosion at 150 °C in the presence of oxygen, shown by a corrosion rate of 0.34 mm/year and pitting corrosion of 20 µm within seven days of exposure. Under this condition, carbon steel exhibits low corrosion resistance according to the EIS measurement. These experimental results showed that the oxygen partial pressure in the composition of geothermal well has significant aggressiveness in conjunction with the increasing temperature (with a temperature limitation at 150 °C). However, with and without the presence of oxygen, pitting corrosion was observed, which necessitate a protection strategy on carbon steel for use in the geothermal environment.

In an attempt to implement a protective coating which can yield good corrosion resistance and thermal stability in the geothermal environment in Indonesia, two additional components were used to modify the alkyd-based commercial coating, i.e. polyaniline and silicon dioxide. The selection of the inorganic and organic part of the filler focuses on the industrial convenience basis, where the coating application procedure should be simple and easy to apply at a reasonable cost. The raw materials of alkyd-based coating and silicon dioxide are locally available in Indonesia, which may also lower the production and process cost. Silicon dioxide can be synthesized from local resources and there is a possibility to further develop silicon dioxide obtained from the scaling of a geothermal site. Accordingly, this alternative will offer a competitive option when set against other available materials, such as stainless steel, or high alloyed steel.

Polyaniline, which has been widely developed over the past decades, was chosen as one of the anticorrosion pigments. To observe the interaction of the polyaniline layer and the geothermal solution, the polyaniline coated carbon steel was exposed to the artificial geothermal water at 25 °C and 150 °C, as discussed in Chapter 5. Electrochemical deposition of polyaniline on carbon steel requires a careful selection of acids, potential range, monomer to acid ratio, and the cycle number to obtain a controllable layer of pure polyaniline. Electrochemically synthesized polyaniline is protective against corrosion in chloride-sulfate containing solution at room temperature. It is, however, prone to the scaling of Ca as observed on the surface of polyaniline coated carbon steel after the test at room temperature and 150 °C. This suggests that there is an interaction of ionic species, such as  $\text{Cl}^-$ ,  $\text{Na}^+$ ,  $\text{Ca}^{2+}$  from the artificial geothermal water with the PANI coated carbon steel, regardless of the temperature. The experimental results suggest that the protection mechanism of polyaniline is not solely based on the physical barrier layer properties, but rather associated with the redox-mediated properties of polyaniline, which selectively allow ionic species intrusion from the electrolyte into the polyaniline layer. At 150 °C, PANI coated carbon steel is not thermally stable as revealed by the morphological characterization. Based on these results, polyaniline is a promising candidate as an anticorrosion agent in the coating system, but its thermal stability needs further improvement to have a better functionality at 150 °C.

Chapter 6 presented the chemical and morphological analysis of the alkyd-based coating before and after exposed to the artificial geothermal water. The individual roles of polyaniline and  $\text{SiO}_2$  in combination with the alkyd-based coating on the corrosion behavior of coated carbon steel were then further discussed. The alkyd-based coating was filled with  $\text{CaCO}_3$ , which led to blisters when exposed to the artificial geothermal water. In the oxygen free solution, the degradation was controlled by chemical and thermal reactions, whereas in the aerated condition, oxygen further accelerated the polymer degradation. The chemical and morphological characterization of PANI-alkyd and  $\text{SiO}_2$ -alkyd coating system showed that coatings were improved, albeit the degradation continued. To optimize the properties of both systems, a combination of both pigments was implemented.

Chapter 7 explored the use of both polyaniline and silicon dioxide as a combinational coating system.  $\text{SiO}_2$ -alkyd coating system was able to prolong the sustainability of coated metals compared to the unmodified alkyd-based coating, albeit only for short-term application. This improvement might be associated with the role of silicon dioxide to proportionate the thermal expansion coefficient of the coating system to be compatible with that of carbon steel. Although thermally enhanced, the electrolyte might still intrude through the coating, resulting in the change of coating color after 28 days of exposure in the artificial geothermal water to brown/orange associated with the iron oxide. Polyaniline was added to the coating system, in which the coating color was not identified as brown/orange after 28 days of exposure, indicating active corrosion protection on the carbon steel surface. The combinational coating of PANI- $\text{SiO}_2$  shows that there are no blisters or discoloration of coatings after 6 months exposed to the artificial geothermal water. The weight loss after 6-month exposure was negligible and did not differ from that of 1-week exposure, indicating that this type of coating is a promising candidate for use in the construction material of geothermal powerplants.

## 8.2. Novel Aspects and Relevance to Future Work and Industry

Based on the experimental results, some key findings are outlined with relevance to industrial application and future work in this field, as presented in the scheme in Figure 8.1. This section describes some novel aspects of the study:

*1. The corrosion behavior of carbon steel at 150 °C in the Sibayak geothermal solution with and without the influence of dissolved oxygen was thoroughly explored.*

This was the first time that the corrosion behavior of carbon steel (St37) has been investigated in such geothermal solution in conjunction with the effect of dissolved oxygen. Uniform corrosion and pitting corrosion were observed both in the deaerated and aerated artificial geothermal water. The corrosion mechanism was discussed, which leads to a better understanding of carbon steel corrosion processes when exposed to a geothermal medium. Based on the experimental results, it is noteworthy to include the type of dissolved gases in the lab-scale experiment, as it may further accelerate the corrosion processes on carbon steel.

*2. The implementation of electrochemically deposited oxalate-doped PANI for corrosion protection in artificial geothermal water.*

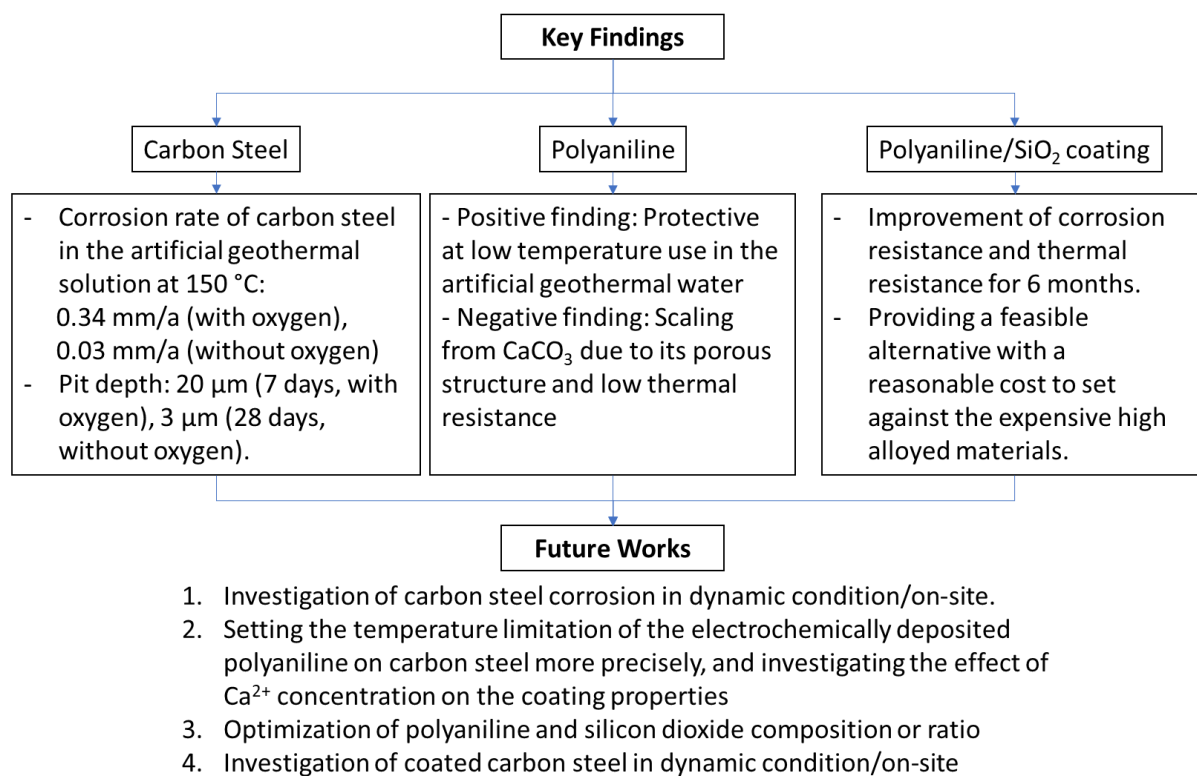
It was proven that electrochemically deposited oxalate-doped polyaniline provides corrosion protection by allowing the ionic species of the electrolyte to pass through the film selectively. However, it is thermally unstable, which requires further modification for high temperature application purposes. The oxalate-doped PANI promotes Ca deposition regardless of applied temperature, possibly due to the amount of  $\text{Ca}^{2+}$  available in the electrolyte.

*3. The development and implementation of in-situ electrochemical test of coated metals at high temperature.*

To date, the electrochemical test in autoclaves at 150 °C has not been extensively used for coated metal, only used previously for metallic materials. Electrochemical measurements indicated the evolution of material degradation or protection related to the exposure time. By measuring the  $E_{\text{corr}}$  and analyzing the impedance spectra of the uncoated carbon steel, iron oxide growth could be identified. It was also possible to determine that the most crucial changes of coating properties occurred within the first few hours, by monitoring the change in the impedance spectra. Electrochemical measurements should be in conjunction with the exposure test as well as other chemical and morphological characterization.

*4. The development of a coating system focusing on the convenience of industrial basis by a simple coating application and utilizing locally available resources.*

By implementing the available alkyd-based coating and silicon dioxide from natural silica sand in Indonesia, an affordable alternative coating system was developed to set against the expensive high alloyed materials. The PANI-1/SiO<sub>2</sub> modified alkyd coating was able to protect carbon steel in the artificial geothermal water for at least 6 months.



**Figure 8.1.** An overview of the key findings and their relevance to possible future work

### 8.3. Outlook

This work has successfully combined the electrochemical test at high temperature and other chemical analyses to understand the protection and degradation of PANI-1/SiO<sub>2</sub>-alkyd coatings used to protect carbon steel in the artificial geothermal water. However, there are many other aspects that can be explored and developed. Some extensions and future works are recommended, as follows.

#### *1. Investigation of carbon steel corrosion in a dynamic condition / on-site test.*

Research on the temperature gradient and temperature cycles to simulate the operation condition during the initial stage and maintenance process. Using a dynamic flowing electrolyte to investigate the effect of fluid velocity as well as the possibility of turbulence. Other dissolved gases found in different geothermal systems, such as carbon dioxide and hydrogen sulfide, need to be considered in the corrosion test rig.

#### *2. Setting the temperature limitation of the electrochemically deposited polyaniline on carbon steel and investigating the effect of Ca<sup>2+</sup> concentration on the coating properties.*

The present work showed the corrosion behavior of polyaniline coated carbon steel at 25 °C and 150 °C, which is a relatively wide range. For the use in geothermal applications, it would be helpful to establish a temperature limitation by testing the polyaniline coated carbon steel at different temperatures systematically, between room temperature and 150 °C. As Ca deposition was observed, this indicates that polyaniline is susceptible to the scaling of Ca from the solution. Electrochemical test and exposure test of polyaniline coated carbon steel in a pure CaCl<sub>2</sub>

solution and NaCl solution to observe the maximum amount of  $\text{Ca}^{2+}$  affecting deposition on polyaniline, which can be fundamental to the proportion of polyaniline to Ca to avoid scaling and to understand the protective behavior on carbon steel.

*3. Optimization of polyaniline and silicon dioxide composition and the development of other coating types.*

This work focuses on the role of individual components of pigments in the coating with a reasonable composition based on the recent knowledge reported in the literature. However, the role of pigments in improving the coating is strongly related to the coating composition, which necessitates further optimization based on the composition. In addition, the protective behavior of polyaniline and silicon dioxide might also be applied for other types of binder. Other types of pigments, such as ZrO, could also be developed for this purpose.

*4. Investigation of PANI-1/SiO<sub>2</sub>-alkyd coated carbon steel in a dynamic condition/on-site test.*

Similar to that of carbon steel, other effects of the environment could be further explored to widen the possible application of the coating. Several possibilities include investigating the coatings in different geothermal medium (chemical composition, temperature, pressure), and performing an on-site test at the geothermal site. In addition, other properties of the coating should be further investigated using various material testing methods, such as contact angle measurement, mechanical testing, crevice corrosion investigation, and stress corrosion cracking.





# Bibliography

- [1] Geothermal World Energy Resources 2016, World Energy Council, 2016.
- [2] I. Stober, K. Bucher, Geothermal Energy: From Theoretical Models to Exploration and Development, Springer Science & Business Media, 2013.
- [3] S. Darma, Indonesia: Vast geothermal potential, modest but growing exploitation, Geothermal Power Generation, Elsevier, 2016, pp. 609-643.
- [4] J.P. Atmojo, R. Itoi, T. Tanaka, M. Fukuda, S. Sudarman, A. Widiyarso, Modeling studies of Sibayak geothermal reservoir, Northern Sumatra, Indonesia, 2000, pp. 2037–2042.
- [5] M.P. Hochstein, S. Sudarman, Indonesian Volcanic Geothermal Systems, Geothermische Energie, 2017, pp. 20-22.
- [6] N. Mundhenk, P. Huttenloch, B. Sanjuan, T. Kohl, H. Steger, R. Zorn, Corrosion and scaling as interrelated phenomena in an operating geothermal power plant, Corrosion Science 70 (2013) 17-28.
- [7] A. Keserovic, Geothermal systems in Indonesia, Dissertation, TU Berlin, 2014.
- [8] A. Keserovic, Suitability of Alloyed Steels in Highly Acidic Geothermal Environments, NACE Corrosion, 2014, pp. 4031.
- [9] A. Keserovic, Material Evaluation for Application in Geothermal Systems in Indonesia, NACE Corrosion, 2013, pp. 2269.
- [10] R. Bäßler, A. Keserović, J. Sobetzki, H.S. Klapper, M. Dimper, Materials Evaluation for Geothermal Applications in Different Geothermal Waters, World Geothermal Congress, 2015.
- [11] R. Bertani, Geothermal Power Generation in the World 2010-2014. Update Report.
- [12] J.W. Tester, E.M. Drake, M.J. Driscoll, M.W. Golay, W.A. Peters, Sustainable Energy: Choosing Among Options, second edition edition ed., The MIT Press, Cambridge, MA, 2012.
- [13] A.J. Ellis, W.A.J. Mahon, Chemistry and geothermal systems, New York: Academic Press, 1977.
- [14] K. Nicholson, Geothermal Fluids: Chemistry and Exploration Techniques, Springer-Verlag, Berlin Heidelberg, 1993.
- [15] G. Stáhl, G. Pátzay, L. Weiser, E. Kálmán, Study of calcite scaling and corrosion processes in geothermal systems, Geothermics 29 (2000) 105-119.
- [16] R.R. Reeber, Coatings in geothermal energy production, Thin Solid Films 72 (1980) 33-48.
- [17] T. Sugama, R. Webster, W. Reams, K. Gawlik, High-performance polymer coatings for carbon steel heat exchanger tubes in geothermal environments, Journal of Materials Science 35 (2000) 2145-2154.
- [18] K. Belas-Dacillo, A.C. de Leon, A.C.R. Panopio, R.C. Advincula, Evaluating Protective Coatings and Metal Alloys in Acidic Geothermal Fluids Using Laboratory Techniques, World Geothermal Congress, 2015.
- [19] E. Armelin, R. Oliver, F. Liesa, J.I. Iribarren, F. Estrany, C. Alemán, Marine paint formulations: Conducting polymers as anticorrosive additives, Progress in Organic Coatings 59 (2007) 46-52.

- [20] U. Rammelt, P.T. Nguyen, W. Plieth, Corrosion protection by ultrathin films of conducting polymers, *Electrochimica Acta* 48 (2003) 1257-1262.
- [21] C.K. Tan, D.J. Blackwood, Corrosion protection by multilayered conducting polymer coatings, *Corrosion Science* 45 (2003) 545-557.
- [22] G.G. Wallace, P.R. Teasdale, G.M. Spinks, L.A.P. Kane-Maguire, *Conductive Electroactive Polymers: Intelligent Polymer Systems*, Third Edition, CRC Press, 2008.
- [23] E. Armelin, C. Ocampo, F. Liesa, J.I. Iribarren, X. Ramis, C. Alemán, Study of epoxy and alkyd coatings modified with emeraldine base form of polyaniline, *Progress in Organic Coatings* 58 (2007) 316-322.
- [24] A. Kalendová, I. Sapurina, J. Stejskal, D. Veselý, Anticorrosion properties of polyaniline-coated pigments in organic coatings, *Corrosion Science* 50 (2008) 3549-3560.
- [25] W.-K. Lu, R.L. Elsenbaumer, B. Wessling, Corrosion protection of mild steel by coatings containing polyaniline, *Synthetic Metals* 71 (1995) 2163-2166.
- [26] J. Nogara, S.J. Zarrouk, Corrosion in geothermal environment: Part 1: Fluids and their impact, *Renewable and Sustainable Energy Reviews* 82 (2018) 1333-1346.
- [27] H.C.H.e. Armstead, *Geothermal energy. Review of research and development*, United Nations Educational, Scientific and Cultural Organization, Paris, 1973.
- [28] N. Hidayat, Istiqomah, M.Y.H. Widiyanto, A. Taufiq, Sunaryono, Triwikantoro, M. Zainuri, M.A. Baqiya, G. Aristia, S. Pratapa, Natural Silica Sand/Alumina Ceramic Composites: Promising Candidates for Fuel-Cell Sealants, *IOP Conference Series: Materials Science and Engineering* 202 (2017) 012060.
- [29] Munasir, A. Sulton, Triwikantoro, M. Zainuri, Darminto, Synthesis of silica nanopowder produced from Indonesian natural sand via alkalifussion route, *International Conference On Theoretical and Applied Physics (ICTAP 2012)*, AIP Publishing, 2013, pp. 28-31.
- [30] R. Yuvakkumar, V. Elango, V. Rajendran, N. Kannan, High-purity nano silica powder from rice husk using a simple chemical method, *Journal of Experimental Nanoscience* 9 (2014) 272-281.
- [31] A. Richter, Indonesia reaches 1,925 MW installed geothermal power generation capacity, *Think GeoEnergy - Geothermal Energy News*.
- [32] W.E. Glassley, *Geothermal Energy: Renewable Energy and the Environment*, CRC Press, 2011.
- [33] M.H. Dickson, M. Fanelli, *Geothermal Energy: Utilization and Technology*, Earthscan, New York, NY, 2005.
- [34] C.N. Hance, *Factors Affecting Costs of Geothermal Power Development*, Geothermal Energy Association for the U.S. Department of Energy, 2005.
- [35] R. Bertani, Geothermal power generation in the world 2005–2010 update report, *Geothermics* 41 (2012) 1-29.
- [36] R.J.G. Bertani, Geothermal power generation in the world 2010–2014 update report, 60 (2016) 31-43.
- [37] A. Richter. Indonesia expects an addition of 255 MW geothermal capacity in 2018. *Think GeoEnergy - Geothermal Energy News*.

- [38] C.R. Davison, T.A. Rutke, Assessment and Characterization of Volcanic Ash Threat to Gas Turbine Engine Performance, *Journal of Engineering for Gas Turbines and Power* 136 (2014) 081210.
- [39] I.B. Fridleifsson, D.H. Freeston, Geothermal energy research and development, *Geothermics* 23 (1994) 175-214.
- [40] E. Barbier, Geothermal energy technology and current status: an overview, *Renewable and Sustainable Energy Reviews* 6 (2002) 3-65.
- [41] R. DiPippo, *Geothermal Power Plants: Principles, Applications and Case Studies*, Elsevier, 2005.
- [42] Ó.G. Flóvenz, K. Saemundsson, Heat flow and geothermal processes in Iceland, *Tectonophysics* 225 (1993) 123-138.
- [43] B. Lund, M.D. Zoback, Orientation and magnitude of in situ stress to 6.5 km depth in the Baltic Shield, *International Journal of Rock Mechanics and Mining Sciences* 36 (1999) 169-190.
- [44] H. Sigurdsson, B. Houghton, S. McNutt, H. Rymer, J. Stix, *The encyclopedia of volcanoes*, Elsevier, 2015.
- [45] Geothermal gradient, *Geology IN*. [www.geologyin.com](http://www.geologyin.com)
- [46] K. Hirowatari, Scale prevention method by brine acidification with biochemical reactors, *Geothermics* 25 (1996) 259-270.
- [47] E. Huenges, P. Ledru, *Geothermal Energy Systems: Exploration, Development, and Utilization*, John Wiley & Sons, 2011.
- [48] R. Corsi, Scaling and corrosion in geothermal equipment: problems and preventive measures, *Geothermics* 15 (1986) 839-856.
- [49] W.D. Callister, D.G. Rethwisch, *Materials Science and Engineering: An Introduction*, 9th Edition: Ninth Edition, Wiley, 2013.
- [50] R.L. Miller, *Chemistry and Materials in Geothermal Systems*, (1980).
- [51] P. Muffler, R. Cataldi, Methods for Regional Assessment of Geothermal Resources, *Geothermics* 7 (1978) 53-89.
- [52] M.P. Hochstein, Assessment and Modelling of Geothermal Reservoirs (Small Utilization Schemes), *Geothermics* 17 (1988) 15-49.
- [53] Y. Benderitter, G. Cormy, Possible approach to geothermal research and relative cost estimate, 1990, pp. 59-69.
- [54] R. Haenel, L. Rybach, L. Stegena, *Fundamentals of Geothermics, Handbook of Terrestrial Heat-Flow Density Determination*, Springer, Dordrecht 1988, pp. 9-57.
- [55] E.E. Stansbury, R.A. Buchanan, *Fundamentals of electrochemical corrosion*, ASM international, 2000.
- [56] M.G. Fontana, *Corrosion Engineering*, Tata McGraw-Hill, 2005.
- [57] A. Groysman, *Corrosion for Everybody*, Springer, 2010.
- [58] N. Perez, *Electrochemistry and Corrosion Science*, Springer, 2016.
- [59] R. Baessler, A. Burkert, A. Saadat, R. Kirchheiner, M. Finke, Evaluation Of Corrosion Resistance Of Materials For Geothermal Applications, *CORROSION 2009*, NACE International, 2009.

- [60] C. Farrar, *The Alloy Tree: A Guide to Low-Alloy Steels, Stainless Steels and Nickel-Base Alloys*, Elsevier, 2004.
- [61] H. Okamoto, T. Massalski, Binary alloy phase diagrams requiring further studies, *Journal of phase equilibria* 15 (1994) 500-521.
- [62] A. Khalifeh, A.D. Banaraki, H.D. Manesh, M.D. Banaraki, Investigating of the tensile mechanical properties of structural steels at high strain rates, *Materials Science and Engineering: A* 712 (2018) 232-239.
- [63] P.F. Ellis, *Companion Study Guide to Short Course on Geothermal Corrosion and Mitigation in Low Temperature Geothermal Heating Systems*, Radian Corporation, Austin, Texas, 1985.
- [64] I. Czernichowski-Lauriol, C. Fouillac, The chemistry of geothermal waters: its effects on exploitation, *Terra Nova* 3 (1991) 477-491.
- [65] S. Regenspurg, T. Wiersberg, W. Brandt, E. Huenges, A. Saadat, K. Schmidt, G. Zimmermann, Geochemical properties of saline geothermal fluids from the in-situ geothermal laboratory Groß Schönebeck (Germany), *Chemie der Erde - Geochemistry* 70 (2010) 3-12.
- [66] P. Iberl, N. Alt, E.J.M. Schluecker, Corrosion, Evaluation of corrosion of materials for application in geothermal systems in Central Europe, 66 (2015) 733-755.
- [67] H.R. Copson, Effects of Velocity on Corrosion by Water, *Industrial & Engineering Chemistry* 44 (1952) 1745-1752.
- [68] M. Conover, P. Ellis, A. Curzon, *Material Selection Guidelines for Geothermal Power Systems—An Overview*, (1980).
- [69] J.P. Carter, S.D. Cramer, *Materials of construction for high-salinity geothermal brines*, U.S. Dept. of the Interior, Bureau of Mines, 1992.
- [70] R.W. Revie, *Uhlig's Corrosion Handbook*, Wiley, 2005.
- [71] J.J. Santana Rodríguez, F.J. Santana Hernández, J.E. González González, Mathematical and electro-chemical characterisation of the layer of corrosion products on carbon steel in various environments, *Corrosion Science* 44 (2002) 2597-2610.
- [72] R.M. Cornell, U. Schwertmann, *The Iron Oxides*, Wiley, 1996.
- [73] Y. Waseda, S. Suzuki, Y. Waseda, *Characterization of corrosion products on steel surfaces*, Springer, 2006.
- [74] P. Dhaiweegan, N. Elangovan, T. Nishimura, N. Rajendran, Weathering Steel in Industrial-Marine-Urban Environment: Field Study, *Materials Transactions* 57 (2016) 148-155.
- [75] N. Mundhenk, P. Huttenloch, T. Kohl, H. Steger, R. Zorn, Metal corrosion in geothermal brine environments of the Upper Rhine graben – Laboratory and on-site studies, *Geothermics* 46 (2013) 14-21.
- [76] H.S. Klapper, R. Bäßler, J. Sobetzki, K. Weidauer, D. Stürzbecher, Corrosion resistance of different steel grades in the geothermal fluid of Molasse Basin, *Materials and Corrosion* 64 (2013) 764-771.
- [77] C.G. Munger, L.D. Vincent, *Corrosion Prevention by Protective Coatings*, NACE International, 2014.
- [78] G. Batis, N. Kouloumbi, K.J.G. Kotsakou, Corrosion and protection of carbon steel in low enthalpy geothermal fluids. The case of Sousaki in Greece, 26 (1997) 65-82.
- [79] *Corrosion Tests and Standards*, ASTM International.

- [80] D. Solomon, J. Hopwood, Reactivity of functional groups in surface coating polymers. Part I. Hydroxyl groups in alkyd resins, *Journal of Applied Polymer Science* 10 (1966) 981-991.
- [81] O. Knudsen, A. Forsgren, *Corrosion Control Through Organic Coatings*, Boca Raton: CRC Press, 2017.
- [82] L.W. McKeen, 4 - Binders, in: L.W. McKeen (Ed.), *Fluorinated Coatings and Finishes Handbook*, William Andrew Publishing, Norwich, NY, 2006, pp. 45-58.
- [83] C.O. Baker, X. Huang, W. Nelson, R.B. Kaner, Polyaniline nanofibers: broadening applications for conducting polymers, *Chemical Society Reviews* 46 (2017) 1510-1525.
- [84] G.G. Wallace, T.W. Lewis, L.A.P. Kane-Maguire, *Conductive Polymers*, Encyclopedia of Smart Materials, John Wiley & Sons, Inc., 2002.
- [85] P.P. Deshpande, D. Sazou, *Corrosion Protection of Metals by Intrinsically Conducting Polymers*, CRC Press, 2016.
- [86] F. Beck, Electrodeposition of polymer coatings, *Electrochimica Acta* 33 (1988) 839-850.
- [87] B. Wessling, Passivation of metals by coating with polyaniline: corrosion potential shift and morphological changes, *Advanced Materials* 6 (1994) 226-228.
- [88] N. Ahmad, A.G. MacDiarmid, Inhibition of corrosion of steels with the exploitation of conducting polymers, *Synthetic Metals* 78 (1996) 103-110.
- [89] D.E. Tallman, G. Spinks, A. Dominis, G.G. Wallace, Electroactive conducting polymers for corrosion control, *Journal of Solid State Electrochemistry* 6 (2002) 73-84.
- [90] D.W. DeBerry, Modification of the Electrochemical and Corrosion Behavior of Stainless Steels with an Electroactive Coating, *Journal of The Electrochemical Society* 132 (1985) 1022-1026.
- [91] A. Nautiyal, S. Parida, Comparison of polyaniline electrodeposition on carbon steel from oxalic acid and salicylate medium, *Progress in Organic Coatings* 94 (2016) 28-33.
- [92] B.N. Grgur, A.R. Elkais, M.M. Gvozdenović, S.Ž. Drmanić, T.L. Trišović, B.Z. Jugović, Corrosion of mild steel with composite polyaniline coatings using different formulations, *Progress in Organic Coatings* 79 (2015) 17-24.
- [93] B. Wessling, Corrosion prevention with an organic metal (polyaniline): surface ennobling, passivation, corrosion test results, *Materials and Corrosion* 47 (1996) 439-445.
- [94] T. Schauer, A. Joos, L. Dulog, C.D. Eisenbach, Protection of iron against corrosion with polyaniline primers, *Progress in Organic Coatings* 33 (1998) 20-27.
- [95] A.J. Dominis, G.M. Spinks, G.G. Wallace, Comparison of polyaniline primers prepared with different dopants for corrosion protection of steel, *Progress in Organic Coatings* 48 (2003) 43-49.
- [96] M. Kendig, M. Hon, L. Warren, 'Smart' corrosion inhibiting coatings, *Progress in Organic Coatings* 47 (2003) 183-189.
- [97] P. Kinlen, Y. Ding, D. Silverman, Corrosion protection of mild steel using sulfonic and phosphonic acid-doped polyanilines, *Corrosion* 58 (2002) 490-497.
- [98] M. Rohwerder, A. Michalik, Conducting polymers for corrosion protection: What makes the difference between failure and success?, *Electrochimica Acta* 53 (2007) 1300-1313.

- [99] A.R. Elkais, M.M. Gvozdenović, B.Z. Jugović, B.N. Grgur, The influence of thin benzoate-doped polyaniline coatings on corrosion protection of mild steel in different environments, *Progress in Organic Coatings* 76 (2013) 670-676.
- [100] T.D. Nguyen, T.A. Nguyen, M. Pham, B. Piro, B. Normand, H. Takenouti, Mechanism for protection of iron corrosion by an intrinsically electronic conducting polymer, *Journal of Electroanalytical Chemistry* 572 (2004) 225-234.
- [101] S. Sathiyarayanan, S. Dhawan, D. Trivedi, K. Balakrishnan, Soluble conducting poly ethoxy aniline as an inhibitor for iron in HCl, *Corrosion Science* 33 (1992) 1831-1841.
- [102] J.O. Iroh, W. Su, Corrosion performance of polypyrrole coating applied to low carbon steel by an electrochemical process, *Electrochimica acta* 46 (2000) 15-24.
- [103] B. Mysen, P. Richet, Chapter 5 - Silica, in: B. Mysen, P. Richet (Eds.), *Silicate Glasses and Melts (Second Edition)*, Elsevier, 2019, pp. 143-183.
- [104] P. Richet, Y. Bottinga, L. Denielou, J. Petitot, C. Tequi, Thermodynamic properties of quartz, cristobalite and amorphous SiO<sub>2</sub>: drop calorimetry measurements between 1000 and 1800 K and a review from 0 to 2000 K, *Geochimica et Cosmochimica Acta* 46 (1982) 2639-2658.
- [105] W.H. Johnson, W.H. Parsons, *Thermal expansion of concrete aggregate materials*, US Government Printing Office, 1944.
- [106] J.J. Valencia, P.N. Quested, *Thermophysical properties*, (2013).
- [107] S. Dalbin, G. Maurin, R.P. Nogueira, J. Persello, N. Pommier, Silica-based coating for corrosion protection of electrogalvanized steel, *Surface and Coatings Technology* 194 (2005) 363-371.
- [108] I. Santana, A. Pepe, E. Jimenez-Pique, S. Pellice, S. Ceré, Silica-based hybrid coatings for corrosion protection of carbon steel. Part I: Effect of pretreatment with phosphoric acid, *Surface and Coatings Technology* 236 (2013) 476-484.
- [109] V. Swamy, S.K. Saxena, B. Sundman, J. Zhang, A thermodynamic assessment of silica phase diagram, *Journal of Geophysical Research: Solid Earth* 99 (1994) 11787-11794.
- [110] A. Richter. Silica – a valuable and healthy geothermal by-product by Icelandic entrepreneurs, *Think GeoEnergy - Geothermal Energy News*.
- [111] G. Aristia, Istiqomah, N. Hidayat, Triwikantoro, M.A. Baqiya, S. Pratapa, Phase Analysis of Natural Silica-Sand-Based Composites as Potential Fuel-Cell Seal Material, *Advanced Materials Research* 1112 (2015) 294-298.
- [112] B.H. Stuart, *Infrared Spectroscopy: Fundamentals and Applications*, Wiley, 2004.
- [113] A.J. Bard, L.R. Faulkner, *Electrochemical Methods: Fundamentals and Applications*, Wiley, 2000.
- [114] M.E. Orazem, B. Tribollet, *Electrochemical impedance spectroscopy*, John Wiley & Sons, 2017.
- [115] G. Instruments, *Basics of electrochemical impedance spectroscopy*, G. Instruments, *Complex impedance in Corrosion* (2007) 1-30.
- [116] J.R. Macdonald, *Impedance spectroscopy*, *Annals of Biomedical Engineering* 20 (1992) 289-305.

- [117] G. Grundmeier, W. Schmidt, M. Stratmann, Corrosion protection by organic coatings: electrochemical mechanism and novel methods of investigation, *Electrochimica Acta* 45 (2000) 2515-2533.
- [118] F. Mansfeld, Use of electrochemical impedance spectroscopy for the study of corrosion protection by polymer coatings, *Journal of Applied Electrochemistry* 25 (1995) 187-202.
- [119] M.E. Orazem, B. Tribollet, Experimental Design, *Electrochemical Impedance Spectroscopy*, John Wiley & Sons, Inc.2008, pp. 129-152.
- [120] M.G. Fontana, R.W. Staehle, *Advances in Corrosion Science and Technology: Volume 1*, Springer US, 1970.
- [121] G.G. Wildgoose, D. Giovanelli, N.S. Lawrence, R.G. Compton, High-Temperature Electrochemistry: A Review, *Electroanalysis* 16 (2004) 421-433.
- [122] R. Bäßler, Beitrag zur Charakterisierung der inhibierenden Wirkung von Octadecylamin auf die Korrosion des Stahles 1.4541 bis 250 °C, Fakultät Mathematik und Naturwissenschaften, Dissertation, Technische Universität Dresden, 1997.
- [123] W.F. Bogaerts, Reference Electrodes for electrochemical measurements in high-temperature high-pressure aqueous environments—Review of potential corrections for ‘external’ reference systems, *Electrochimica Acta* 212 (2016) 102-112.
- [124] A. Vallejo Vitaller, U.M. Angst, B. Elsener, Corrosion Behaviour of L80 Steel Grade in Geothermal Power Plants in Switzerland, *Metals* 9 (2019) 331.
- [125] S. Soylemezoglu, R.J.G. Harper, Oxygen ingress into geothermal steam and its effect on corrosion of low carbon steel at Broadlands, New Zealand, 11 (1982) 31-42.
- [126] V. Goossens, J. Wielant, S. Van Gils, R. Finsy, H. Terryn, Optical properties of thin iron oxide films on steel, *Surface and Interface Analysis: An International Journal devoted to the development and application of techniques for the analysis of surfaces, interfaces and thin films* 38 (2006) 489-493.
- [127] F.F. Eliyan, E.-S. Mahdi, A.J.C.S. Alfantazi, Electrochemical evaluation of the corrosion behaviour of API-X100 pipeline steel in aerated bicarbonate solutions, 58 (2012) 181-191.
- [128] Q. Zhang, R. Tang, K. Yin, X. Luo, L.J.C.S. Zhang, Corrosion behavior of Hastelloy C-276 in supercritical water, 51 (2009) 2092-2097.
- [129] D.E. Talbot, J.D. Talbot, *Corrosion science and technology*, CRC press, 2018.
- [130] H. Leckie, H.J.J.o.t.e.s. Uhlig, Environmental factors affecting the critical potential for pitting in 18–8 stainless steel, 113 (1966) 1262-1267.
- [131] G. Baril, G. Galicia, C. Deslouis, N. Pébère, B. Tribollet, V. Vivier, An Impedance Investigation of the Mechanism of Pure Magnesium Corrosion in Sodium Sulfate Solutions, *Journal of The Electrochemical Society* 154 (2007) C108-C113.
- [132] R. Taylor, Influence of chloride on the formation of iron oxides from Fe (II) chloride. II. Effect of [Cl] on the formation of lepidocrocite and its crystallinity, *Clays and Clay Minerals* 32 (1984) 175-180.
- [133] R. Taylor, Influence of chloride on the formation of iron oxides from Fe (II) chloride. I. Effect of [Cl]/[Fe] on the formation of magnetite, *Clays and Clay Minerals* 32 (1984) 167-174.
- [134] T.-H. Le, Y. Kim, H. Yoon, Electrical and electrochemical properties of conducting polymers, *Polymers* 9 (2017) 150.

- [135] G.M.S. Gordon G . Wallace , Leon A . P . Kane-Maguire , and Peter R . Teasdale *Conductive Electroactive Polymers Intelligent Polymer Systems*, Third Edition, 2009.
- [136] M.V. Kulkarni, A.K. Viswanath, R. Marimuthu, T. Seth, Synthesis and characterization of polyaniline doped with organic acids, *Journal of Polymer Science Part A: Polymer Chemistry* 42 (2004) 2043-2049.
- [137] D. Sazou, C. Georgolios, Formation of conducting polyaniline coatings on iron surfaces by electropolymerization of aniline in aqueous solutions, *Journal of Electroanalytical Chemistry* 429 (1997) 81-93.
- [138] P.P. Deshpande, N.G. Jadhav, V.J. Gelling, D. Sazou, Conducting polymers for corrosion protection: a review, *Journal of Coatings Technology and Research* 11 (2014) 473-494.
- [139] T. Kobayashi, H. Yoneyama, H. Tamura, Oxidative degradation pathway of polyaniline film electrodes, *Journal of electroanalytical chemistry and interfacial electrochemistry* 177 (1984) 293-297.
- [140] J. Stejskal, P. Kratochvíl, A.D. Jenkins, The formation of polyaniline and the nature of its structures, *Polymer* 37 (1996) 367-369.
- [141] Y. Leng, *Materials Characterization: Introduction to Microscopic and Spectroscopic Methods*, John Wiley & Sons, 2009.
- [142] D.G. Weldon, *Failure analysis of paints and coatings*, John Wiley & Sons, 2009.
- [143] B.C. Smith, *Infrared spectral interpretation: a systematic approach*, CRC press, 2018.
- [144] M. Stratmann, 2005 W.R. Whitney Award Lecture: Corrosion Stability of Polymer-Coated Metals—New Concepts Based on Fundamental Understanding, *CORROSION* 61 (2005) 1115-1126.
- [145] W. Funke, The role of adhesion in corrosion protection by organic coatings, *Journal of the oil and colour chemists' association* 68 (1985) 229-232.
- [146] N.N.M. Emanuel, A.L. Buchachenko, *Chemical physics of polymer degradation and stabilization*, VSP, 1987.
- [147] C.H. Bamford, C.F.H. Tipper, R. Compton, *Ester formation and hydrolysis and related reactions*, Elsevier, 1972.
- [148] W.H. Cubberly, *Tool and Manufacturing Engineers Handbook Desk Edition*, Society of Manufacturing Engineers, 1989.
- [149] W.-H. Huang, C.-Y. Lin, Iron phosphate modified calcium iron oxide as an efficient and robust catalyst in electrocatalyzing oxygen evolution from seawater, *Faraday Discussions* 215 (2019) 205-215.
- [150] G. Górecki, Iron Phosphate Coatings—Composition and Corrosion Resistance, *CORROSION* 48 (1992) 613-616.
- [151] G. Górecki, Improved iron phosphate corrosion resistance by modification with metal ions, *Metal Finishing* 93 (1995) 36-39.
- [152] J.-M.R. Génin, L. Dhouibi, P. Refait, M. Abdelmoula, E. Triki, Influence of Phosphate on Corrosion Products of Iron in Chloride-Polluted-Concrete-Simulating Solutions: Ferrihydrite vs Green Rust, *CORROSION* 58 (2002) 467-478.
- [153] M.G. Han, Y.J. Lee, S.W. Byun, S.S. Im, Physical properties and thermal transition of polyaniline film, *Synthetic Metals* 124 (2001) 337-343.



- [154] Y. Cao, P. Smith, A.J. Heeger, Counter-ion induced processibility of conducting polyaniline and of conducting polyblends of polyaniline in bulk polymers, *Synthetic Metals* 48 (1992) 91-97.
- [155] D. Han, Y. Chu, L. Yang, Y. Liu, Z. Lv, Reversed micelle polymerization: a new route for the synthesis of DBSA–polyaniline nanoparticles, *Colloids and Surfaces A: Physicochemical and Engineering Aspects* 259 (2005) 179-187.
- [156] M.G. Han, S.K. Cho, S.G. Oh, S.S. Im, Preparation and characterization of polyaniline nanoparticles synthesized from DBSA micellar solution, *Synthetic Metals* 126 (2002) 53-60.
- [157] C.N.R. Rao, *Ultraviolet and Visible Spectroscopy*, 2nd Revised edition edition ed., Butterworth & Co Publishers Ltd, 1967.
- [158] M.D. Alam Khan, A. Akhtar, S. Ashfaq Nabi, Investigation of the electrical conductivity and optical property of polyaniline-based nanocomposite and its application as an ethanol vapor sensor, *New Journal of Chemistry* 39 (2015) 3728-3735.
- [159] S. Goswami, S. Nandy, T.R. Calmeiro, R. Igreja, R. Martins, E. Fortunato, Stress Induced Mechano-electrical Writing-Reading of Polymer Film Powered by Contact Electrification Mechanism, *Scientific Reports* 6 (2016) 19514.
- [160] G. Aristia, C. Roth, L.Q. Hoa, R. Bäßler, The Effect of Different Polyaniline Types in Silicon Dioxide Containing Coatings for Carbon Steel Protection in Artificial Geothermal Brines, *CORROSION 2019, NACE International, Nashville, Tennessee, USA, 2019*, pp. 14.
- [161] A.A. Salem, B.N. Grgur, The influence of the polyaniline initial oxidation states on the corrosion of steel with composite coatings, *Progress in Organic Coatings* 119 (2018) 138-144.
- [162] H. Jeon, C. Yoon, Y.-G. Song, J. Han, S. Kwon, S. Kim, I. Chang, K. Lee, Reducing the Coefficient of Thermal Expansion of Polyimide Films in Microelectronics Processing Using ZnS Particles at Low Concentrations, *ACS Applied Nano Materials* 1 (2018) 1076-1082.
- [163] R.-M. Wang, S.-R. Zheng, Y.-P. Zheng, 11 - Other properties of polymer composites, in: R.-M. Wang, S.-R. Zheng, Y.-P. Zheng (Eds.), *Polymer Matrix Composites and Technology*, Woodhead Publishing 2011, pp. 513-548.
- [164] F.B. Reig, J.V.G. Adelantado, M.C.M. Moya Moreno, FTIR quantitative analysis of calcium carbonate (calcite) and silica (quartz) mixtures using the constant ratio method. Application to geological samples, *Talanta* 58 (2002) 811-821.
- [165] L.H. Sperling, *Introduction to physical polymer science*, John Wiley & Sons, 2005.
- [166] J.N. Murray, Electrochemical test methods for evaluating organic coatings on metals: an update. Part I. Introduction and generalities regarding electrochemical testing of organic coatings, *Progress in Organic Coatings* 30 (1997) 225-233.
- [167] W. Von Baeckmann, W. Schwenk, W. Prinz, *Handbook of cathodic corrosion protection*, Elsevier, 1997.



# Appendix

## 1. Error Bar

Range and standard deviation (SD) are descriptive error bars used in the data analysis to show how the experimental data are spread. For example, corrosion rate graph shows error bars calculated by the formula:

$$SD = \sqrt{\frac{\sum(X - M)^2}{n - 1}}$$

where X refers to the individual data points, M is the mean, and n is the number of datapoints. Range and standard deviation were used in corrosion rate calculation, pit depth measurement by taking values of several pits from optical microscope.

### a). Values for Figure 4.1

#### 7 days, deaerated (Ar)

T (°C)	Corr Rate (mm/y)			
	Run 1	Run 2	Average	SD
25	0.0129	0.0160	0.0145	0.0015
70	0.0107	0.0080	0.0093	0.0013
150	0.0350	0.0321	0.0336	0.0014

#### 7 days, aerated

T (°C)	Corr Rate (mm/y)			
	Run 1	Run 2	Average	SD
25	0.0886	0.0802	0.0844	0.0042
70	0.1643	0.1748	0.1696	0.0052
150	0.3874	0.3083	0.3479	0.0396

#### 7 days, CO<sub>2</sub>

T (°C)	Corr Rate (mm/y)			
	Run 1	Run 2	Average	SD
70	0.1826	0.1280	0.1553	0.0273
150	0.2493	0.2310	0.2401	0.0091

### b). Values for Figure 4.8

#### 150 °C, deaerated (Ar)

days	Corr Rate (mm/y)				
	Run 1	Run 2	Run 3	Average	SD
7	0.0350	0.0321	0.0346	0.0339	0.0013
28	0.0019	0.0012	0.0019	0.0017	0.0003

#### 150 °C, aerated

days	Corr Rate (mm/y)				
	Run 1	Run 2	Run 3	Average	SD
7	0.3874	0.3083	N/A	0.3479	0.0396
28	0.0407	0.0367	0.0431	0.0387	0.0020

## 2. Crystallography Data for Quartz, and results from Match!3

*Matched Phases*

<b>Index</b>	<b>Amount (%)</b>	<b>Name</b>	<b>Formula sum</b>
A	100.0	Quartz	O2 Si
	0.9	Unidentified peak area	

A: Quartz (100.0 %)

Formula sum	O2 Si
Entry number	96-900-9667
Figure-of-Merit (FoM)	0.955236
Total number of peaks	35
Peaks in range	14
Peaks matched	14
Intensity scale factor	1.00
Space group	P 31 2 1
Crystal system	trigonal (hexagonal axes)
Unit cell	a= 4.9158 Å c= 5.4091 Å
I/Ic	4.52
Calc. density	2.644 g/cm <sup>3</sup>

Reference Gualtieri A. F., "Accuracy of XRPD QPA using the combined Rietveld-RIR method Locality: Baveno, Novara, Italy", *Journal of Applied Crystallography* 33, 267-278 (2000).

# Publication List

## International Conference

**Gabriela Aristia**, Le Quynh Hoa, and Ralph Bäßler, “Study of Polyaniline/Silicon Dioxide based Coating on Carbon Steel in Artificial Geothermal Brine”, *World Geothermal Congress 2020, Reykjavik, Iceland, Apr. 2020*.

**Gabriela Aristia**, Le Quynh Hoa, and Ralph Bäßler, “Effect of CO<sub>2</sub> Gas on Carbon Steel Corrosion in an Acidic-Saline Geothermal Solution”, *The European Corrosion Congress (EUROCORR), Seville, Spain, Sep. 2019*.

**Gabriela Aristia**, Christina Roth, Le Quynh Hoa, and Ralph Bäßler, “The Effect of Different Polyaniline Types in Silicon Dioxide Containing Coatings for Carbon Steel Protection in Artificial Geothermal Brines”, *NACE International’s CORROSION Conference & Expo, Nashville, TN, USA, Mar. 2019*.

**Gabriela Aristia**, Le Quynh Hoa, and Ralph Bäßler, “Electrochemical Deposition of Polyaniline on Carbon Steel for Corrosion Study in Geothermal Solution”, *The 4<sup>th</sup> International Conference of Functional Material Science, Bali, Indonesia, Nov. 2018*.

**Gabriela Aristia**, Ralph Bäßler, and Christina Roth, “Polyaniline/Silicon Dioxide Containing Coating for Use in Artificial Geothermal Brines”, *NACE International’s CORROSION Conference & Expo, Phoenix, AZ, USA, Mar. 2018*.

## Poster

**Gabriela Aristia**, Le Quynh Hoa, and Ralph Bäßler, “The Effect of CO<sub>2</sub> Gas in Geothermal Aquifer Fluid on the Corrosion Behaviour of Carbon Steel”, *The European Corrosion Congress (EUROCORR), Krakow, Poland, Sep. 2018*.

**Gabriela Aristia**, Ralph Bäßler, and Christina Roth. “Electrochemical Study of Polyaniline/Silicon Dioxide Containing Coatings in Geothermal Solution”, *NACE International’s CORROSION Conference & Expo, Phoenix, USA, Mar. 2018*.

**Gabriela Aristia**, Ralph Bäßler, and Christina Roth, “SiO<sub>2</sub> - Containing Organic Coatings for Geothermal Application”, *Gesellschaft für Korrosionsschutz (Gf-Korr) Jahrestagung, Frankfurt, Germany, Nov. 2017*.



# Acknowledgment

First and foremost, I would like to thank my primary PhD advisor Dr. Ralph Bäßler, for his continuous support, advice, encouragement, and patience throughout my PhD study. Without his support, supervision, knowledge, and his willingness to share his experiences, all this work would not have been possible. I would also like to thank Prof. Christina Roth, who has been very supportive throughout this work. I greatly appreciate all the time she spent to give me advice, in terms of my academic progress and scientific writing, and her continuous encouragement during my PhD. I would like to thank my PhD committee board member, especially Prof. Biprajit Sarkar, who is willing to review my dissertation.

I would like to express my gratitude and sincere appreciation to the Ministry of Finance of Indonesia for providing the financial support throughout my PhD study in the scheme of Indonesian Endowment Fund for Education (Lembaga Pengelola Dana Pendidikan, LPDP), so that the work was possible. I would also like to acknowledge Dr. Triwikantoro from Institut Teknologi Sepuluh Nopember Surabaya, Indonesia (ITS) who supported the work by providing silicon dioxide particles and commercial marine coatings available in Indonesia.

I am grateful to my colleague and friend, Dr. Le Quynh Hoa, who has been extremely helpful from the start to finish. She has been giving me a lot of help and inputs in my day-to-day experimental work, advice to solve some technical problems and she has always been open to have a scientific discussion, including during the process of writing my thesis and publications. I would like to thank Ulrich Klein who has always been supporting me to maintain the experimental equipment in order and functional, especially his tremendous help to fix and maintain the autoclaves. I greatly appreciate the help of Heike Strehlau, for her continuous support in the chemical laboratory. I also greatly appreciate the help of Sybille Engel and Andreas Grunewald for their support in preparing the cross sections of my samples and in taking the optical microscopic images. I would like to thank Michaela Buchheim and Romeo Saliwan Neumann from division 5.1 at BAM for their support and assistance in the SEM-EDX measurements and to Max Ebbisch from division 6.5 at BAM for his support in the FTIR and TGA measurements.

I am sincerely grateful for all the tremendous support, help, and friendship I received from my colleagues at the division 7.6. Corrosion and Corrosion Protection at BAM, both past and present. I am also grateful to all researchers, PhD students and Postdocs who are sharing the big office at BAM with me (both past and present) for the friendship and the valuable experiences in terms of research and personal life.

Finally, I would like to express my special gratitude to my family (my dad, mom, and brother) and my boyfriend for their continuous support during my PhD study.